School of Earth and Planetary Sciences

Mapping Planetary Surface Ages at Ultimate Resolutions with Machine Learning: The Moon

John Hugh Fairweather
0000-0002-3854-6311

This thesis is presented for the Degree of
Doctor of Philosophy - Applied Geology
of
Curtin University

September 2023

Declaration

To the best of my knowledge and belief this thesis contains no material previously published by any other person except where due acknowledgement has been made.

This thesis contains no material which has been accepted for the award of any other degree or diploma in any university.

Signature: 

Date: 28/03/2024

Abstract

The Moon's absence of an atmosphere and significant erosional mechanisms make it an ideal celestial body for preserving impact craters. When using a known crater accumulation rate, the number of impact craters across a given surface can be used to estimate a celestial surface's age. However, this method requires all craters above a specific size to be recorded and measured – a task typically accomplished by hand. Manual counting methodologies can be tedious as craters can number in the thousands across any surface. Therefore, a Crater Detection Algorithm (CDA) was developed to efficiently identify and record impact craters down to 10 pixels in size on high-resolution images. This thesis presents the development, evaluation, and use of the lunar CDA with three key phases. (1) The development and showcase of the CDA framework, which involves model training and evaluation. The overall evaluation results (True Positive rate) for the presented CDA are 93% and 98% for the Lunar Reconnaissance Orbiter - Narrow Angle Camera (LRO-NAC) images and Kaguya Terrain Camera (TC) images, respectively. (2) Using the CDA to derive model ages for young lunar craters and mare surfaces. It was shown that our CDA-derived ages are equivalent to published manually-derived ages while also emphasising the need to apply a CDA carefully. (3) Investigating the crater production over the last ~3 Ga. Here, we date 211 lunar impact craters and infer shifts in the crater production – highlighting that the crater production for impact craters may not be as constant as initially thought, wherein we see significant fluctuations within the large impactor population at ~500 Ma. Overall, this PhD project has emphasised the significance and challenges of high-resolution automated crater mapping while also opening the door to in-depth global lunar analysis, all of which aids in our understanding of the temporal evolution of our solar system.

The Acknowledgements

Before reading into all the aspects of teaching a stubborn computer algorithm to identify millions of small impact craters on the Moon, I would first like to thank and acknowledge some important people.

I would first like to thank my two supervisors. To Anthony, thank you for your unwavering ability to help in any number of ways throughout this PhD. I am honoured to be your first PhD student, which must have been a learning curve for us both, one for which I am eternally grateful. To Gretchen, thank you for the supervision throughout and the ability to pursue a PhD in a field of earth sciences that few can experience. From a small database volunteer to a complete PhD project, I am grateful for such an opportunity. Finally, I would like to thank Kosta. Though not an official supervisor, you were someone who helped me become semi-adept in the art of the Unix command line, script files, and probably much more.

It cannot be overstated how much I need to thank the Pit Crew, mainly Seamus and Hely, but also those who left, Andrea, Patrick, Tanja, and those who arrived, Ash, Sophie, Dale, and Ola. The dynamic in our office was much appreciated, and I hope it continues.

Ultimately, I thank my family (i.e., Mum) the most – without their (her) ongoing support, I would have happily become a garbageman.

Acknowledgement of Country

It is with my deepest respect; I acknowledge custodial and first nation communities all across Australia. In particular, I pay homage to the Whadjuk Noongar people of the Perth Boodja (region/country), my home. I give my respect to their ancestors and to all members, both present and emerging. I value their continuing culture and contribution to life in this region and this country. The dedication to collaborating with all individuals from Australia and around the globe lies at the heart of all work, embodying my values and commitment to advancing science in Australia as one.

Table of Contents

List of Figures

List of Tables

Chapter 1: Introduction

1.1 The Moon

The Moon has been an object of interest for humans for thousands of years, from its use in ancient cultures for navigation and timekeeping to solar system exploration by national space administrations (Galilei, 1610; Heiken et al., 1991). The Moon orbiting the Earth (at ~394,000 km away, on average) has significantly influenced the evolutionary development of our planet. As the Earth's only natural satellite, it dictates the ocean tides and stabilises the axial tilt, harbouring favourable conditions for our way of life (Morgan, 2001). Possibly one of the most infamous and significant aspects of the Moon is the countless impact craters covering its surface. One impact crater can be incredible, but hundreds of millions of craters can, and have, generated a whole field of geological science (see Baldwin, 1964; Opik, 1960; Shoemaker and Hackman, 1962). Studying impact craters upon the Moon's surface provides a unique window into the solar system's history, which can be used to unravel a series of chronological cosmic events that have influenced our planet (Shoemaker and Hackman, 1962; Shoemaker et al., 1963). The importance of understanding the Moon's surface goes beyond satisfying our curiosity; it allows for in-depth investigations into life's cosmic story.

The Moon formed approximately 4.5 billion years (Ga) ago, shortly after the Earth's accretion. There are many hypotheses regarding the specifics of its formation (Heiken et al., 1991). However, the leading and most accepted theory is that the Moon formed from the debris left over after a Mars-sized object [Theia] collided with the proto-Earth [Gaia] (Canup and Asphaug, 2001; Hartmann and Davis, 1975). This impact created a large disk of material around the Earth, eventually coalescing to form the Moon. After this stage, the Moon was an ocean of magma that slowly cooled and crystallised. This resulted in a pristine surface that would preserve billions of years of geological events (Wilhelms, 1987). The formation theory introduced above is supported by the samples collected during the Apollo (1969-1972) and Luna (1970-1976) missions, which indicate that the Moon and the Earth were very similar in terms of their primordial isotopic composition (Stöffler and Ryder, 2001). These samples also laid the groundwork for understanding lunar chronology (Heiken et al., 1991).

Moon’s surface is broadly subdivided into two terrains: Highlands and Mare. The highlands are an extensive region that covers approximately 85% of the lunar surface (Fortezzo et al., 2020; Wilhelms, 1987). The term lunar highlands can also be used interchangeably with the terms lunar crust or lunar terrain, as it is characteristic of what the majority of the Moon looks like (Heiken et al., 1991; Wilhelms, 1987). The highlands are a light-coloured, heavily cratered, rugged surface, making up the oldest regions across the Moon’s surface (Figure 1.1). When the Moon’s surface was completely molten shortly after its formation, lighter minerals (Such as plagioclase feldspar, a mineral high in Calcium and Aluminium) accumulated at the surface. As the Moon’s surface cooled, those minerals formed into rocks, forming the light-coloured lunar crust (Heiken et al., 1991). Over time, this terrain became very cratered, turning it into the rugged regolith we see today.

On the other hand, the lunar mare is dark-grey-coloured, relatively smooth and still heavily cratered. The term 'mare' is derived from the Latin word for 'sea'; early astronomers believed these regions to be similar to oceans (i.e., Galilei, 1610). Specifically, mare plains are basaltic flows formed from ancient volcanic eruptions, sometimes induced by significant impacts that fractured the lunar crust or other major mantle processes (Heiken et al., 1991). The majority (~94%) of the mare surfaces cluster on the Moon's near side, creating a significant dichotomy between the two sides of the Moon (Figure 1.1).

Although not celestially unusual, an exciting feature of the Moon is that it is tidally locked with the Earth. This means that the same side of the Moon always faces the Earth, giving the two lunar sides the terms 'near side' and 'far side'; this also made studying the Moon's far side impossible until the late 1950s (Heiken et al., 1991). Additionally, the mare dichotomy explained above is likely the result of variable crustal thickness between the Moon’s two sides, likely linked to the Moon being tidally locked with the Earth (Jolliff et al., 2000; Heiken et al., 1991).

In the decades since the first samples were brought back to the Earth, these lunar surfaces have been imaged in unprecedented detail by orbiters, such as Clementine (Bussey and Spudis, 2004), Lunar Reconnaissance Orbiter (Robinson et al., 2010), and SELENE/Kaguya (Haruyama et al., 2008). These image datasets provided an immense wealth of high-resolution information.

The data gathered by these missions have helped researchers get a more detailed understanding of the Moon's surface through digital elevation models (DEMs) (Figure 1.1), spectral maps in the UV and IR wavelengths, and millions of images. Using this remote sensing data, planetary scientists can quickly and accurately study the lunar surface.

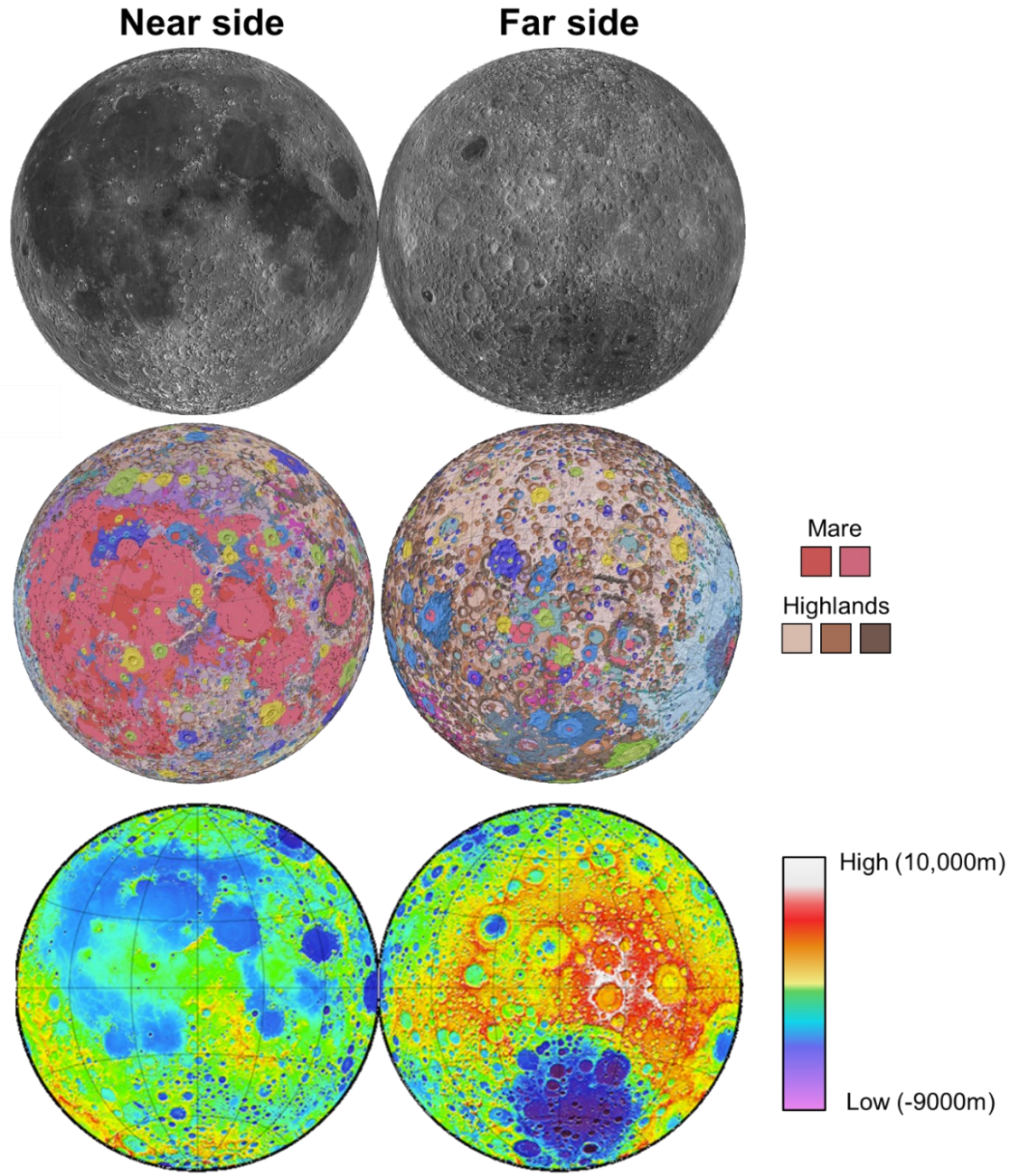

Figure 1.1: The near and far sides of the Moon's surface in an orthographic map projection. (Top) LRO Wide Angle Camera (WAC) mosaic (Speyerer et al., 2011); (Middle) unified geological map of the Moon in 1:5,000,000 scale with the simple colour key of the major lunar terrains. Note that the other colours not shown in the colour key refer to impact units (Fortezzo et al., 2020; NASA/USGS); (Bottom) Digital Elevation Model of the Moon (Smith et al., 2010).

1.2 Impact Craters

Impact cratering is the geological phenomenon wherein a crater forms when a smaller body collides with a larger one. This process happens across a wide range of sizes, from fractions of a meter to several hundreds of kilometres. The energy of an impact creates a shock wave that deforms and melts the target material, creating a bowl-shaped cavity (Melosh, 1989). In the early 1900s, the academic community was divided over the origin of lunar craters and their distribution across the surface (see Buratti, 2003; Dietz, 1946; Fielder, 1965; Hannay, 1892; Jaggar, 1947). Early studies by Gilbert (1893) and Gifford (193) strongly suggested that explosions of much magnitude caused the cavities seen on the Moon. However, they could not develop a systematic process to prove this (Gilvarry and Hill, 1956). Further analyses by MacDonald (1931) and Young (1940) quantified crater frequency distributions and indicated that cavities on this scale were not likely a result of volcanic activity but instead of an impact regime. Crater Size-Frequency Distribution (CSFD) analyses, where one looks at the relationship between the number of craters and their diameter size, provide more evidence tying craters to an impact origin (Baldwin, 1949; Fielder, 1965). However, this discussion slowly continued into the 1960s (Shoemaker, 1962), though it was mostly accepted that craters originated from impacts (see Opik, 1960). Ultimately, this was solved when the first Apollo samples were returned, and impact glasses and minerals were found (Chao et al., 1970; Gault, 1970a; Shoemaker et al., 1970; Vdovikina et al., 1975). Now we understand that crater formation through impacts is the most common phenomenon within the Solar System (Hartmann, 1965; Melosh, 1989).

1.2.1 Types of Impact Craters

Overall, there are two main types of impact craters that are commonly referred to in the literature. These are (1) Primary craters and (2) Secondary craters.

1. **Primary craters** are formed by the impact of a celestial object, which excavates and ejects material from the target surface, creating a large circular cavity (Melosh, 1989). Typically, these craters have an ejecta blanket of radially scattered fragments and material from the impact site. These craters are directly tied to the movement of space material within the solar system.
2. **Secondary craters** are formed by the ejected material from a primary impact (Pike and Wilhelms, 1978). As material is ejected from the primary crater, it

can travel long distances and impact surrounding terrains, typically at a lower velocity than primary impacts. They often appear in clusters/rays around primary craters (Figure 1.2). Mapping secondary craters can provide key information on the distribution/direction of ejected material (Dundas and McEwen, 2007). However, they are problematic when dating a surface, as they do not directly represent the movement of celestial material around the solar system.

Distinguishing primary craters from secondary craters can be challenging and interpretive, especially if the projectile fractures and/or disintegrates before impact. Atmospheric conditions, the velocity and composition of the projectile and the target body, and the observation scale can all influence one's ability to identify the crater type correctly. In some cases, smaller fragments separated from a main impacting body may strike the planet's surface far from the parent crater, giving rise to numerous randomly scattered secondary craters following the initial impact. Such craters would be indistinguishable from primary craters.

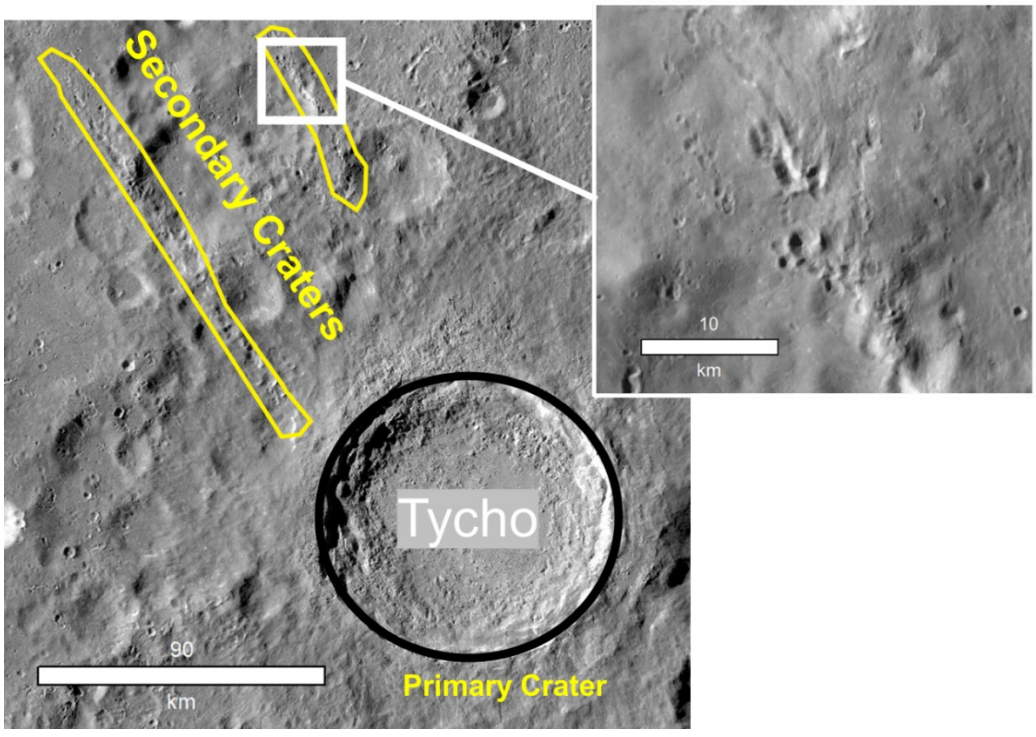

Figure 1.2: Example of a primary crater (Tycho) with radiating secondary craters. Note how the secondary craters form in clusters and chains, are much smaller, and radiate away from the primary they originate. The base image is the Wide-Angle Camera mosaic (Speyerer et al., 2011).

1.2.2 Impact Crater Formation

As impact craters form, they do so in 3 stages, which are described below. Below is a synthesis from Collins et al. (2012), French (1998), Ivanov et al. (1986), and Melosh (1989):

1. **Contact and Compression Stage** (Figure 1.3.a): At the collision, the impact generates enormous energy, leading to the compression and deformation of both the impacting object and the target material. The compression of the target material generates shock waves that radiate outwards from the point of impact.
2. **Excavation Stage** (Figure 1.3.b): in this stage, the shock waves generated by the impact cause the target material to be rapidly ejected and displaced. This ejection forms a transient cavity, known as the transient crater or the excavation cavity. The material in the transient cavity is highly fragmented and sometimes melted, and it is pushed outward and upward from the impact site. The size and depth of the transient crater depend on various factors, including the size, velocity, and angle of the impacting object, as well as the physical properties of the target material (density, porosity, and composition).
3. **Modification Stage** (Figure 1.3.c): The modification stage involves the collapse and modification of the transient cavity to form the final impact crater. The collapsing walls of the transient cavity rebound and slump back into the cavity, producing a raised rim around the crater. The collapsing material often undergoes fracturing and deformation, forming various features like central peaks, terraced walls, and uplifted rings (if the impact event is large enough). Secondary processes like tectonic activity (i.e., faults) can further modify the impact crater during this stage. These processes can alter the original shape of the crater, change the rim, and fill it with material.

It is important to note that the final stages of impact crater formation (Figure 1.3.d) can vary depending on the size, velocity, and angle of the impacting object, as well as the composition and structure of the target material (Holsapple and Schmidt, 1982; Melosh, 1989). Larger impacts exhibit more complex features and undergo additional processes, such as forming a central uplift and large-scale normal faults (Ivanov, 1986; Melosh, 1989).

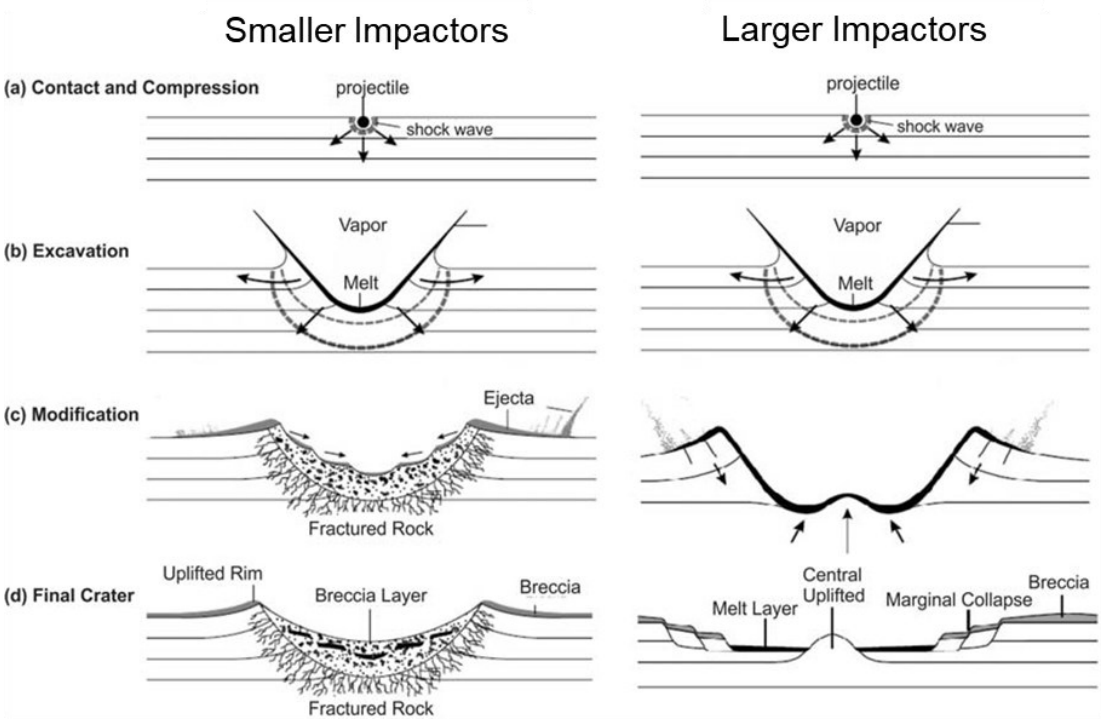

Figure 1.3: Stages of impact crater formation for a ~small impact event (Left) and a ~large impact event (Right). Notice how the stages (a) and (b) are the same in both cases but significantly differ during the modification stage (c), resulting in vastly different final crater morphologies (d). The figure was taken and adapted from French (1998).

1.2.3 Impact Crater Morphology

There are also four different crater morphologies associated with impact craters. Each shape depends on the impactor's size, host body size, and physical properties such as density and porosity. (Melosh and Ivanov, 1999). These crater morphologies are given descriptors: (1) simple, (2) complex, (3) peak-ring, and (4) multi-ring (Krüger et al., 2018; Melosh, 1989; Melosh and Ivanov, 1999). Each morphology and size described below is specific to the Moon.

1. **Simple Craters** are relatively small, smooth, and bowl-shaped in appearance (Figure 1.4). They usually have relatively flat or concave crater floors and raised rims, with no central peak or terraces. Simple craters are generally less than 20 km in diameter (Melosh, 1989; Stopar et al., 2017) and are the most common crater morphology across the Moon's surface.
2. **Complex Craters** are larger and have a complex internal structure (Figure 1.4). They characteristically have a central peak (or uplift) formed by the rebounding host rock after impact. The central peak can be surrounded by a raised rim that is hilly and irregular. Complex craters are between ~20 to

~140 km in diameter (Head, 2010; Melosh, 1989; Stopar et al., 2017). The transition between simple and complex craters occurs at ~17 km on the highlands and ~14 km on the mare terrains (Krüger et al., 2018).

3. **Peak-ring Craters/Basins** are complex craters with a central up-lifted ring rather than a single central peak (Figure 1.4). This ring is a circular ridge surrounding a central depression. Peak-ring basins vary in size but are mainly greater than ~140 km (Melosh, 1989; Morgan et al., 2016).

   The terms 'crater' and 'basin' can both be used to describe a significant circular depression, such as a peak-ring crater. The use of either term is dependent on the size and scale of the depression, where large impact structures (> 300 km) are called basins (Melosh, 1989).

4. **Multi-ring Basins** are the largest and most complex impact structures (Figure 1.4). They have multiple concentric rings with one or more uplifted ridges (Head, 2010; Melosh, 1989). Multi-ring craters are rarer than other impact structures (Melosh, 1989; Spudis, 1993). Understanding the formational processes of multi-ring basins is still a hot topic of ongoing research (see Bjonnes et al., 2023; Osinski et al., 2023).

A helpful metric to identify crater/basin morphology is the depth-to-diameter (d/D) ratio (Daubar et al., 2014; Pike, 1977). It is important to note that these ratios are generalisations, and there can be significant variations depending on specific factors, such as the size, velocity, angle of impact, and the properties of the target surface (Melosh, 1989). Typically, for craters less than 20 km in diameter, the depth-to-diameter ratio can be ~1:5 (Stopar et al., 2017). However, as the size of the impact crater increases, this ratio tends to decrease. The depth-to-diameter ratio becomes lower in larger impact craters, such as those with diameters greater than >20-100 km (Pike, 1977; Stopar et al., 2017). These craters tend to have flat bottoms and gently sloping sides. Therefore, the depth-to-diameter ratios can be ~1:10 or even much lower (Pike, 1977; Stopar et al., 2017).

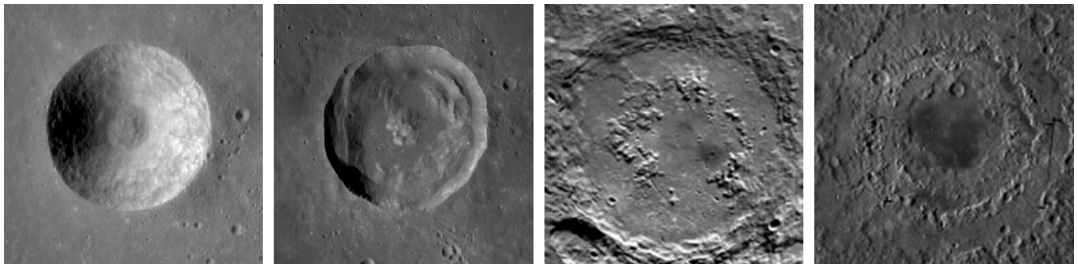

Figure 1.4: Impact craters morphologies on the Moon. (left to right): Simple crater [Euclides, 12 km diameter], Complex crater called [Euler crater, 28 km diameter], Peak-ring impact basin [Schrödinger basin, 320 km diameter], and Multi-ring impact basin called [Orientale basin, 970 km diameter]. Images are from the LROC-WAC mosaic (Speyerer et al., 2011).

1.2.4 Impactors

An 'impactor' is the name given to an object that collides with a host body, forming an impact crater. Impactors can originate from various sources within the solar system. The main types of impactors are (1) comets, (2) asteroids, (3) meteoroids, and (4) ejected material from other terrestrial bodies (Bailey, 1991; Gråe Jørgensen et al., 2009; Sears, 1978).

1. Comets are primarily icy bodies originating from the solar system's outer regions. As a comet approaches the Sun, the heat causes the ice to vaporise, releasing gas and dust, forming a glowing coma and a tail. An exciting thing about these impactors is the presence of volatiles (e.g., water) in these bodies (Alexander et al., 2018; Gaffey et al., 2011), which has implications for volatiles found on other planetary bodies. For example, the impact of asteroids and comets can be an appropriate explanation for how water was 'transported' to the Moon's surface (Barnes et al. 2016).
2. Asteroids are some of the most common impactors for the inner solar system. They primarily originate from the main asteroid belt and the Near Earth Object population (Strom et al., 2005, 2015), where material can change orbit due to collisional cascades and YORP (Yarkovsky-O'Keefe-Radzievskii-Paddack) effects, causing them to be ejected and cross paths with the Earth-Moon system (Baily, 1991; Rubincam, 2000; Spoto et al., 2015). It is important to note that many asteroids also contain significant amounts of water and volatiles bound in phyllosilicates (Alexander et al., 2018).

3. Meteoroids are smaller, rocky, or metallic objects remnants of asteroids or comets. They are smaller than the typical asteroid-sized impactor and can range in size from particles (mm-scale) to large boulders (m-scale). The exact transition between the terms small asteroid and large meteoroid is arbitrary.
4. Another event that can produce a significant amount of impactors is when a very large impactor strikes another terrestrial surface, and the energy of such impact can eject large fragments and accelerate them to escape velocities, launching them off the planet (see Artemieva and Ivanov, 2004). These fragments can later impact other bodies, such as the Moon or the Earth, transferring material between planets (Vickery and Melosh, 1987).

Due to the level of computational impact modelling over the last 50 years, researchers can now accurately estimate the sizes and properties of impactors [unknown variables] by studying the observable impact craters [measurable variables] (see Collins et al., 2004; 2012; Holsapple and Schmidt 1982; Hughes, 2003; Melosh, 1989). Using the measured values from prior studies (e.g., Hartmann, 1973; Kieffer and Simonds, 1980; Oberbeck and Quaide, 1968; Opik, 1936; 1958; Papike et al., 1982; Stopar et al., 2012), we can accurately estimate the initial size, speed, and compositions of impactors (Melosh, 1989). This helps planetary scientists estimate how much material can move around the solar system at any given time (see Sears, 1978). We can also understand past events in greater detail and extrapolate such data to grasp future events better (Grady et al., 1998; Hughes, 2003).

1.3 The Lunar Geological Timescale

The Moon has been subdivided into vastly different geological periods compared to the Earth's. On Earth, we can assign the different positions of the continents and living organisms to very accurate geological periods using radiometric dating of the samples collected worldwide; the Moon has a simpler geological timescale governed by significant impacts and major volcanic eruptions. It is important to note that the geological periods of the Moon are not as well-defined as those of the Earth, being based primarily on telescopic images and limited samples; the exact boundaries and durations of these periods are still the subject of scientific debate and ongoing research (Fortezzo et al., 2020; Stoffler and Ryder, 2001; Stoffler, 2006).

The Moon's geological history is divided into five geological periods. Described below are the accepted lunar periods with their respective age ranges defined by Wilhelms (1987):

1. [1]**Pre-Nectarian Period** [~4.5 to 3.92 Ga] (Figure 1.5.a): This period represents the earliest period of the Moon. During this time, the Moon was significantly bombarded by magnitudes of comets, asteroids, and meteoroids, all remnant material from the solar system's formation (Petro and Pieters, 2004). This period is defined by heavy cratering and the formation of massive impact basins, such as the South Pole–Aitken basin (D ≈ 2,500 km).
2. [1]**Nectarian Period** [3.92 to 3.85 Ga] (Figure 1.5.b): This period is defined by the formation of one of the Moon's oldest impact basins, the Nectaris basin. This basin was formed by a powerful impact, creating a significant circular depression in the Moon’s crust.
3. [1]**Imbrian Period** [3.85 to 3.2 Ga] (Figure 1.5.c, d): This period is subdivided into Early and Late epochs.
    a. [1]**Early Imbrian Epoch** [3.85 to 3.8 Ga] (Figure 1.5.c): This epoch takes its namesake from a significant impact event that formed the Imbrium impact basin. This epoch also includes the formation of other major lunar basins, such as Crisium, Tranquillitatis, Serenitatis, and Fecunditatis, which are predominantly located on the Moon's near side (Hiesinger et al., 2011; Spudis, 1993; Wilhelms, 1987), under the assumption that the ages of the Apollo and Luna samples date the

formation of these basins, which is still under debate within the scientific community[1].

b. **Late Imbrian Epoch** [3.8 to 3.2 Ga] (Figure 1.5.d): This epoch is characterised by volcanic eruptions, which led to the basins filled with erupted basalt lavas. The melting is believed to have been triggered by the large impact events during the late Imbrian period (Zhang et al., 2015).

4. **Eratosthenian Period** [3.2 to 1.1 Ga] (Figure 1.5.e): This was a time of continued volcanic activity and impact cratering across the Moon. This period is mainly defined by recent impact craters that lack a significant ray system or bright ejecta blanket. This period is also the longest, spanning 2.1 Ga. It reflects a time of steady cumulative impact crater formation as opposed to the exponential decay of the impact rate in earlier periods (Neukum, 1984).
5. **Copernican Period** [1.1 Ga to ~Present day] (Figure 1.5.f): This period is characterised by the formation of the youngest impact craters on the Moon. The largest of them (D > 10-20km) have distinct and definable crater ejecta blankets.

[1] It has been proposed that an additional period of intense celestial bombardment existed between 4.1 to 3.8 Ga, coined the Late Heavy Bombardment (LHB) or The Lunar Cataclysm (Wetherill, 1975). The LHB hypothesis emerged from preliminary observations of the Moon's surface, where evidence was found that alluded to a period of significantly bombardment. It has been suggested that this was sudden increase in the rate of large impacts outside the normal cratering rate. The objectives of this PhD thesis are not related to the investigation of the LHB hypothesis, this theory is not further discussed in this manuscript – see Bottke and Norman (2017) for an extensive review of the LHB.

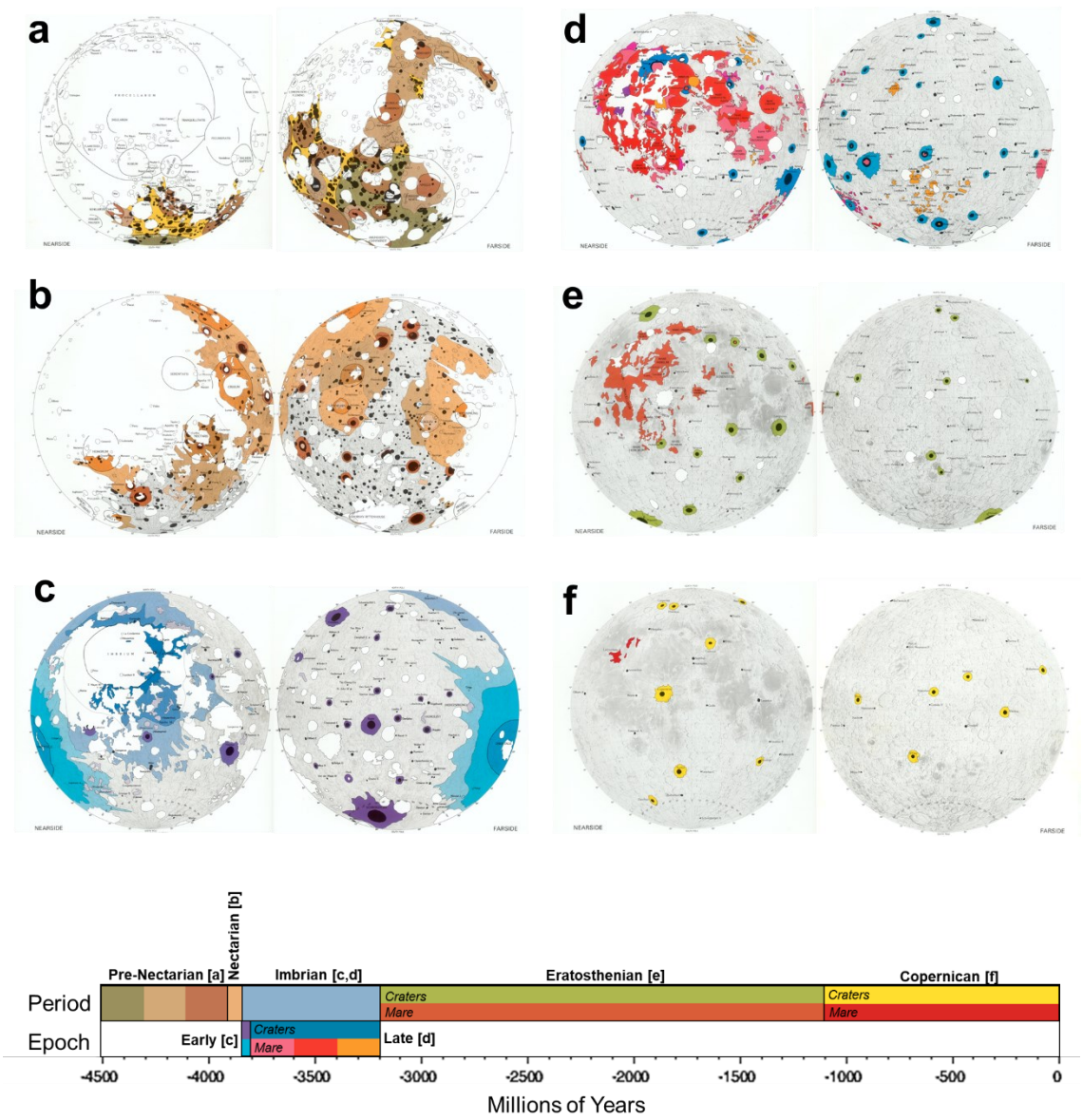

Figure 1.5: Geologic Periods of the Moon: (a) Pre-Nectarian Period [4.5 to 3.92 Ga]; (b) Nectarian Period [3.92 to 3.85 Ga]; (c) Early Imbrian Epoch [3.85 to 3.8 Ga]; (d) Late Imbrian Epoch [3.8 to 3.2 Ga]; (e) Eratosthenian Period [3.2 to 1.1 Ga]; and (f) Copernican Period [1.1 to 0.0 Ga]. Figure panels were modified from Wilhelms (1987). Both near and far-side lunar landscapes are subdivided and colour-coded by period; refer to the timescale key. Note that other timescales for the Moon have been proposed (see Appendix 1.1), but we will only use the Wilhelms (1987) timescale for this PhD.

1.4 The Moon as a Celestial Record

The different lunar terrains (Highland and Mare) are perfect for candidates generating a relative chronology system. Geologists and planetary scientists use relative chronologies to determine the order of events without knowing their true age. The fundamental law in any chronology system is superposition and cross-cutting relations, which state that the oldest layer is underneath and is cross-cut by the youngest layer (in an undisturbed natural sequence). Using this observation, scientists can use the stratigraphic relationships and positions of features to infer their relative order. Features such as lava flows and impact craters can be used for the Moon (Opik, 1960). Relative lunar chronologies can be refined by comparing different surfaces using crater densities (Shoemaker and Hickman, 1962). In the presence of a spatially random impact flux, the density of impact craters on a surface and how that density can change over time is the fundamental observation that has allowed scientists to date planetary bodies for the past 70 years (Opik, 1960; Hartmann, 1965; Shoemaker et al., 1970).

During the 1930s, the crater-time relationship was investigated and defined (see Young, 1940), and methods for counting craters were established (Opik, 1936; 1960; Hartmann, 1972; 1977). As the Moon has been subject to fewer geological processes that might erase or obliterate impact craters (such as aqueous or aeolian erosion or plate tectonics), defining a surface and determining a complete cratering density is a feasible task (Heiken et al., 1991; Hiesinger et al., 2011; Robbins, 2019; Shoemaker, 1964; Wilhelms, 1987). Additionally, impact craters on the Moon are well-preserved, allowing one to observe a record of events going back to ~4 Ga (Gault, 1970b; Hartmann, 1984; Neukum, 1984). The Moon's surface has been well studied, characterised, and visited by several international missions, such as the Apollo (11, 12, 14, 15, 16, 17), Luna (16, 20, 24) (Heiken et al., 1991; Stöffler and Ryder, 2001), and Chang'E (5) (Qian et al., 2021) missions. The samples brought back by these missions have been radiometrically dated and used to calibrate the lunar chronology system and geological time scale. These samples allow one to develop a function for calculating Absolute Model Ages (AMA) for any cratered lunar surface (Neukum, 1984; Neukum et al., 2001).

1.5 The Importance of Impact Crater Statistics

The study of impact craters is an integral part of planetary science, providing crucial insights into the history, evolution, and dynamics of planets, moons, and asteroids throughout the solar system (Fassett, 2016; Opik, 1960; Neukum et al., 2001). When analysing the distribution of impact craters on a planetary surface, researchers can estimate the changes in the frequency/rate of impactors that have impacted the planet over time (Kirchoff et al., 2021; Lagain et al., 2020; 2022; Mazrouei et al. 2019; Terada et al., 2020). Additionally, this provides meaningful insights into the movement and position of asteroids in the main asteroid belt, which is crucial for understanding the dynamics of the solar system and the potential hazards posed by near-Earth objects (Brown et al., 2002; Terada et al., 2020).

Impact craters are highly useful sources of information about the internal structure and composition of an impacted planetary body (see Fassett and Thomson, 2014). The size and shape of an impact crater can be used to estimate the size or speed of the impacting object (Melosh, 1989). Also, as described further above, during crater formation, impact craters excavate and distribute material (Sharpton, 2014). Therefore, looking at that originally buried material, we can infer the composition and structure of the lunar crust (He, 2020; McKay and Ming, 1990). Essentially, impact craters give a realistic way to analyse and investigate indirectly and sample worlds or areas humans cannot visit (van der Bogert et al., 2017).

Most importantly, by counting the number of craters of different sizes on a planetary surface, researchers estimate the age of the surface and the duration and intensity of geological processes (Opik, 1960; Hiesinger et al., 2011; Neukum et al., 2001). Therefore, investigating the differences in impact crater populations between planets and moons allows researchers to interpret the broader processes involved in planetary evolution (Head and Wilson, 2020; Hiesinger et al., 2016; Xie and Xiao, 2023). Any additional technique and method that aids in analysing impact craters will significantly contribute to all aspects of planetary science.

1.6 The Advent of Machine Learning in Planetary Science

The advancement of Machine Learning (ML) techniques has revolutionised many fields, and planetary science is no exception. In the last 10 years alone, ML technologies have significantly increased the amount of data researchers can process and interpret (Bhavsar and Ganatra, 2012; DeLatte et al., 2019; Zhang, 2010). This leap forward in data processing arose from the development of modern Convolutional Neural Networks (CNNs), which exponentially made ML methods more efficient and accurate (DeLatte et al., 2019). However, analysing large and cumbersome planetary datasets, including images, gravity surveys, and spectral data, can be challenging. Modern ML algorithms became the go-to answer as they can be used to analyse enormous datasets, make predictions, or classify data in a way that is faster and more efficient than traditional manual methods (Anantrasirichai et al., 2019; Anderson et al., 2020; Benedix et al., 2020; Cadogan, 2020; Fairweather et al., 2022; Lagain et al., 2021; Silburt et al., 2019; Wu et al., 2019).

The fundamental idea behind an ML algorithm is to process information to identify patterns and relationships within the data (Bhavsar and Ganatra, 2012). This information is then used to make predictions about new unseen data. The accuracy of these predictions can be improved by adjusting the algorithm's parameters and running it multiple times on the same dataset, a process known as training (Bhavsar and Ganatra, 2012; DeLatte et al., 2019). The algorithm's speed and accuracy depend on the dataset size and complexity. Each algorithm has specific strengths and weaknesses and is suited to different applications. However, ML algorithms are versatile and can be adjusted, future-proofing the technique. Some examples of the application of ML algorithms in planetary science are: surface feature detection (Anantrasirichai et al., 2019; Benedix et al., 2020; Bickel et al., 2019; Cadogan, 2020; Chen et al., 2021; Lagain et al., 2021; Silburt et al., 2019), meteorite detection (Anderson et al., 2020; 2022), global material and resource mapping (Kodikara and McHenry, 2020; Wu et al., 2019), and spectral analysis (Camboini et al., 2019; Lee et al., 2015).

1.7 Significance and Research Objective of This PhD Project

The study of impact craters on planetary surfaces is essential. However, traditional crater mapping methods rely on humans to manually identify and count craters, which can be time-consuming and subject to recognition bias and variabilities (see Lagain et al., 2021; Robbins et al., 2014). Early Crater Size-Frequency Distribution (CSFD) analyses derived a clear power law relationship between crater size and frequency. This means that when impact craters get smaller, there are exponentially more of them, making manual counting an unreasonably time-consuming task. Crater counting is particularly challenging for areas with high crater densities, especially when dating younger surfaces where one must count numerous small craters across large areas. More generally, crater statistical analyses require a complete crater population across a wide range of diameters, which can become very tedious when multiple surfaces need to be dated. Utilising an ML approach to crater counting overcomes these challenges by automating the process and allowing for a more objective and efficient analysis. ML algorithms can be trained to quickly identify and classify craters based on their shape and size, reducing the time and effort required by the manual counter. Additionally, the ability of algorithms to learn and adapt over time means that they can be improved.

The research objective of this PhD project was to train and optimise the Crater Detection Algorithm (CDA) developed by Benedix et al. (2020) and Lagain et al. (2021a,b) to detect impact craters across global high-resolution lunar imagery. The CDA will be applied to the highest resolution image datasets available for the Moon: Narrow-Angle Camera (NAC) and Kaguya Terrain Camera (TC) images. Here, we aim to uncover the cratering densities at the highest possible resolution. The automatic crater densities will be benchmarked against published manual measurements before the technique is deployed on numerous crater ejecta blankets to investigate potential temporal changes in crater production. This PhD project pushes above previous implementations of ML techniques on the grounds of scale.

The PhD project has three main aims, which are as follows:

1. To train and optimise a CDA model priorly used for Mars crater detection to detect lunar craters. This will be achieved with the following steps:
    a. Development of a machine learning training dataset consisting of labelled LRO-NAC (0.5-50 m/pixel) and Kaguya Terrain Camera (TC) (~7.5 m/pixel) image tiles;
    b. Using the training dataset, we will train two crater detection models, one optimised for NAC and one for Kaguya images;
    c. Finally, we will evaluate their accuracy using the Metrics Recall, Precision and F1 scores (these are explained in Chapter 3).
2. To show that the CDA models can be used for accurate model age derivation. This is done by implementing new NAC and Kaguya TC CDA models to detect craters for surface model age derivation for six relatively young areas across the moon's surface (three impact craters < 1 Ga and three mare areas < 3 Ga). This will be accomplished by:
    a. Deriving a CSFD and model age for each area and comparing them against published manual counts;
    b. Develop a systematic method to use automatic crater reliably counts across impact crater ejecta blankets.
    c. Further quantifying the accuracy of our model ages and method with the comparison data;
3. Investigating the global lunar crater production over the last 3 Ga using the CDA across the Kaguya TC images. This will be accomplished by:
    a. Calculating the model ages from the ejecta blankets of ~200 Copernican and Eratosthenian craters larger than 20 km;
    b. Plotting the total age-frequency distribution of the dated large craters and investigating the geospatial and diameter trends of the age distribution;
    c. Calculate statistically significant trends within the age distributions;
    d. Determine changes within the crater production for the Eratosthenian and Copernican periods and compare this against the prior crater production models.

1.8 Thesis Structure

This thesis presents the development, optimisation, evaluation, and use of a lunar Crater Detection Algorithm. Each chapter explores a different stage of the development and use of the Crater Detection Algorithm. Due to the composite style of this thesis, which includes peer-reviewed articles and unpublished manuscripts, there will be some repetition in each chapter's introductory and methodology sections. Additionally, as Chapters 3 and 4 have already been published, the formatting within this thesis will be different from the published formatting.

This thesis has a total of six chapters (including this Chapter [1]):

- **Chapter 2:** Methodology and Data. This chapter explains the inner workings of the crater count chronologies, how Convolutional Neural networks work, and finally, the resources used throughout the PhD.
- **Chapter 3:** Automatic Mapping of Small Lunar Impact Craters Using LRO-NAC Images. This methodology-based chapter details the processes needed to make and train our NAC version of the CDA and the current evaluations undertaken to determine the accuracy. This chapter has been published (Fairweather et al., 2022, https://doi.org/10.1029/2021EA002177).
- **Chapter 4:** Lunar Surface Model Age Derivation: Comparison Between Automatic and Human Crater Counting Using LRO-NAC and Kaguya TC Images. This chapter shows the accuracy and viability of using the crater detections produced by the CDA to date young lunar impact craters and surfaces. It compares our automatic results to published manual work. This chapter has been published (see Fairweather et al., 2023, https://doi.org/10.1029/2023EA002865).
- **Chapter 5:** Global analysis of Copernican and Eratosthenian craters using the CDA to test the hypothesis that all craters have formed consistently on the lunar surface over the last ~3.2 Ga. This chapter is being prepared for publication.
- **Chapter 6:** Conclusion and Synthesis. This chapter summarises the project's methodology, results, and findings, discusses the implications of machine learning algorithms in planetary science, and opens the discussion to possible future works.

1.9 Publications and Conference Papers

A list of all the publications and conference abstracts that have been submitted or work contributed to throughout this PhD is presented here. This project's contributions to the space science community have focused on ML, particularly the automatic detection of impact craters. This PhD has published two research articles. These articles comprise Chapters 3 and 4, focusing on developing and using the lunar crater detection model. Additionally, This PhD (which began in January 2020) was subject to the restrictions set in place during the COVID-19 global pandemic. This unfortunately led to limited opportunities to attend in-person conferences between 2020 and 2022. However, there was still participation in online conferences/meetings, such as 52nd and 53rd Lunar and Planetary Science Conference, the European Planetary Science Congress of 2022, and the Annual Meeting of Planetary Geologic Mappers of 2021. Fortunately, towards the end, it was possible to attend the 85th Annual Meeting of The Meteoritical Society in Glasgow and the 54th Lunar and Planetary Science Conference in Houston.

1.9.1 Research Articles: First Author

Fairweather, J. H., Lagain, A., Servis, K., & Benedix, G. K. (2023). Lunar Surface Model Age Derivation: Comparisons Between Automatic and Human Crater Counting Using LRO-NAC and Kaguya TC Images. Earth and Space Science, 10(7), e2023EA002865. https://doi.org/10.1029/2023EA002865

Fairweather, J. H., Lagain, A., Servis, K., Benedix, G. K., Kumar, S. S., & Bland, P. A. (2022). Automatic Mapping of Small Lunar Impact Craters Using LRO-NAC Images. Earth and Space Science, 9(7). https://doi.org/10.1029/2021EA002177

1.9.2 Research Articles: Co-author

Anderson, S. L., Towner, M. C., **Fairweather, J**., Bland, P. A., Devillepoix, H. A. R., Sansom, E. K., Cupák, M., Shober, P. M., & Benedix, G. K. (2022). Successful Recovery of an Observed Meteorite Fall Using Drones and Machine Learning. The Astrophysical Journal Letters, 930(2), L25. https://doi.org/10.3847/2041-8213/ac66d4

Lagain, A., Devillepoix, H. A. R., Vernazza, P., Robertson, D., Granvik, M., Pokorny, P., Ozerov, A., Shober, P. M., Jorda, L., Servis, K., **Fairweather, J. H.**, Quesnel, Y., & Benedix, G. K. (2024). Recalibration of the lunar chronology due to spatial cratering-rate variability. Icarus, 411, 115956. https://doi.org/10.1016/j.icarus.2024.115956

1.9.3 Conference Abstracts/Contributions

Fairweather, J. H., Lagain, A., Servis, K., Benedix, G. K (March 2023). Lunar Surface Model Age Derivation: Comparing Automatic and Human Crater Counting Across LRO-NAC and Kaguya TC Images. 54th Lunar and Planetary Science Conference, LPI Contribution No. 1234.

Fairweather, J. H., Lagain, A., Servis, K., Nemchin, A., Benedix, G. K., Bland, P. A. (August 2022). Finding Secondary Crater Clusters Using Automated Crater Detection Across Chang'E-5 Landing Site. 85th Annual Meeting of The Meteoritical Society, LPI Contribution No. 2695.

Fairweather, J. H., Lagain, A., Servis, K., Benedix, G. K., Bland, P. A. (March 2022). Using an Automated Crater Detection Algorithm as a Tool for Mapping Secondary Crater Clusters on the Moon: Chang'E 5 Landing Site. 53rd Lunar and Planetary Science Conference, LPI Contribution No. 2678.

Fairweather, J., Lagain, A., Servis, K., Benedix, G., and Bland, P. (September 2021). High-resolution Automated Crater Detection of Small Lunar Craters on LRO-NAC Images. European Planetary Science Congress 2021, EPSC2021-460.

Fairweather, J. H., Lagain, A., Servis, K., Benedix, G. K., Kumar, S. S., Bland, P. A. (June 2021). Using the Spatial Distribution of Automatically Detected Impact Crater's as a Tool to Map the Lunar Surface at High-Resolution. 2021 Annual Meeting of Planetary Geologic Mappers, LPI Contribution No. 2610.

Fairweather, J. H., Lagain, A., Servis, K., Benedix, G. K., Kumar, S. S., Bland, P. A. (March 2021). Automated Crater Detection on the Moon at High-Resolutions. 52nd Lunar and Planetary Science Conference, LPI Contribution No. 2548.

1.10 References

Alexander, C. M. O., McKeegan, K. D., & Altwegg, K. (2018). Water Reservoirs in Small Planetary Bodies: Meteorites, Asteroids, and Comets. Space Science Reviews, 214(1), 36. https://doi.org/10.1007/s11214-018-0474-9

Anantrasirichai, N., Biggs, J., Albino, F., & Bull, D. (2019). A deep learning approach to detecting volcano deformation from satellite imagery using synthetic datasets. Remote Sensing of Environment, 230, 111179. https://doi.org/10.1016/j.rse.2019.04.032

Anderson, S. L., Towner, M. C., Fairweather, J., Bland, P. A., Devillepoix, H. A. R., Sansom, E. K., Cupák, M., Shober, P. M., & Benedix, G. K. (2022). Successful Recovery of an Observed Meteorite Fall Using Drones and Machine Learning. The Astrophysical Journal Letters, 930(2), L25. https://doi.org/10.3847/2041-8213/ac66d4

Anderson, S., Towner, M., Bland, P., Haikings, C., Volante, W., Sansom, E., Devillepoix, H., Shober, P., Hartig, B., Cupak, M., Jansen-Sturgeon, T., Howie, R., Benedix, G., & Deacon, G. (2020). Machine learning for semi-automated meteorite recovery. Meteoritics & Planetary Science, 55(11), 2461–2471. https://doi.org/10.1111/maps.13593

Artemieva, N., & Ivanov, B. (2004). Launch of martian meteorites in oblique impacts. Icarus, 171(1), 84–101. https://doi.org/10.1016/j.icarus.2004.05.003

Bailey, M. E. (1991). Comet craters versus asteroid craters. Advances in Space Research, 11(6), 43–60. https://doi.org/10.1016/0273-1177(91)90231-8

Baldwin, R. B. (1949). The Craters of the Moon. Scientific American, 181(1), 20–24. https://doi.org/10.1038/scientificamerican0749-20

Baldwin, R. B. (1964). Lunar crater counts. The Astronomical Journal, 69, 377. https://doi.org/10.1086/109289

Barnes, J. J., Kring, D. A., Tartèse, R., Franchi, I. A., Anand, M., & Russell, S. S. (2016). An asteroidal origin for water in the Moon. Nature Communications, 7(1), 11684. https://doi.org/10.1038/ncomms11684

Benedix, G. K., Lagain, A., Chai, K., Meka, S., Anderson, S., Norman, C., Bland, P. A., Paxman, J., Towner, M. C., & Tan, T. (2020). Deriving Surface Ages on Mars Using Automated Crater Counting. Earth and Space Science, 7(3). https://doi.org/10.1029/2019EA001005

Bhavsar, H., & Ganatra, A. (2012). A Comparative Study of Training Algorithms for Supervised Machine Learning. International Journal of Soft Computing and Engineering (IJSCE), 2(4), 74–81.

Bhavsar, H., & Ganatra, A. (2012). A Comparative Study of Training Algorithms for Supervised Machine Learning. International Journal of Soft Computing and Engineering (IJSCE), 2(4), 74–81.

Bickel, V. T., Conway, S. J., Tesson, P.-A., Manconi, A., Loew, S., & Mall, U. (2020). Deep Learning-Driven Detection and Mapping of Rockfalls on Mars. IEEE Journal of Selected Topics in Applied Earth Observations and Remote Sensing, 13, 2831–2841. https://doi.org/10.1109/JSTARS.2020.2991588

Bjonnes, E., Johnson, B. C., & Andrews-Hanna, J. C. (2023). Basin Crustal Structure at the Multiring Basin Transition. Journal of Geophysical Research: Planets, 128(4), e2022JE007507. https://doi.org/10.1029/2022JE007507

Bogard, D. D. (1995). Impact ages of meteorites: A synthesis. Meteoritics, 30(3), 244–268. https://doi.org/10.1111/j.1945-5100.1995.tb01124.x

Bottke, W. F., & Norman, M. D. (2017). The Late Heavy Bombardment. Annual Review of Earth and Planetary Sciences, 45(1), 619–647. https://doi.org/10.1146/annurev-earth-063016-020131

Brown, P., Spalding, R. E., ReVelle, D. O., Tagliaferri, E., & Worden, S. P. (2002). The flux of small near-Earth objects colliding with the Earth. Nature, 420(6913), 294–296. https://doi.org/10.1038/nature01238

Bulyshev, A., Vanek, M., Amzajerdian, F., Pierrottet, D., Hines, G., & Reisse, R. (2011). A super-resolution algorithm for enhancement of FLASH LIDAR data (C. A. Bouman, I. Pollak, & P. J. Wolfe, Eds.; p. 78730F). https://doi.org/10.1117/12.876283

Buratti, B. J. (2003). Moon. In Encyclopedia of Physical Science and Technology (pp. 161–172). Elsevier. https://doi.org/10.1016/B0-12-227410-5/00460-9

Bussey, B., & Spudis, P. (2004). The Clementine Atlas of the Moon (1st ed.). Cambridge University Press. https://doi.org/10.1017/CBO9780511470820

Cadogan, P. H. (2020). Automated precision counting of very small craters at lunar landing sites. Icarus, 348, 113822. https://doi.org/10.1016/j.icarus.2020.113822

Cambioni, S., Delbo, M., Ryan, A. J., Furfaro, R., & Asphaug, E. (2019). Constraining the thermal properties of planetary surfaces using machine learning: Application to airless bodies. Icarus, 325, 16–30. https://doi.org/10.1016/j.icarus.2019.01.017

Canup, R. M., & Asphaug, E. (2001). Origin of the Moon in a giant impact near the end of the Earth's formation. Nature, 412(6848), 708–712. https://doi.org/10.1038/35089010

Chao, E. C. T., Boreman, J. A., Minkin, J. A., James, O. B., & Desborough, G. A. (1970). Lunar glasses of impact origin: Physical and chemical characteristics and geologic implications. Journal of Geophysical Research, 75(35), 7445–7479. https://doi.org/10.1029/JB075i035p07445

Collins, G. S., Melosh, H. J., & Ivanov, B. A. (2004). Modeling damage and deformation in impact simulations. Meteoritics & Planetary Science, 39(2), 217–231. https://doi.org/10.1111/j.1945-5100.2004.tb00337.x

Collins, G. S., Melosh, H. J., & Osinski, G. R. (2012). The Impact-Cratering Process. Elements, 8(1), 25–30. https://doi.org/10.2113/gselements.8.1.25

Daubar, I. J., Atwood-Stone, C., Byrne, S., McEwen, A. S., & Russell, P. S. (2014). The morphology of small fresh craters on Mars and the Moon: Fresh Crater d/D on Mars and the Moon. Journal of Geophysical Research: Planets, 119(12), 2620–2639. https://doi.org/10.1002/2014JE004671

DeLatte, D. M., Crites, S. T., Guttenberg, N., & Yairi, T. (2019). Automated crater detection algorithms from a machine learning perspective in the convolutional neural network era. Advances in Space Research, 64(8), 1615–1628. https://doi.org/10.1016/j.asr.2019.07.017

Dietz, R. S. (1946). The Meteoritic Impact Origin of the Moon's Surface Features. The Journal of Geology, 54(6), 359–375. JSTOR.

Drozd, R. J., Hohenberg, C. M., Morgan, C. J., & Ralston, C. E. (1974). Cosmic-ray exposure history at the Apollo 16 and other lunar sites: Lunar surface

dynamics. Geochimica et Cosmochimica Acta, 38(10), 1625–1642. https://doi.org/10.1016/0016-7037(74)90178-1

Drozd, R. J., Hohenberg, C. M., Morgan, C. J., Podosek, F. A., & Wroge, M. L. (1977). Cosmic Ray Exposure History at Taurus-Littrow. 8, 254.

Dundas, C. M., & McEwen, A. S. (2007). Rays and secondary craters of Tycho. Icarus, 186(1), 31–40. https://doi.org/10.1016/j.icarus.2006.08.011

Fairweather, J. H., Lagain, A., Servis, K., & Benedix, G. K. (2023). Lunar Surface Model Age Derivation: Comparisons Between Automatic and Human Crater Counting Using LRO-NAC and Kaguya TC Images. Earth and Space Science, 10(7), e2023EA002865. https://doi.org/10.1029/2023EA002865

Fairweather, J. H., Lagain, A., Servis, K., Benedix, G. K., Kumar, S. S., & Bland, P. A. (2022). Automatic Mapping of Small Lunar Impact Craters Using LRO-NAC Images. Earth and Space Science, 9(7). https://doi.org/10.1029/2021EA002177

Fassett, C. I. (2016). Analysis of impact crater populations and the geochronology of planetary surfaces in the inner solar system: Crater Populations and Surface Chronology. Journal of Geophysical Research: Planets, 121(10), 1900–1926. https://doi.org/10.1002/2016JE005094

Fassett, C. I., & Thomson, B. J. (2014). Crater degradation on the lunar maria: Topographic diffusion and the rate of erosion on the Moon: Crater degradation on the lunar maria. Journal of Geophysical Research: Planets, 119(10), 2255–2271. https://doi.org/10.1002/2014JE004698

Fielder, G. (1965). Distribution of Craters on the Lunar Surface. Monthly Notices of the Royal Astronomical Society, 129(5), 351–361. https://doi.org/10.1093/mnras/129.5.351

Fortezzo, C. M., Spudis, P. D., & Harrel, S. L. (2020). Release of the Digital Unified Global Geologic Map of the Moon at 1:5,000,000-Scale. 2760.

French, B. M. (1998). Traces of Catastrophe: A Handbook of Shock-Metamorphic Effects in Terrestrial Meteorite Impact Structures. In Traces of Catastrophe: A Handbook of Shock-Metamorphic Effects in Terrestrial Meteorite Impact Structures. LPI Contribution No. 954. https://ui.adsabs.harvard.edu/abs/1998trca.book.....F

Gaffey, M. J., Telles, E., Dupke, R., & Lazzaro, D. (2011). Mineralogy of Asteroids. 129–169. https://doi.org/10.1063/1.3636041

Galilei, G. (1610). Sidereus Nuncius. Thomas Baglioni, Venice, Italy, 1–29.

Gault, D. E. (1970a). Glass produced in the lunar regolith by meteoritic impact. Meteoritics, 5, 199.

Gault, D. E. (1970b). Saturation and Equilibrium Conditions for Impact Cratering on the Lunar Surface: Criteria and Implications. Radio Science, 5(2), 273–291. https://doi.org/10.1029/RS005i002p00273

Gifford, A. C. (1931). The Origin of the Surface Features of the Moon. Journal of the Royal Astronomical Society of Canada, 25, 70.

Gilbert, G. K. (1893). The moon's face. A study of the origin of its features. In Washington. https://ui.adsabs.harvard.edu/abs/1893mfso.book.....G

Gilvarry, J. J., & Hill, J. E. (1956). The Impact Theory of The Origin Of Lunar Craters. Publications of the Astronomical Society of the Pacific, 68(402), 223–229. JSTOR.

Grady, M. M., Hutchison, R., McCall, G. J. H., & Rothery, D. A. (1998). Meteorites: Their flux with time and impact effects. Geological Society, London, Special Publications, 140(1), 1–5. https://doi.org/10.1144/GSL.SP.1998.140.01.01

Gråe Jørgensen, U., Appel, P. W. U., Hatsukawa, Y., Frei, R., Oshima, M., Toh, Y., & Kimura, A. (2009). The Earth–Moon system during the late heavy bombardment period – Geochemical support for impacts dominated by comets. Icarus, 204(2), 368–380. https://doi.org/10.1016/j.icarus.2009.07.015

Grier, J. A., McEwen, A. S., Lucey, P. G., Milazzo, M., & Strom, R. G. (2001). Optical maturity of ejecta from large rayed lunar craters. Journal of Geophysical Research: Planets, 106(E12), 32847–32862. https://doi.org/10.1029/1999JE001160

Hannay, J. B. (1892). Formation of Lunar Volcanoes. Nature, 47(1201), 7–8. https://doi.org/10.1038/047007c0

Hartmann, W. K. (1965). Terrestrial and lunar flux of large meteorites in the last two billion years. Icarus, 4(2), 157–165. https://doi.org/10.1016/0019-1035(65)90057-6

Hartmann, W. K. (1972). Paleocratering of the Moon: Review of post-Apollo data. Astrophysics and Space Science, 17(1), 48–64. https://doi.org/10.1007/BF00642541

Hartmann, W. K. (1973). Ancient lunar mega-regolith and subsurface structure. Icarus, 18(4), 634–636. https://doi.org/10.1016/0019-1035(73)90066-3

Hartmann, W. K. (1977). Relative crater production rates on planets. Icarus, 31(2), 260–276. https://doi.org/10.1016/0019-1035(77)90037-9

Hartmann, W. K., & Davis, D. R. (1975). Satellite-sized planetesimals and lunar origin. Icarus, 24(4), 504–515. https://doi.org/10.1016/0019-1035(75)90070-6

Haruyama, J., Ohtake, M., Matsunaga, T., Morota, T., Yokota, Y., Honda, C., Hirata, N., Demura, H., Iwasaki, A., Nakamura, R., & Kodama, S. (2008). Planned radiometrically calibrated and geometrically corrected products of lunar high-resolution Terrain Camera on SELENE. Advances in Space Research, 42(2), 310–316. https://doi.org/10.1016/j.asr.2007.04.062

He, F. (2020). Remote sensing of planetary space environment. Chinese Science Bulletin, 65(14), 1305–1319. https://doi.org/10.1360/TB-2019-0804

Head, J. W. (2010). Transition from complex craters to multi-ringed basins on terrestrial planetary bodies: Scale-dependent role of the expanding melt cavity and progressive interaction with the displaced zone: COMPLEX CRATERS TO MULTI-RINGED BASINS. Geophysical Research Letters, 37(2), n/a-n/a. https://doi.org/10.1029/2009GL041790

Head, J. W., & Wilson, L. (2020). Rethinking Lunar Mare Basalt Regolith Formation: New Concepts of Lava Flow Protolith and Evolution of Regolith Thickness and Internal Structure. Geophysical Research Letters, 47(20). https://doi.org/10.1029/2020GL088334

Heiken, G., Vaniman, D., & French, B. M. (1991). Lunar Sourcebook: A User's Guide to the Moon. CUP Archive.

Hiesinger, H., Head, J. W., Wolf, U., Jaumann, R., & Neukum, G. (2011). Ages and stratigraphy of lunar mare basalts: A synthesis. In W. A. Ambrose & D. A. Williams, Recent Advances and Current Research Issues in Lunar

Stratigraphy. Geological Society of America. https://doi.org/10.1130/2011.2477(01)

Hiesinger, H., Marchi, S., Schmedemann, N., Schenk, P., Pasckert, J. H., Neesemann, A., O'Brien, D. P., Kneissl, T., Ermakov, A. I., Fu, R. R., Bland, M. T., Nathues, A., Platz, T., Williams, D. A., Jaumann, R., Castillo-Rogez, J. C., Ruesch, O., Schmidt, B., Park, R. S., … Raymond, C. A. (2016). Cratering on Ceres: Implications for its crust and evolution. Science, 353(6303), aaf4759. https://doi.org/10.1126/science.aaf4759

Holsapple, K. A., & Schmidt, R. M. (1982). On the scaling of crater dimensions: 2. Impact processes. Journal of Geophysical Research, 87(B3), 1849. https://doi.org/10.1029/JB087iB03p01849

Hughes, D. W. (2003). The approximate ratios between the diameters of terrestrial impact craters and the causative incident asteroids. Monthly Notices of the Royal Astronomical Society, 338(4), 999–1003. https://doi.org/10.1046/j.1365-8711.2003.06157.x

Ivanov, B., Bazilevskiy, A., & Sazonova, L. G. (1986). Formation of the central uplift in meteoric craters. Meteoritika, 40.

Jaggar, T. A. (1947). Origin and Development of Craters (Vol. 21). Geological Society of America. https://doi.org/10.1130/MEM21

Jolliff, B. L., Gillis, J. J., Haskin, L. A., Korotev, R. L., & Wieczorek, M. A. (2000). Major lunar crustal terranes: Surface expressions and crust-mantle origins. Journal of Geophysical Research: Planets, 105(E2), 4197–4216. https://doi.org/10.1029/1999JE001103

Kieffer, S. W., & Simonds, C. H. (1980). The role of volatiles and lithology in the impact cratering process. Reviews of Geophysics, 18(1), 143. https://doi.org/10.1029/RG018i001p00143

Kirchoff, M. R., Marchi, S., Bottke, W. F., Chapman, C. R., & Enke, B. (2021). Suggestion that recent (≤ 3 Ga) flux of kilometer and larger impactors in the Earth-Moon system has not been constant. Icarus, 355, 114110. https://doi.org/10.1016/j.icarus.2020.114110

Kodikara, G. R. L., & McHenry, L. J. (2020). Machine learning approaches for classifying lunar soils. Icarus, 345, 113719. https://doi.org/10.1016/j.icarus.2020.113719

Krüger, T., Hergarten, S., & Kenkmann, T. (2018). Deriving Morphometric Parameters and the Simple-to-Complex Transition Diameter From a High-Resolution, Global Database of Fresh Lunar Impact Craters (D ≥ ~ 3 km). Journal of Geophysical Research: Planets, 123(10), 2667–2690. https://doi.org/10.1029/2018JE005545

Lagain, A., Benedix, G. K., Servis, K., Baratoux, D., Doucet, L. S., Rajšic, A., Devillepoix, H. A. R., Bland, P. A., Towner, M. C., Sansom, E. K., & Miljković, K. (2021b). The Tharsis mantle source of depleted shergottites revealed by 90 million impact craters. Nature Communications, 12(1), 6352. https://doi.org/10.1038/s41467-021-26648-3

Lagain, A., Bouley, S., Baratoux, D., Costard, F., & Wieczorek, M. (2020). Impact cratering rate consistency test from ages of layered ejecta on Mars. Planetary and Space Science, 180, 104755. https://doi.org/10.1016/j.pss.2019.104755

Lagain, A., Kreslavsky, M., Baratoux, D., Liu, Y., Devillepoix, H., Bland, P., Benedix, G. K., Doucet, L. S., & Servis, K. (2022). Has the impact flux of

small and large asteroids varied through time on Mars, the Earth and the Moon? Earth and Planetary Science Letters, 579, 117362. https://doi.org/10.1016/j.epsl.2021.117362

Lagain, A., Servis, K., Benedix, G. K., Norman, C., Anderson, S., & Bland, P. A. (2021a). Model Age Derivation of Large Martian Impact Craters, Using Automatic Crater Counting Methods. Earth and Space Science, 8(2). https://doi.org/10.1029/2020EA001598

Lee, C. M., Cable, M. L., Hook, S. J., Green, R. O., Ustin, S. L., Mandl, D. J., & Middleton, E. M. (2015). An introduction to the NASA Hyperspectral InfraRed Imager (HyspIRI) mission and preparatory activities. Remote Sensing of Environment, 167, 6–19. https://doi.org/10.1016/j.rse.2015.06.012

MacDonald, T. L. (1931). A statistical investigation of diameter and distribution of lunar craters. J. Brit. Astron. Assoc, 41, 288.

Mazrouei, S., Ghent, R. R., Bottke, W. F., Parker, A. H., & Gernon, T. M. (2019). Earth and Moon impact flux increased at the end of the Paleozoic. Science, 363(6424), 253–257. https://doi.org/10.1126/science.aar4058

Mckay, D. S., & Ming, D. W. (1990). Properties of Lunar Regolith. In Developments in Soil Science (Vol. 19, pp. 449–462). Elsevier. https://doi.org/10.1016/S0166-2481(08)70360-X

Melosh, H. J. (1989). Impact Cratering: A Geologic Process. Oxford University Press. https://books.google.com.au/books?id=nZwRAQAAIAAJ

Melosh, H. J., & Ivanov, B. A. (1999). Impact Crater Collapse. Annual Review of Earth and Planetary Sciences, 27(1), 385–415. https://doi.org/10.1146/annurev.earth.27.1.385

Morgan, E. (2001). The Moon and Life on Earth. In C. Barbieri & F. Rampazzi (Eds.), Earth-Moon Relationships (pp. 279–290). Springer Netherlands. https://doi.org/10.1007/978-94-010-0800-6_25

Morgan, J. V., Gulick, S. P. S., Bralower, T., Chenot, E., Christeson, G., Claeys, P., Cockell, C., Collins, G. S., Coolen, M. J. L., Ferrière, L., Gebhardt, C., Goto, K., Jones, H., Kring, D. A., Le Ber, E., Lofi, J., Long, X., Lowery, C., Mellett, C., … Zylberman, W. (2016). The formation of peak rings in large impact craters. Science, 354(6314), 878–882. https://doi.org/10.1126/science.aah6561

Neukum, G. (1984). Meteoritenbombardement und Datierung planetarer Oberflachen (Meteorite bombardment and dating of planetary surfaces). University of Munich, Germany.

Neukum, G., Ivanov, B. A., & Hartmann, W. K. (2001). Cratering Records in the Inner Solar System in Relation to the Lunar Reference System. In R. Kallenbach, J. Geiss, & W. K. Hartmann (Eds.), Chronology and Evolution of Mars (Vol. 12, pp. 55–86). Springer Netherlands. https://doi.org/10.1007/978-94-017-1035-0_3

Oberbeck, V. R., & Quaide, W. L. (1968). Genetic implications of Lunar regolith thickness variations. Icarus, 9(1–3), 446–465. https://doi.org/10.1016/0019-1035(68)90039-0

Opik, E. J. (1936). Researches on the Physical Theory of Meteor Phenomena. I. Theory of the Formation of Meteor Craters. Publications of the Tartu Astrofizica Observatory, 28, 1–12.

Opik, E. J. (1960). The Lunar Surface as an Impact Counter. Monthly Notices of the Royal Astronomical Society, 120(5), 404–411. https://doi.org/10.1093/mnras/120.5.404

Osinski, G. R., Melosh, H. J., Andrews-Hanna, J., Baker, D., Denevi, B., Dhingra, D., Ghent, R., Hayne, P. O., Hill, P., James, P. B., Jaret, S., Johnson, B., Kenkmann, T., Kring, D., Mahanti, P., Minton, D., Neish, C. D., Neumann, G., Plescia, J., … Zellner, N. (2023). Lunar Impact Features and Processes. Reviews in Mineralogy and Geochemistry, 89(1), 339–371. https://doi.org/10.2138/rmg.2023.89.08

Papike, J. J., Simon, S. B., & Laul, J. C. (1982). The lunar regolith: Chemistry, mineralogy, and petrology. Reviews of Geophysics, 20(4), 761. https://doi.org/10.1029/RG020i004p00761

Petro, N. E., & Pieters, C. M. (2004). Surviving the heavy bombardment: Ancient material at the surface of South Pole-Aitken Basin. Journal of Geophysical Research, 109(E6), E06004. https://doi.org/10.1029/2003JE002182

Pike, R. J. (1977). Apparent depth/apparent diameter relation for lunar craters. Lunar and Planetary Science Conference Proceedings, 3, 3427–3436.

Pike, R. J., & Wilhelms, D. E. (1978). Secondary-Impact Craters on the Moon: Topographic Form and Geologic Process. 907–909.

Qian, Y., Xiao, L., Wang, Q., Head, J. W., Yang, R., Kang, Y., van der Bogert, C. H., Hiesinger, H., Lai, X., Wang, G., Pang, Y., Zhang, N., Yuan, Y., He, Q., Huang, J., Zhao, J., Wang, J., & Zhao, S. (2021). China's Chang'e-5 landing site: Geology, stratigraphy, and provenance of materials. Earth and Planetary Science Letters, 561, 116855. https://doi.org/10.1016/j.epsl.2021.116855

Robbins, S. J. (2019). A New Global Database of Lunar Impact Craters >1–2 km: 1. Crater Locations and Sizes, Comparisons With Published Databases, and Global Analysis. Journal of Geophysical Research: Planets, 124(4), 871–892. https://doi.org/10.1029/2018JE005592

Robbins, S. J., Antonenko, I., Kirchoff, M. R., Chapman, C. R., Fassett, C. I., Herrick, R. R., Singer, K., Zanetti, M., Lehan, C., Huang, D., & Gay, P. L. (2014). The variability of crater identification among expert and community crater analysts. Icarus, 234, 109–131. https://doi.org/10.1016/j.icarus.2014.02.022

Robinson, M. S., Brylow, S. M., Tschimmel, M., Humm, D., Lawrence, S. J., Thomas, P. C., Denevi, B. W., Bowman-Cisneros, E., Zerr, J., Ravine, M. A., Caplinger, M. A., Ghaemi, F. T., Schaffner, J. A., Malin, M. C., Mahanti, P., Bartels, A., Anderson, J., Tran, T. N., Eliason, E. M., … Hiesinger, H. (2010). Lunar Reconnaissance Orbiter Camera (LROC) Instrument Overview. Space Science Reviews, 150(1–4), 81–124. https://doi.org/10.1007/s11214-010-9634-2

Rubincam, D. P. (2000). Radiative Spin-up and Spin-down of Small Asteroids. Icarus, 148(1), 2–11. https://doi.org/10.1006/icar.2000.6485

Sears, D. W. (1978). The nature and origin of meteorites. In Monographs on Astronomical Subjects. https://ui.adsabs.harvard.edu/abs/1978nom..book.....S

Sharpton, V. L. (2014). Outcrops on lunar crater rims: Implications for rim construction mechanisms, ejecta volumes and excavation depths: Outcrops constrain crater rim components. Journal of Geophysical Research: Planets, 119(1), 154–168. https://doi.org/10.1002/2013JE004523

Shoemaker, E. M. (1962). Chapter 8: Interpretation of lunar craters. In Physics and Astronomy of the Moon (Vol. 6, pp. 283–359). Soviet Astronomy.

Shoemaker, E. M. (1964). The Geology of the Moon. Scientific American, 211, 38–47.

Shoemaker, E. M., & Hackman, R. J. (1962). Stratigraphic Basis for a Lunar Time Scale. In The Moon (Vol. 14, pp. 289–300). https://ui.adsabs.harvard.edu/abs/1962IAUS...14..289S

Shoemaker, E. M., Hackman, R. J., & Eggleton, R. E. (1963). Interplanetary Correlation of Geologic Time. Advances in Astronautical Sciences, 8.

Shoemaker, E. M., Hait, M. H., Swann, G. A., Schleicher, D. L., Dahlem, D. H., Schaber, G. G., & Sutton, R. L. (1970). Lunar Regolith at Tranquillity Base. Science, 167(3918), 452–455. https://doi.org/10.1126/science.167.3918.452

Smith, D. E., Zuber, M. T., Neumann, G. A., Lemoine, F. G., Mazarico, E., Torrence, M. H., McGarry, J. F., Rowlands, D. D., Head, J. W., Duxbury, T. H., Aharonson, O., Lucey, P. G., Robinson, M. S., Barnouin, O. S., Cavanaugh, J. F., Sun, X., Liiva, P., Mao, D., Smith, J. C., & Bartels, A. E. (2010). Initial observations from the Lunar Orbiter Laser Altimeter (LOLA): LOLA INITIAL OBSERVATIONS. Geophysical Research Letters, 37(18), n/a-n/a. https://doi.org/10.1029/2010GL043751

Speyerer, E. J., Robinson, M. S., Denevi, B. W., & LROC Science Team. (2011). Lunar Reconnaissance Orbiter Camera Global Morphological Map of the Moon. 2387.

Spoto, F., Milani, A., & Knezevic, Z. (2015). Asteroid family ages. https://doi.org/10.48550/ARXIV.1504.05461

Spudis, P. D. (1993). The Geology of Multi-ring Impact Basins. In The Geology of Multi-ring Impact Basins. https://ui.adsabs.harvard.edu/abs/1993gmri.book.....S

Stoffler, D. (2006). Cratering History and Lunar Chronology. Reviews in Mineralogy and Geochemistry, 60(1), 519–596. https://doi.org/10.2138/rmg.2006.60.05

Stöffler, D., & Ryder, G. (2001). Stratigraphy and Isotope Ages of Lunar Geologic Units: Chronological Standard for the Inner Solar System. Space Science Reviews, 96(1/4), 9–54. https://doi.org/10.1023/A:1011937020193

Stopar, J. D., Robinson, M. S., Barnouin, O. S., McEwen, A. S., Speyerer, E. J., Henriksen, M. R., & Sutton, S. S. (2017). Relative depths of simple craters and the nature of the lunar regolith. Icarus, 298, 34–48. https://doi.org/10.1016/j.icarus.2017.05.022

Stopar, J. D., Robinson, M. S., Speyerer, E. J., Burns, K., Gengl, H., & Lroc Team. (2012). Regolith Characterization Using LROC NAC Digital Elevation Models of Small Lunar Craters. 2729.

Terada, K., Morota, T., & Kato, M. (2020). Asteroid shower on the Earth-Moon system immediately before the Cryogenian period revealed by KAGUYA. Nature Communications, 11(1), 3453. https://doi.org/10.1038/s41467-020-17115-6

van der Bogert, C. H., Hiesinger, H., Dundas, C. M., Krüger, T., McEwen, A. S., Zanetti, M., & Robinson, M. S. (2017). Origin of discrepancies between crater size-frequency distributions of coeval lunar geologic units via target property contrasts. Icarus, 298, 49–63. https://doi.org/10.1016/j.icarus.2016.11.040

Vdovikina, V. G., Vdovikin, G. P., & Turkina, L. F. (1975). The origin of the lunar regolith. Akademiia Nauk Ukrains Koi RSR Dopovidi Seriia Fiziko Matematichni Ta Tekhnichni Nauki, 1059–1062.

Vickery, A. M., & Melosh, H. J. (1987). The Large Crater Origin of SNC Meteorites. Science, 237(4816), 738–743. https://doi.org/10.1126/science.237.4816.738

Wetherill, G. W. (1975). Late heavy bombardment of the moon and terrestrial planets. Lunar and Planetary Science Conference Proceedings, 2, 1539–1561.

Wilhelms, D. E. (1987). The geologic history of the Moon (USGS Numbered Series No. 1348; Professional Paper, p. 337). United States Geological Survey. https://doi.org/10.3133/pp1348

Wu, B., Ross W. K., P., Ludivig, P., Chung, A. S., & Seabrook, T. (2019). Absolute Localization Through Orbital Maps and Surface Perspective Imagery: A Synthetic Lunar Dataset and Neural Network Approach. 2019 IEEE/RSJ International Conference on Intelligent Robots and Systems (IROS), 3262–3267. https://doi.org/10.1109/IROS40897.2019.8968124

Xu, L., & Xie, M. (2020). Ejecta Thickness Distribution of the Schrödinger Basin on the Moon. Journal of Geophysical Research: Planets, 125(12). https://doi.org/10.1029/2020JE006506

Young, J. (1940). A statistical investigation of diameter and distribution of lunar craters. J. Brit. Astron. Assoc, 50(9), 309–326.

Zhang, J., Yang, W., Hu, S., Lin, Y., Fang, G., Li, C., Peng, W., Zhu, S., He, Z., Zhou, B., Lin, H., Yang, J., Liu, E., Xu, Y., Wang, J., Yao, Z., Zou, Y., Yan, J., & Ouyang, Z. (2015). Volcanic history of the Imbrium basin: A close-up view from the lunar rover Yutu. Proceedings of the National Academy of Sciences, 112(17), 5342–5347. https://doi.org/10.1073/pnas.1503082112

Zhang, Y. (2010). New Advances in Machine Learning. InTech. 978-953-307-034-6.

Chapter 2: Methodology, Techniques, and Datasets

2.1 Crater Count Chronologies

Crater counting is the primary technique used in this project to determine the ages of the lunar surface. The technique has two major assumptions: (1) that the rate of crater formation is defined and that crater production (dependent on the impact flux of asteroids) is homogeneous across the surface, and (2) that the number of craters larger than a given size has been retained since the surface formation, and this density of accumulated craters represents the surface's age (Crater analysis techniques working group, 1979; Hartmann, 1984; Neukum, 2001). Using these assumptions, we can determine a chronological age for any surface by plotting the density of mapped craters within a determined count area and interpreting the crater population's size-frequency distribution. This technique is the primary method used to determine the age of any surface across all cratered terrestrial bodies, not only the Moon (Neukum et al., 2001) but also on Mars (Hartmann, 2007; Hartmann and Daubar, 2017), Mercury (Le Feuvre and Wieczorek, 2011), Vesta (Schmedemann et al., 2014), and Ceres (Hiesinger et al., 2016).

2.1.1 The Development of Crater Chronologies

The fundamental principles for crater chronologies were primarily defined in the late 1950s by Opik (1958, 1960), who quantitively determined that the number of superimposed craters would define how old a surface could be. Shoemaker and Hickman (1962) and Baldwin (1964) took it further. They discussed the capability of using estimated cratering rates and the flux of meteoritic material to establish a chronology model for the formation of cratered geological units and events. These estimates came from examining impact craters, bolide detonations, and nuclear explosions on Earth (see Brown et al., 2002; Nemtchinov et al., 1997; Nordyke, 1961). From this, they derived a log-linear relationship between crater size and cumulative number per unit area. Hartmann (1965) combined all the previous work and unified them into a framework that we still use today. The return of lunar samples has also dramatically improved the accuracy of this technique. Crater counting is now standard practice used in all areas of planetary sciences (Crater Analysis Techniques Working Group, 1979).

2.1.2 The Production Function

In crater counting, the Production Function (PF) is a mathematical model used to estimate the number of craters that should exist on the surface of a planetary body over time (Hartmann, 1984; Neukum, 1984; Neukum et al., 2001). The critical idea of the PF is that craters are produced over time due to impacts via asteroids and comets. The number of craters that form depends on several factors, including the size of the body, the surface rheology, position in the solar system, and the calculated frequency of orbiting/impacting material (Hartmann, 1984; Neukum, 1984). The PF quantifies these factors by using an equation that defines the rate of crater formation (known as the production rate) to the relative age of the surface (see Ivanov (2008) for a review). The production rate is often expressed in units of craters per unit area per unit time, such as craters per square kilometre per billion years (craters/km²/Ga). Different PFs have been defined over the years, but the two most used are the Hartmann (1984; 1995) Production Function (HPF) and the Neukum (1984) Production Function (NPF). Here, we describe the widely used NPF [Eq. 2.1] (defined as an 11^{th} degree polynomial equation):

[**Eq. 2.1**]

$$\log_{10}(N) = \sum_{j=0}^{11} aj \times [\log_{10}(D)]^j$$

Where D is the crater diameter in km, N is the number of craters per km^2 per billion years (craters/km²/Ga), and the coefficients aj are given in Table 2.1.

The NPF is defined for impact craters between 10 m to 300 km in diameter (Neukum et al., 2001). The coefficients (Table 2.1) are determined by fitting the function to measured CSFDs on a planetary surface, the Moon in this case. Using the function with these coefficients, one can estimate the production of craters across the lunar surface. The HPF serves the same purpose but chooses a piecewise $\log_{10}$ approach (see Ivanov et al. (2002) for a review), defining the PF using three equations valid for different crater size ranges (i.e., [1] 300 m < D < 1.41 km, [2] 1.41 km < D < 64 km, [3] D > 64km) (Hartmann, 1984, 1994, 1999).

Table 2.1: Coefficients for Neukum (1984)'s PF and Neukum et al. (2001)'s updated PF. Coefficients are used in Eq. 2.1.

Coefficient	**(N1km) values** (Neukum, 1984)	**(N1km) values** (Neukum et al., 2001)
a_0	-3.0768	-3.0876
a_1	-3.6269	-3.557528
a_2	+0.4366	+0.781027
a_3	+0.7935	+1.021521
a_4	+0.0865	-0.156012
a_5	-0.2649	-0.444058
a_6	-0.0664	+0.019977
a_7	+0.0379	+0.086850
a_8	+0.0106	-0.005874
a_9	-0.0022	-0.006809
a_{10}	-5.18×10^{-4}	$+8.25\times10^{-4}$
a_{11}	$+3.97\times10^{-5}$	$+5.54\times10^{-5}$

2.1.3 The Chronology Function

The crater counting Chronology Function (CF) is another key model used to determine the age of a planetary surface (see Neukum, 1984; Neukum et al., 2001). The principle of this function is that older surfaces will have a higher density of differently-sized impact craters, while younger surfaces will have a lower density of impact craters. Where the production function estimates the number and size of craters that would form on the surface, the CF determines a surface's numerical age (in years) (Neukum, 1984; Neukum et al., 2001). The CF has been defined using the relationship between the radiometric surface age and the cratering density (Neukum, 1984). The function is determined and calibrated by measuring the density of craters on the surface in combination with known radiometric ages taken from lunar samples (Figure 2.1.a; Table 2.2). The combination of absolute radiometric ages and the geographic distribution of craters defines a best-fit curve (i.e., the Chronology Function).

[**Eq. 2.2**]

$$N(1km) = 5.44 \times 10^{-14} \times \left(e^{(6.93 \times T)}\right) + 8.38 \times 10^{-4} \times T$$

Here is an example of the widely used Neukum (1984) CF for the Moon [Eq. 2.2], Where *N (1km)* is the cumulative density of craters with diameter >1 km per square kilometre, and *T* is the age of the surface in Ga. The graphical representation of this function, with a reference diameter of 1 km, is displayed in Figure 2.1.a.

It is common when displaying the model age calculated by a CF one also displays the N(1) value (also commonly written as 'N_{cum}(1km)', 'N(≥1km)', or a combination of the three). Traditionally, the N(1) value represents the count of craters for the largest diameter category or the largest individual crater on the planetary surface (Crater Analysis Techniques Working Group, 1979). However, it is important to remember that N(1) can have two meanings. (1) The measured N(1) (i.e., the number of craters >1 km observed and measured on the counting area), and (2) the extrapolated N(1) (i.e., the number of craters >1km that you extract from the PF that you fitted with your CSFD). Therefore, when reporting absolute model ages, the N(1) value typically refers to the extrapolated value.

It is important to note that our understanding of the frequency of craters over time is based on various datasets (i.e., lunar samples and crater density observations). However, the general understanding is that the impact cratering rate decreased over time until 3 Ga ago (Figure 2.1.b), before being constant (within a factor of ~2 of uncertainties) over the last 3 Ga (Neukum et al., 2001). While the exact rate and shape of this decrease are still a topic of ongoing research (e.g., Kirchoff et al., 2021; Lagain et al., 2020, 2022; Mazrouei et al., 2019; Terada et al., 2020), and the impact cratering rates may not be as smooth or linear, as typically shown (Figure 2.1.b).

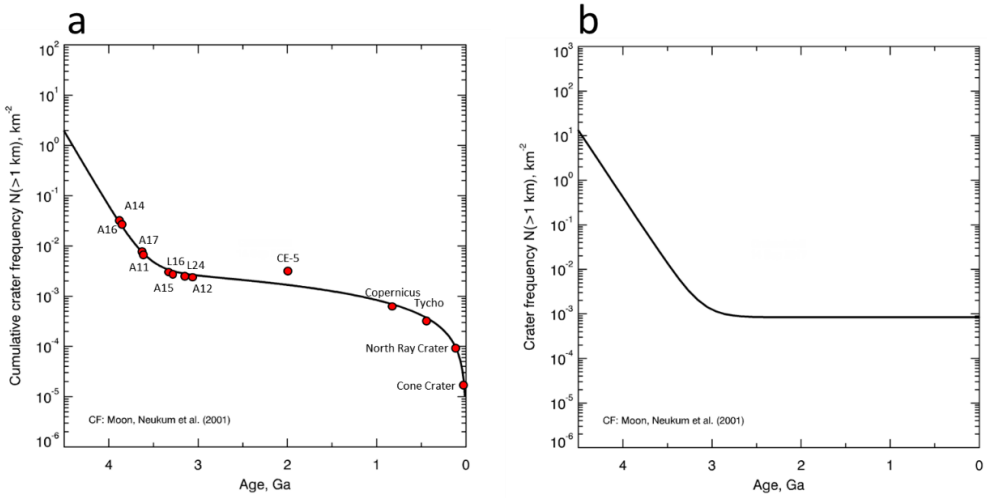

Figure 2.1: (a) The lunar Chronology Function [CF] (Neukum et al., 2001). The Apollo [A], Luna [L], Chang'e-5 [CE-5], and Crater [Copernicus, Tycho, North Ray, Cone Crater] calibration points are shown in red and presented in Table 2.2. (b) Lunar impact/crater production rate for >1 km craters shows the rate of expected 1 km impact craters that the Moon has received over 4.5 Ga. Note that the CE-5 calibration point was not used in developing the chronology function proposed by Neukum et al. (2001).

Table 2.2: Calibration points used to establish the lunar Chronology Function. Note that the N(1) values are reported using either the Neukum (1984) or the Neukum et al. (2001) Production Function (PF).

Sample Site	Latitude (°)	Longitude (°)	Age (Ga)	N(1)	PF
Descartes Formation (A16)[a]	-8.97	15.50	3.866±0.009	$3.47x10^{-2} \pm 7.00x10^{-3}$	Neukum (1984)
Fra Mauro Formation (A14)[b]	-3.64	-17.47	3.85±0.02	$3.70x10^{-2} \pm 7.00x10^{-3}$	Neukum (1984)
Mare Serenitatis (A17)[b]	20.19	30.77	3.75±0.01	$1.00x10^{-2} \pm 3.00x10^{-3}$	Neukum (1984)
Mare Tranquilitatis (A11)[b]	0.67	23.47	3.60±0.01	$6.42x10^{-3} \pm 5.40x10^{-4}$	Neukum et al. (2001)
Mare Imbrium (A15)[b]	26.13	3.50	3.30±0.02	$3.20x10^{-3} \pm 1.10x10^{-3}$	Neukum (1984)
Oceanus Procellarum (A12)[b]	-3.01	-23.42	3.15±0.04	$2.81x10^{-3} \pm 9.93x10^{-4}$	Neukum et al. (2001)
Mare Fecunditatis (L16)[b]	-0.51	56.37	3.41±0.04	$3.30x10^{-3} \pm 1.00x10^{-4}$	Neukum (1984)
Mare Crisium(L24)[b]	12.71	62.20	3.22±0.02	$3.00x10^{-2} \pm 6.00x10^{-4}$	Neukum (1984)
Northern Oceanus Procellarum (CE5)[c]	43.05	-51.80	2.03±0.004	$2.61x10^{-3} \pm 8.10x10^{-5}$	Neukum et al. (2001)
Copernicus (indirect measurement)[a]	9.62	-20.08	0.78±0.015	$6.67x10^{-4} \pm 5.27x10^{-5}$	Neukum et al. (2001)
Tycho (indirect measurement)[a]	-43.31	-11.36	0.109±0.004	$7.12x10^{-5} \pm 1.88x10^{-5}$	Neukum et al. (2001)
North Ray (A16)[a]	-8.82	15.48	0.053±0.008	$3.84x10^{-5} \pm 1.14x10^{-5}$	Neukum et al. (2001)
Cone (A14)[b]	-3.62	-17.43	0.025±0.012	$2.10x10^{-5} \pm 5.00x10^{-6}$	Neukum (1984)

[a]Norman (2009).
[b]Stöffler and Ryder (2001)
[c]Giguere et al. (2022)

2.1.4 Crater Equilibrium

The term ‘equilibrium’, also commonly called ‘saturation’, refers to the theoretical state where the number of new craters forming is equal to the number of old craters being erased (Gault, 1970; Hartmann, 1984; Minton et al., 2019; Trask, 1966; Xiao and Werner, 2015). Therefore, at equilibrium, the density of craters on a surface (per km^2) cannot increase beyond a specific value, and the surface's history beyond a specific time frame becomes unknown (Trask, 1966; Gault, 1970; Hartmann, 1984).

This process is challenging to quantify, as each crater's diameter is theorised to reach equilibrium at a different density. Crater equilibria are influenced by many geological processes that can erase or diffuse impact craters over time (Fassett and Thompson, 2014; Xiao and Werner, 2015). Additionally, as craters are constantly forming on the surface of the Moon, the longer a surface has been exposed to meteoric bombardment, the more crater diameter sizes will reach a theorised equilibrium. Here is an example of an empirical lunar equilibrium function defined by Hartmann (1984):

[**Eq. 2.3**]

$$\log_{10}(N) = -1.83 \times \log_{10} D - 1.33$$

N is the cumulative cratering density for a region, and D is the crater diameter in km. A graphic representation of this function is shown in Figure 2.2. It is not sensible to define a single equilibrium function for the entire surface of a planetary body (see Trask, 1966; Hartmann, 1984). The equilibrium functions should only be used as a guide for making interpretations, not as a strict requirement.

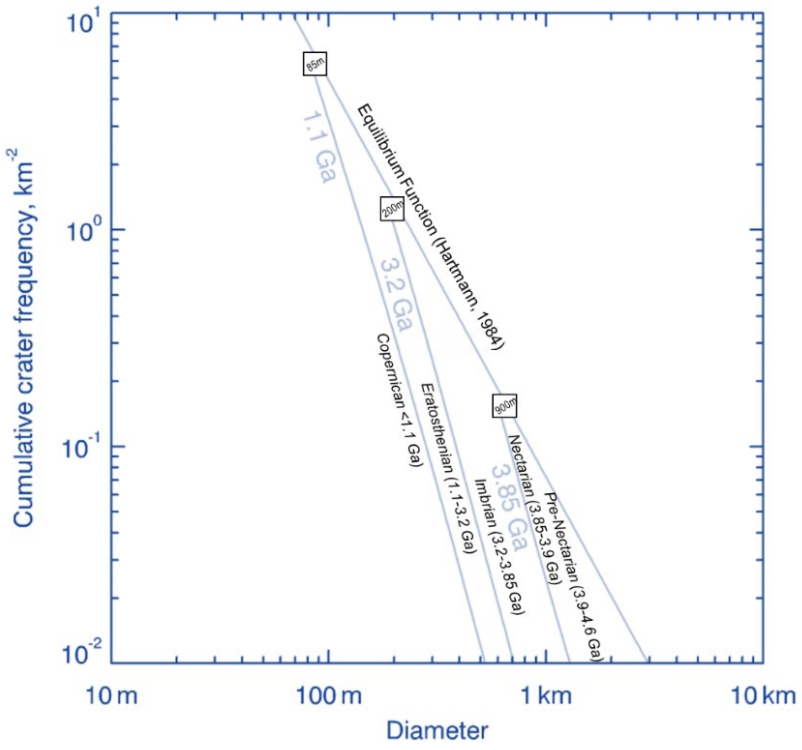

Figure 2.2: Equilibrium frequencies and diameters for the major timescale boundaries for the Moon along the Hartmann (1984) equilibrium function curve. CSFD note, the younger the surface age, the more smaller scale craters are needed to define it. Intervals for the lunar time periods are from Wilhelms (1987).

2.1.5 Crater Count Area Mapping

Crater mapping must involve analysing and viewing data from various sources, for example, lunar orbiter images, telescopic observations, and samples returned to Earth. This is most easily accomplished using geospatial data (such as optical images from satellites) in Geographical Information Systems (e.g., ArcGIS – see Kneissl et al., 2011). Defining a specific area to count craters upon also requires forethought and interpretation to ensure the area best represents the geological event we want to date. Mapping on the Moon is ongoing, as new image data are constantly being collected and analysed. Once an area is defined, such as an impact crater ejecta blanket (Figure 2.3), all craters within the count area must be mapped/counted to a given size. Counting involves determining the position and diameter of a crater, which can be tedious if one wants to record ~100,000 craters for dating. Many geologic maps have been produced for the Moon, and Wilhelms (1987) and team published the most widely used maps, which have been modernised into a unified geologic map by Fortezzo et al. (2020). These maps serve as a starting point for defining count areas at large spatial scales.

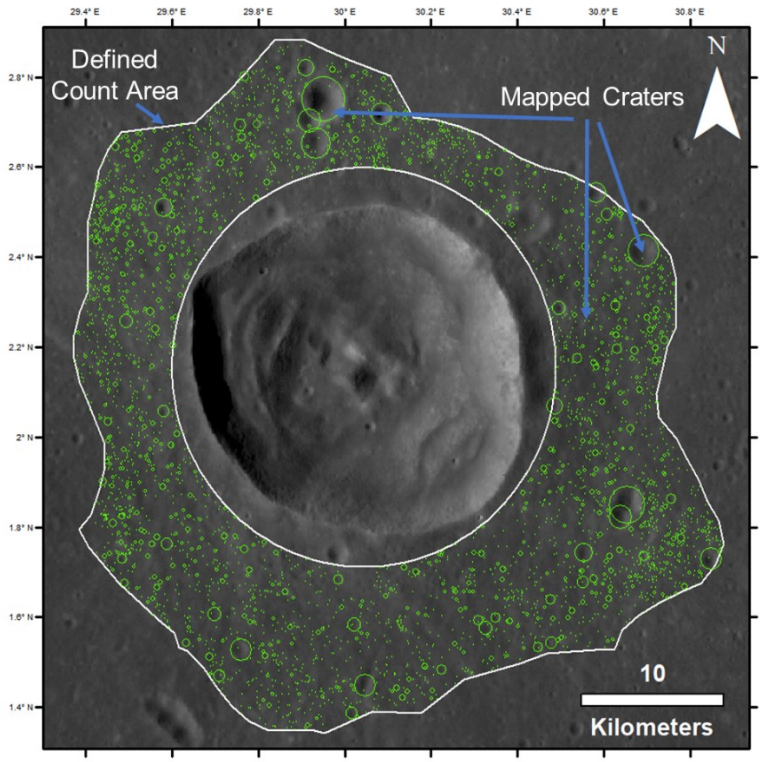

Figure 2.3: Mapped crater counts (green circles) within the ejecta blanket (white boundary) for Maskelyne crater (D = 22 km).

2.1.6 Crater Size-Frequency Distributions (CSFD)

The CSFD represents the crater counting data over a study area (e.g., Figure 2.3). CSFDs can be presented/plotted in several ways, the most common plots are the cumulative, differential, incremental (referred to as the 'Hartmann plot'; Michael and Neukum, 2010), and relative (R) plots (Figure 2.4; Crater Analysis Techniques Working Group, 1979; Michael, 2013; Fassett, 2016). Below, we briefly describe each plotting technique. For more details, refer to Crater Analysis Techniques Working Group (1979) or Fassett (2016).

The cumulative plot represents the cumulative (or total) counts of craters above a specific diameter size (Figure 2.4.a). Each crater is represented by a point on the graph per unit area (i.e., N/km^2). It is common practice to subdivide the crater data into diameter bins, traditionally defined by $\sqrt{2}$ (i.e., D = 1 km, 2 km, 4 km, …). Cumulative plots are the preferred visualisation method as they offer the advantage of being simple to plot and comprehend. However, the data points are not independent, limiting the ability to quantify error (Chapman and Haefner, 1967). Additionally, cumulative plots do not convey density changes with resurfacing (Michael, 2013), a typical process on planetary surfaces.

A differential plot can be used to address these limitations in using a cumulative plot (Crater Analysis Techniques Working Group, 1979; Michael, 2013). This plot divides the count data into diameter ranges (e.g., 1 km to 3 km) and calculates the frequency of craters per unit area in each range (Figure 2.4.b). Differential plots provide independence for each data point (i.e., the following point is not dependent on the previous point's value), making it easier to recognize and account for size-dependent effects, such as resurfacing and erosion (e.g., Michael, 2013). Modern crater counting analyses tend to use differential plots over cumulative plots. Additionally, Incremental plots, referred to as 'Hartmann plots' by Michael and Neukum (2010), are very similar, except they use a fixed bin diameter that increases in fixed intervals ($\sqrt{2}$ intervals in this case; Hartmann, 1966).

Relative plots (Figure 2.4.d), also known as 'R plots', are a derivation of the differential plot. They are more complex and involve dividing the differential crater frequencies by the power of -3 (Crater Analysis Techniques Working Group, 1979). R plots display several important properties, such as the ability to quickly interpret

cumulative power law slopes of -2 (i.e., a constant/standard accumulation rate of craters) as they show as a horizontal line. Likewise, a downward-sloping line is -3, and an upward-sloping line is -1 (see Fassett (2016) for details). R plots allow for a rapid assessment of variations within the crater population (Figure 2.4.d). However, they may not be as instinctive to visualise for non-crater-statistics-experts and suffer from bin limitations.

Generating a CSFD is essential to interpret, plot, and fit an isochron to a crater distribution (see Neukum, 1984; Neukum et al., 2001). An isochron within the context of crater counting refers to a modelled crater distribution of a constant age (Figure 2.4). Using a PF [e.g., Eq. 2.1], we can extrapolate an N(1) value and then by applying a CF [e.g., Eq 2.2] to that N(1) value, we can determine a model age for a cratered surface (Figure 2.4). This whole process is computerised and is now conducted through a program interface called CraterStatsII (see Michael and Neukum, 2010), though in the past, one would have to derive an age by hand. Within the CraterStats interface, the researcher can import their count data and interpret the CSFDs using different PFs, CFs, plotting techniques (i.e., cumulative, differential, relative, Hartmann), and isochron fitting techniques. CSFDs were the primary method we used to interpret and analyse all our cratering data throughout this project. To further understand how we used CSFDs in this Ph. D., refer to Chapters 4 and 5.

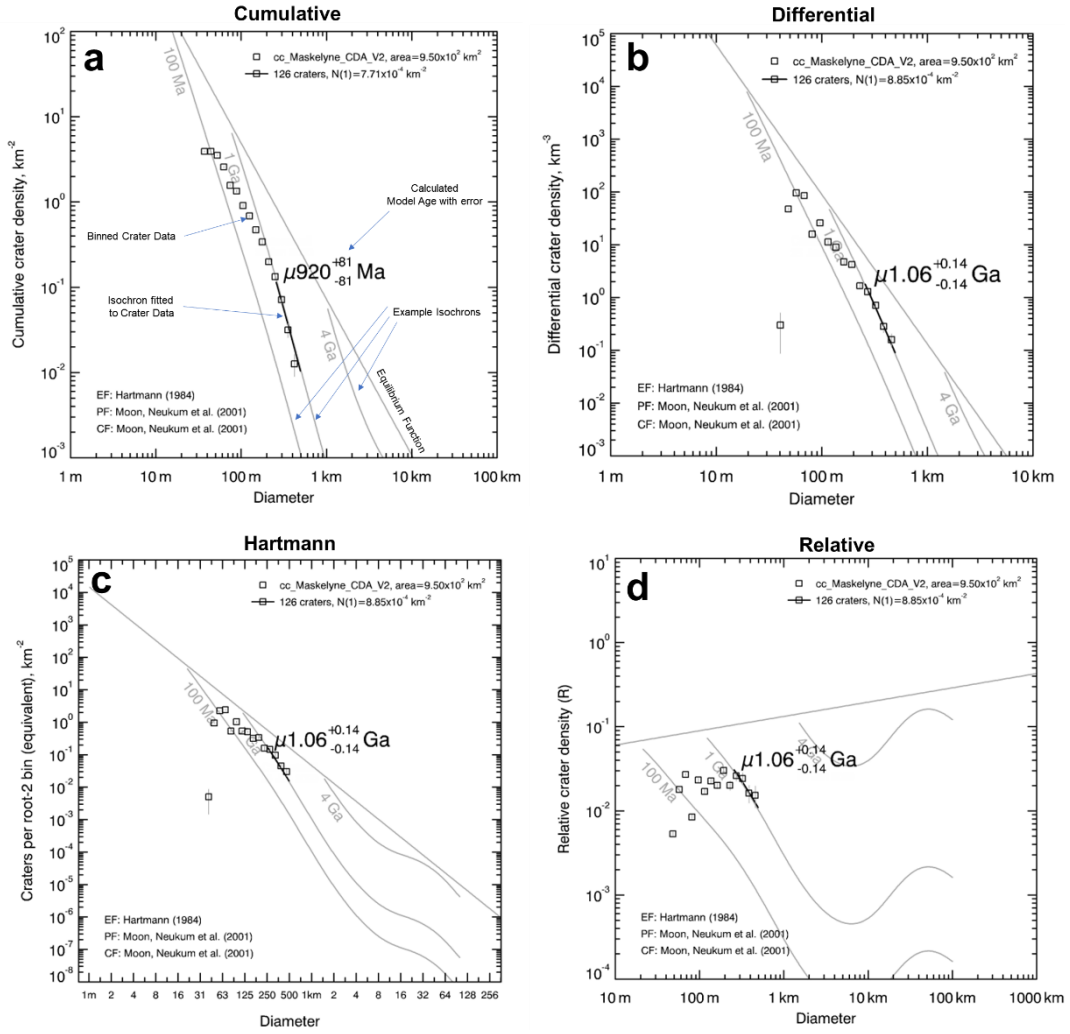

Figure 2.4: Example CSFDs and derived model ages for Maskelyne crater (Figure 2.3). (a) Annotated cumulative CSFD in 4th root-2 bins; (b) Differential CSFD in 4th root-2 bins; (c) Hartmann CSFD in 4th root-2 bins;(d) Relative (R) CSFD in 4th root-2 bins. All isochrons were fitted over the same diameter interval and in their respective fitting techniques. Ages are reported to 3 significant figures. CSFD plots made in CraterStatsII (Michael and Neukum, 2010).

2.1.7 The Limitations of Crater Counting

Although crater counting methodologies can determine an age for any (cratered) extraterrestrial surface, the 'meaningfulness' or 'usefulness' of these Ages can be limited. If a derived age is to be placed into a planetary chronology, it is important to consider all possible sources of error. In the following paragraphs, we describe the significant factors of crater count chronologies to provide context for the age results and interpretations presented in future chapters.

Firstly, distinguishing which impact crater populations can be used for surface age derivation from other craters or crater-like circular features is not always straightforward. Many circular or pseudo-circular features, such as volcanic vents/mounts, hills, or large boulders, exist across planetary surfaces (Basilevsky et al., 2013; He, 2020). In certain lighting conditions and image pixel resolutions, these features can be almost impossible to distinguish from an impact crater (Richardson et al., 2022). Therefore, it is accepted that craters within an image must be ≥ 10 pixels in diameter to be reliably identified and mapped as a crater (see Robbins et al., 2014; Wang et al., 2020). Moreover, differentiation of primary and secondary craters (Figure 1.2) can be difficult. When solely counting craters across a defined surface, secondary craters often appear similar to small primary craters (Chapman and Haefner, 1967; Namiki and Honda, 2003).

Classififng such craters is significant because the crater count methodology is only accurate when all craters used for dating are primary impacts – note, the PFs (e.g., Neukum et al., 2001) account for some background secondary contamination (see, Xiao, 2016). For a detailed overview of the community's view on secondary cratering in crater count chronologies, refer to Bierhaus et al. (2018). Furthermore, fitting an isochron to a crater population heavily contaminated by secondary craters will lead to an inaccurate age and thus will not be very meaningful (Bierhaus et al., 2005). However, this can be mitigated by analysing the densities of impact craters of a similar size and quantifying their clustering and/or randomness. This will indicate if a population of craters are secondary (Michael et al., 2012; Lagain et al., 2020; 2021a, b). Moreover, accurately recognising and identifying small craters can be difficult and is highly researcher-dependent (see Figure 2.5).

Another key consideration in crater counting methodologies is that the models used to derive an age rely on a 'known' rate of cratering over time (see Hartmann, 1984; Neukum et al., 2001; Brown et al., 2002). Cratering rates will change over time and across different terrains (and planets), making a model highly terrain/planet-dependent. Some studies have developed functions to represent the cratering differences on different terrains (i.e., Le Feuvre and Wieczorek (2011)'s PF for porous/non-porous terrains on Mercury). However, when writing this thesis, none existed for the Moon. Additionally, the history of impacts on a surface can be very complex, with some surfaces with the same formation age being hit more frequently than others (see Lagain et al., 2024; Ito and Malhotra, 2010; Le Feuvre and Wieczorek, 2011; Robertson et al., 2021,2023), which can result in a non-uniform distribution of craters across the Moon.

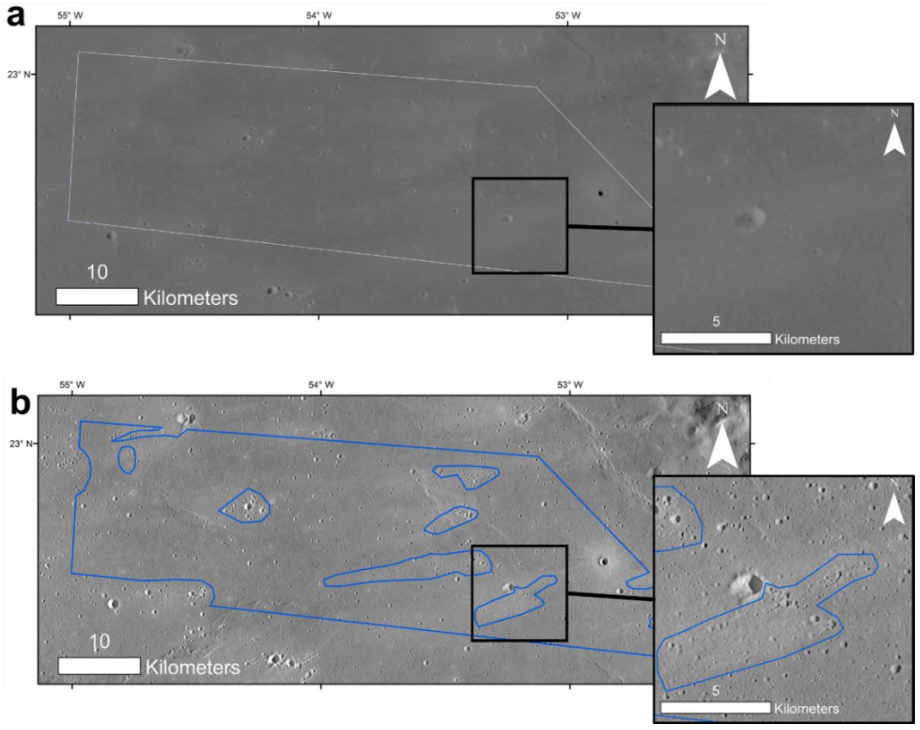

Figure 2.5: Distinction of secondary craters in two image mosaics at different pixel resolutions within the same crater count area [pale-blue polygons] (mid-eastern Oceanus Procellarum). (a) WAC Mosaic [100 m/px] (Speyerer et al., 2011), and (b) Kaguya TC Morning Mosaic [7.5 m/px] (Isbell et al., 2014). Note, if crater counts were conducted on lower-resolution images large secondary craters could be easily interpreted as primary craters, as one cannot see the smaller craters making up the cluster. The dark blue polygons in panel (b) denote an 'adapted' count area that has avoided secondary craters.

Crater chronologies can give either a relative or absolute model age (AMA). Both come with drawbacks. By comparing the number of craters in different regions, researchers can make relative estimations of the age of those surfaces. Whereas, chronology models estimate the absolute model ages of geological features based on various data and assumptions. These models often rely on assumptions about the rates of geological processes. Using crater counts in a relative way, we can avoid the need for specific chronology models because they assess the relative ages of surfaces based solely on the number and distribution of impact craters. This approach can be beneficial when absolute dating methods are challenging to apply or when there are uncertainties in the chronology models. It has been noted that the lunar chronology function has insufficient calibration points to accurately define ages between ~3.0 and ~0.8 Gyr (see Robbins, 2014). This is due to the lack of dated samples between 3.0 and 0.8 Gyr (see Table 2.2), indicating that more sample data is needed (Robbins, 2014). Fortunately, the recent Chang'E-5 sample return (Che et al., 2021; Qian et al., 2021) has provided a new calibration point in the ~2 Ga-wide gap.

Furthermore, crater chronologies require a statistically significant number of craters to be counted, and the craters that have been counted must be recorded down to a specific diameter; this ensures that the model can be fitted to a 'complete population' (Chapman and Haefner 1967; Chapman, 2015). Completeness refers to a crater population (of a specific size range) fully captured by crater counting. For example, all primary craters >1 km in diameter have been counted within the defined area. This ensures that the interpretation of the calculated CSFD is accurate (i.e., that the counted crater population represents the crater record since the formation of the dated surface; Chapman and Haefner 1967; Crater Analysis Techniques Working Group, 1979).

It is also good to outline that the error margins on the AMAs are directly proportional to the number of craters counted (described by $\sqrt{n}$, where n is the number of craters) (Crater Analysis Techniques Working Group, 1979). The number of craters needed is ambiguous, and there is no clear consensus on the minimum number or diameter. Thus, error margins can significantly vary between datasets and studies. The number of craters that need to be counted can be rationally estimated. For example, if the surface is ~young and/or small, one will need a lot of small

craters (< 1 km) to derive an age (refer to Figure 2.2). Michael et al. (2012; 2016) and Michael & Neukum (2010) described the statistical errors within crater counts. They outline that attention is needed when reporting model surface ages, errors, and any parameters used (such as production and chronology functions, bin sizes, and isochron fitting ranges).

The above points imply that crater counting methods cannot precisely determine a surface's ground truth age. However, a derived model age can be scientifically valuable and meaningful if one uses well-established functions and chronology models with an adequate understanding of how interpretations are made within data and in the presence of geological common sense. Crater counting, even with its limitations, is a fantastic technique for determining a surface age without physically collecting rock samples or comparing distant geologic units (Hartman and Neukum, 2001; Ivanov et al., 2002; Neukum et al., 2001; Robbins and Hynek, 2012). With technological advances in the last ten years and the increasing computing power, even at the desktop level, the accuracy and scale in which we can analyse the craters and quantify error have significantly increased (km/pixel to cm/pixel).

2.2 Convolutional Neural Networks

Within the PhD project, we focused on machine learning and the value of integrating new technology with crater science. This section will explore the algorithms and methodologies attached to this focus. The style of Machine Learning algorithm we implemented for crater detection was a Convolutional Neural Network (CNN) developed by Benedix et al. (2020) and Lagain et al. (2021a, b). Specifically, a CNN is a variety of artificial neural networks adapted for image recognition and object detection (Ajiit et al., 2020; Gu et al., 2018; O'Shea and Nash, 2018). A Neural Network is a type of deep-learning algorithm inspired by the structure and function of the human brain (Ajiit et al. 2020). It consists of interconnected nodes (or neurons) that process information and communicate with each other to solve a particular problem or to make a prediction (Gu et al., 2018) (Figure 2.6). The primary purpose of CNNs is to apply filters, or 'convolutions', to input data to identify and extract relevant objects/details (Gu et al., 2018). The input to a CNN is an image, where the data is represented as a two-dimensional array of pixels, X and Y (Ajiit et al., 2020; Wang et al. 2019; Zang 2010). Below, we briefly describe the process of a typical CNN, like the one we utilised for crater detection.

The goal of any CNN is to identify patterns in the image, such as edges, shapes, and textures, that indicate the object within the image. It completes this goal by placing a layer over an image called a convolution/filter layer (Figure 2.6) (Albawi et al. 2017; Gu et al., 2018; Koushik, 2016). Each filter is a small matrix of weights (or metrics) that moves systematically over the image, computing an average weight between the filter weight and the image (Gu et al., 2018). The output of this convolution is a single-weight feature map, which represents the total weight values of the features within the image (Figure 2.6). The output of the convolutional layer is then passed through a non-linear activation function to introduce non-linearity into the model (Koushik, 2016). A non-linear activation function applies a transformation to the input (Dureja and Pahwa, 2019), so the function's output is not the same as the input. When using a non-linear activation function, the model can learn more complex and slight relationships between different inputs, improving its ability to classify and recognise image patterns (Dureja and Pahwa, 2019). The convolution and non-lineation steps go through many iterations, slightly changing the starting weights and filters each time.

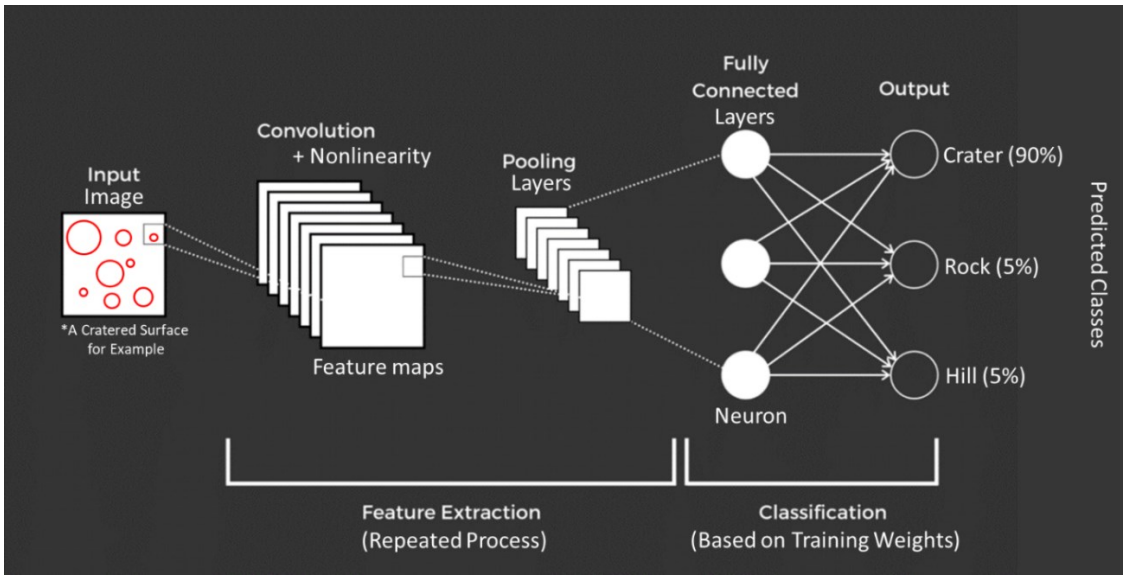

Figure 2.6: Schematic diagram illustrating the computational steps within the Convolutional Neural Network algorithm specialised for image object detection. Figure modified from The Click Reader (2020).

Next is the pooling layer (Figure 2.6), which is used to downsample the features, reducing their dimensionality/resolution (the number of attributes or dimensions used to define an object) while retaining some information (Albawi et al. 2017; Koushik, 2016). This is done to decrease the network's computational time and memory usage while also helping to prevent overfitting (Albawi et al. 2017). The pooling layer divides each convolution feature into a grid and computes a single output value for each region (Albawi et al. 2017). Finally, the fully connected layers map every neuron from one layer to the following layer (Figure 2.6). These layers are located at the end, and the final classification decision is based on the features extracted by the convolutional and pooling layers (Albawi et al., 2017; Koushik, 2016).

Applying convolutional layers, activation functions, and pooling layers is repeated (10s to 1000s of times) in a standard CNN (Figure 2.6; Albawi et al. 2017; Koushik, 2016). The final output of the CNN is a series of probabilities representing the likelihood that the region of an input image contains the defined class (Figure 2.6; Albawi et al. 2017; Koushik, 2016; Redmon et al. 2016). The weights of all these connections are recorded in a process we call ‘training’.

2.2.1 Training a Machine Learning Algorithm

There are two different methods for training an ML algorithm: supervised or unsupervised. Supervised is where the algorithm is trained on a labelled dataset (Bhavsar and Genatra, 2012; Gu et al., 2018), where each image has one or several classes/objects labelled. During training, the weights of the filters are adjusted to minimise the errors between the predicted classes/objects and the ground truth classes/objects (Bhavsar and Genatra, 2012). In contrast, unsupervised learning is where the algorithm is run on a dataset and is tasked with finding patterns and relationships in the data (Golovko, 2016). The algorithm will attempt to discover a structure within the data, such as clusters or patterns, without prior knowledge of the labels (Golovko, 2016). Unsupervised learning is very computationally inefficient but has benefits when the data patterns are complex and/or unknown (Golovko, 2016). In this project, we use a supervised learning structure. We gave the ML examples of craters to learn from; this way, we could have greater control over the algorithm's ability to detect certain craters.

2.2.2 Object Detection Algorithm: 'You Only Look Once'

For this project, we used a specialised CNN architecture (algorithm design) called You Only Look Once (YOLO) (Redmon et al., 2016), exclusively the Ultalytics' implementation (Jocher, 2022, 2023). We specifically utilised two architecture versions: YOLO version 3 (YOLOv3; Jocher, 2022) and YOLO version 5 (YOLOv5; Jocher, 2023). YOLO is an object detection algorithm designed to quickly identify multiple objects within an image (Redmon, 2016; Redmon and Farhadi, 2018). The use of YOLO over other CNNs was warranted due to how it approaches object detection. YOLO takes an input image of a set pixel size (the pixel sizes can be decreased to improve efficiency). Next, the image is tiled (Figure 2.7) and bounding boxes are drawn for each object within that tile. The algorithm can only draw a fixed number of bounding boxes, which are defined as [x, y, w, h] pixel coordinates (the [x, y] coordinates represent the centre of the bounding box, while the [w, h] coordinates represent the width and height of the box). Each bounding box has a confidence score, indicating how likely it is that the box contains an object. As multiple bounding boxes may be drawn to the same object (each with a different confidence score), YOLO uses a non-max suppression approach to remove duplicate predictions (Figure 2.7; refer to Chapter 3, Section 3.2.3.a for details).

The final output of the algorithm is a set of bounding boxes (Figure 2.7), where each box corresponds to one object. As a result, the algorithm excels in ~simultaneously identifying small, medium, and large objects within a single image. This capability is particularly well-suited for addressing the small crater detection problem, as it can map craters to meter- and kilometre-scales.

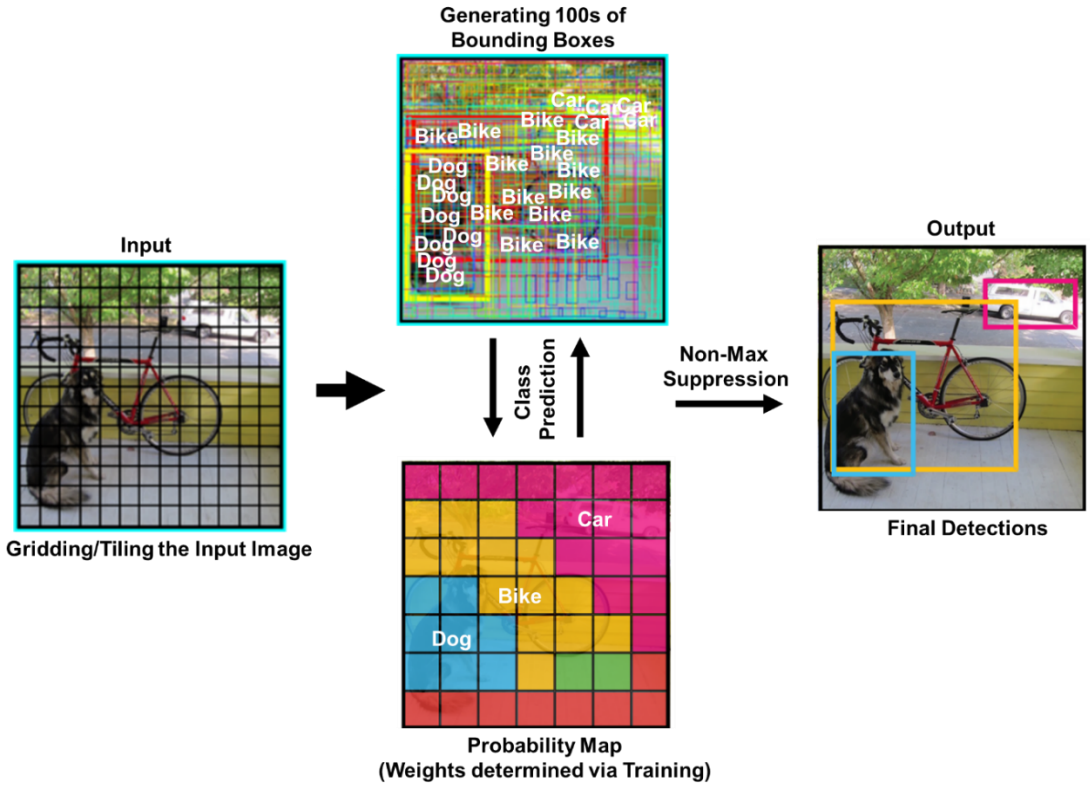

Figure 2.7: Schematic flow diagram illustrating how the CNN 'You Only Look Once' (YOLO) will classify/detect three objects/features (e.g., Dog, Bike, Car) across a given image. Figure modified from Redmon (2016).

2.2.3 Optimisation of YOLO for Crater Detection

The YOLO(v3/v5) architecture was optimised to detect impact craters efficiently (Figure 2.7). Several steps were taken to adapt the architecture for impact crater detection. These changes aim to enhance the algorithm's ability to detect craters of various sizes and improve its overall detective performance. Some of the following adaptations are from Benedix et al. (2020) and Lagain et al. (2021a, b). Through design, the algorithm will learn from a given training dataset. Therefore, a dataset containing images of a planetary surface (e.g., the Moon, Mars, Mercury) needs to be compiled, specifically focusing on areas with craters. These images should cover a wide range of crater sizes, geological terrains, planetary features (including pseudo-circular features that are not impact craters), and lighting conditions. When training, the dataset is also augmented by applying image changes such as rotation, scaling, flipping, and hue transformations. These changes are called hyper-parameters and are quantified (the hyper-parameters we used for our detection model are listed in Appendix 2.1). We also implemented multiscale training by re-scaling the dataset with different pixel-resolution images. This increases the training probability that larger craters are entirely included within tile boundaries but also increases the diversity of crater appearances and helps the model better detect different crater sizes and orientations.

Another key change we made was adjusting the detection tile sizes. YOLO divides the input image into tiles of cells and predicts bounding boxes within each cell. When adjusting the tile pixel resolution, the algorithm is optimised to better capture the range of crater sizes in the lunar images. This involves increasing the grid size to include more pixels for smaller craters or decreasing the grid size to focus on larger craters. This process is called downsampling (Benedix et al., 2020).

2.2.4 The YOLO Label Tool

To build our crater detection training dataset, we used 'YOLO Label' (https://github.com/developer0hye/Yolo_Label), which is a software that allows users to manually label images by drawing bounding boxes around objects of interest and assigning them a class (e.g., crater) (Figure 2.8). This tool allowed us to quickly and efficiently create a labelled image dataset that will be used to train the YOLO detection model. The output of this process is an image file (.jpeg) with a corresponding text file (.txt); the text file contains the bounding box coordinates in (pixel percentages) and class IDs. This process is described in further detail in Chapter 3.

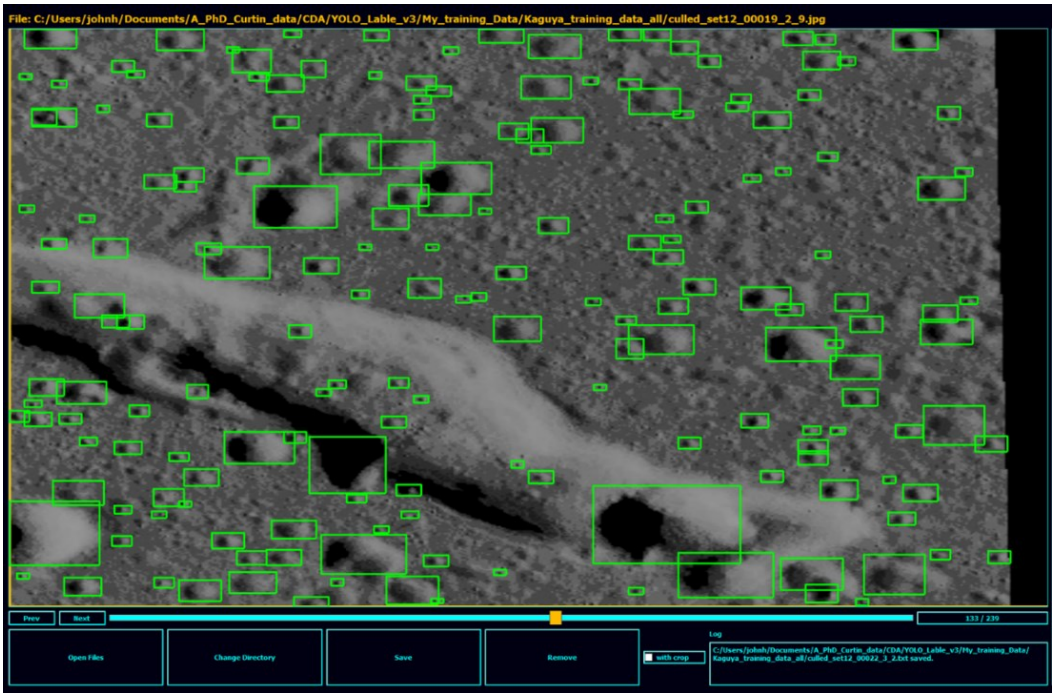

Figure 2.8 is an example of a surface image used for crater marking (green boxes) within the YOLO Label interface (available at https://github.com/developer0hye/Yolo_Label). The manual crater detections were used to train the YOLO crater detection model.

2.3 Supercomputing Resources

Any ML algorithm requires a lot of computational processing power, especially when working with 1000s of high-resolution images. Due to this, standard desktop computers cannot process the needed information in a timely manner. We utilised supercomputers to aid training and crater detection. A supercomputer is a highly advanced computer system designed to perform complex computations at a very high speed. Computations include simulations, modelling, data analysis, and engineering tasks that are difficult to perform on a desktop computer. A supercomputer breaks down a significant computational problem into smaller sub-problems that can be processed simultaneously on different nodes or processors. The nodes are connected through a high-speed network, allowing them to exchange data and coordinate their processing. This parallel processing technique enables supercomputers to perform processes faster than traditional computers (Wu, 1999). Each node in a supercomputer contains multiple processing units, such as CPUs, GPUs, and memory.

To train and run our CDA, we used the resources at the Pawsey Supercomputing Centre in Perth, Western Australia. Pawsey hosts powerful supercomputer clusters, such as Magnus, Topaz, and the new Setonix (Pawsey, 2023). The main computer we used was the Magnus supercomputer (retired in 2022). Magnus processed 1.2 petaflops at full performance, performing up to 1.2 quadrillion (a million billion) calculations per second (Pawsey, 2023). The cluster comprises 35,712 cores and has a total memory of 156 terabytes. Magnus also had GPU nodes with 144 NVIDIA V100 GPUs (Pawsey, 2023). Magnus was used for various scientific applications, not just machine learning algorithms but processes, including climate modelling, geoscience, and genetics (Pawsey, 2023).

2.4 High-Resolution Image Datasets

The detailed detection and analysis of lunar craters require using the highest-resolution image datasets. In this section, we describe two high-resolution image datasets we used. The two instruments that captured the images were (1) the Lunar Reconnaissance Orbiter Camera (LROC) and (2) the Kaguya Terrain Camera (TC). The high-resolution datasets enable us to discern subtle details and accurately identify impact craters across different sizes over global terrains.

2.4.1 Lunar Reconnaissance Orbiter Camera Image Datasets

The Lunar Reconnaissance Orbiter Camera (LROC) is a sophisticated imaging system that was developed and is controlled by NASA to provide detailed images of the Moon. The LROC is one of the seven science instruments aboard the Lunar Reconnaissance Orbiter (LRO) spacecraft, which launched in 2009 and is still in operation, downlinking 1000s of images per year. The instrument has two cameras that produce images at different resolutions: the Wide-Angle Camera (WAC) and the Narrow-Angle Camera (NAC) (Robinson et al., 2010).

The WAC system has captured images of the Moon's surface with an average resolution of ~100 m/px, allowing large-scale mapping with an area of ~60,000 km^2 per image (Robinson et al., 2010). This dataset is mosaicked together to form a single global WAC mosaic with a resolution of 100 m/px (Figure 2.9.a) (Speyerer et al., 2011). This dataset is valuable as it has a near-perfect global coverage (excluding the permanently shadowed regions at the lunar poles). In comparison, the NAC system consists of two high-resolution stereo cameras that capture images at a resolution of ~0.5 m/px, with a range of 0.5-2 m/px (Figure 2.9.b; Robinson et al., 2010). This allows for detailed analysis of specific lunar surface features with twice the field of view (100s to 1000s km^2 per image, depending on the altitude) (Robinson et al., 2010). The NAC dataset currently sits as an extensive dataset comprised of raw 4,000,000+ image pairs (subdivided into Left (L) and Right (R) images), with each image averaging 50-250 MB in size. The NAC pairs take the form of rectangular (~5 km by ~20 km) images, covering relatively small sections of the Moon's surface, though if combined, they could cover ~90+% of the Moon's surface (Figure 2.9.b).

As many other studies have compiled manual (Head et al., 2010; Jia et al., 2020; Povilaitis et al., 2018; Robbins, 2019) and automatic (Salamunićcar et al., 2012; Wang et al., 2021) crater catalogues using the WAC image mosaic, this project focused on automatically mapping craters using images from the NAC dataset to identify small craters down to ~20 m in diameter [on ~2 m/px images] (see, Robbins et al., 2014; Wang et al., 2020).

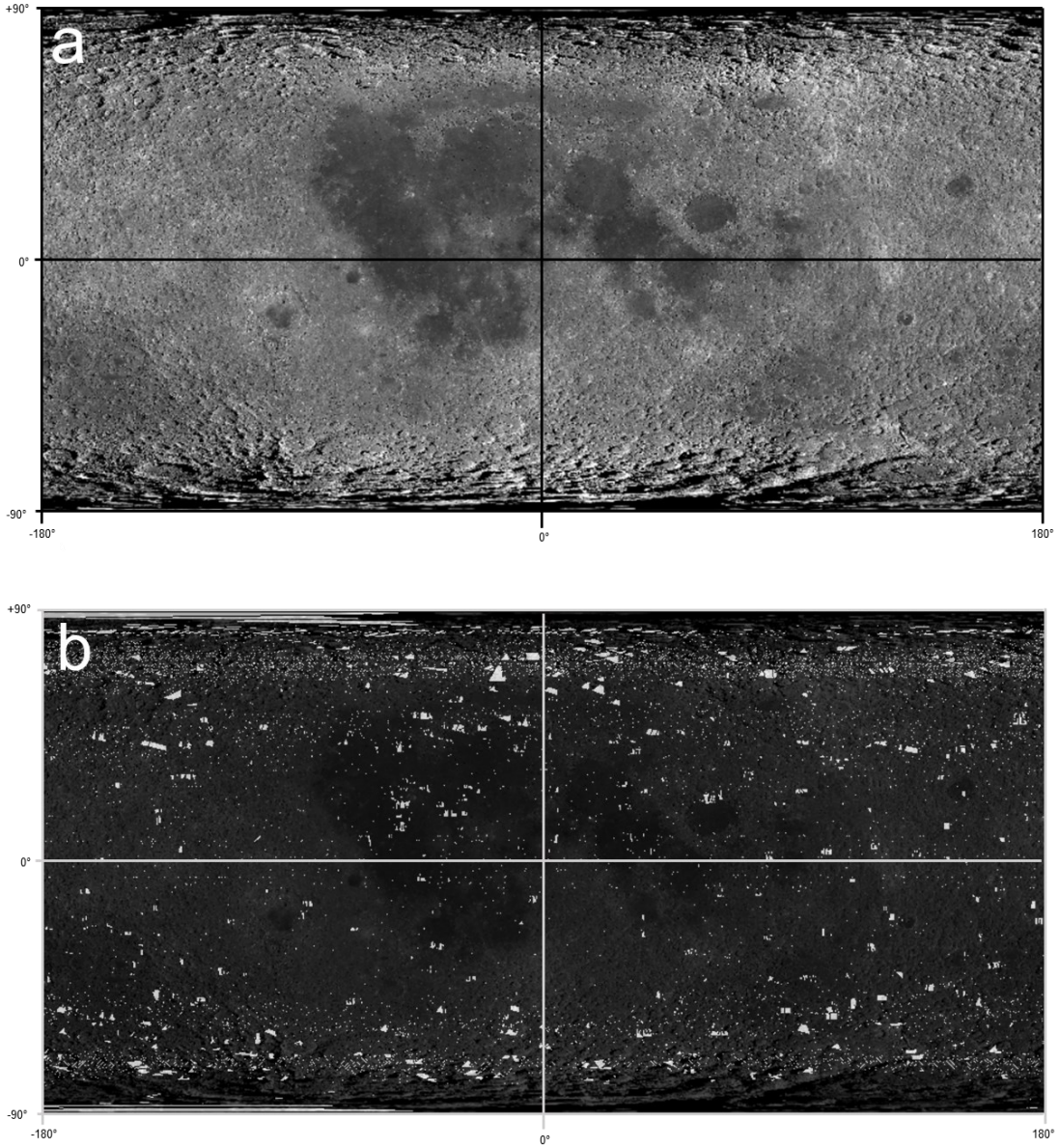

Figure 2.9: Lunar Reconnaissance Orbiter Camera image coverages: (a) Wide-Angle Camera mosaic (Speyerer et al., 2011); (b) Narrow-Angle Camera images, the black polygons depict the image footprints, as the individual images cannot be shown (n = 4,170,508 NAC Left-Right images). Both images are displayed in an equirectangular map projection.

2.4.2 Kaguya Terrain Camera Image Dataset

The Kaguya Terrain Camera (TC) is a high-resolution camera system onboard the SELENE/Kaguya spacecraft (SELenological and ENgineering Explorer), which was launched by the Japan Aerospace Exploration Agency (JAXA) in 2007 and decommissioned in 2009.

The Kaguya TC system consists of three camera units with different fields of view, resolutions, and spectral bands. The TC was designed to capture images with resolutions ranging between ~1 m/px to ~10 m/px and with an average of ~7.5 m/px, depending on the altitude and pointing angles of the spacecraft (Haruyama et al., 2008). The Kaguya cameras were designed to study the lunar surface in detail, aiming to produce a global image map of the Moon (Figure 2.10). The TC camera images were map-projected and mosaicked into three global variations with a resolution of ~7.5 m/px (Isbell et al., 2014): Morning (early low-sun [~65° Incidence], right-to-left illumination) (Figure 2.10.a), and Evening (late low-sun [~65° Incidence], left-to-right illumination) (Figure 2.10.b), and an ortho-mosaic (merged image data displaying a simulated vertical ['Noon', 0° Incidence] illumination).

The Morning and Evening datasets provide two opposing lighting directions to map craters, increasing the total surface coverage (for example, a cratered terrain obscured by shadows in the morning dataset will be visible in the evening dataset). For this project, we utilised the morning and evening TC image datasets. The pixel resolutions are an order of magnitude less than the NAC images but have the added benefit of being pre-processed (i.e., the images are already georeferenced; Isbell et al., 2014). Additionally, this dataset has been tiled into 3° by 3° longitude-latitude tiles, which increases the processing times for crater detection. Using the Kaguya dataset, we can reliably map craters down to ~75-100m in diameter [on ~7.5-10 m/px images] (Robbins et al., 2014; Wang et al., 2020).

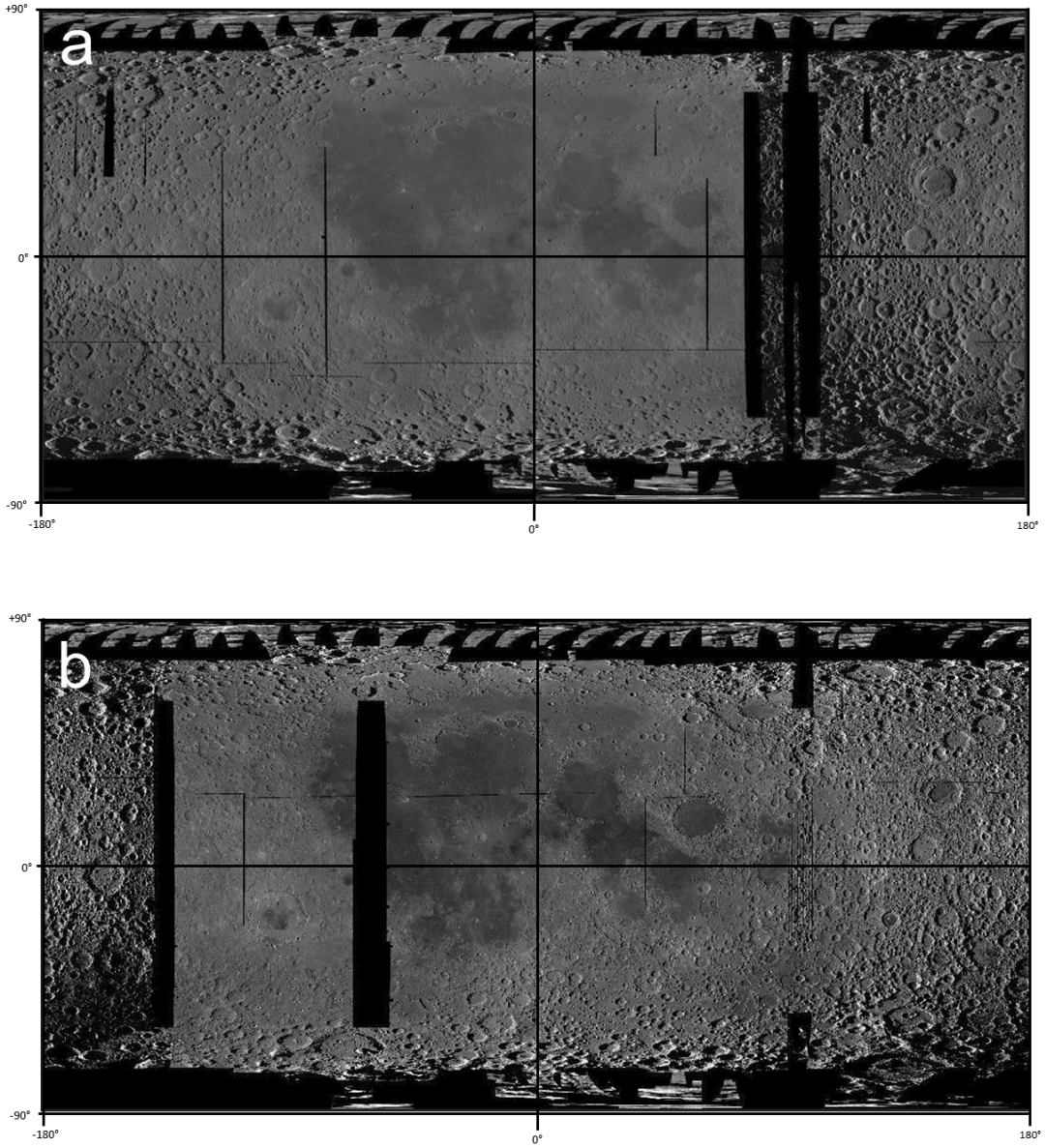

Figure 2.10: SELENE/Kaguya TC image mosaics in an equirectangular map projection: (a) Morning illumination mosaic; (b) Evening illumination mosaic (Isbell et al., 2014). Note the coverage differences between the two mosaics. Both images are displayed in an equirectangular map projection.

2.5 Image Data Pre-processing

Here, we detail the image pre-processing we undertook for our images and the implications of using processed image datasets. The LRO-NAC images do not have the needed geographical information embedded within the image data; thus, they cannot be ingested into the CDA (see Chapter 3, Section 3.2) or GIS software. The following is a detailed description of how the NAC images were pre-processed and reformatted. On the other hand, Kaguya TC mosaics are already georeferenced and can be downloaded through the SELENE Data archive (https://data.darts.isas.jaxa.jp/pub/pds3/). Refer to Chapter 3 for the specifics relating to the image processing workflows in automated crater detection.

2.5.1 Integrated Software for Imagers and Spectrometers

To process the LRO-NAC images, we used the Integrated Software for Imagers and Spectrometers (ISIS3, 2021; https://github.com/DOI-USGS/ISIS3). ISIS is a software package for processing and analysing data from spacecraft missions. It was initially developed by the US Geological Survey (USGS) and is maintained by the USGS and NASA. ISIS contains tools for processing and analysing remote sensing data, such as images and spectral signatures from spacecraft instruments, including geo-processing, calibration, and visualisation modules, and tools for creating and editing digital terrain models. Here is a detailed explanation of how one needs to use ISIS to process a single LRO-NAC image (the ISIS script we used for NAC image processing is given in Appendix 2.2).

Once ISIS3 is installed correctly and EDR (Engineer Data Records), LRO-NAC images are downloaded via the Planetary Data System (PDS) archive (https://pds-imaging.jpl.nasa.gov/data/). The '.img' files must be converted into the ISIS cube format using the "pds2isis" command. For example:

```
pds2isis from=NAC.IMG to=NACE.cub
```

The next and most crucial step is to calibrate the NAC images to correct for geometric distortions and other sensor-specific properties (i.e., SPICE kernels). The SPICE (Spacecraft Planet Instrument C-matrix Events) kernels are data that provides information about the spacecraft's position and orientation during image acquisition. This step is achieved using the "spiceinit" command. For example:

```
spiceinit from=NACE.cub spksmithed=true web=true
```

The additional variables “spksmithed” and “web” are optional but increase the accuracy of the spacecraft calibrations, and, in the case of the “web=true” variable, it means the user does not have to download 200+ GB worth of calibration data. It is very important to note that it is at this step that the NAC images are corrected against the lunar DEM (Smith et al., 2010), which has a resolution ~100 m/px. This can introduce some unexpected errors as the software moves calibrated high-resolution images (~2 m/px) to a lower-resolution DEM (refer to Section 2.5.2 for details). After the images are calibrated relative to the spacecraft, the user can modify/enhance the image. Two important options are “lronaccal” and “lronacecho”. By performing these two enhancement steps, the NAC cube file is converted into a calibrated image (and the NAC ID is given the suffix “C” for the calibrated image file) that can be used for scientific analysis and interpretation.

```
lronaccal from=NACE.cub to=NACC.cal.cub
lronacecho from= NACC.cal.cub to= NACC.echo.cub
```

Additional modifications that do not strictly need to be applied within ISIS could include removing the image borders by an amount in pixels (“trim”; 40 pixels) and colour balances within the image by a specific amount (“stretch”; 0:1 0.5:1 99.5:254 100:254 [8-bit colour]).

```
trim from= NACC.echo.cub to= NACC.cub left=40 right=40
stretch from= NACC.tr.cub to= NACC.str.cub
usepercentages=yes pairs="0:1 0.5:1 99.5:254 100:254"
```

Once all the image calibrations and modifications are complete, the image must be map-projected to the Moon’s surface. Here we use the "cam2map" command to accomplish, specifying the projection type (e.g., equirectangular; “EQmoon.map”; see Appendix 2.2.1):

```
cam2map from=NACC.str.cub to=NACC.map.cub map=EQmoon.map
```

Finally, the processed NAC cube file (“NACC.map.cub”) must to be exported in a standard image file format (e.g., Geo-Tif file). One can convert files within ISIS, with "isis2std", or within GDAL (Geospatial Data Abstraction Library) using “gdal_translate” (our preferred formatting method):

```
isis2std from=NACC.map.cub to=NACC_map format=tiff
gdal_translate -of GTiff NACC.map.cub NACC_map.tif
```

Depending on the research objectives, ISIS can perform additional processing tasks, such as mosaicking multiple images together (after the above steps are complete) and generating DEMs with stereo images (see Öhman, 2015). For this study, these steps were conducted using ISIS within a Linux-based system/environment. This process was also optimised to be batched and processed in parallel so we could pre-process NAC images quickly.

2.5.2 Implications for Using NAC Images

When analysing the assemblage of processed NAC images, we observe a significant offset between consecutive and overlapping images. After the georeferencing process, the exact geographic position of the NAC image can vary across two or more images. These offsets are due to boresight offsets (the effect of the relative alignment between paired NAC images), different orbital altitudes, orbital periods, DEM accuracy, spacecraft positioning, and SPICE kernels (Wu and Liu, 2017). All these factors result in the same feature being slightly offset between two or more NAC pair sets (Figure 2.11). The offsets can be minimal (~10-80 m; Figure 2.11.a-c) and, in most cases, do not warrant any user intervention or re-alignment, as the craters are significantly bigger than the offset. However, when the offsets are significant enough (>100 m; Figure 2.11.d), they might display the same craters (e.g., small craters) in significantly different positions. This offset issue is significant when identifying millions of craters over 1000s of NAC images (Figure 2.11.e), where we cannot quantify the accuracy of the position of a detected crater – which is essential for accurate model age derivation (Figure 2.11.f).

To successfully remove the offsets, one must manually go through the NAC images and generate a series of control points to link to user-defined ground control points (points of known location between two or more images). The process can be completed through ISIS. The images can also be processed and repositioned through GIS software, but both will require manual marking and manipulation of images. These processes are very time-consuming and labour-intensive, making them suitable only for a few images with minimal overlaps. This process is imperative for making high-accuracy-controlled planetary mosaics. Note that using ground control points to tie images together on two or more NAC Images gives the resulting mosaic/images the prefix of ‘controlled’ NAC images. In this project, manually

controlling the images is not always necessary when dealing with 1000s of NACs over large swaths of longitudes and latitudes. A good way of mediating the production of duplicate craters is to remove/reduce the number of overlapping NAC images. This can be achieved through mosaicking. When applying the CDA to many individual images, craters are detected several times, each with varying degrees of accuracy. When images are mosaicked, a crater is only represented in one image (Figure 2.11.f).

Moreover, downloading and georeferencing the NAC dataset requires storage. There are ~4,000,000+ images, which requires ~1000+ TB of storage for only the output NAC files, not including the temporary files made during the pre-processing stages. This is logistically intensive and would require an extensive archive system. Mosaicking the NAC dataset is a reasonable data reduction method; combining only the needed NAC images can reduce the storage needed to keep the separate images.

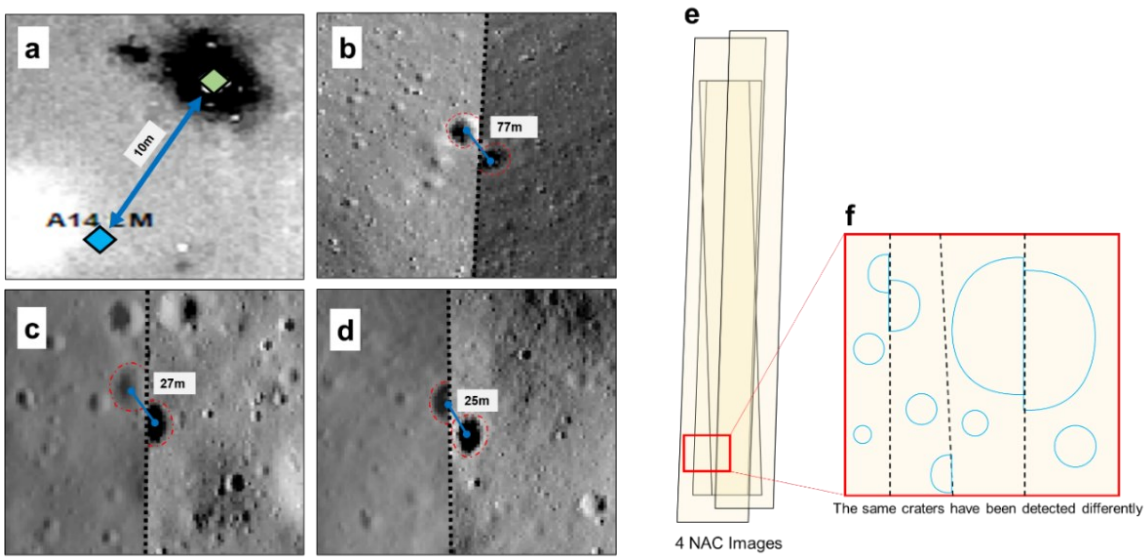

Figure 2.11: The range of offsets in the georeferenced lunar NAC images: (a) 10m offset shown by the Apollo 14 LM location (image M1361298694L), the blue-dot is the actual geographical location (3.64° S,17.47° W), while the yellow-dot is the Apollo LM location on georeferenced NAC image; panels (b), (c), and (d) are other offsets observed across neighbouring NAC image pairs; (e) and (f) is a schematic diagram illustrating the overlapping image offset problem with the NAC images and crater detection, and the difficulty in creating controlled seamless mosaics.

For example, 1725 NACL-R images would individually take up 425 GB of storage, but when turned into a mosaic image, it only requires 55 GB. Conversely, the Kaguya TC image dataset consists of 14,400 3° by 3° tiles (7,200 morning tiles, 7,200 evening tiles) (Isbell et al., 2014), requiring only 4.32 TB of storage. The Kaguya TC dataset is more feasible within the scope of this project, not only logistically (Figure 2.12) but also scientifically: the Kaguya TC dataset presents two versions of the Moon's surface with consistent lighting conditions – a major factor that controls the quality of crater detections (Richardson et al., 2022).

Ultimately, the limitations relating to the NAC image offsets and needed storage systems could not be resolved within this project. This restricted our use of NAC images. We determined that the NAC image datasets will be used for local, finer-scale analysis (<100 km^2) - where resolution is needed more than coverage. Consequently, for global, large-scale analysis, we used the Kaguya TC image dataset (see Chapter 4 for examples of small- and large-scale crater count analyses).

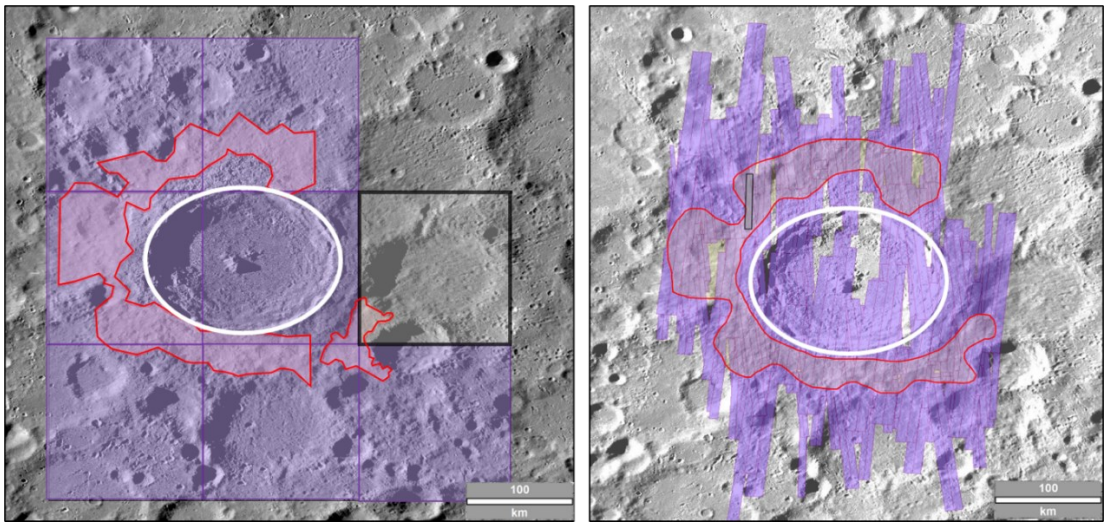

Figure 2.12: [Left] Visual representation of the difference between Kaguya TC image tiles (n=7) and [Right] NAC images (n=381) [purple footprints] needed to cover [red] count area for Tycho crater (e.g., Hiesinger et al. (2012)'s WAC TE area). The shown NAC image footprints are all images with incidence angles between 60° and 80° that transect the count area. NAC image M104599198L is selected to show the area covered by a single NAC image (NW crater rim). Likewise, Kaguya TC image TCO_MAPe04_S42E351S45E354SC is selected to show the area covered by a single TC tile. Note that even with 381 images, there are still gaps in the coverage.

2.6 Summary

Crater count chronologies constitute a fundamental method in planetary science, allowing scientists to infer the relative ages of different planetary surfaces by analyzing the density and distribution of impact craters. The underlying principle is based on the assumption that older surfaces accumulate more craters over time, providing a valuable tool for understanding the geological history of celestial bodies. This method has been extensively employed on various planetary bodies, including the Moon and Mars, contributing significantly to our understanding of their surface evolution.

In recent years, advancements in Machine Learning (ML) have revolutionized the field of planetary science, with Convolutional Neural Networks (CNNs) emerging as powerful tools for image recognition tasks. CNNs are particularly adept at identifying image patterns and features, making them well-suited for tasks like crater detection. By training CNNs on datasets of known craters, scientists can develop robust models capable of automatically identifying and cataloguing craters in planetary images. The You Only Look Once (YOLO) is an object detection CNN algorithm. YOLO is valuable for its real-time processing capabilities, making it an attractive choice for applications where speed is crucial. In the context of planetary science, the YOLO algorithm has been employed for automated crater detection in lunar images. By swiftly identifying and delineating craters, YOLO facilitates the rapid analysis of large datasets, expanding crater count chronologies.

One notable application of ML algorithms in crater analysis involves the Lunar Reconnaissance Orbiter Camera (LROC) Narrow Angle Camera (NAC) images. These high-resolution images captured by the LROC have provided unprecedented details of the lunar surface, enabling scientists to create more accurate crater count chronologies. Such ML methodologies can also be applied to lunar images captured by the Kaguya Terrain Camera (TC), which provides high-quality images of the lunar surface. Kaguya TC images allow us to extend their crater analysis techniques to different regions of the Moon, providing a comprehensive understanding of its geological history. These techniques enhance the efficiency of crater analysis and open avenues for exploring and deciphering the geological evolution of the Moon.

2.7 References

Ajit, A., Acharya, K., & Samanta, A. (2020). A Review of Convolutional Neural Networks. 2020 International Conference on Emerging Trends in Information Technology and Engineering (Ic-ETITE), 1–5. https://doi.org/10.1109/ic-ETITE47903.2020.049

Albawi, S., Mohammed, T. A., & Al-Zawi, S. (2017). Understanding of a convolutional neural network. 2017 International Conference on Engineering and Technology (ICET), 1–6. https://doi.org/10.1109/ICEngTechnol.2017.8308186

Baldwin, R. B. (1964). Lunar crater counts. The Astronomical Journal, 69, 377. https://doi.org/10.1086/109289

Basilevsky, A. T., Head, J. W., & Horz, F. (2013). Survival times of meter-sized boulders on the surface of the Moon. Planetary and Space Science, 89, 118–126. https://doi.org/10.1016/j.pss.2013.07.011

Benedix, G. K., Lagain, A., Chai, K., Meka, S., Anderson, S., Norman, C., Bland, P. A., Paxman, J., Towner, M. C., & Tan, T. (2020). Deriving Surface Ages on Mars Using Automated Crater Counting. Earth and Space Science, 7(3). https://doi.org/10.1029/2019EA001005

Bierhaus, E. B., Chapman, C. R., & Merline, W. J. (2005). Secondary craters on Europa and implications for cratered surfaces. Nature, 437(7062), 1125–1127. https://doi.org/10.1038/nature04069

Brown, P., Spalding, R. E., ReVelle, D. O., Tagliaferri, E., & Worden, S. P. (2002). The flux of small near-Earth objects colliding with the Earth. Nature, 420(6913), 294–296. https://doi.org/10.1038/nature01238

Chapman, C. R. (2015). A Critique of Methods for Analysis of Crater Size-Frequency Distributions.

Chapman, C. R., & Haefner, R. R. (1967). A critique of methods for analysis of the diameter-frequency relation for craters with special application to the Moon. Journal of Geophysical Research, 72(2), 549–557. https://doi.org/10.1029/JZ072i002p00549

Chapman, C. R., & Haefner, R. R. (1967). A critique of methods for analysis of the diameter-frequency relation for craters with special application to the Moon. Journal of Geophysical Research, 72(2), 549–557. https://doi.org/10.1029/JZ072i002p00549

Che, X., Nemchin, A., Liu, D., Long, T., Wang, C., Norman, M. D., Joy, K. H., Tartese, R., Head, J., Jolliff, B., Snape, J. F., Neal, C. R., Whitehouse, M. J., Crow, C., Benedix, G., Jourdan, F., Yang, Z., Yang, C., Liu, J., … Webb, S. G. (2021). Age and composition of young basalts on the Moon, measured from samples returned by Chang'e-5. Science, 374(6569), 887–890. https://doi.org/10.1126/science.abl7957

Crater analysis techniques working group. (1979). Standard techniques for presentation and analysis of crater size-frequency data. Icarus, 37(2), 467–474. https://doi.org/10.1016/0019-1035(79)90009-5

Dureja, A., & Pahwa, P. (2019). Analysis of Non-Linear Activation Functions for Classification Tasks Using Convolutional Neural Networks. Recent Patents on Computer Science, 12(3), 156–161. https://doi.org/10.2174/2213275911666181025143029

Fassett, C. I. (2016). Analysis of impact crater populations and the geochronology of planetary surfaces in the inner solar system: Crater Populations and Surface

Chronology. Journal of Geophysical Research: Planets, 121(10), 1900–1926. https://doi.org/10.1002/2016JE005094
Fassett, C. I., & Thomson, B. J. (2014). Crater degradation on the lunar maria: Topographic diffusion and the rate of erosion on the Moon: Crater degradation on the lunar maria. Journal of Geophysical Research: Planets, 119(10), 2255–2271. https://doi.org/10.1002/2014JE004698
Gault, D. E. (1970). Saturation and Equilibrium Conditions for Impact Cratering on the Lunar Surface: Criteria and Implications. Radio Science, 5(2), 273–291. https://doi.org/10.1029/RS005i002p00273
GDAL documentation. (2021). GDAL. https://gdal.org/
Giguere, T. A., Boyce, J. M., Gillis-Davis, J. J., Trang, D., & Stopar, J. D. (2022). Lava flow ages in northeastern Oceanus Procellarum: The need for calibrating crater counting procedures. Icarus, 375, 114838. https://doi.org/10.1016/j.icarus.2021.114838
Golovko, V., Kroshchanka, A., & Treadwell, D. (2016). The nature of unsupervised learning in deep neural networks: A new understanding and novel approach. Optical Memory and Neural Networks, 25(3), 127–141. https://doi.org/10.3103/S1060992X16030073
Gu, J., Wang, Z., Kuen, J., Ma, L., Shahroudy, A., Shuai, B., Liu, T., Wang, X., Wang, G., Cai, J., & Chen, T. (2018). Recent advances in convolutional neural networks. Pattern Recognition, 77, 354–377. https://doi.org/10.1016/j.patcog.2017.10.013
Hartmann, W. K. (1965). Terrestrial and lunar flux of large meteorites in the last two billion years. Icarus, 4(2), 157–165. https://doi.org/10.1016/0019-1035(65)90057-6
Hartmann, W. K. (1966). Martian Cratering. Icarus, 5(1–6), 565–576. https://doi.org/10.1016/0019-1035(66)90071-6
Hartmann, W. K. (1984). Does crater “saturation equilibrium” occur in the solar system? Icarus, 60(1), 56–74. https://doi.org/10.1016/0019-1035(84)90138-6
Hartmann, W. K. (1995). Planetary cratering 1. The question of multiple impactor populations: Lunar evidence. Meteoritics, 30(4), 451–467. https://doi.org/10.1111/j.1945-5100.1995.tb01152.x
Hartmann, W. K. (2007). Martian cratering 9: Toward resolution of the controversy about small craters. Icarus, 189(1), 274–278. https://doi.org/10.1016/j.icarus.2007.02.011
Hartmann, W. K., & Daubar, I. J. (2017). Martian cratering 11. Utilizing decameter scale crater populations to study Martian history. Meteoritics & Planetary Science, 52(3), 493–510. https://doi.org/10.1111/maps.12807
Hartmann, W. K., & Neukum, G. (2001). Cratering Chronology and the Evolution of Mars. In R. Kallenbach, J. Geiss, & W. K. Hartmann (Eds.), Chronology and Evolution of Mars (Vol. 12, pp. 165–194). Springer Netherlands. https://doi.org/10.1007/978-94-017-1035-0_6
Haruyama, J., Ohtake, M., Matsunaga, T., Morota, T., Yokota, Y., Honda, C., Hirata, N., Demura, H., Iwasaki, A., Nakamura, R., & Kodama, S. (2008). Planned radiometrically calibrated and geometrically corrected products of lunar high-resolution Terrain Camera on SELENE. Advances in Space Research, 42(2), 310–316. https://doi.org/10.1016/j.asr.2007.04.062
He, F. (2020). Remote sensing of planetary space environment. Chinese Science Bulletin, 65(14), 1305–1319. https://doi.org/10.1360/TB-2019-0804

Hiesinger, H., Marchi, S., Schmedemann, N., Schenk, P., Pasckert, J. H., Neesemann, A., O'Brien, D. P., Kneissl, T., Ermakov, A. I., Fu, R. R., Bland, M. T., Nathues, A., Platz, T., Williams, D. A., Jaumann, R., Castillo-Rogez, J. C., Ruesch, O., Schmidt, B., Park, R. S., … Raymond, C. A. (2016). Cratering on Ceres: Implications for its crust and evolution. Science, 353(6303), aaf4759. https://doi.org/10.1126/science.aaf4759

Isbell, C., Gaddis, L., Garcia, P., Hare, T., & Bailen, M. (2014). Kaguya Terrain Camera Mosaics. 2268.

ISIS3. (2021). [C++]. USGS Astrogeology. https://github.com/USGS-Astrogeology/ISIS3

Ito, T., & Malhotra, R. (2010). Asymmetric impacts of near-Earth asteroids on the Moon. Astronomy and Astrophysics, 519, A63. https://doi.org/10.1051/0004-6361/200912901

Ivanov, B. A., Neukum, G., Bottke, W. F., & Hartmann, W. K. (2002). The Comparison of Size-Frequency Distributions of Impact Craters and Asteroids and the Planetary Cratering Rate. Asteroids III, 1. https://www.researchgate.net/publication/253429785

Ivanov, B. A., Neukum, G., Bottke, W. F., & Hartmann, W. K. (2002). The Comparison of Size-Frequency Distributions of Impact Craters and Asteroids and the Planetary Cratering Rate. Asteroids III, 1. https://www.researchgate.net/publication/253429785

Jocher, G. (2021). Ultralytics YOLOv3 [Python]. Ultralytics. https://github.com/ultralytics/yolov3

Jocher, G. (2022). Ultralytics YOLOv5 [Python]. Ultralytics. https://github.com/ultralytics/yolov5

Kneissl, T., van Gasselt, S., & Neukum, G. (2011). Map-projection-independent crater size-frequency determination in GIS environments—New software tool for ArcGIS. Planetary and Space Science, 59(11–12), 1243–1254. https://doi.org/10.1016/j.pss.2010.03.015

Koushik, J. (2016). Understanding Convolutional Neural Networks. https://doi.org/10.48550/ARXIV.1605.09081

Lagain, A., Benedix, G. K., Servis, K., Baratoux, D., Doucet, L. S., Rajšic, A., Devillepoix, H. A. R., Bland, P. A., Towner, M. C., Sansom, E. K., & Miljković, K. (2021b). The Tharsis mantle source of depleted shergottites revealed by 90 million impact craters. Nature Communications, 12(1), 6352. https://doi.org/10.1038/s41467-021-26648-3

Lagain, A., Devillepoix, H. A. R., Vernazza, P., Robertson, D., Granvik, M., Pokorny, P., Ozerov, A., Shober, P. M., Jorda, L., Servis, K., Fairweather, J. H., Quesnel, Y., & Benedix, G. K. (2024). Recalibration of the lunar chronology due to spatial cratering-rate variability. Icarus, 411, 115956. https://doi.org/10.1016/j.icarus.2024.115956

Lagain, A., Servis, K., Benedix, G. K., Norman, C., Anderson, S., & Bland, P. A. (2021a). Model Age Derivation of Large Martian Impact Craters, Using Automatic Crater Counting Methods. Earth and Space Science, 8(2). https://doi.org/10.1029/2020EA001598

Le Feuvre, M., & Wieczorek, M. A. (2011). Nonuniform cratering of the Moon and a revised crater chronology of the inner Solar System. Icarus, 214(1), 1–20. https://doi.org/10.1016/j.icarus.2011.03.010

Le Feuvre, M., & Wieczorek, M. A. (2011). Nonuniform cratering of the Moon and a revised crater chronology of the inner Solar System. Icarus, 214(1), 1–20. https://doi.org/10.1016/j.icarus.2011.03.010

Melosh, H. J. (1989). Impact Cratering: A Geologic Process. Oxford University Press. https://books.google.com.au/books?id=nZwRAQAAIAAJ

Michael, G. G., & Neukum, G. (2010). Planetary surface dating from crater size–frequency distribution measurements: Partial resurfacing events and statistical age uncertainty. Earth and Planetary Science Letters, 294(3–4), 223–229. https://doi.org/10.1016/j.epsl.2009.12.041

Michael, G. G., Platz, T., Kneissl, T., & Schmedemann, N. (2012). Planetary surface dating from crater size–frequency distribution measurements: Spatial randomness and clustering. Icarus, 218(1), 169–177. https://doi.org/10.1016/j.icarus.2011.11.033

Michael, G. G., Platz, T., Kneissl, T., & Schmedemann, N. (2012). Planetary surface dating from crater size–frequency distribution measurements: Spatial randomness and clustering. Icarus, 218(1), 169–177. https://doi.org/10.1016/j.icarus.2011.11.033

Minton, D. A., Fassett, C. I., Hirabayashi, M., Howl, B. A., & Richardson, J. E. (2019). The equilibrium size-frequency distribution of small craters reveals the effects of distal ejecta on lunar landscape morphology. Icarus, 326, 63–87. https://doi.org/10.1016/j.icarus.2019.02.021

Namiki, N., & Honda, C. (2003). Testing hypotheses for the origin of steep slope of lunar size-frequency distribution for small craters. Earth, Planets and Space, 55(1), 39–51. https://doi.org/10.1186/BF03352461

Nemtchinov, I. V., Svetsov, V. V., Kosarev, I. B., Golub', A. P., Popova, O. P., Shuvalov, V. V., Spalding, R. E., Jacobs, C., & Tagliaferri, E. (1997). Assessment of Kinetic Energy of Meteoroids Detected by Satellite-Based Light Sensors. Icarus, 130(2), 259–274. https://doi.org/10.1006/icar.1997.5821

Neukum, G. (1984). Meteoritenbombardement und Datierung planetarer Oberflachen (Meteorite bombardment and dating of planetary surfaces). University of Munich, Germany.

Neukum, G., Ivanov, B. A., & Hartmann, W. K. (2001). Cratering Records in the Inner Solar System in Relation to the Lunar Reference System. In R. Kallenbach, J. Geiss, & W. K. Hartmann (Eds.), Chronology and Evolution of Mars (Vol. 12, pp. 55–86). Springer Netherlands. https://doi.org/10.1007/978-94-017-1035-0_3

Neukum, G., Ivanov, B. A., & Hartmann, W. K. (2001). Cratering Records in the Inner Solar System in Relation to the Lunar Reference System. In R. Kallenbach, J. Geiss, & W. K. Hartmann (Eds.), Chronology and Evolution of Mars (Vol. 12, pp. 55–86). Springer Netherlands. https://doi.org/10.1007/978-94-017-1035-0_3

Nordyke, M. D. (1961). Nuclear craters and preliminary theory of the mechanics of explosive crater formation. Journal of Geophysical Research, 66(10), 3439–3459. https://doi.org/10.1029/JZ066i010p03439

Norman, M. D. (2009). The Lunar Cataclysm: Reality or 'Mythconception'? Elements, 5(1), 23–28. https://doi.org/10.2113/gselements.5.1.23

O'Shea, K., & Nash, R. (2015). An Introduction to Convolutional Neural Networks. https://doi.org/10.48550/ARXIV.1511.08458

Öhman, T. (2015). A beginner's guide to stereo-derived DEM production and analysis using ISIS, ASP, and ArcMap. https://doi.org/10.13140/RG.2.1.1743.7609

Opik, E. J. (1958). Meteor Impact on Solid Surface. Irish Astronomical Journal, 5, 14.

Opik, E. J. (1960). The Lunar Surface as an Impact Counter. Monthly Notices of the Royal Astronomical Society, 120(5), 404–411. https://doi.org/10.1093/mnras/120.5.404

Pawsey. (2023). Pawsey Supercomputing Centre. https://pawsey.org.au/

Qian, Y., Xiao, L., Head, J. W., van der Bogert, C. H., Hiesinger, H., & Wilson, L. (2021). Young lunar mare basalts in the Chang'e-5 sample return region, northern Oceanus Procellarum. Earth and Planetary Science Letters, 555, 116702. https://doi.org/10.1016/j.epsl.2020.116702

Redmon, J., & Farhadi, A. (2018). YOLOv3: An Incremental Improvement. ArXiv Preprint ArXiv. https://arxiv.org/abs/1804.02767

Redmon, J., Vivvala, S., Girshick, R., & Farhadi, A. (2016). You Only Look Once: Unified, Real-Time Object Detection. Proceedings of the IEEE Conference on Computer Vision and Pattern Recognition (CVPR), 779–788.

Richardson, M., Malagón, A. A. P., Lebofsky, L. A., Grier, J., Gay, P., Robbins, S. J., & Team, T. C. (2022). The CosmoQuest Moon Mappers Community Science Project: The Effect of Incidence Angle on the Lunar Surface Crater Distribution. https://doi.org/10.48550/ARXIV.2110.13404

Robbins, S. J. (2014). New crater calibrations for the lunar crater-age chronology. Earth and Planetary Science Letters, 403, 188–198. https://doi.org/10.1016/j.epsl.2014.06.038

Robbins, S. J., & Hynek, B. M. (2012). A New Global Database of Mars Impact Craters ≥1 km: 1. Database creation, properties, and parameters. Journal of Geophysical Research: Planets, 117(E5), n/a-n/a. https://doi.org/10.1029/2011JE003966

Robbins, S. J., Antonenko, I., Kirchoff, M. R., Chapman, C. R., Fassett, C. I., Herrick, R. R., Singer, K., Zanetti, M., Lehan, C., Huang, D., & Gay, P. L. (2014). The variability of crater identification among expert and community crater analysts. Icarus, 234, 109–131. https://doi.org/10.1016/j.icarus.2014.02.022

Robbins, S. J., Riggs, J. D., Weaver, B. P., Bierhaus, E. B., Chapman, C. R., Kirchoff, M. R., Singer, K. N., & Gaddis, L. R. (2018). Revised recommended methods for analyzing crater size-frequency distributions. Meteoritics & Planetary Science, 53(4), 891–931. https://doi.org/10.1111/maps.12990

Robertson, D., Ozerov, A., Wheeler, L., Pokorný, P., Granvik, M., & Rumpf, C. (2023). Erratum: "Latitude Variation of Flux and Impact Angle of Asteroid Collisions with Earth and the Moon" (2021, PSJ, 2, 88). The Planetary Science Journal, 4(1), 19. https://doi.org/10.3847/PSJ/aca1a7

Robertson, D., Pokorný, P., Granvik, M., Wheeler, L., & Rumpf, C. (2021). Latitude Variation of Flux and Impact Angle of Asteroid Collisions with Earth and the Moon. The Planetary Science Journal, 2(3), 88. https://doi.org/10.3847/PSJ/abefda

Robinson, M. S., Brylow, S. M., Tschimmel, M., Humm, D., Lawrence, S. J., Thomas, P. C., Denevi, B. W., Bowman-Cisneros, E., Zerr, J., Ravine, M. A., Caplinger, M. A., Ghaemi, F. T., Schaffner, J. A., Malin, M. C., Mahanti, P., Bartels, A., Anderson, J., Tran, T. N., Eliason, E. M., … Hiesinger, H. (2010).

Lunar Reconnaissance Orbiter Camera (LROC) Instrument Overview. Space Science Reviews, 150(1–4), 81–124. https://doi.org/10.1007/s11214-010-9634-2

Schmedemann, N., Kneissl, T., Ivanov, B. A., Michael, G. G., Wagner, R. J., Neukum, G., Ruesch, O., Hiesinger, H., Krohn, K., Roatsch, T., Preusker, F., Sierks, H., Jaumann, R., Reddy, V., Nathues, A., Walter, S. H. G., Neesemann, A., Raymond, C. A., & Russell, C. T. (2014). The cratering record, chronology and surface ages of (4) Vesta in comparison to smaller asteroids and the ages of HED meteorites. Planetary and Space Science, 103, 104–130. https://doi.org/10.1016/j.pss.2014.04.004

Shoemaker, E. M., & Hackman, R. J. (1962). Stratigraphic Basis for a Lunar Time Scale. In The Moon (Vol. 14, pp. 289–300). https://ui.adsabs.harvard.edu/abs/1962IAUS...14..289S

Speyerer, E. J., Robinson, M. S., Denevi, B. W., & LROC Science Team. (2011). Lunar Reconnaissance Orbiter Camera Global Morphological Map of the Moon. 2387.

Stöffler, D., & Ryder, G. (2001). Stratigraphy and Isotope Ages of Lunar Geologic Units: Chronological Standard for the Inner Solar System. Space Science Reviews, 96(1/4), 9–54. https://doi.org/10.1023/A:1011937020193

Strom, R. G., Malhotra, R., Ito, T., Yoshida, F., & Kring, D. A. (2005). The Origin of Planetary Impactors in the Inner Solar System. Science, 309(5742), 1847–1850. https://doi.org/10.1126/science.1113544

Strom, R. G., Malhotra, R., Xiao, Z.-Y., Ito, T., Yoshida, F., & Ostrach, L. R. (2015). The inner solar system cratering record and the evolution of impactor populations. Research in Astronomy and Astrophysics, 15(3), 407–434. https://doi.org/10.1088/1674-4527/15/3/009

The Click Reader. (2020, November 24). Building A Convolutional Neural Network—The Click Reader. https://www.theclickreader.com/building-a-convolutional-neural-network/

Trask, N. J. (1966). Size and spatial distribution of craters estimated from the Ranger photographs. https://ntrs.nasa.gov/citations/19660015760

Wang, Y., Xie, M., Xiao, Z., & Cui, J. (2020). The minimum confidence limit for diameters in crater counts. Icarus, 341, 113645. https://doi.org/10.1016/j.icarus.2020.113645

Wang, Y., Zhu, X., & Wu, B. (2019). Automatic detection of individual oil palm trees from UAV images using HOG features and an SVM classifier. International Journal of Remote Sensing, 40(19), 7356–7370. https://doi.org/10.1080/01431161.2018.1513669

Wu, B., & Liu, W. C. (2017). Calibration of boresight offset of LROC NAC imagery for precision lunar topographic mapping. ISPRS Journal of Photogrammetry and Remote Sensing, 128, 372–387. https://doi.org/10.1016/j.isprsjprs.2017.04.012

Wu, X. (1999). Performance evaluation, prediction and visualization of parallel systems. Boston : Kluwer Academic Publishers. http://archive.org/details/performanceevalu0000wuxi

Xiao, Z., & Werner, S. C. (2015). Size-frequency distribution of crater populations in equilibrium on the Moon. Journal of Geophysical Research: Planets, 120(12), 2277–2292. https://doi.org/10.1002/2015JE004860

Yolo_Label. (2021). [C++]. https://github.com/developer0hye/Yolo_Label

Zhang, Y. (2010). New Advances in Machine Learning. BoD – Books on Demand.

Chapter 3: Automatic Mapping of Small Lunar Impact Craters Using LRO NAC Images

This chapter is published under Fairweather, J. H., Lagain, A., Servis, K., Benedix, G. K., Kumar, S. S., & Bland, P. A. (2022). Automatic Mapping of Small Lunar Impact Craters Using LRO-NAC Images. Earth and Space Science, 9(7). https://doi.org/10.1029/2021EA002177. Please note that slight modifications were made in this chapter to improve the readability.

Abstract

Impact craters are the most common feature on the Moon's surface. Crater size–frequency distributions provide critical insight into the timing of geological events, surface erosion rates, and impact fluxes. The impact crater size–frequency follows a power law (meter-sized craters are a few orders of magnitude more numerous than kilometric ones), making it tedious to manually measure all the craters within an area to the smallest sizes. We can bridge this gap by using a machine-learning algorithm. We adapted a Crater Detection Algorithm to work on the highest resolution lunar image data set (Lunar Reconnaissance Orbiter Narrow-Angle Camera [NAC] images). We describe the retraining and application of the detection model to pre-processed NAC images and discuss the accuracy of the resulting crater detections. We evaluated the model by assessing the results across six NAC images, each covering a different lunar area at differing lighting conditions. We present the model's average true positive rate for small impact craters (down to 20 m in diameter) is 93%. The model does display a 15% overestimation in calculated crater diameters. The presented crater detection model shows acceptable performance on NAC images with incidence angles ranging between ∼50° and ∼70° and can be applied to many lunar sites independent of morphology.

3.1 Introduction

Mapping and recording structural features across celestial bodies is one of the ways researchers gather spatial and temporal context about the evolution of our solar system. As a readily available structure across a host of bodies, impact craters give us the interface to understanding and interpreting extra-terrestrial geological events (see Young, 1940; Opik, 1960; Hartmann, 1966; Fassett, 2016; Shoemaker & Hackman, 1962; Neukum et al., 2001; Ivanov et al., 2002). Rocky bodies, such as the Moon, act as cosmic records for the solar system, where impact craters accumulate on the surface over time (Hartmann, 1965; Melosh, 1989). The development of modern space technologies and satellite systems has made locating and mapping impact craters with ever-increasing detail a familiar task for many planetary scientists (Fassett, 2016; Ivanov et al., 2002). Craters of all sizes inform us of the physical characteristics of the impacted terrains, such as their density, porosity, and composition (e.g., Melosh, 1989; van der Bogert et al., 2017), as well as areas of scientific interest (potential landing sites). For example, the Moon has varying amounts of regolith with different degrees of thicknesses, and by measuring impact craters, we can model and estimate those regolith thicknesses (Bart et al., 2011; Rajšić et al., 2021; Stopar et al., 2012, 2017; Wilcox et al., 2005). Specifically, small impact craters (<1 km) aid in determining the rate of erosion (Fassett & Thomson, 2014; Soderblom, 1970) and calculating surface retention ages (Qiao et al., 2017).

Crater chronology methods, based on recording cratering densities across different surfaces, give the ability to assign model ages to different geological units and events (Baldwin, 1965; Hartmann, 1965; Moore et al., 1980; Neukum et al., 2001; Shoemaker & Hackman, 1962; Williams et al., 2018). Surfaces with more craters are older than less cratered surfaces, as they have been exposed longer (Neukum et al., 2001; Shoemaker & Hackman, 1962). This relative age relationship becomes a model age when defined by the radiometrically dated returned lunar samples (Apollo, Luna, and now Chang'e). However, this method is not without error and requires the ability to map impact craters accurately within an area (Baldwin, 1964; Povilaitis et al., 2018; Robbins, 2014). Secondary craters, which can dominate a crater population (<1 km), are formed from ejected material which fails to reach escape velocity. These craters typically occur in clusters radiating away from the

primary impact (McEwen and Bierhaus, 2006). This ejected material contains crucial information about the primary impactor and impacted surface (Lagain et al., 2021a). Secondary craters should not be used when calculating model ages, though it can be challenging to differentiate secondaries from small primary impacts (McEwen and Bierhaus, 2006; Povilaitis et al., 2018; Stadermann et al., 2018). Small craters across the Moon's surfaces are in a state of equilibrium (<1 km for post-Nectarian surfaces), meaning the number of craters being obliterated is proportional to the crater density of the impacted surface of a given age (Hartmann, 1971; Moore et al., 1980; Minton et al., 2019; Povilaitis et al., 2018; Schultz et al., 1977; Xiao and Werner, 2015). Creating a dataset of small impact craters allows us to gather more detail on the equilibrium and retention states across younger terrains (Minton et al., 2019). Recording the small crater population in and around larger craters and landforms also gives spatial context to the secondary clusters and transported material (McEwen and Bierhaus, 2006; Schultz et al., 1977).

All such crater analyses rely on a complete cratering record (all craters to a given size counted) across a range of diameters (Crater Analysis Techniques Working Group, 1979; Xiao & Strom, 2012). It is well-established that the cumulative number of impact craters on a planetary surface follows an inverse power law relationship (Hartmann, 1965; Shoemaker & Hackman, 1962; Ivanov et al., 2001; Robbins et al., 2018). This relationship means that to count ever-smaller craters reliably across a surface, one must count exponentially increasing numbers. The task of counting craters has historically (pre-2000) been restricted to manual mapping methods, first using maps, rulers, and pencils (see Baldwin, 1964, 1987a, 1987b; Hartmann, 1965, 1977), and now using Geographical Information System (GIS) tools (see, Kneissl et al., 2011 [for the GIS Tool]; Head et al., 2010; Povilaitis et al., 2018; Robbins, 2019 [for the Moon]; Robbins & Hynek, 2012; Lagain et al., 2021b [for Mars]; Herrick et al., 2018 [for Mercury]; Zeilnhofer, 2020 [for Ceres]; Liu et al., 2018 [for Vesta]). These manual methods have resulted in hundreds of thousands to millions of craters counted on different bodies. However, studies of human attention span have shown that the ability to identify any feature consistently and reliably significantly decreases with time spent on the task (See et al., 1995; Langner and Eickhoff, 2013). This, and personal interpretation, leads to variability of impact crater identification between researchers (Robbins et al., 2014).

Robbins (2019) compiled a comprehensive, manual, global database of lunar impact craters (~1.3 million entries), complete down to 1-2 km in diameter using the LRO-WAC (Lunar Reconnaissance Orbiter – Wide Angle Camera) imagery (resolution = 100 m/px) and Digital Elevation Models (DEM) from LOLA (Lunar Orbiter Laser Altimeter)/SELENE Kaguya (resolution = 59 m/px at ± 60° latitude and 100m/px across ± 90° latitude) (Robinson et al., 2010; Smith et al., 2010). This vast dataset clarified the manual mapping level that can be accomplished using the latest satellite datasets and GIS. At present, the highest resolution images available for the Moon are the LRO-NAC images (Narrow-Angle Camera images, at 0.25-2 m/px), which allows scientists to map and record hundreds of thousands of decimetre-sized craters within a single NAC image (~5 km by ~25 km) (Robinson et al., 2010). As the orbiter is still actively imaging the lunar surface and the image dataset is continually updated, we can map the lunar surface completely. However, creating a global record of small (deci-metre diameter range) craters on the Moon using manual mapping techniques is inconvenient (Cadogan, 2020; Lee and Hogan, 2021; Hashimoto and Mori, 2019). Automated crater mapping techniques can provide the bridge into the global analysis of deci-metre-sized craters.

Significant progress in automated lunar crater detection within the last decade has allowed researchers to increase the scale and consistency in which we map craters. Comprehensive reviews by DeLatte et al. (2019) and Stepinski et al. (2012) show that automating crater detections has been investigated since the early 1980s. The advancement of modern Convolutional Neural Networks (CNN), a type of deep machine learning algorithm that focuses on object detection in visual datasets (see Goodfellow et al., 2016, Chapter 9 for a review), has provided a leap forward for planetary science. The heavily cratered surfaces of the Moon and Mars have been key targets for generating and testing automated crater datasets. Current published automated datasets (discussed further below) use both DEM-based and optical imagery-based methods to high degrees of accuracy (measured in true detection rate or Recall) when compared against manual crater datasets (e.g. Head et al., 2010; Jia et al., 2020a; Povilaitis et al., 2018; Robbins, 2019). Hybrid automated methodologies (crater datasets based on DEM and optical imagery), such as Salamunićcar et al. (2012, 2014), had success in using an automatic crater detection algorithm for the lunar surface, producing a published catalogue of 19,396 detections

– which was incorporated into the Salamuniccar et al. (2012) LU60645GT catalogue (see, LU78287GT catalogue, 78,287 craters complete to ~8 km). Their method was one of the few to utilise both Hough transforms (a different type of algorithm that detects crater boundaries) and crater shape interpolation, which combines detections from a modified LOLA DEMs and WAC Images to generate a crater dataset. Their dataset had a detection rate of 83% (Salamunićcar et al., 2012) and ~85% (Salamunićcar et al., 2014).

DEM-based methods, such as Silburt et al. (2019), developed a CDA trained on the LOLA/Kaguya DEM. In their study, the team detected 15,658 craters between ~2 km to ~90 km (across the eastern side of the Moon, 60°E to 180°E), with a high detection rate of 92%. Silburt et al. (2019)'s CDA stands out as their team showed the transferability of their lunar detection model to different celestial bodies, such as Mercury (using MESSENGER DEM, 665 m/px) with promising preliminary results (also see, Lee (2019) for the model's modification for Mars craters). Wang et al. (2021) also developed a DEM-based CDA for use across LOLA DEM, which detected craters with three-dimensional morphological characteristics (such as rim height, interior slope, and depth). Their crater dataset (LU1319373) consists of a massive 1 million craters >1 km, with a detection rate of ~85%.

Strictly image-based methods, such as Hashimoto and Mori (2019), aimed at detecting small craters (<50 pixels) across the lunar south pole using LRO-NAC imagery. Their two-staged method cuts the image data into grids/tiles, runs a semantic segmentation algorithm (a CNN algorithm that outputs a modified image instead of a list of detections), followed by an object detection algorithm to gather the position of the craters within in the grid, with a detection rate 80.5%. Another image-based CDA by Cadogan (2020) tested the automatic detection of small craters (>2.5 m) by using six overlapping LRO-NAC images. His analyses were conducted over the Apollo, Luna, Lunokhod, and Ranger sites, with the most extensive analysis over the Lunokhod 1 site, where >300,000 craters over 2.5 m in diameter were automatically detected with a calculated detection rate of 86%.

Many of these studies recommend using a DEM (Di et al., 2014; Silburt et al., 2019; Wang et al., 2021) or a hybrid-based method (Salamunićcar et al., 2011; Yang et al., 2020) for making a global crater dataset.

While DEMs have excellent, consistent global coverage, they lack the resolution to map craters to the sub-kilometre scale (Urbach and Stepinski, 2009). The benefit of using an image-based CNN object detection algorithm for the Moon (as opposed to DEM-based CNN) is the availability of LRO-NAC high-resolution image data. Compared to the lower-resolution global DEMs, the image data's global coverage allows for far greater effectiveness in small crater (<1 km) detection.

Our approach aims for a reliable detection model for small impact craters. We make a dataset complete to the small (20 m) crater scale, wherever suitable NAC images are available, using an object detection, image-based, machine learning algorithm. We accomplish this by adapting an existing object detection Convolutional Neural Network (CNN) model designed to globally identify impact structures on high-resolution planetary images of Mars (see Benedix et al., 2020; Lagain et al., 2021a; Lagain et al., 2021c) to the Moon. A trained Crater Detection Algorithm (CDA) can potentially address the large variabilities in consistency, time consumption, and reproducibility, which influence manual crater counts. This paper presents the methodology and evaluation of our automated Crater Detection Algorithm across LRO-NAC images.

3.2 Methodology

The machine learning framework we adopted in this study, initially outlined in Benedix et al. (2020), works in three phases (Figure 3.1). The first phase (Figure 3.1.a) pre-processes the input NAC imagery by changing image projection and file format. The second phase (Figure 3.1.b) is a supervised learning and validation cycle series, producing a trained detection model. Finally, the third phase (Figure 3.1.c) uses that detection model to identify craters across a suite of input images to produce a list of detections. The subsequent detections are analysed for duplicates and, where found, are removed through a Non-Maximum Suppression (NMS) approach using detection location and confidence value (see Benedix et al., 2020) (Figure 3.1.c, and further explained in Section 3.2.3.a). In this study, we utilised an open-source software workflow framework called Nextflow (Di Tommaso et al., 2017) to concatenate and run phases a and c (Figure 3.1).

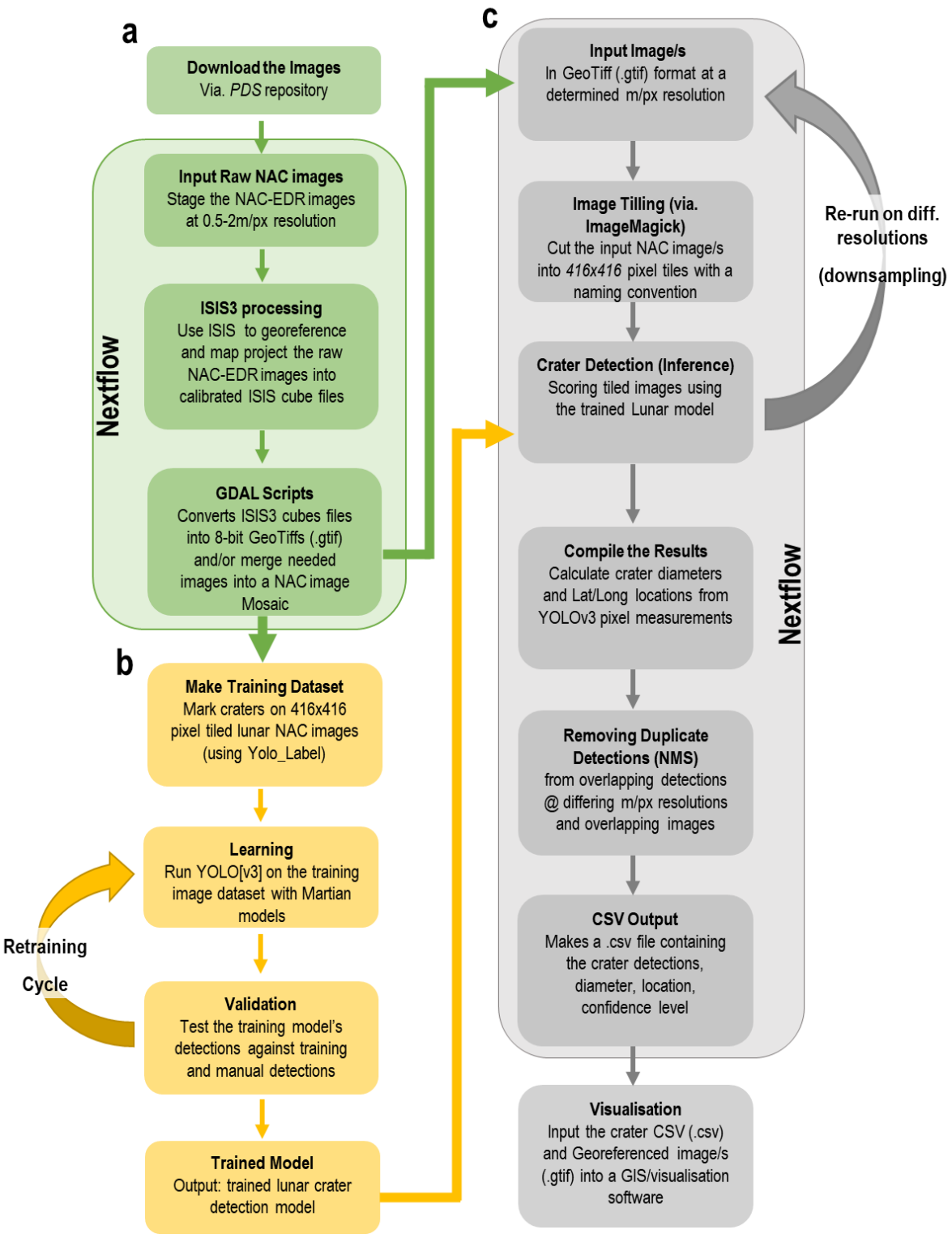

Figure 3.1: Overview flow diagram depicting the processing pipeline for our CDA. (a) The pre-processing needed to georeference the raw NAC images ready for algorithm training and inference; (b) the workflow for model training; (c) the processes for impact crater detection across NAC images.

3.2.1 (Phase 1) Image Pre-Processing

The image dataset used for crater detection, the LRO-NAC dataset, is the highest resolution global image repository (0.25 - 2 m/px spatial resolution) available for the Moon; however, it is not available in the georeferenced format (e.g., geotiff/gtif) required to determine the coordinates of detected craters (see, Benedix et al., 2020; Lagain et al., 2021c). The LRO-NAC images were downloaded from the publicly available Planetary Data System (https://pds.nasa.gov/). Relevant images were map-projected using United States Geological Survey (USGS) Integrated Software for Imagers and Spectrometers (ISIS) and converted into the GeoTiffs using GDAL (see Appendix 3.1 for details). A supercomputer cluster at Pawsey Supercomputing, Perth, Western Australia (https://pawsey.org.au/) processes each image. Using this resource, a single NAC image (~5 km by ~25 km, ~250MB) takes only seconds to process, magnitudes faster than an average personal computer.

3.2.1.a Image Selection Rationale

The performance of any object detection algorithm depends significantly on the quality of the training dataset and the images analysed (DeLatte et al., 2019). The more representative the selection of training images, the more robust the CDA results will be. Therefore, it is imperative that training occurs on NAC images with favourable lighting conditions (i.e., illumination angles that do not hinder crater recognition) and across different lunar terrains. Terrain selection is relatively straightforward. The surface of the Moon is divided into two broad terrains: Highlands and Mare, where each terrain has a different impact crater morphology (Shoemaker, 1964; Wilhelms, 1987). The lunar Highlands are older, anorthositic in composition, with a rugged mountainous morphology (Wilhelms, 1987); the Mare terrains are younger, smooth flood basalt plains primarily found within huge impact basins on the lunar nearside (Hiesinger et al., 2011; Wilhelms, 1987). For our training dataset, we chose NAC images that display both terrains. This selection will ensure our model can detect craters across any lunar surface.

Illumination angle selection took a little more work. The NAC dataset (from https://wms.lroc.asu.edu/lroc/search) is very extensive, consisting of 3,000,000+ images (each ~200-500 MB in size) with more routinely added each year, resulting in different areas imaged many times over with different angles of sun lighting.

Since launch (2009), the LRO spacecraft has taken many images over the same regions with differing conditions (refer to Appendix 3.2, Figure S3.1), allowing us to choose the images that best illuminate the different terrains for crater detection. The image lighting conditions are defined by the solar incidence angle (Figure 3.2), with vertical illumination (noon) at 0° and horizontal illumination (sunrise/sunset) at 90°. Low incidence angles (<40°) have high contrasts, where fresh, bright crater ejecta can mask smaller or mature craters (Figure 3.2.a). Similarly, lunar topography interpretation is affected by higher incidence angles (>80°) due to large shadows cast by peaks/rims covering swaths of the lunar surface (Figure 3.2.c). Therefore, images with incidence angles between ~50° and 70° are the most reliable for identifying all features necessary for counting craters (Cadogan, 2020; Head et al., 2010; Robbins, 2019). However, Richardson et al. (2022) analysed crater populations acquired on different incidence angle images and found that fewer craters are identified on images with incidence angles lower than 58°. Therefore, our primary focus is to train our network using NAC images with incidence angles of approximately 60° (Figure 3.2.b). These images must also depict both highland and mare terrains.

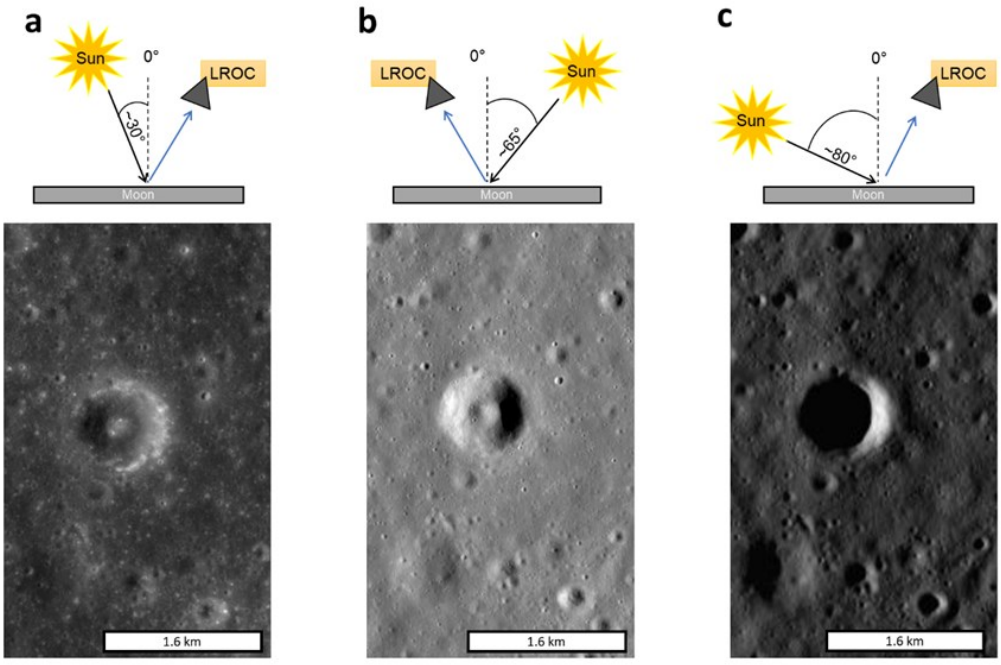

Figure 3.2: Example of NAC images illustrating the effect of three different lighting conditions on the features (the image's incidence angles in degrees and indicate lighting condition). (a) NAC image M1282458049L, incidence angle of 27.7°; (b) NAC image M1108275380R, incidence angle of 66.5°; (c) NAC image M1277755323L, incidence angle of 83.2°. The 800 m centroid crater in the three images is at 0.68°S 0.91°E.

3.2.2 (Phase 2) Network Training

This CDA is a CNN image object detection algorithm, using an Ultralytics implementation of You Only Look Once version 3 (YOLOv3-ultralytics) as the base neural network architecture (Jocher, 2021; Redmon & Farhadi, 2018; Redmon et al., 2016). We trained the computer through a process that required a series of supervised learn and validate cycles – where each learn cycle compares the results against a control dataset (DeLatte et al., 2019). In our case, the control is a ground-truth dataset of manually marked craters across images. To train efficiently, we chose and processed NAC images that best represented the lunar surface and the variability in craters.

3.2.2.a The Training NAC Images

We chose a suite of NAC images for training based on their variability in crater form and lighting conditions. The Apollo 14 landing region (Figure 3.3) hosts a sufficient variability of mappable craters across both highland and mare terrains (specifically, Fra Mauro highlands, Mare Insularum, and Mare Cognitum). Highland terrains are older than mare terrains, hosting more craters, where the complex topography affects the crater shape (Robbins et al., 2014). This difference in shape means more visual variability between highland craters; thus, more marked craters are required to capture that variability. As the Apollo 14 landing site region is an area of interest, there is a larger pool of NAC images and mosaics. Moreover, when detecting craters across the moon down to <1 km, the morphological differences between craters on the near and far sides are negligible (Daubar et al., 2014).

The chosen image dataset used to train the detection model comprised 16 NAC images. Of these, 14 were from areas within a ~300 km radius of the Apollo 14 landing site. The 14 images, grouped by terrain, are (see Figure 3.3) are Mare Insularum (M1127206936L, M119964604LE, M119998529L, M1320200353L, M1363614226L); Mare Cognitum (M1215555724L); and the Fra Mauro Highlands (M102265088L/R and M1096608496L/R, M1249655817L, M1310797424L, M131772598L, M1363656518L). The remaining NAC images sampled Oceanus Procellarum (M1305167327L) and Terra Vitae (M1378458043L; Figure 3.3).

These two additional areas ensure the CDA has a broader detection scope, and the subsequent detection model is more representative of the range of terrains of the Moon. These test images have incidence angles ranging between 45.67° to 81.81°. Ten images have a narrower range of 64.76° to 76.23°, which is favourable for detecting craters (Schultz et al., 1977; Cadogan, 2020; Richardson et al., 2022).

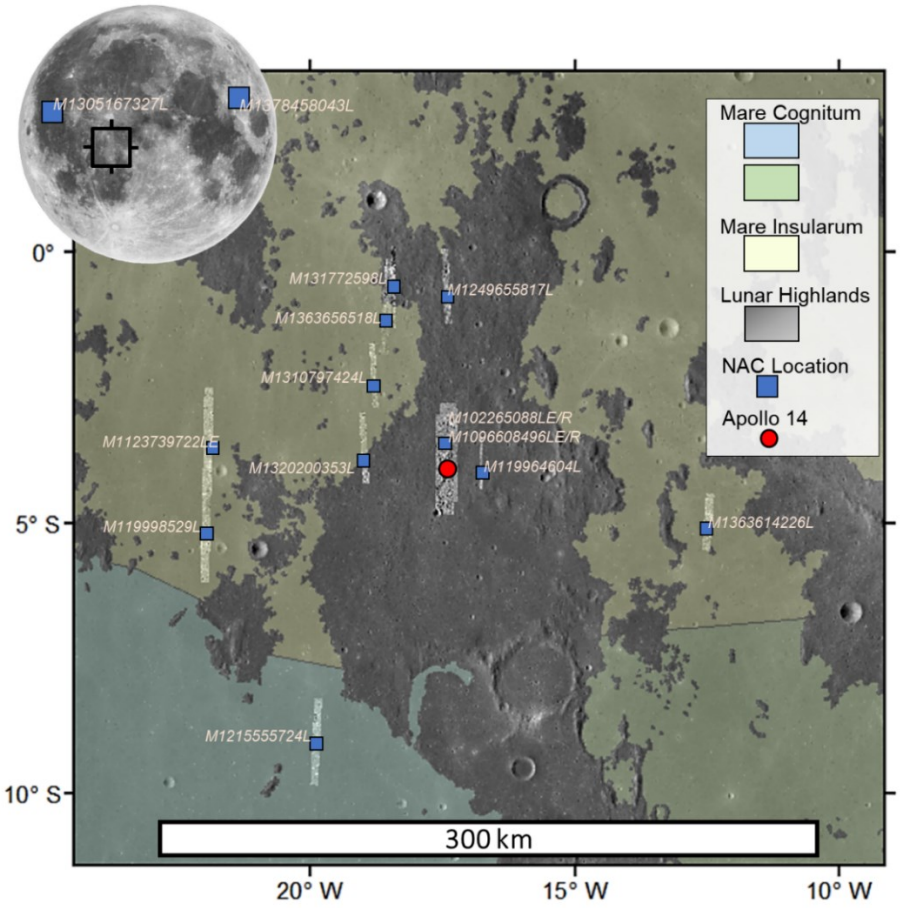

Figure 3.3: Lunar terrains (Highland [Fra Mauro highlands] and Mare [Mare Insularum and Mare Cognitum]) surrounding the Apollo 14 landing site (red marker, 3.65°S 17.47°W), and the image footprint locations and ID #s of the 16 NAC images used for training (blue marker and text). Image locations not within the Apollo 14 region are denoted in the inset globe in the upper left. The base image is the WAC global mosaic (Speyerer et al., 2011), and the mare boundaries are from Nelson et al. (2014).

3.2.2.b Creating the Training Dataset

For the algorithm to efficiently learn and validate on the NAC images, the images were tiled (cut the image into 416-by-416 pixel thumbnails) using the ImageMagick editing package (Still, 2006). This resulted in 100s of image tiles per NAC image. As the pixel dimensions of the tiles are fixed and that NAC resolution can vary from 0.25 to 2 m/px, the maximum sized crater we could mark would be 416 pixels in diameter, i.e., between 104 m and 832 m, depending on the image resolution (if the crater was situated ideally in the middle of the tile). The pixel resolutions of the 16 NACs were downsampled to 2m/px, 10m/px, and 20 m/px (maximum crater diameter of 832 m, 4160 m, and 8320 m within a tile, respectively). Marking was carried out on semi-randomly chosen image tiles. This resulted in 248 tiles from the 16 NAC images, where we marked impact craters manually. We used the Yolo_Label software tool to label the tiles with boxes. These bounding boxes fit the crater rim as accurately as possible to get a precise crater size measurement (refer to Appendix 3.2, Figure S3.2 for an example of a marked tile). Because object detection algorithms can only reliably detect objects larger than ~10 pixels (Wang et al., 2020), we marked impact craters down to 10 pixels wide on the training tiles. Note that this size threshold constitutes a lower limit from which impact craters are accurately recognized and measured manually (Robbins et al., 2014). The craters marked within the tiles are primarily simple craters, as the simple-complex transition diameter on the Moon is 15 km (Kruger et al., 2018). Thus, the CDA is optimised to detect simple craters. After following through with this process, our ground truth training dataset comprised 43,402 impact craters (~200 craters per tile on average) with a diameter range of ~5 m to ~3 km (all tiles used available in supplemental Dataset S3). This quantity of marked craters is significantly higher relative to other ground truth datasets for similar published algorithms: Hashimoto and Mori (2019) with 4,967; Benedix et al. (2020) with 1762; Yang et al. (2020) with 14,406 craters; and Lagain et al. (2021a) with 2142 craters.

3.2.2.c Training the Network

Training in YOLOv3-ultralytics entailed running a series of learning and validation cycles, which required marked objects on images for learning (learning dataset) and objects on images to compare against (validation dataset). The outcome after a specified number of cycles is a detection model. To make the learning and validation datasets, we followed the approach outlined in Benedix et al. (2020), where the whole ground truth dataset (248 marked tiles) was randomly subdivided into the learning and validation datasets with a ratio of 3:1. The training process is a series of finite cycles called epochs (Bhavsar & Ganatra, 2012; Goodfellow et al., 2016; Zhang, 2010). Each epoch comprises a learning stage followed by a validation stage. Consecutive epochs adjust image augmentations to slightly change the image's visual characteristics (i.e., rotation, translation, shear, and scale). This step removes the significance of sunlight direction (solar azimuth) across the dataset but is beneficial as it effectively extends the training set to more crater variations. There is a possibility of under-training (i.e., the model is very generalised and detects objects that generally look like craters) or over-training (i.e., the model detects very specific-looking craters). The key is finding a balance (DeLatte et al., 2019; Silburt et al., 2019) to get a model with homogeneous performance.

3.2.2.d Transfer Learning

Optimising the lunar detection model required two training sessions using a transfer learning approach. The first session ran from 300 to 600 epochs (Figure 4) and trained on 188 NAC image tiles with a narrow range of incidence angles (56°-73°). This particular training session used a Martian crater detection model (see Lagain et al., 2021a; Lagain et al., 2021c) that used HiRISE (High-Resolution Imaging Science Experiment, 25 cm/px) images as the benchmark starting point. YOLO needs a starting point, so providing a model already optimised for impact craters helps the training algorithm look for circular crater-like features immediately, significantly increasing the efficiency of initial learn-validate cycles. The second training session was on 248 image tiles, which contained the original 188 tiles plus an additional 60 tiles and had a broader range of incidence angles (45°-81°). This session used the first model as a starting point and continued to an additional 200 epochs (a total of 500 epochs for the Moon; Figure 3.4).

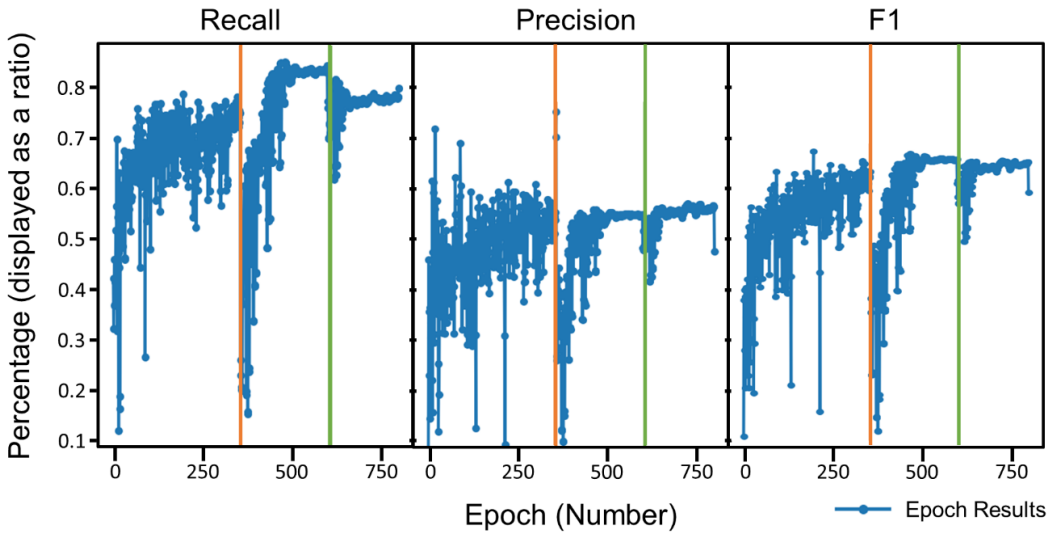

Figure 3.4: Training metrics for the lunar crater detection model in YOLOv3. The orange line marks the start of the first training session (300-600) from the model initially trained on HiRISE images (0-300, from Benedix et al. 2020; Lagain et al., 2021a; Lagain et al. 2021c), the green line marks the start of the second training session (600-800). As the training and validation cycles increase, the Recall, Precision, and F1 values converge to roughly constant values. See the main text for the definition of the recall, precision and F1 score percentage values.

Three essential metrics derived from the results of the training sessions are used to evaluate the performance of the algorithm: Recall, Precision, and F1 score (metrics also used by (Lee and Hogan, 2021; Lee, 2019; Salamunićcar et al., 2014; and Silburt et al., 2019). These are calculated after each epoch and training session (Figure 3.4; see Appendix 3.2, Figure S3.3 for all metrics). Each metric is defined based upon a confusion matrix (see Appendix 3.2, Figure S3.4; True Positive (TP), True Negative (TN), False Positive (FP), False Negative (FN), and Ground Truth data (GT)) and defined as follows:

(1) Recall is the ratio of True Positive to Ground Truth values [$\frac{TP}{GT=(TP+FN)}$], which indicates the proportion of manual detections the algorithm correctly identified (i.e., True Positive detection rate).

(2) Precision [$\frac{TP}{TP+FP}$], indicates the proportion of true craters the CDA detected (i.e., how many of the total positive detections are True Positive detections).

(3) F1 score [$\frac{TP}{TP+\frac{1}{2}(FP+FN)}$], the harmonic mean (numerical average) between Precision and Recall.

High False Positive and False Negative values result in lower Precision and Recall values. The F1 score serves as an indication of the overall error (lower values indicate more errors).

These performance indicators are discussed in detail in section 3.1. Precision, Recall, and F1 values indicate whether the model is overtrained or undertrained. Low Recall and Precision would indicate the model is undertrained, as it fails to recognise craters. An overtrained model performs exceptionally well on the training data and poorly across an evaluation (test) dataset (images the model did not train on). The final choice of which model to use is based on the highest performance results; in this case, epoch 790 has the best balance between these metrics.

3.2.3 (Phase 3) Running the Trained CDA on NAC Images

Inference, the process of running input data (pre-processed NAC images) through a trained model to produce a scored output, is the final phase of the CDA. As the volume of input data can reach a few terabytes if entire NAC images are analysed, using YOLO as the CNN architecture is particularly relevant for our purpose because it subdivides the input images. Each is scored only once using weighted bounding boxes around identified craters, thus making the detection process extremely fast compared to other CNN architectures (Redmon and Farhadi, 2018). Each detection receives a confidence value calculated by the CNN, which is a ratio comparing the detected crater to the trained crater model (Redmon & Farhadi, 2018). Only detections with a confidence value higher than 0.3 are kept. The resulting detection data, in the form of bounding boxes per image tile, are reassembled back into a complete NAC image. The detections, however, are still in a YOLO format, with the box location defined by pixel per cent ratio. For example, in an image tile that is 100-by-100 pixels, a random point on that image would be [x] 0.6 (60% or 60 px), [y] 0.3 (30% or 30 px). The CDA has code to convert the YOLO dimensions into lunar longitude-latitude coordinates using the embedded geographical data of the original NAC image.

As mentioned in Section 3.2.2.b, when detecting craters across an NAC image tile (416-by-416 pixels), the resolution limits the largest possible complete crater the algorithm can mark. To mediate this, we used an approach widely used in object detection (e.g., Salamuniccar et al., 2014; Lee et al., 2019; Benedix et al., 2020), where we iteratively downsampled each NAC image to a lower resolution for consecutive executions of the CDA. This pyramidal approach allows the CDA to detect craters across a large dynamical range of sizes (Figure 3.5). To build crater

detections across a range of diameters, the CDA evaluated three different versions of the same NAC image: one at 2 m/px (the lowest homogenous resolution that can be applied to the global NAC dataset) (Figure 3.5.a), the next at 10 m/px (Figure 3.5.b); and finally at 20 m/px (Figure 3.5.c). Since the smallest size for an accurate CDA object is 10 pixels (Wang et al., 2020), our minimum crater sizes are 20 m, 100 m, and 200 m, respectively. The downsampled pixel resolutions allow different crater diameter targets, meaning the algorithm runs across an image multiple times (similar to the method outlined in Cadogan (2020)), collating the crater detections across a range of diameters. This process is parallelised to run across multiple NAC images, significantly speeding up the processing. The computation time for inference depends on the size of the image and computer setup. However, generally, analysis of a single NAC image covering a ~125 km^2 area is ~ 30 seconds on the supercomputer cluster at Pawsey Supercomputing Centre.

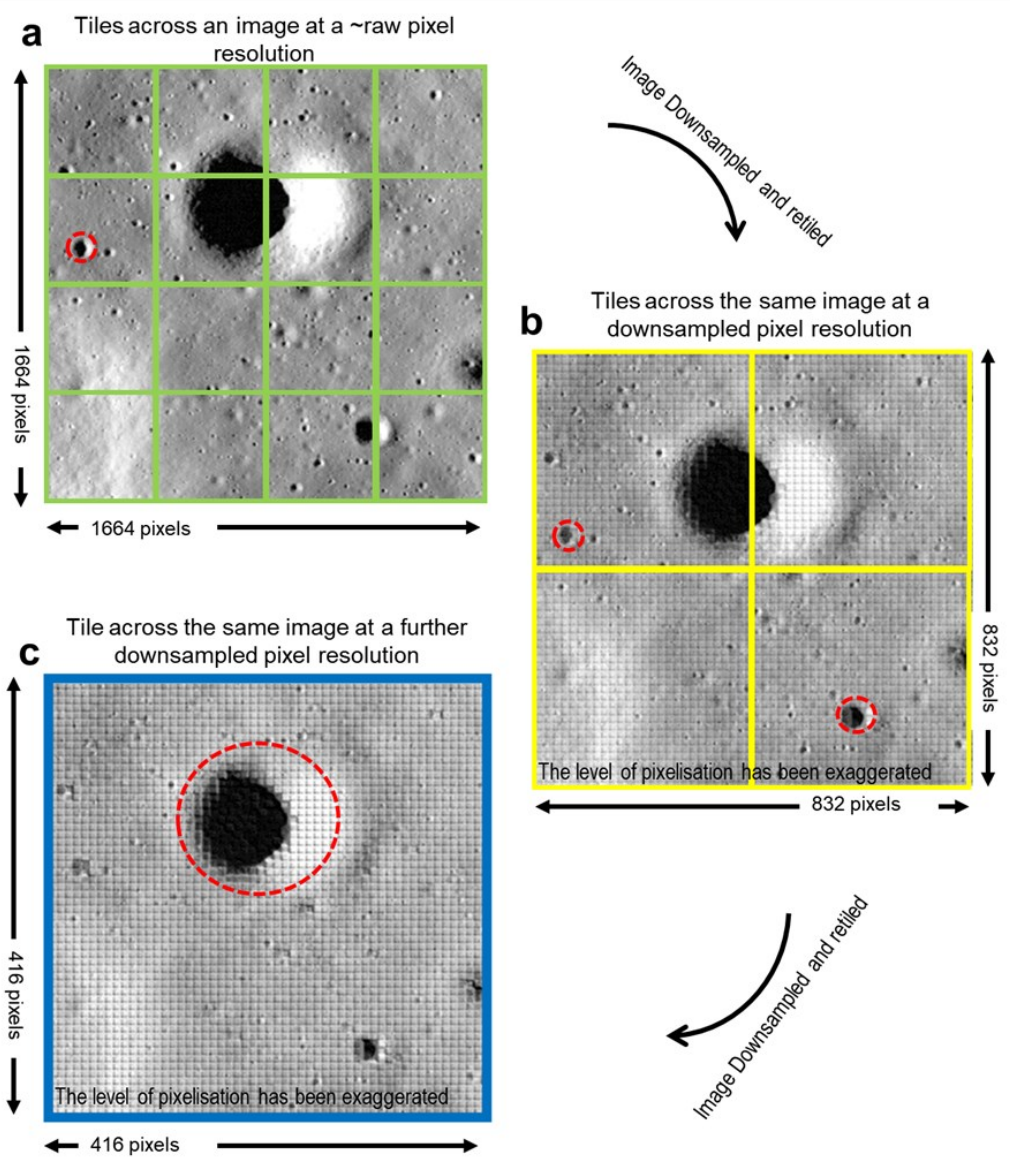

Figure 3.5: Effect of downsampling and then tiling a NAC image for impact crater detection (base image is a square clip of NAC image M1096608496L, Fra Mauro highlands). (a) The green, 16-box-grid represents 416 x416 pixels tile boundaries generated at the image's ~raw pixel resolution; note that at this resolution, many significant craters are bisected by tiling; (b) the yellow 4-box-grid represents the tiles generated at a downsampled pixel resolution; (c) the final large blue-box represents tile boundaries generated at a further downsampled pixel resolution, note that are no craters are cut by tile lines, but there is trade-off in image detail. The level pixelization in (a) and (b) has been exaggerated for illustrative purposes. These illustrate the three pixel-resolution levels an input image would go through for crater detection. The red-dashed-circles in each image outline the craters that the CDA can completely detect at that resolution. Note that when downsampling and then tiling an image, you allow bigger structures to fit within a single tile boundary (c) and greatly decrease the chance of truncating features.

3.2.3.a Detection Data Post-Processing

Running the CDA on downsampled and/or overlapping images potentially results in multiple detections of the same craters. It is essential to remove the duplicate detections (see Appendix 3.2, Figure S3.5), but their size and location vary slightly due to differences in conditions between NAC images. To remove duplicates, we use the same method as Benedix et al. (2020): a spatial statistical-based approach called Non-Maximum Suppression (NMS) that uses Intersection over Union (IoU) values to determine duplicates within a dataset of spatial information (Figure 3.6). This technique removes all overlapping detections, keeping only the one with the highest confidence value. Specifically, the IoU value is a ratio describing how much one object's area overlaps with another (Figure 3.6.b). The higher the ratio value (e.g., 0.9), the more of a match they are and, therefore, are most likely duplicates (Figure 3.6.c). We used an IoU value of 0.3 as the threshold where a crater might have been multiply detected. This process compares each detected crater's area against all other detected craters nearby and determines IoU values for those overlapping relationships. This process repeated for every crater until it compared all craters. Theoretically, this can remove non-duplicates if the overlap exceeds the threshold. However, the condition where two real craters of similar enough size overlap over the IoU threshold (> 0.3) is negligible compared to real duplicates influencing the data.

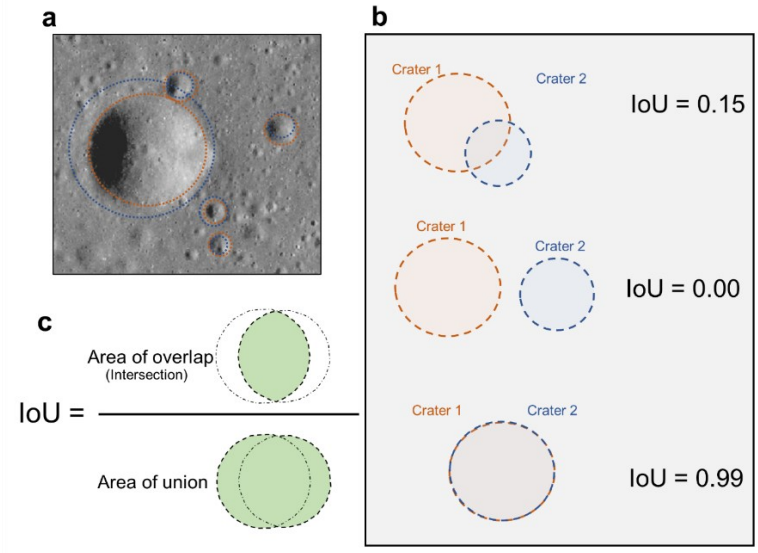

Figure 3.6: Intersection over Union (IoU) in crater duplicate removal. (a) example of CDA duplicates in the overlap region between NAC image M1157749492L and M1123590516L; (b) the IoU equation; and (c) visualisation of the overlap relationship between two craters.

3.3 Evaluation of the Crater Detection Algorithm

3.3.1 Training Sessions

Across both training sessions, the final Recall, Precision, and F1 values were high, with instability during the first ~100 epochs of each session (Figure 4). The instability reflects the algorithm learning, with a general upward trend to higher values as the model learns. The Recalls were notably high, with an end value of ~0.86 in session one and ~0.81 in session two. This ~0.05 change is a function of the additional marked craters across a more comprehensive incidence angle range (45°-81°). The enhanced training set significantly increases the CDA's ability to (1) utilise more of the NAC dataset and (2) detect more craters across a more extensive scope of lunar surfaces (global coverage). Considering the increased amount of data, where our model can return accurate results, we consider this slight performance loss acceptable.

On the other hand, the Precision values are consistent across both sessions, sitting at ~0.55, with a slight increase in the second session to ~0.56 (Figure 4). In the case of crater detection on ultra-high-resolution images, Precision can be a misleading but informative metric. The relatively low values do not always indicate poor performance, as these values reflect the limitations in the completeness of the ground truth training dataset and image resolutions. As described earlier, our 43,402-crater ground truth dataset is incomplete for very small craters (<10 px/5-10 m). Therefore, during validation, the CDA detected a (very small) crater that had not been manually marked. The resulting detection is flagged as a False Positive (detection of a false crater), lowering the precision. This trend is noted in other CDA studies, such as Silburt et al. (2019), whose Precision values were in the mid-50s (53% on a validation dataset and 56% on a test dataset) for similar reasons.

3.3.2 The Evaluation Dataset

To evaluate the performance and accuracy of the CDA, we executed the model on twelve regions of interest from six semi-randomly chosen NAC images, where each image chosen represented one of the two major lunar terrains over a range of lighting conditions (incidence angles of 41°-67°) (Figure 3.2).

There were two areas per NAC image, one specifically for comparing smaller craters (>20 m - 100m) and another for comparing larger craters (>100 m - 1km) (See Table 1 and Appendix 3.4, Dataset S3.3 for images of each area). This evaluation consists of three analyses, which quantify how the detection model performs in detecting craters of increasing diameter. (1) The quantification of Recall, Precision and F1 score for all detections across different diameter ranges, (2) the computation of the same metrics across three different states of crater degradation, and (3) the accuracy of the crater size estimation.

Table 3.1: Image information of the six NAC images used in our evaluation. Locations are also represented in Figure 3.7.

Image ID	Depicted Terrain	Incidence Angle (degrees)	Centroid Long / Lat (decimal degrees)
M1338833866L	Near side Highland	66.9°	6.52° / -10.62°
M1325197569L	Far side Highland	56.4°	115.94° / 9.99°
M1288076949L	Far side Highland	48.9°	-142.06° / 30.39°
M1320016983L	Near side Mare	66.7°	7.48° / 27.18°
M112963850L	Far side Mare	51.7°	151.64° / 29.05°
M1361391010L	Near side Mare	41.8°	-28.12° / 36.84°

For coherence, we input three groups of lighting conditions: IA-1 (‘good/favourable’ lighting for crater detection, 66.9°, 66.7°), IA-2 (‘medium' lighting, 56.4°, 51.7°), and IA-3 (‘poor’ lighting, 48.9°, 41.8°). Running the CDA and NMS over these 6 images (~900 km^2) took ~30 mins and detected ~1.8 million craters (~10 m to 3 km). Furthermore, we instigated a 1 km diameter cut-off to set a maximum limit for evaluation, as we do not wish to compare against larger craters (>1 km) which many prior algorithms have already accomplished (e.g., Silburt et al., 2019; Wang et al., 2021; Yang et al., 2020). This translates to comparing ground truth craters to CDA-detected craters between >20 m and 1 km in diameter. Two ground truth datasets, each focusing on a different crater diameter, allowed evaluation of the CDA. The first is a ‘Small Crater Dataset’ that compares 2780 CDA detections against 2159 manually mapped craters. This dataset consists of marked craters with diameters of 20 m to ~500 m (±10%) across six 1 km^2 to 9 km^2 areas. The second dataset is a ‘Large Crater Dataset’ consisting of 1540 CDA detected craters and 1343 manually mapped craters. This dataset focussed on evaluating larger craters with diameters of 100 m to 1 km (±10%) across six 20 km^2 to 150 km^2 areas (See Appendix 3.4, Dataset S3.1, S3.2 and S3.3).

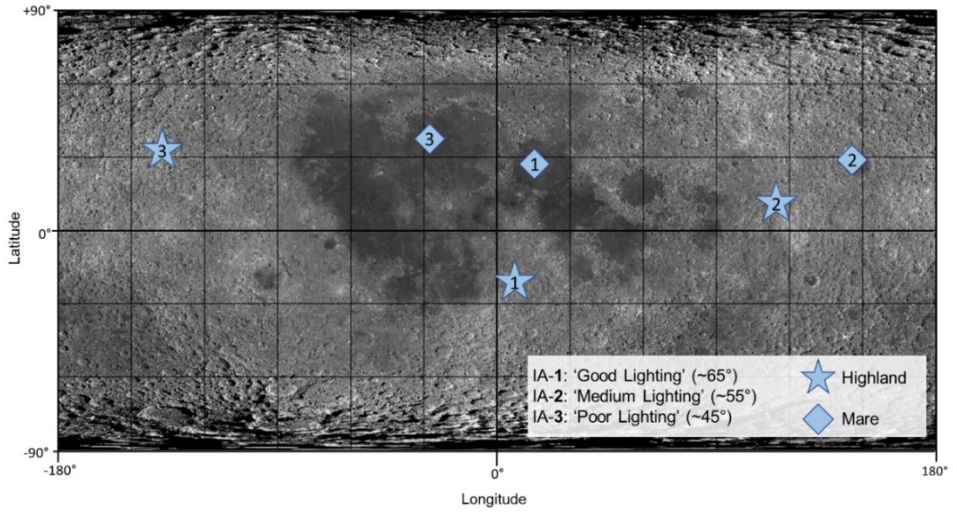

Figure 3.7: Locations of the NAC images used in the evaluation (in a simple cylindrical projection). Blue stars are Highland terrains, blue diamonds are Mare terrains, the numbering (1-3) indicates the lighting condition group: IA-1 (66.9°,66.7°), IA-2 (56.4°, 51.7°), and IA-3 (48.9°, 41.8°).

3.3.3 CDA Performance

Recall, Precision, and F1 scores for each evaluation test were calculated based on the values from a confusion matrix presented in Appendix 3.2, Figure S3.4. The Small Crater Dataset (20 m to ~500 m, Table 3.2) had an overall average Recall of 0.93, Precision of 0.66, and F1 score of 0.77. Across the images with favourable lighting conditions (IA-1), the CDA performed well, with an average recall of 0.90, precision of 0.71, and F1 score of 0.79. The CDA also performed similarly across the medium lighting condition (IA-2). However, the CDA performance decreased significantly on images with poorer lighting conditions (IA-3), specifically the F1 score, with an average of 0.72. This difference is due to the difficulty of consistently identifying craters in high-contrast lighting conditions (Cadogan, 2020; Robbins et al., 2014; Wilcox et al., 2005).

The Large Crater Dataset (100 m to 1 km, Table 3.2) had a lower overall average Recall of 0.89, a similar Precision of 0.67 and a lower F1 score of 0.74. The values of the Recall, Precision, and F1 scores across the Large Crater Dataset were more varied, with high F1 values (0.84) across all craters (≥100 m) and lower values (0.62, 0.77) across the larger craters (≥300 m, ≥500 m).

These errors stem from the CDA's crater diameter calculation and are exaggerated due to the larger diameters (further discussed in Section 3.3.3.b). Interestingly, across both crater datasets (Table 3.2), there are no significant differences in the numerical performance (Recall, Precision, and F1 score) between the near side or far side Highland and Mare terrains.

In summary, the average Recall, Precision, and F1 scores of our CDA across NAC images with favourable and medium lighting conditions (IA-1/IA-2/Highland/Mare only) are 0.93, 0.70, and 0.79, respectively, for the Small Crater Dataset, and 0.86, 0.68 and 0.74 for the Large Crater Dataset. This aligns with the recall results of recently published lunar image-based CDAs such as Hashimoto and Mori (2019) with ~0.81 and Cadogan (2020) with ~0.86.

Table 3.2: Summary of the performance metrics for the 'Small Crater Dataset' and 'Large Crater Dataset'. The values are grouped based on their lighting condition, respective terrain, and diameter (the results for each cell are in Appendix 3.3, Table S3.1).

		IA-1		IA-2		IA-3		
		66.7°	66.9°	51.7°	56.4°	41.8°	48.9°	
Metric	Diameter	Near side Mare	Near side Highland	Far side Mare	Far side Highland	Near side Mare	Far side Highland	Average
Small Crater Dataset								
Recall	≥20m	0.98	0.97	0.88	0.90	0.86	0.92	0.92
	≥40m	0.90	0.95	0.94	0.96	0.76	0.92	0.90
	≥60m	0.84	0.92	1.00	1.00	0.91	1.00	0.94
	≥80m	0.80	0.89	1.00	1.00	1.00	1.00	0.95
	≥100m	0.83	0.89	1.00	1.00	1.00	1.00	0.95
Precision	≥20m	0.76	0.68	0.84	0.90	0.70	0.79	0.78
	≥40m	0.68	0.68	0.68	0.82	0.63	0.51	0.67
	≥60m	0.77	0.54	0.50	0.64	0.53	0.50	0.58
	≥80m	0.75	0.66	0.67	0.80	0.50	0.50	0.65
	≥100m	0.76	0.76	0.40	0.67	0.63	0.60	0.64
F1	≥20m	0.85	0.80	0.86	0.90	0.77	0.85	0.84
	≥40m	0.78	0.79	0.79	0.88	0.69	0.66	0.77
	≥60m	0.81	0.68	0.67	0.78	0.67	0.67	0.71
	≥80m	0.77	0.76	0.80	0.89	0.67	0.67	0.76
	≥100m	0.79	0.82	0.57	0.80	0.77	0.75	0.75
Large Crater Dataset								
Recall	≥100m	0.91	0.85	0.97	0.95	0.91	0.90	0.91
	≥300m	0.80	0.83	1.00	0.67	1.00	0.89	0.87
	≥500m	0.80	0.85	-	0.78	1.00	1.00	0.88
Precision	≥100m	0.74	0.87	0.75	0.80	0.70	0.78	0.77
	≥300m	0.47	0.63	0.40	0.73	0.42	0.41	0.51
	≥500m	0.29	0.92	-	0.88	1.00	0.60	0.74
F1	≥100m	0.82	0.86	0.84	0.87	0.79	0.84	0.84
	≥300m	0.59	0.72	0.57	0.70	0.59	0.57	0.62
	≥500m	0.42	0.88	-	0.82	1.00	0.75	0.77

3.3.3.a Effects of Crater Degradation in CDA Performance

To evaluate the CDA's effectiveness across different degradation levels, we classified craters >100 m based on their degradation state. We assigned each crater a degradation class, A, B, or C, based on visual criteria and descriptions used by Pohn and Offield (1970), Trask (1971), Basilevsky (1976), Stopar et al. (2012) and Mahanti et al. (2018). The description of each class is A, craters with sharp rims, steep slopes, crisp internal shadows, and visible rocky ejecta; B, craters with smooth rims, shallow slopes, internal shadow, and little ejecta; and C, craters with ill-defined rims, very shallows slopes, and little internal shadows (Figure 3.8).

We did not include craters degraded beyond these classifications. False Positives are impossible to calculate, as we are only comparing to a specific attribute of the ground truth crater dataset throughout this analysis. The aim was to quantify the detection rate (Recall) of the CDA in detecting actual craters across three degradation classes. We can only determine if the CDA failed or succeeded in detecting marked degraded craters.

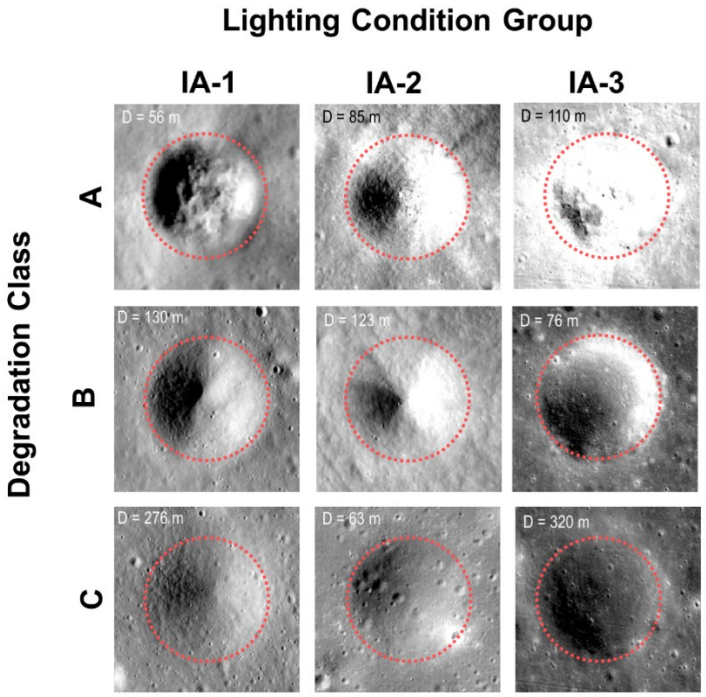

Figure 3.8: Examples of the crater degradation classes (A/B/C) for each lighting condition (IA-1/IA-2/IA-3). Red dashed circles denote the crater boundaries. Each crater image is taken directly from the NAC images used within this study.

Results show that our model is excellent at detecting class-A and class-B craters (Figure 3.8, Table 3.2). The average Recall across these two classes is 0.99 (Table 3). There are also no significant differences between the Recall values across the lighting conditions (IA-1/2/3) and terrains. However, the Recall notably decreased (-0.15) across highly degraded (class-C) craters (Figure 8), with an average Recall of 0.85 (Table 3.3). There is more variability in recording the size of very degraded craters for both Humans (Fassett and Thomson, 2014; Robbins et al., 2014) and machines (Delatte et al., 2019; Jia et al., 2020b; Wang et al., 2020). For the CDA, the detection variability of degraded craters ranges from 0% to 30% (Table 3.3), roughly within the range of manual datasets (see Robbins et al., 2014).

Table 3.3: Recall values for the 'Large Crater Dataset' degradation evaluation. Values are grouped by degradation class (A, B, and C) and lighting condition (IA-1, 2, and 3) (the results for each cell are in Appendix 3.4, Table S3.2).

		IA-1		IA-2		IA-3		
		66.7°	66.9°	51.7°	56.4°	41.8°	48.9°	
Degradation Class	Diameter	Near side Mare	Near side Highland	Far side Mare	Far side Highland	Near side Mare	Far side Highland	Average
A	≥100m	0.91	1.00	1.00	1.00	1.00	1.00	0.98
	≥300m	-	1.00	-	1.00	-	-	1.00
	≥500m	-	1.00	-	-	-	-	1.00
B	≥100m	1.00	0.98	1.00	1.00	0.93	0.98	0.98
	≥300m	1.00	1.00	1.00	-	1.00	1.00	1.00
	≥500m	1.00	1.00	-	-	1.00	-	1.00
C	≥100m	0.88	0.80	0.96	0.93	0.89	0.88	0.89
	≥300m	0.74	0.74	-	0.70	1.00	0.88	0.81
	≥500m	0.75	0.78	-	0.88	-	1.00	0.85

3.3.3.b Crater Diameter Error Estimation

We evaluated how effective the CDA is at quantitatively determining the diameter of the detected craters. This analysis included a total of 3261 true positive crater detections (2058 from the Small Crater Dataset and 1203 from the Large Crater Dataset), comparing crater diameters from the ground truth (D_{GT}) with diameters estimated by the CDA (D_{TP}). We calculated a percentage difference in the following way:

$$\frac{D_{TP} - D_{GT}}{D_{TP}} \times 100$$

Positive values reflect an overestimation, while negative values are an underestimation of the crater diameter by the algorithm. Any True Positive detections with diameter estimations beyond ±50% were re-recorded as False Positive. Even though the CDA has identified the correct position of the crater, a diameter estimation beyond ±50% is not accurate nor reliable and, therefore, not useable for analysis (the True Positive data is available in Appendix 3.4, Dataset S3.2).

The results show that the algorithm overestimates the crater's true diameter across small and large crater datasets by ~15% (Figure 3.9). Specifically, the overestimation is less across the Large Crater dataset (100 m - 1 km), with the median at ~10% (Figure 10b). In comparison, manual mapping of impact craters shows variability in the crater size measurements of up to ±15% (Robbins et al., 2014). Although the origin of the crater size overestimation by our network is currently unknown, it is unlikely that this comes from the training dataset. This will be the subject of future investigation and improvement using other object detection architectures such as YOLOv5. To see how this can affect a crater count model age, please see Appendix 4.3, Figure S4.3.

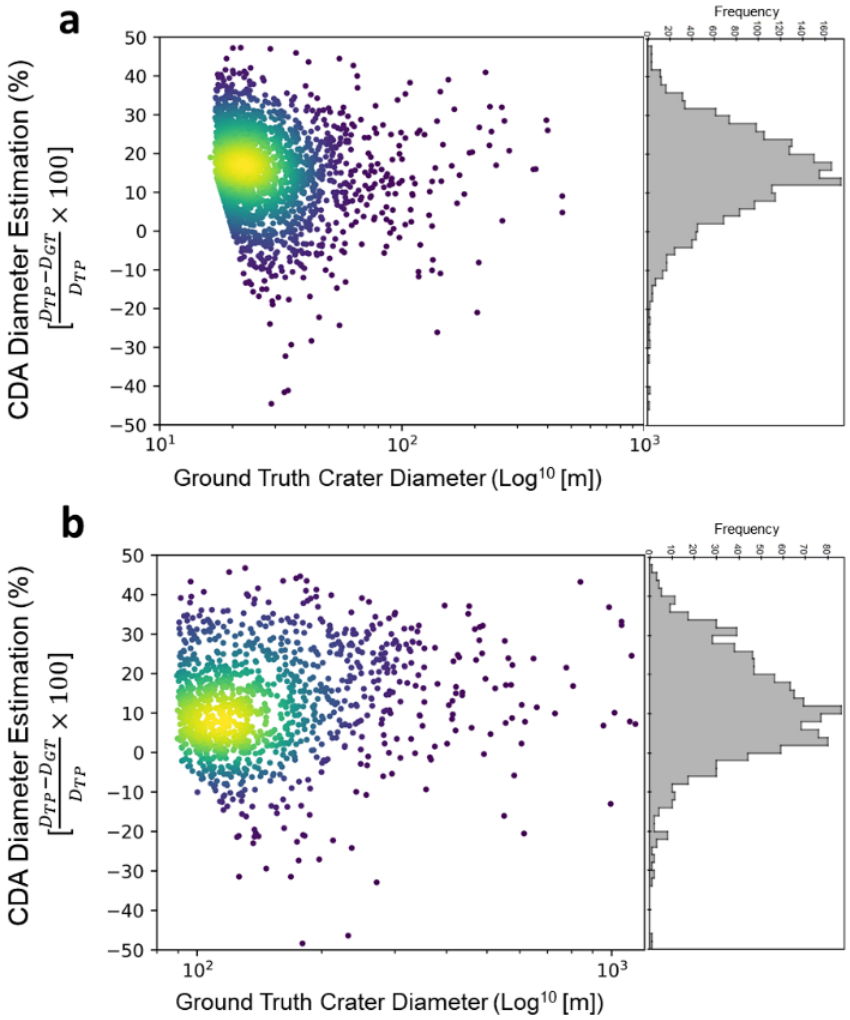

Figure 3.9: True Positive crater diameter estimation by the CDA for (a) Small Crater Dataset (n = 2058, D =20 m to ~500 m) and (b) Large Crater Dataset (n = 1203, D =100 m to 1 km). The colour coding, via Kernel Density Estimation (KDE), helps visualise the spatial density of the points relative to each other; yellow indicates more craters, and blue indicates fewer craters. The frequency of detection size estimation is computed per increment of 2%. For the vertical axis, DTP refers to the CDA crater diameter of true positive detection, and DGT refers to the ground truth crater diameter.

3.4 Conclusion

Automated crater mapping is critical for quickly and consistently mapping small impact craters across heavily cratered surfaces, such as the Moon. Current lunar global impact crater datasets are limited to craters >1-2 km in diameter (e.g., Robbins, 2019), which restricts the ability to gather small-scale information on the physical properties and degradation rates of geological surfaces, as well as the model age of the youngest events occurred on the Moon, such as Copernican impacts. Understanding the spatial densities of small craters can link primary impact events to secondary crater clusters and ejecta (Lagain et al., 2021a) and aid in future lunar missions.

By adapting a published image-based CNN algorithm initially trained in the detection of Martian craters (see Benedix et al., 2020; Lagain et al., 2021c) for use across the Moon using LRO-NAC images, we demonstrate the versatility of machine learning in planetary mapping. This paper's methodology, technical description, and rationale showcase the workflow and accuracy of our Crater Detection Algorithm. We trained a detection model on 43,402 lunar craters identified in NAC images, with an initial transfer learning cycle using a published Martian crater detection model (see Lagain et al., 2021a; Lagain et al., 2021c; Benedix et al., 2020). We ran the CDA across six NAC images at different resolution scales to evaluate our model. The evaluation focused on quantifying the effectiveness of the CDA model across crater diameter, lighting conditions, lunar terrains, crater degradation, and diameter estimation.

We show our CDA has good performance metrics across NAC images with lighting conditions/incidence angles between ~50° to ~70° regardless of lunar terrain, with an average Recall of 0.93, Precision of 0.7, and an F1 score of 0.79 for impact craters larger than 20 m. From 100 m in diameter, we find that Recall, Precision and F1 scores are 0.86, 0.68 and 0.74. Analysing images with incidence angles lower than ~50° leads to a significant decrease in performance. Our network is very effective at detecting fresh and moderately degraded craters but less efficient at detecting very degraded craters, with a loss of 0.1-0.2 for all metrics.

Although our analysis shows that the CDA displays a 15% overestimation of the crater diameter, we have created the infrastructure needed to process 1000s of raw LRO-NAC images, embed them with geographical information and convert them into a useable file format. Our pipeline allows us to run these images through a trained lunar crater model to generate fast crater detections with acceptable accuracy for detecting fresh and moderately degraded impact craters >20 m on NAC images with incidence angle > 50° covering both Mare and Highland terrains.

Data Availability Statement

All the processing steps, publicly available codes, and materials required to reproduce the presented CDA, and evaluation are listed here, described throughout the paper, and located within the supplemental materials. The supplementary data are available at Fairweather et al. (2022; https://zenodo.org/record/6386231). The version and implementation of YOLO we used for our Crater Detection Algorithm is available at Ultralytics-yolov3 (2020). The tool we used to label craters in the ground truth data set (available in the supplementary material, link above) is available at Yolo_Label (2021). The NAC images were downloaded using the LROC website located at The Lunar Reconnaissance Orbiter Narrow-Angle Camera (2022). The United States Geological Survey Integrated Software for Imagers and Spectrometers (ISIS) used to process the downloaded NAC images is available at ISIS3 (2021) or ISIS Documentation (2021).

Acknowledgments

We thank the two anonymous reviewers for their helpful comments and feedback. This work was supported by the resources provided by the Pawsey Supercomputing Centre with funding from the Australian Government, The Commonwealth Scientific and Industrial Research Organisation, the Australian Space Data Analysis Facility, Curtin University, and the Government of Western Australia. This research is grant funded by the Australia Research Council (DP210100336 and FT170100024) and Curtin University. We are also thankful to the LROC and NASA PDS teams for their work in making the NAC dataset freely available for use and download.

3.5 References

Acton, C. H. (1996). Ancillary data services of NASA's Navigation and Ancillary Information Facility. Planetary and Space Science, 44(1), 65–70. https://doi.org/10.1016/00320633(95)00107-7

Baldwin, R. B. (1964). Lunar crater counts. The Astronomical Journal, 69, 377. https://doi.org/10.1086/109289

Baldwin, R. B. (1965). Mars: An Estimate of the Age of Its Surface. Science, 149(3691), 1498–1499. https://doi.org/10.1126/science.149.3691.1498

Baldwin, R. B. (1987a). On the relative and absolute ages of seven lunar front face basins: I. From Viscosity Arguments. Icarus, 71(1), 1–18. https://doi.org/10.1016/0019-1035(87)90158-8

Baldwin, R. B. (1987b). On the relative and absolute ages of seven lunar front face basins: II. From the Crater Counts. Icarus, 71(1), 19–29. https://doi.org/10.1016/0019-1035(87)90159-X

Barker, M. K., Mazarico, E., Neumann, G. A., Zuber, M. T., Haruyama, J., & Smith, D. E. (2016). A new lunar digital elevation model from the Lunar Orbiter Laser Altimeter and SELENE Terrain Camera. Icarus, 273, 346–355. https://doi.org/10.1016/j.icarus.2015.07.039

Bart, G. D., Nickerson, R. D., Lawder, M. T., & Melosh, H. J. (2011). Global survey of lunar regolith depths from LROC images. Icarus, 215(2), 485–490. https://doi.org/10.1016/j.icarus.2011.07.017

Basilevskii, A. T. (1976). On the evolution rate of small lunar craters. In Lunar and Planetary Science Conference Proceedings, 7, 1005-1020.

Benedix, G. K., Lagain, A., Chai, K., Meka, S., Anderson, S., Norman, C., Bland, P. A., Paxman, J., Towner, M. C., & Tan, T. (2020). Deriving Surface Ages on Mars Using Automated Crater Counting. Earth and Space Science, 7(3). https://doi.org/10.1029/2019EA001005

Bhavsar, H., & Ganatra, A. (2012). A Comparative Study of Training Algorithms for Supervised Machine Learning. International Journal of Soft Computing and Engineering (IJSCE), 2(4), 74–81.

Cadogan, P. H. (2020). Automated precision counting of very small craters at lunar landing sites. Icarus, 348, 113822. https://doi.org/10.1016/j.icarus.2020.113822

Crater analysis techniques working group. (1979). Standard techniques for presentation and analysis of crater size-frequency data. Icarus, 37(2), 467–474. https://doi.org/10.1016/0019-1035(79)90009-5

Daubar, I. J., Atwood-Stone, C., Byrne, S., McEwen, A. S., & Russell, P. S. (2014). The morphology of small fresh craters on Mars and the Moon: Fresh Crater d/D on Mars and the Moon. Journal of Geophysical Research: Planets, 119(12), 2620–2639. https://doi.org/10.1002/2014JE004671

DeLatte, D. M., Crites, S. T., Guttenberg, N., & Yairi, T. (2019). Automated crater detection algorithms from a machine learning perspective in the convolutional neural network era. Advances in Space Research, 64(8), 1615–1628. https://doi.org/10.1016/j.asr.2019.07.017

Di Tommaso, P., Chatzou, M., Floden, E. W., Barja, P. P., Palumbo, E., & Notredame, C. (2017). Nextflow enables reproducible computational workflows. Nature Biotechnology, 35(4), 316–319. https://doi.org/10.1038/nbt.3820

Di, K., Li, W., Yue, Z., Sun, Y., & Liu, Y. (2014). A machine learning approach to crater detection from topographic data. Advances in Space Research, 54(11), 2419–2429. https://doi.org/10.1016/j.asr.2014.08.018

Fassett, C. I. (2016). Analysis of impact crater populations and the geochronology of planetary surfaces in the inner solar system: Crater Populations and Surface Chronology. Journal of Geophysical Research: Planets, 121(10), 1900–1926. https://doi.org/10.1002/2016JE005094

Fassett, C. I., & Thomson, B. J. (2014). Crater degradation on the lunar maria: Topographic diffusion and the rate of erosion on the Moon: Crater degradation on the lunar maria. Journal of Geophysical Research: Planets, 119(10), 2255–2271. https://doi.org/10.1002/2014JE004698

GDAL documentation. (2021). GDAL. https://gdal.org/

Goodfellow, I., Bengio, Y., & Courville, A. (2016). Deep learning. MIT press.

Hartmann, W. K. (1965). Terrestrial and lunar flux of large meteorites in the last two billion years. Icarus, 4(2), 157–165. https://doi.org/10.1016/0019-1035(65)90057-6

Hartmann, W. K. (1966). Martian Cratering. Icarus, 5(1–6), 565–576. https://doi.org/10.1016/0019-1035(66)90071-6

Hartmann, W. K. (1971). Martian cratering III: Theory of crater obliteration. Icarus, 15(3), 410–428. https://doi.org/10.1016/0019-1035(71)90119-9

Hartmann, W. K. (1977). Relative crater production rates on planets. Icarus, 31(2), 260–276. https://doi.org/10.1016/0019-1035(77)90037-9

Hartmann, W. K. (1999). Martian cratering VI: Crater count isochrons and evidence for recent volcanism from Mars Global Surveyor. Meteoritics & Planetary Science, 34(2), 167–177. https://doi.org/10.1111/j.1945-5100.1999.tb01743.x

Hartmann, W. K. (1995). Planetary cratering 1. The question of multiple impactor populations: Lunar evidence. Meteoritics, 30(4), 451–467. https://doi.org/10.1111/j.1945-5100.1995.tb01152.x

Hashimoto, S., & Mori, K. (2019). Lunar Crater Detection based on Grid Partition using Deep Learning. 2019 IEEE 13th International Symposium on Applied Computational Intelligence and Informatics (SACI), 75–80. https://doi.org/10.1109/SACI46893.2019.9111474

Head, J. W., Fassett, C. I., Kadish, S. J., Smith, D. E., Zuber, M. T., Neumann, G. A., & Mazarico, E. (2010). Global Distribution of Large Lunar Craters: Implications for Resurfacing and Impactor Populations. Science, 329(5998), 1504–1507. https://doi.org/10.1126/science.1195050

Head, J. W., Fassett, C. I., Kadish, S. J., Smith, D. E., Zuber, M. T., Neumann, G. A., & Mazarico, E. (2010). Global Distribution of Large Lunar Craters: Implications for Resurfacing and Impactor Populations. Science, 329(5998), 1504–1507. https://doi.org/10.1126/science.1195050

Herrick, R. R., Bateman, E. M., Crumpacker, W. G., & Bates, D. (2018). Observations From a Global Database of Impact Craters on Mercury with Diameters Greater than 5 km. Journal of Geophysical Research: Planets, 123(8), 2089–2109. https://doi.org/10.1029/2017JE005516

Hiesinger, H., Head, J. W., Wolf, U., Jaumann, R., & Neukum, G. (2011). Ages and stratigraphy of lunar mare basalts: A synthesis. In W. A. Ambrose & D. A. Williams, Recent Advances and Current Research Issues in Lunar Stratigraphy. Geological Society of America. https://doi.org/10.1130/2011.2477(01)

ISIS Documentation. (2021). ISIS: Integrated Software for Imagers and Spectrometers. https://isis.astrogeology.usgs.gov/UserDocs/index.html

ISIS3. (2021). [C++]. (Version 3). USGS Astrogeology. https://github.com/USGS-Astrogeology/ISIS3

Ivanov, B. A., Neukum, G., Bottke, W. F., & Hartmann, W. K. (2002). The Comparison of Size-Frequency Distributions of Impact Craters and Asteroids and the Planetary Cratering Rate. Asteroids III, 1. https://www.researchgate.net/publication/253429785

J. H. Fairweather, A. Lagain, K. Servis, G. K. Benedix, S. S. Kumar, & P. A. Bland. (2022). Supporting Material for "Automatic Mapping of Small Lunar Impact Craters Using LROC NAC Images" (Version 1) [Data set]. Zenodo. https://doi.org/10.5281/zenodo.6386231

Jia, M., Yue, Z., Di, K., Liu, B., Liu, J., & Michael, G. (2020a). A catalogue of impact craters larger than 200 m and surface age analysis in the Chang'e-5 landing area. Earth and Planetary Science Letters, 541, 116272. https://doi.org/10.1016/j.epsl.2020.116272

Jia, Y., Liu, L., Wan, G., & Zhang, C. (2020b). Research Progress of Lunar Impact Crater Detection. 2020 International Conference on Computer Science and Management Technology (ICCSMT), 91–95. https://doi.org/10.1109/ICCSMT51754.2020.00025

Jocher, G. (2021). Ultralytics YOLOv3 [Python]. Ultralytics. https://github.com/ultralytics/yolov3

Kneissl, T., van Gasselt, S., & Neukum, G. (2011). Map-projection-independent crater size-frequency determination in GIS environments—New software tool for ArcGIS. Planetary and Space Science, 59(11–12), 1243–1254. https://doi.org/10.1016/j.pss.2010.03.015

Krüger, T., Hergarten, S., & Kenkmann, T. (2018). Deriving Morphometric Parameters and the Simple-to-Complex Transition Diameter From a High-Resolution, Global Database of Fresh Lunar Impact Craters ($D \geq \sim 3$ km). Journal of Geophysical Research: Planets, 123(10), 2667–2690. https://doi.org/10.1029/2018JE005545

Lagain, A., Benedix, G. K., Servis, K., Baratoux, D., Doucet, L. S., Rajšic, A., Devillepoix, H. A. R., Bland, P. A., Towner, M. C., Sansom, E. K., & Miljković, K. (2021a). The Tharsis mantle source of depleted shergottites revealed by 90 million impact craters. Nature Communications, 12(1), 6352. https://doi.org/10.1038/s41467-021-26648-3

Lagain, A., Bouley, S., Baratoux, D., Marmo, C., Costard, F., Delaa, O., Pio Rossi, A., Minin, M., Benedix, G. K., Ciocco, M., Bedos, B., Guimpier, A., Dehouck, E., Loizeau, D., Bouquety, A., Zhao, J., Vialatte, A., Cormau, M., Le Conte des Floris, E., … Gamblin, O. (2021). Mars Crater Database: A participative project for the classification of the morphological characteristics of large Martian craters. In W. U. Reimold & C. Koeberl (Eds.), Large Meteorite Impacts and Planetary Evolution VI. Geological Society of America. https://doi.org/10.1130/2021.2550(29)

Lagain, A., Servis, K., Benedix, G. K., Norman, C., Anderson, S., & Bland, P. A. (2021c). Model Age Derivation of Large Martian Impact Craters, Using Automatic Crater Counting Methods. Earth and Space Science, 8(2). https://doi.org/10.1029/2020EA001598

Langner, R., & Eickhoff, S. B. (2013). Sustaining attention to simple tasks: A meta-analytic review of the neural mechanisms of vigilant attention. Psychological Bulletin, 139(4), 870–900. https://doi.org/10.1037/a0030694

Lee, C. (2019). Automated crater detection on Mars using deep learning. Planetary and Space Science, 170, 16–28. https://doi.org/10.1016/j.pss.2019.03.008

Lee, C., & Hogan, J. (2021). Automated crater detection with human level performance. Computers & Geosciences, 147, 104645. https://doi.org/10.1016/j.cageo.2020.104645

Liu, Z., Yue, Z., Michael, G. G., Gou, S., Di, K., Sun, S., & Liu, J. (2018, March). A Global Database and Analyses of (4) Vesta Craters. In 49th Annual Lunar and Planetary Science Conference (Vol. 49, abstract #2083).

Mahanti, P., Robinson, M. S., Thompson, T. J., & Henriksen, M. R. (2018). Small lunar craters at the Apollo 16 and 17 landing sites—Morphology and degradation. Icarus, 299, 475–501. https://doi.org/10.1016/j.icarus.2017.08.018

McEwen, A. S., & Bierhaus, E. B. (2006). The importance of secondary cratering to age constraints on planetary surfaces. Annual Review of Earth and Planetary Sciences, 34(1), 535–567. https://doi.org/10.1146/annurev.earth.34.031405.125018

McMahon, S. K. (1996). Overview of the Planetary Data System. Planetary and Space Science, 44(1), 3–12. https://doi.org/10.1016/0032-0633(95)00101-8

Melosh, H. J. (1989). Impact Cratering: A Geologic Process. Oxford University Press. https://books.google.com.au/books?id=nZwRAQAAIAAJ

Minton, D. A., Fassett, C. I., Hirabayashi, M., Howl, B. A., & Richardson, J. E. (2019). The equilibrium size-frequency distribution of small craters reveals the effects of distal ejecta on lunar landscape morphology. Icarus, 326, 63–87. https://doi.org/10.1016/j.icarus.2019.02.021

Moore, H. J., Boyce, J. M., & Hahn, D. A. (1980). Small impact craters in the lunar regolith—Their morphologies, relative ages, and rates of formation. The Moon and the Planets, 23(2), 231–524.

Nelson, D. M., Koeber, S. D., Daud, K., Robinson, M. S., Watters, T. R., Banks, M. E., & Williams, N. R. (2014). Mapping lunar maria extents and lobate scarps using LROC image products. In Lunar and Planetary Science Conference (Vol. 45, abstract #2861).

Neukum, G., Ivanov, B. A., & Hartmann, W. K. (2001). Cratering Records in the Inner Solar System in Relation to the Lunar Reference System. In R. Kallenbach, J. Geiss, & W. K. Hartmann (Eds.), Chronology and Evolution of Mars, 12, 55–86. Springer Netherlands. https://doi.org/10.1007/978-94-017-1035-0_3

Öpik, E. J. (1960). The Lunar Surface as an Impact Counter. Monthly Notices of the Royal Astronomical Society, 120(5), 404–411. https://doi.org/10.1093/mnras/120.5.404

Pohn, H. A., & Offield, T. W. (1970). Lunar crater morphology and relative-age determination of lunar geologic units–Part 1. Classification. US Geological Survey Prof. Paper, 153-162.

Povilaitis, R. Z., Robinson, M. S., van der Bogert, C. H., Hiesinger, H., Meyer, H. M., & Ostrach, L. R. (2018). Crater density differences: Exploring regional resurfacing, secondary crater populations, and crater saturation equilibrium on the moon. Planetary and Space Science, 162, 41–51. https://doi.org/10.1016/j.pss.2017.05.006

Qiao, L., Head, J. W., Xiao, L., Wilson, L., & Dufek, J. D. (2018). The role of substrate characteristics in producing anomalously young crater retention ages in volcanic deposits on the Moon: Morphology, topography, subresolution roughness, and mode of emplacement of the Sosigenes lunar irregular mare patch. Meteoritics & Planetary Science, 53(4), 778–812. https://doi.org/10.1111/maps.13003

Rajšić, A., Miljković, K., Wójcicka, N., Collins, G. S., Onodera, K., Kawamura, T., Lognonné, P., Wieczorek, M. A., & Daubar, I. J. (2021). Numerical Simulations of the Apollo S-IVB Artificial Impacts on the Moon. Earth and Space Science, 8(12). https://doi.org/10.1029/2021EA001887

Redmon, J., & Farhadi, A. (2018). YOLOv3: An Incremental Improvement. ArXiv Preprint ArXiv. https://arxiv.org/abs/1804.02767

Redmon, J., Vivvala, S., Girshick, R., & Farhadi, A. (2016). You Only Look Once: Unified, Real-Time Object Detection. Proceedings of the IEEE Conference on Computer Vision and Pattern Recognition (CVPR), 779–788.

Robbins, S. J. (2019). A New Global Database of Lunar Impact Craters >1–2 km: 1. Crater Locations and Sizes, Comparisons with Published Databases, and Global Analysis. Journal of Geophysical Research: Planets, 124(4), 871–892. https://doi.org/10.1029/2018JE005592

Robbins, S. J., & Hynek, B. M. (2012). A New Global Database of Mars Impact Craters ≥1 km: 1. Database creation, properties, and parameters. Journal of Geophysical Research: Planets, 117(5). https://doi.org/10.1029/2011JE003966

Robbins, S. J., Antonenko, I., Kirchoff, M. R., Chapman, C. R., Fassett, C. I., Herrick, R. R., Singer, K., Zanetti, M., Lehan, C., Huang, D., & Gay, P. L. (2014). The variability of crater identification among expert and community crater analysts. Icarus, 234, 109–131. https://doi.org/10.1016/j.icarus.2014.02.022

Robbins, S. J., Riggs, J. D., Weaver, B. P., Bierhaus, E. B., Chapman, C. R., Kirchoff, M. R., Singer, K. N., & Gaddis, L. R. (2018). Revised recommended methods for analyzing crater size-frequency distributions. Meteoritics & Planetary Science, 53(4), 891–931. https://doi.org/10.1111/maps.12990

Robinson, M. S., Brylow, S. M., Tschimmel, M., Humm, D., Lawrence, S. J., Thomas, P. C., Denevi, B. W., Bowman-Cisneros, E., Zerr, J., Ravine, M. A., Caplinger, M. A., Ghaemi, F. T., Schaffner, J. A., Malin, M. C., Mahanti, P., Bartels, A., Anderson, J., Tran, T. N., Eliason, E. M., McEwen, A. S., Turtle, E., Jolliff, B. L., Hiesinger, H. (2010). Lunar Reconnaissance Orbiter Camera (LROC) Instrument Overview. Space Science Reviews, 150(1–4), 81–124. https://doi.org/10.1007/s11214-010-9634-2

Salamunićcar, G., Lončarić, S., & Mazarico, E. (2012). LU60645GT and MA132843GT catalogues of Lunar and Martian impact craters developed using a Crater Shape-based interpolation crater detection algorithm for topography data. Planetary and Space Science, 60(1), 236–247. https://doi.org/10.1016/j.pss.2011.09.003

Salamunićcar, G., Lončarić, S., Grumpe, A., & Wöhler, C. (2014). Hybrid method for crater detection based on topography reconstruction from optical images and the new LU78287GT catalogue of Lunar impact craters. Advances in Space Research, 53(12), 1783–1797. https://doi.org/10.1016/j.asr.2013.06.024

Salamunićcar, G., Lončarić, S., Pina, P., Bandeira, L., & Saraiva, J. (2011). MA130301GT catalogue of Martian impact craters and advanced evaluation of crater detection algorithms using diverse topography and image datasets.

Planetary and Space Science, 59(1), 111–131. https://doi.org/10.1016/j.pss.2010.11.003

Scholten, F., Oberst, J., Matz, K.-D., Roatsch, T., Wählisch, M., Speyerer, E. J., & Robinson, M. S. (2012). GLD100: The near-global lunar 100 m raster DTM from LROC WAC stereo image data: THE 100 M RASTER DTM GLD100. Journal of Geophysical Research: Planets, 117(E12). https://doi.org/10.1029/2011JE003926

Schultz, P., Greeley, R., & Gault, D. (1977). Interpreting Statistics of Small Lunar Craters, Vol. 3, Planetary and Lunar Surfaces.

See, J. E., Howe, S. R., Warm, J. S., & Dember, W. N. (1995). Meta-analysis of the sensitivity decrement in vigilance. Psychological Bulletin, 117(2), 230–249. https://doi.org/10.1037/0033-2909.117.2.230

Shoemaker, E. M., & Hackman, R. J. (1962). Stratigraphic Basis for a Lunar Time Scale. In The Moon, 14, 289–300. https://ui.adsabs.harvard.edu/abs/1962IAUS...14..289S

Silburt, A., Ali-Dib, M., Zhu, C., Jackson, A., Valencia, D., Kissin, Y., Tamayo, D., & Menou, K. (2019). Lunar crater identification via deep learning. Icarus, 317, 27–38. https://doi.org/10.1016/j.icarus.2018.06.022

Smith, D. E., Zuber, M. T., Neumann, G. A., Lemoine, F. G., Mazarico, E., Torrence, M. H., McGarry, J. F., Rowlands, D. D., Head, J. W., Duxbury, T. H., Aharonson, O., Lucey, P. G., Robinson, M. S., Barnouin, O. S., Cavanaugh, J. F., Sun, X., Liiva, P., Mao, D., Smith, J. C., & Bartels, A. E. (2010). Initial observations from the Lunar Orbiter Laser Altimeter (LOLA): lola initial observations. Geophysical Research Letters, 37(18). https://doi.org/10.1029/2010GL043751

Smith, D. E., Zuber, M. T., Neumann, G. A., Lemoine, F. G., Mazarico, E., Torrence, M. H., McGarry, J. F., Rowlands, D. D., Head, J. W., Duxbury, T. H., Aharonson, O., Lucey, P. G., Robinson, M. S., Barnouin, O. S., Cavanaugh, J. F., Sun, X., Liiva, P., Mao, D., Smith, J. C., & Bartels, A. E. (2010). Initial observations from the Lunar Orbiter Laser Altimeter (LOLA): LOLA INITIAL OBSERVATIONS. Geophysical Research Letters, 37(18), https://doi.org/10.1029/2010GL043751

Soderblom, L. A. (1970). A model for small-impact erosion applied to the lunar surface. Journal of Geophysical Research, 75(14), 2655–2661. https://doi.org/10.1029/JB075i014p02655

Speyerer, E. J., Robinson, M. S., Denevi, B. W., & LROC Team. (2011). Lunar Reconnaissance Orbiter Camera Morphological Map of the Moon. In Lunar and Planetary Science Conference (Vol. 42, abstract #2387). https://www.lpi.usra.edu/meetings/lpsc2011/pdf/2387.pdf

Stadermann, A. C., Zanetti, M. R., Jolliff, B. L., Hiesinger, H., van der Bogert, C. H., & Hamilton, C. W. (2018). The age of lunar mare basalts south of the Aristarchus Plateau and effects of secondary craters formed by the Aristarchus event. Icarus, 309, 45–60. https://doi.org/10.1016/j.icarus.2018.02.030

Stepinski, T. F., Ding, W., & Vilalta, R. (2012). Detecting impact craters in planetary images using machine learning. In Intelligent Data Analysis for Real-Life Applications: Theory and Practice, 146-159. IGI Global.

Still, M. (2006). The definitive guide to ImageMagick. Apress, 2560 Ninth Street, Suite 219, Berkeley, CA. https://link.springer.com/content/pdf/10.1007/978-1-4302-0112-0.pdf

Stopar, J. D., Robinson, M. S., Barnouin, O. S., McEwen, A. S., Speyerer, E. J., Henriksen, M. R., & Sutton, S. S. (2017). Relative depths of simple craters and the nature of the lunar regolith. Icarus, 298, 34–48. https://doi.org/10.1016/j.icarus.2017.05.022

Stopar, J. D., Robinson, M. S., Speyerer, E. J., Burns, K., Gengl, H., & Team, L. (2012, March). Regolith characterization using lroc nac digital elevation models of small lunar craters. In Lunar and Planetary Science Conference (Vol. 43, abstract #2387).

The Lunar Reconnaissance Orbiter Narrow-Angle Camera. (2022). LROC Image Search [website]. http://wms.lroc.asu.edu/lroc/search.

Trask, N. J. (1971). Geologic comparison of mare materials in the lunar equatorial belt, including Apollo 11 and Apollo 12 landing sites. US Geol. Surv. Prof. Pap., 750D, 138-148.

Ultralytics-yolov3. (2020). (Python). [Code] Ultralytics. https://github.com/ultralytics/yolov3 (Original work published 2018).

Urbach, E. R., & Stepinski, T. F. (2009). Automatic detection of sub-km craters in high resolution planetary images. Planetary and Space Science, 57(7), 880–887. https://doi.org/10.1016/j.pss.2009.03.009

van der Bogert, C. H., Hiesinger, H., Dundas, C. M., Krüger, T., McEwen, A. S., Zanetti, M., & Robinson, M. S. (2017). Origin of discrepancies between crater size-frequency distributions of coeval lunar geologic units via target property contrasts. Icarus, 298, 49–63. https://doi.org/10.1016/j.icarus.2016.11.040

Wang, Y., Wu, B., Xue, H., Li, X., & Ma, J. (2021). An Improved Global Catalog of Lunar Impact Craters (≥1 km) With 3D Morphometric Information and Updates on Global Crater Analysis. Journal of Geophysical Research: Planets, 126(9). https://doi.org/10.1029/2020JE006728

Wang, Y., Xie, M., Xiao, Z., & Cui, J. (2020). The minimum confidence limit for diameters in crater counts. Icarus, 341, 113645. https://doi.org/10.1016/j.icarus.2020.113645

Wetzler, P. G., Honda, R., Enke, B., Merline, W. J., Chapman, C. R., & Burl, M. C. (2005). Learning to Detect Small Impact Craters. 2005 Seventh IEEE Workshops on Applications of Computer Vision (WACV/MOTION'05), 1, 178–184. https://doi.org/10.1109/ACVMOT.2005.68

Wilcox, B. B., Robinson, M. S., Thomas, P. C., & Hawke, B. R. (2005). Constraints on the depth and variability of the lunar regolith. Meteoritics & Planetary Science, 40(5), 695–710. https://doi.org/10.1111/j.1945-5100.2005.tb00974.x

Wilhelms, D. E. (1987). The geologic history of the Moon (USGS Numbered Series No. 1348; Professional Paper, 337). United States Geological Survey. https://doi.org/10.3133/pp1348

Williams, J. P., van der Bogert, C. H., Pathare, A. V., Michael, G. G., Kirchoff, M. R., & Hiesinger, H. (2018). Dating very young planetary surfaces from crater statistics: A review of issues and challenges. Meteoritics & Planetary Science, 53(4), 554–582. https://doi.org/10.1111/maps.12924

Xiao, Z., & Strom, R. G. (2012). Problems determining relative and absolute ages using the small crater population. Icarus, 220(1), 254–267. https://doi.org/10.1016/j.icarus.2012.05.012

Xiao, Z., & Werner, S. C. (2015). Size-frequency distribution of crater populations in equilibrium on the Moon: Crater equilibrium on the moon. Journal of Geophysical Research: Planets, 120(12), 2277–2292. https://doi.org/10.1002/2015JE004860

Yang, C., Zhao, H., Bruzzone, L., Benediktsson, J. A., Liang, Y., Liu, B., Zeng, X., Guan, R., Li, C., & Ouyang, Z. (2020). Lunar impact crater identification and age estimation with Chang'E data by deep and transfer learning. Nature Communications, 11(1), 6358. https://doi.org/10.1038/s41467-020-20215-y

Yolo_Label. (2021). (Version 1.1.1) [Code]. https://github.com/developer0hye/Yolo_Label.

Young, J. (1940). A statistical investigation of diameter and distribution of lunar craters. J. Brit. Astron. Assoc, 50(9), 309–326.

Zeilnhofer, M. (2020). A Global Analysis of Impact Craters on Ceres. ProQuest Dissertations & Theses Global, 1-251, proquest: 27963349, URL: https://search.proquest.com/openview/4e9a383f80b524bf68f755ff3649d02d

Zhang, Y. (2010). New Advances in Machine Learning. Intech. https://doi.org/10.5772/225

Chapter 4: Lunar Surface Model Age Derivation: Comparisons Between Automatic and Human Crater Counting Using LRO-NAC And Kaguya TC Images

This Chapter is published under Fairweather, J. H., Lagain, A., Servis, K., & Benedix, G. K. (2023). Lunar Surface Model Age Derivation: Comparisons Between Automatic and Human Crater Counting Using LRO-NAC and Kaguya TC Images. Earth and Space Science, 10(7), e2023EA002865. https://doi.org/10.1029/2023EA002865. Please note that slight modifications were made in this chapter to improve the readability.

Abstract

Dating young lunar surfaces, such as impact ejecta blankets and terrains associated with recent volcanic activities, provides critical information on the recent events that shaped the surface of the Moon. Model age derivation of young or small areas using a crater chronology is typically achieved through manual counting, which requires a lot of small impact craters to be tediously mapped. In this study, we present the use of a Crater Detection Algorithm (CDA) to extract crater populations on Lunar Reconnaissance Orbiter—Narrow Angle Camera (LRO-NAC) and Kaguya Terrain Camera images. We applied our algorithm to images covering the ejecta blankets of four Copernican impact craters and across four young mare terrains, where manually derived model ages were already published. Across the eight areas, 10 model ages were derived. We assessed the reproducibility of our model using two populations for each site: (a) an unprocessed population and (b) a population adjusted to remove contaminations of secondary and buried craters. The results showed that unprocessed detections led to overestimating crater densities by 12%–48%, but "adjusted" populations produced consistent results within <20% of published values in 80% of cases. Regarding the discrepancies observed, we found no significant error in our detections that could explain the differences with crater densities manually measured. With careful processing, we conclude that a CDA can be used to determine model ages and crater densities for the Moon. We also emphasize that automated crater datasets must be processed, interpreted and used carefully, in unity with geologic reasoning. The presented approach can offer a consistent and reproducible way to derive model ages.

4.1 Introduction

The surface of the Moon has recorded the impact history of the inner solar system for the last ~4 billion years (Öpik, 1960; Shoemaker & Hackman, 1962). The counts of impact craters that have accumulated on geological units, which have been radiometrically dated thanks to sample return missions, have allowed researchers to establish a lunar chronology system that can link the measured crater density with a model age for any mapped unit (e.g., Neukum et al., 2001; Shoemaker & Hackman, 1962). When applied to the ejecta blanket, or the floor, of large impact craters, the crater counts allow one to estimate the age of the impact event (Hiesinger et al., 2012; Kirchoff et al., 2021; Lagain, Benedix, et al., 2021; Lagain, Servis, et al., 2021; Lagain et al., 2020). Copernican-aged craters (<1.1 Ga) are interpreted as the most recent impacts across the Moon's surface. These craters are characterized by their bright ejecta and fresh morphology, making them ideal for mapping (Dundas & McEwen, 2007; Wilhelms, 1987). However, many Copernican craters smaller than ~20 km in diameter have few or no associated ages, which impedes the investigation of smaller-scale events in recent lunar times. Small and/or recent (<3 Ga) geological units associated with later volcanic episodes are also sporadically dated. This has been due to time limitations in geological mapping on high-resolution image datasets and crater identification (i.e., mapping all craters <1 km in diameter). Therefore, a method for quickly and systematically analysing Copernican craters of all sizes and, more generally, young geological units is needed.

Introducing machine learning (ML) techniques, such as convolutional neural networks (CNNs), can help overcome some limitations. Crater Detection Algorithms (CDA) have already been developed and optimized for use on planetary images to detect impact structures quickly and accurately (e.g., Benedix et al., 2020; DeLatte et al., 2019; Lagain, Benedix et al., 2021; Lagain, Bouley, et al., 2022; Lagain, Kreslavsky, et al., 2022; Lagain, Servis, et al., 2021; Fairweather et al., 2022). If a CNN's performance is similar to human-level error (Robbins et al., 2014; Wang et al., 2020) and used with caution (e.g., removal of secondary crater clusters and avoidance of overprinted craters (Fassett, 2016; Fassett & Thomson, 2014; Xu et al., 2022)), automatically detected crater datasets can be used to derive meaningful Crater Size-Frequency Distributions (CSFD) and model ages (Benedix et al., 2020; Lagain, Bouley, et al., 2022).

With further use and analysis of the crater detections, it is possible to derive acceptable surface ages for hundreds of sites (Lagain, Bouley, et al., 2022). Although there have been many successful attempts to create CDAs to address the lunar crater populations (e.g., Ali-Dib et al., 2020; Cadogan, 2020; Salamunićcar et al., 2014; Sawabe et al., 2006; Yang et al., 2020), to our knowledge, no study has systematically used automatic crater counts to derive model ages and determined if they are comparable with manual methods. The ML approach is particularly relevant for investigating younger surfaces, such as those around the Chang'E-5 (CE-5) landing site (LS) and Copernican crater ejecta.

To quantify the viability and accuracy of using a CDA to analyse Copernican impacts and relatively recent lunar surfaces, we compare a set of published model ages with the model ages derived using our CDA. The automatically detected craters were obtained from the global Kaguya Terrain Camera (TC) images (~7 m/px resolution) (Haruyama et al., 2008) and the Lunar Reconnaissance Orbiter - Narrow Angle Camera (LRO-NAC, ~0.25–2 m/px resolution) (Robinson et al., 2010) image datasets. Specifically, we focused on model ages and cratering densities reported for North Ray, Tycho, Copernicus (see Hiesinger et al., 2012) and Lalande craters (see Xu et al., 2022), as well as two mare areas in the vicinity of the Chang'E-5 mission LS (areas #05 and #21 in Giguere et al., 2022); and two regional mare units, Oceanus Procellarum unit P60 (see Hiesinger, 2003), and Imbrium unit I30 (see Hiesinger et al., 2000). These sites are well-known and commonly investigated; therefore, they serve as acceptable points of comparison.

4.2 Data and Methodology

The following sections describe the locations of the crater count areas we selected. We then describe the two CDA detection models optimized for NAC (Fairweather et al., 2022) and the Kaguya TC image dataset (this study). Finally, we detail the process for deriving the model ages and removing potential contaminations from secondary and overprinted craters (referred to as ‘pre-existing’ craters within this study).

4.2.1 Surface Model Age of the Crater Counts Areas

Each count area was chosen based on four main criteria: (1) the availability of high-resolution image (either in NAC, Kaguya TC, or both), (2) relatively young published model ages (either Copernican or Eratosthenian, i.e. <3.2 Ga), (3) the ability to compare against prior manual crater directly counts within the literature, and (4) a spread across lunar terrains among the selected study areas. Four Copernican impact craters (North Ray, Lalande, Tycho, Copernicus) and four Eratosthenian mare surfaces (CE-5 #05 and #21, P60, I30) were selected based on these criteria (Figure 4.1 and Table 4.1). In the case of Lalande crater, two crater densities are reported from the same count area: one related to the crater emplacement and another to the terrain underlying the ejecta blanket. In total, ten crater density measurements (Table 4.1) across seven areas were investigated (Figure 4.1).

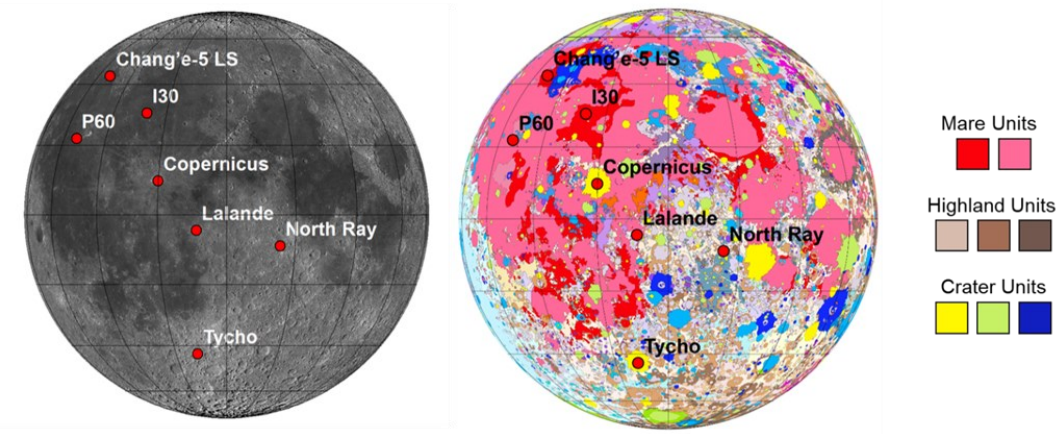

Figure 4.1: Left: Locations of the chosen crater count areas investigated in this study. The two areas around the Chang'e-5 landing site (LS) are symbolized by one dot on the map. The background is a stereographic projection of the LRO-WAC mosaic (Speyerer et al., 2011). Right: The unified geologic map of the near side of the Moon in a stereographic projection, with a simplified geological unit key (For the whole map, see Fortezzo et al., 2020).

Table 4.1: Information on each count area location investigated within this study. Coordinates are in decimal degrees. *Denotes the locations indirectly sampled.

Type	Location/Count Area		Diameter/Area		Latitude	Longitude	Terrain	Radiometric age
Copernican Crater	North Ray		1 km		8.82° S	15.48° E	Nearside Descartes Highlands	50.3 ± 0.8 Ma [Drozd et al., 1974]
	Lalande		24 km		4.4° S	8.6° W	Eastern Mare Insularum	/
	*Tycho	NAC	85 km	1.65km²	43.31° S	11.36° W	Nearside southern Highlands	110 ± 4 Ma [Drozd et al. 1977]
		WAC		6710km²				
	*Copernicus		95 km		9.62° N	20.08° W	Eastern Oceanus Procellarum	800 ± 15 Ma [Bogard et al., 1992]
Eratosthenian Mare	Chang' E-5	#05	48 km²		43.05° N	51.91° W	North-Eastern Oceanus Procellarum	2030 ± 4 Ma [Li et al., 2021]
		#21	272 km²					
	Mare Unit P60		1429 km²		22.0° N	53.0° W	Central Eastern Oceanus Procellarum	/
	Mare Unit I30		3108 km²		30.0° N	27.0° W	Western Mare Imbrium	/

4.2.1.a The Copernican Craters

The craters investigated within this study are all younger than 1.1 Ga and lie within the Copernican chronology system. Each crater can be defined by its bright crater ray systems, visible ejecta blankets, and clean crater rims (Dundas and McEwen, 2007; Wilhelms, 1987). The four chosen craters are North Ray, Lalande, Tycho, and Copernicus (from smallest to largest). These impacts are spread across the Moon's nearside and are superimposed across a range of lunar lithologies (Figure 4.1 and Table 4.1). The smallest investigated crater, North Ray (D ~ 1 km), was visited and sampled during the Apollo 16 mission, where the exposure age of some material collected nearby allowed to provide a calibration point for the lunar chronology model (Table 4.1). Lalande crater (D ~ 24 km) was dated and investigated in depth by Xu et al. (2022); their findings are reported in later sections. Finally, the two most prominent lunar impacts are Tycho crater (D ~ 85 km) and Copernicus crater (D ~ 95 km). These craters have been thoroughly mapped and investigated over the years (e.g., Dundas and McEwen, 2007; Mazrouei et al., 2019; Pozzobon et al., 2020; Wilhelms, 1987). Their formation has been associated with lunar material collected from Apollo 17 and Apollo 12 missions, respectively (Table 4.1). However, we note that a 1:1 comparison with the radiometric age of some of the Apollo 17 samples and the model age obtained from crater counts performed on Tycho's ejecta has been recently questioned by the community and ruled out in recent lunar chronology recalibrations (e.g., Robbins, 2014; Xie and Xiao, 2023). Indeed, Schmitt et al. (2017) argued that the avalanche deposits on which crater

counts were performed and interpreted initially as being triggered by Tycho's formation would instead be associated with the Lee-Lincoln fault. Therefore, we will not compare the exposure age of the light mantle avalanche debris within Taurus-Littrow, and the crater counts on Tycho's ejecta. These four craters have been investigated using crater count methods in the literature, especially Tycho and Copernicus (see Mazrouei et al., 2019; Xiao & Strom, 2012; Xiao & Werner, 2015; Terada et al., 2020). Therefore, they are good candidates to analyse and compare our CDA model results to investigate differences and viability in dating such impacts. Reported age results from the chosen crater studies (i.e., Hiesinger et al., 2012; Xu et al., 2022) are summarized in Table 4.2.

4.2.1.b The Mare Units

The analysed mare units cluster in the north-western hemisphere of the Moon's near side (Figure 4.1). Two sites associated with the Chang'E-5 sample return mission (Che et al., 2021) were chosen due to a significant variation in the reported cratering densities (see Giguere et al., 2022). They are both located within Oceanus Procellarum, a mare unit of great interest as it is estimated to be one of the youngest mare flows on the Moon's surface (Figure 4.1) and has had extensive investigation within recently published studies (e.g., Jia et al., 2020; Wu et al., 2018; Qian et al., 2021; Giguere et al., 2022) (Table 4.2). The first area, mare unit (#21), is near the Chang'E-5 lunar lander (Table 4.1). Count area #05 is ~15 km east of area #21. The remaining units are also young mare flows: Oceanus Procellarum mare unit P60 and Imbrium mare unit I30 (Figure 4.1 and Table 4.1). These areas were defined and dated with crater counts by Hiesinger et al. (2000, 2011) and Hiesinger (2003) (Table 4.2). Unlike the Change-5 landsite, these mare units do not have any known associated radiometric ages assigned to their formation (Table 4.1).

Table 4.2: Published information of each location, image data, unit ID, size of count area, $N_{cum}(1)$ [per km^2], and model age (with errors). Model ages for North Ray, Lalande, Tycho, Copernicus and Chang'E-5 areas were calculated from the fit of the cumulative CSFD to the Neukum et al. (2001) production function. The model ages for Oceanus Procellarum unit P60 and Mare Imbrium unit I30 were calculated from the fit of cumulative CSFD to the Neukum et al. (1984) production function.

Location	Study	Image Data	Count Area	Area (km^2)	Number of Craters	Fit Range	$N_{cum}(1)$	Model age (Ma)	Error (Ma)
North Ray	Hiesinger et al. (2012)	NAC	*NR1-4*	2.12	4177*	20m-100m	3.94E-05	47	4
									-4
Lalande	Xu et al. (2022)	Kaguya TC	*Ejecta blanket on Mare*	1780	1540**	100m-170m	3.35E-04	400	9
									-9
					12**	>1.2km	1.81E-02	3800	40
									-60
Tycho	Hiesinger et al. (2012)	NAC	*NAC TE1-4*	1.65	12698*	20m-100m	7.12E-05	85	15
									-18
		WAC	*WAC TE*	6710	266*	150m-1km	1.04E-04	124	12
									-12
Copernicus	Hiesinger et al. (2012)	WAC	*WAC CE1-3*	2630	534*	200m-1km	6.53E-04	779	110
									-120
Chang'E-5	Giguere et al. (2022)	NAC	#21	48	49**	200m-600m	2.61E-03	3030	200
									-300
		NAC	#05	272	100**	200m-1km	2.15E-03	2560	200
									-300
Oceanus Procellarum P60	Hiesinger (2003)	Lunar Orbiter IV	*P60*	1429	/	>400m	1.01E-03	1200	320
									-320
Mare Imbrium I30	Hiesinger et al. (2000)	Lunar Orbiter IV	*I30*	3108	/	>400m	1.68E-03	2010	140
									-140

Note: the published N(1) = 1.86E-02 km^{-2} value reported in Xu et al. (2022) for Lalande's impacted mare terrain using 12 craters > 1.2 km was incorrect for the reported model age. Therefore, we have reported the corrected value of N(1) = 1.81E-02 km^{-2}.

* Number of craters counted within the count area.

** Number of craters within the fit range.

4.2.2 The Image Datasets

We used images from two lunar image datasets to analyse each crater count area. The first was the LRO-NAC image dataset, which has a spatial resolution ranging between 0.25-2 m/px (Robinson et al., 2010), allowing consistent mapping of craters down to ~20m in diameter (Robbins et al., 2014; Wang et al., 2019). For the small North Ray and Tycho (NAC TE) count areas (Table 4.2), we used NAC image pairs M129187331R/L (with an incidence angle of 54°) and M104570590R/L (with an incidence angle of 62°). These are the same NAC images Hiesinger et al. (2012) used in their study of the same locations. The NAC images were downloaded through the online LROC PDS portal (https://wms.lroc.asu.edu/lroc/search) and were processed through the USGS Integrated Software for Imagers and Spectrometers (ISIS).

The second image dataset was the global mosaicked Kaguya TC images (Haruyama et al., 2008; Isbell et al., 2014). Across the cited literature we analysed within this study, the count areas for Tycho (WAC TE), Copernicus, and Lalande craters, Chang'E-5 (#05, #21), P60 and I30 units were derived from crater counts performed on WAC, Lunar Orbiter IV, and Kaguya TC camera images (Table 4.2). Among these areas, the smallest crater diameter used to derive a model age was 100 m, measured on Kaguya TC images by Xu et al. (2022). The Kaguya TC dataset provides an excellent bridge to the resolution gaps between Lunar Orbiter IV/LRO-WAC and LRO-NAC datasets, with a near-global coverage at ~7.4 m/px in resolution (Haruyama et al., 2008). Therefore, we used the Kaguya TC images instead of the LRO-WAC and Lunar Orbiter IV images for Tycho (area WAC TE), Copernicus, P60 and I30 count areas. Two mosaicked versions of the Kaguya TC dataset were used: a morning version (with early or right-to-left low-angle solar illumination) and an evening version (with late or left-to-right solar illumination). Both datasets are released as 3° by 3° image tiles (see Isbell et al., 2014; Kaguya Data Archive, https://darts.isas.jaxa.jp/planet/pdap/selene/). The Kaguya TC image tile ID list for each count area is reported in Appendix Table S4.1.

4.2.3 The Crater Detection Algorithm

Our CDA is a CNN image-based object detection algorithm which has been developed to identify impact craters on multiple scales across both Martian (Benedix et al., 2020; Lagain et al., 2021a,b) and lunar (Fairweather et al., 2022) images. Specifically, the prior CNN models use the Ultralytics implementation of YOLOv3 (You Only Look Once version 3, Redmon et al., 2016).

Within this study, we have utilized two crater detection CNN models. The first was trained for detection across LRO-NAC images with intermediate lighting conditions (incidence angle ~50° - ~70°) (Fairweather et al., 2022). This detection model has good detection accuracy, with an average Recall of 0.93 (crater detection rate), a Precision of 0.66, and an F1 score of 0.77 for craters down to ~20 m in size (Fairweather et al., 2022). When evaluating against craters >100 m in diameter, we obtained a Recall of 0.99 for fresh and moderately degraded craters, which decreases to 0.85 for very-degraded craters (see Fairweather et al., 2022). The NAC model was applied on images M129187331R/L and M104570590R/L (in a stereographic map projection), where we determined the CSFDs for North Ray and Tycho ejecta, respectively. An example of raw CDA detections on NAC images is shown in Figure 4.2.a. While using the NAC detection model, crater diameters were overestimated by ~15% (see Fairweather et al., 2022). Therefore, following the findings from Fairweather et al. (2022), the diameter sizes for the detections on the NAC images used within this study were corrected by a factor of -0.13 to display the model ages more accurately (see Figure S3 for the before and after 15% diameter correction).

To detect impact craters across Kaguya TC mosaics, our algorithm was updated with the Ultralytics' YOLOv5 (Jocher, 2022; https://github.com/ultralytics/yolov5) and newly trained on both morning and evening Kaguya versions (refer to the Text S1 for a description of the model retraining). The training dataset comprised 55,348 craters over 485 image tiles, with a 3:1 learning-validation split. The metrics obtained at the end of the training session were 0.8 for the Recall and 0.8 for the Precision, leading to an F1 score of 0.8 (Appendix Figure S4.1). The prior analysis by Fairweather et al. (2022) recommended compiling manual crater test datasets for both morning and evening Kaguya TC tiles to evaluate our model's performance further.

Each dataset has two subsets, each over the same mare and highland terrains (refer to Text S4.2 for a complete description of the evaluation results). This resulted in a Recall of 0.98, a Precision of 0.94 and an F1 score of 0.96 for craters >100 m in diameter (see Appendix 3.4, Table S4.2; Appendix 4.5, Dataset S4.1). The reader is referred to Fairweather et al. (2022), section 3.1, for further explanations of the metrics differences obtained between the validation and test datasets. Furthermore, the new model removed the systematic size overestimation (Appendix 4.3, Figure S4.2) displayed by the prior YOLOv3 NAC model (see Fairweather et al., 2022).

The updated Kaguya CDA model was applied to both Kaguya TC morning and evening mosaic tiles covering Tycho, Copernicus, and Lalande ejecta count areas, as well as the Chang'E-5 areas, P60, and I30 units (all in stereographic map projections). The model was applied to the images in Table S1 using the Pawsey Supercomputing Centre's supercomputer clusters (see Pawsey, 2023 and Fairweather et al., 2022). Due to the difference in illumination angles and data quality between the two versions of the Kaguya TC mosaics (Isbell et al., 2014), only the tile datasets with the highest number of detections were kept. Some examples of raw CDA detections across Kaguya TC images are shown in Figures 2.b and 2.c.

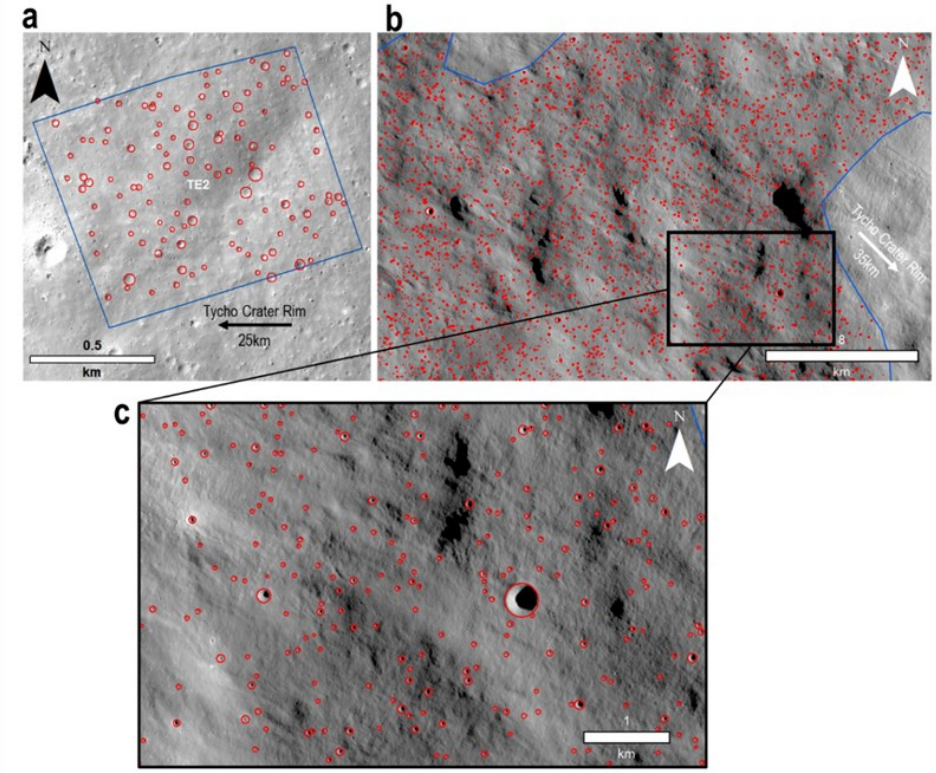

Figure 4.2: Examples of raw crater detections over Tycho's ejecta. (a) Sample of 115 craters (10m < D < 40m) detected over Hiesinger et al. (2012)'s TE2 region on NAC image M104570590L; (b) Sample of 3176 craters (38m < D < 396m) detected over Hiesinger et al. (2012)'s north-eastern WAC TE region on Kaguya image tile TCO_MAPm04_S39E345S42E348SC (see Figure 4 for crater context); (c) Zoomed in excerpt of the [b] Kaguya sample showing of 396 craters (38m < D < 396m). All crater detections in Dataset S2. Note that the missing crater detections across these images are below the 10-pixel reliability threshold for the CDA - these small craters are shown here but were not used to our derived model age.

4.2.3 Count Areas and Crater Data Selection

Our automatic approach does not discriminate secondary craters (Figure 4.3.a) and pre-existing craters (buried or overlapped by ejecta blankets, Figure 4.3.b) from primary craters. Therefore, we adapted a crater selection method to overcome these limitations and extract a crater population that best represents the formation age of the unit. Before applying the method, the smallest possible crater that can be accurately mapped and reliably identified across planetary images must be ≥ 10 pixels in diameter (Robbins et al., 2014; Wang et al., 2020). For this study, this translates to craters ~20 m and ~70 m in diameter for LRO-NAC images and Kaguya TC images, respectively. Therefore, when using a CDA, we cannot reliably derive ages from craters smaller than the stated thresholds.

Also, deriving model ages from recent impact events requires careful counting of small craters superimposed on the ejecta blanket and removing areas dominated by secondary craters (Zanetti et al., 2017; Xu et al., 2022; Lagain et al., 2020, 2021a). Here, we describe a suitable method for discarding/identifying such craters from within the determined count areas.

Firstly, we split our model age derivation analysis in two to keep the analysis as transparent as possible. The first set of analyses compared our 'raw' CSFDs, derived from the raw CDA craters within the same published counting areas (Table 4.2), to the published values. This analysis reflects a fully automatic approach, using every crater our algorithm detects. The second set of comparisons compared CSFDs from an 'adjusted' CDA dataset across updated counting crater count areas and crater counts with contaminates removed. The process for generating the adjusted crater datasets is described below.

Prominent secondary crater clusters and areas unsuitable for crater identification (i.e., Figure 4.3.a,b) were manually identified and removed across the analysed sites. Secondary craters lead to overestimating the cratering densities, and topographically unsuitable terrains do not retain the needed small craters (Craddock and Howard, 2000), thus leading to erroneous model ages. Some of the cited literature did not clearly outline identifying and removing such features in their method. Xu et al. (2022) identified and removed a secondary crater cluster from their counting area on Lalande's ejecta. Giguere et al. (2022) also described and removed a secondary crater cluster from the Chang'E-5 area #21. However, except for two areas corresponding to secondary clusters within the WAC CE2 area, Hiesinger et al. (2000, 2003, 2011, 2012) did not report any other crater clusters within their mapped areas for North Ray, Tycho and Copernicus. It is reasonable to think that obvious secondary craters were not included in their crater count datasets. Therefore, we adjusted the count areas outlined by Hiesinger et al. (2000, 2003, 2011, 2012) by discarding areas displaying obvious clusters and inadequate morphologies (Figure 4.3.b). Moreover, Hiesinger et al. (2012)'s NAC count area TE3 was excluded from our analysis due to lighting challenges and count area topography difficulties (see Appendix 4.3, Figure S4.5). Therefore, the comparative analysis only used count areas TE1, 2, and 4.

Additionally, Hiesinger et al. (2000, 2003, 2011) do not specifically report or show their crater size ranges used to fit the CSFD isochrons for units P60 and I30. However, the resolutions of the images used (~60-150 m/px, Hiesinger et al., 2011) imply that craters larger than ~400 m were used, thus constituting the cut-off size we applied to the detections obtained from the Kaguya TC images over these two areas.

The identification and removal of craters overprinted by impact ejecta blankets (i.e., 'pre-existing' craters, Figure 4.3.c) was performed by implementing a semi-automatic technique outlined by Fassett and Thomson (2014) and used by Xu et al. (2022). The technique estimates if a pre-existing crater should be seen/detected after an impact event, accounting for its distance from the impact crater and the radial ejecta blanket thickness. This process was replicated and adapted from Xu et al. (2022)'s dating technique for Lalande crater. However, our method differs slightly: where Xu et al. (2022) used one ejecta thickness model (i.e., Pike (1974)'s equation [Eq. 4.3]), we introduced two additional models by Sharpton (2014), for simple (2.2 – 17km) [Eq. 4.1] and complex craters (17 – 45km) [Eq. 4.2], defined as follows:

$$T = 0.014 \times R^{1.01} \times \left(\frac{r}{R}\right)^{-3} \qquad (2.2 \text{ km} < D < 17 \text{ km}) \qquad \textbf{[Eq. 4.1]}$$

$$T = 3.95 \times R^{0.399} \times \left(\frac{r}{R}\right)^{-3} \qquad (17 \text{ km} < D < 45 \text{ km}) \qquad \textbf{[Eq. 4.2]}$$

$$T = 0.033 \times R \times \left(\frac{r}{R}\right)^{-3} \qquad (D > 45 \text{ km}) \qquad \textbf{[Eq. 4.3]}$$

Where T is the ejecta thickness at a distance of r from the impact crater centre, and R is the transient radius of the impact crater, calculated using R x 0.85 (Baldwin, 1963; Pike, 1974; Melosh, 1989; Hildebrand et al., 1998).

However, this set of equations estimates the ejecta thickness deposited on a planar surface. Previous studies (e.g., Xie and Zhu, 2016; Xu and Xie, 2020) have shown that the thickness of ejecta filling up pre-existing craters is approximately ~2.9 times thicker than that deposited on flat surfaces due to the concave shape of the crater cavity. Therefore, following on with Xu and Xie (2020)'s method, Eq. 4.1-4.3 were modified to account for the increased thickness of ejecta material within pre-existing craters by applying a factor of 2.9 to the calculated ejecta thickness (T).

Additionally, using average depth-to-diameter ratios (0.12 for craters 40m < D < 100m, 0.15 for 100m < D < 400m, and 0.2 for 400m < D < 5km) for simple craters ranging between 40 m and 5 km inferred by Stopar et al. (2017), we can assume the maximum depth of all detected craters and compare it to the ejecta deposited at each crater. We used MS Excel to compare a crater's assumed depth to the estimated ejecta thickness. Craters with a cavity depth greater than the ejecta thickness were automatically flagged. Flagged craters should represent a detectable old crater overlain by a recent ejecta blanket. Therefore, all flagged craters were discarded from the current crater list. (The unmodified crater list can be found in Appendix 4.5, Dataset S4.2, Files *_V1). Based on this procedure, the count area polygons were adjusted. Areas dominated by secondary craters, pre-existing craters, and regions unsuitable for crater identification (all shown in Figure 4.3) were removed. These changes combine to form the 'adjusted' CDA crater datasets used to produce the adjusted CFSDs. All crater detections are available in Appendix 4.5 and Dataset S4.2.

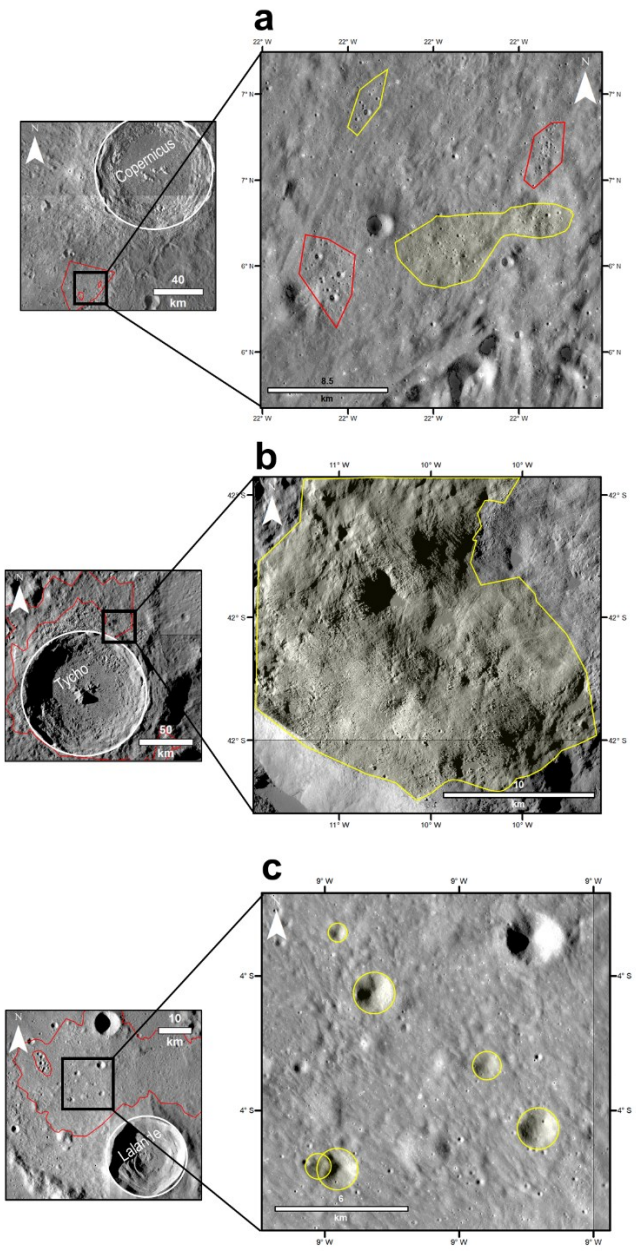

Figure 4.3: Examples of the features removed from the crater count datasets. (a) Secondary crater clusters within the Copernicus count area, red polygons denote the areas defined and identified by Hiesinger et al. (2012), yellow polygons denote an additional cluster identified and removed within this study; (b) Rocky regions with poor lighting conditions within the Tycho count area, red polygons denote the count area defined by Hiesinger et al. (2012), yellow polygon denotes an unsuitable area for crater identification; and (c) Pre-existing craters (yellow circles) across the Lalande count area, red polygon denotes the count area defined by Xu et al. (2022). Kaguya image tile IDs for each site are in Appendix 4.3, Table S4.1. Raw and adjusted count areas for all sites are available in Appendix 4.5, Dataset S4.2.

4.3 Results

The following two sub-sections present the results from the comparative crater count analysis that was undertaken to show the application of the CDA in determining the ages of young/small geological units. We present the 'raw' and 'adjusted' CSFDs inferred from our CDA crater dataset for each crater count area. All CSFD isochrons were fitted using the same crater fit ranges as the published studies (see Table 4.2). The crater size ranges we used to derive the model ages are not in equilibrium (defined by the Trask (1966) stand lunar equilibrium function). All CSFDs were made using CraterStats II (Michael and Neukum, 2010). We kept the chronology systems for each count area as the published studies (outlined in the Table 4.2 caption). All CSFDs were binned in the 4^{th} root-2 system, as not all the cited datasets consistently stated the binning method used. All model age errors are a function of the number of craters counted. The error margins are calculated using $\sqrt{n}$, where n is the number of craters in a size bin (Crater Analysis Techniques Working Group, 1979). All the crater detections, counting areas, and CraterStats II files are in Appendix 4.5, Datasets S4.3.

4.3.1 Craters

The NAC and Kaguya CDA models were run over images of within published crater count areas for North Ray (Figure 4.4.a), Lalande (Figure 4.5.a), Tycho (NAC and WAC areas) (Figure 4.6.a) and Copernicus craters (Figure 4.7.a). The raw crater detections within these count areas produced the presented 'raw' CSFDs. Each of the four crater sites resulted in varying differences between the published values and our values. For example, the greatest differences (of 45% and 35%) were observed for Lalande's crater formation age (Figure 4.5.b) and the Tycho NAC count areas (Figure 4.6.c-d), respectively. In addition, Lalande's underlying mare unit age was also derived from the successful detection of large impact craters (see Figure 4.5.b). Xu et al. (2022) also calculated and reported this model age in their crater analysis. Conversely, we found the lowest age difference, where the CDA and published values are identical (Figure 4.11.c).

In order to better understand the effects of secondary and pre-existing crater contamination within all impact crater count areas, we tried to remove all contaminants from the datasets.

Based on their relative spatial distribution of the crater directions, areas determined to be secondary crater clusters and craters flagged as pre-existing were mapped and subtracted from all the count areas. This was done for North Ray (Figure 4.6.c), Tycho WAC (Figure 4.6.b), and Copernicus craters (Figure 4.7.c). The count areas for Lalande and Tycho NAC were not adjusted, as no significant secondary crater clusters were mapped. However, flagged pre-existing craters were removed from the Lalande crater dataset. The area files and crater detections are in Appendix 4.5, Dataset S4.2.

New CFSDs were plotted for each site from the 'adjusted' data, and isochrons were drawn using the same fit ranges as before (Figure 4.4.d, 4.5.c, 4.6.e, 4.7.d). Across the four sites, three sites (North Ray, Lalande, and Copernicus) showed minimal differences (<20%) between the adjusted and published values (Figure 4.11.f). The greatest differences (>30%) were observed for both Tycho WAC and NAC count areas (Figure 4.11.f). All the results for each crater site are summarised and displayed in Table 4.3 and Figure 4.11.

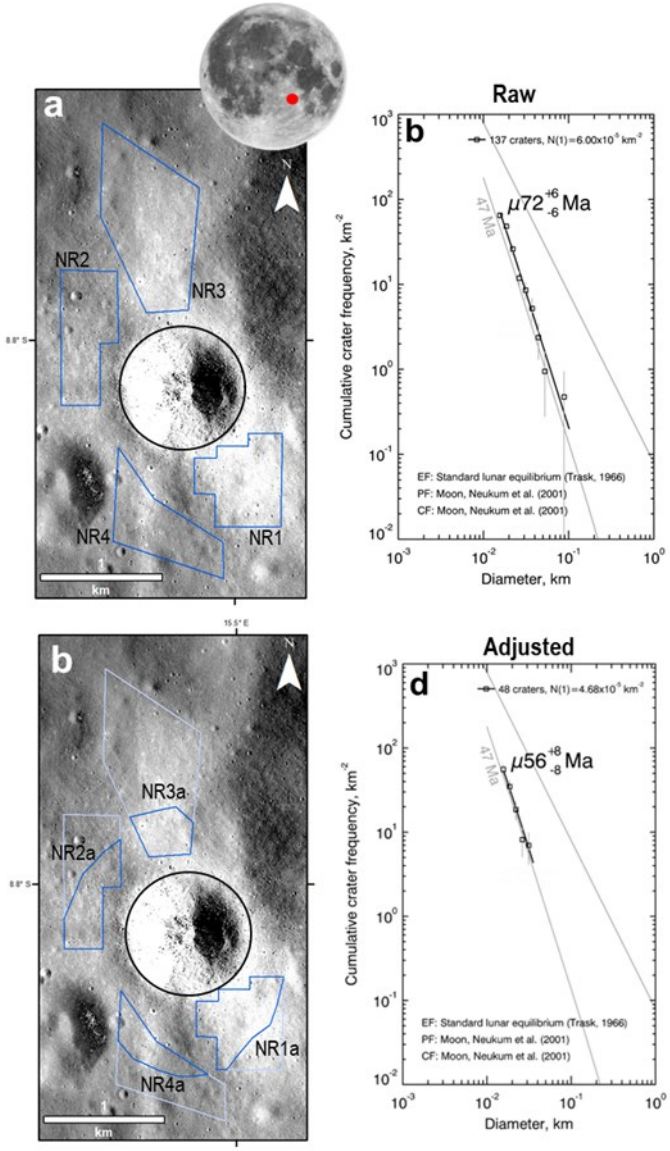

Figure 4.4: (a) Hiesinger et al. (2012)'s North Ray crater count areas NR1-4 (blue polygons, 2.12 km^2) on NAC image pair M129187331R/L; (b) CSFD and model age for areas NR1-NR4 using 137 craters between 17 and 100m in diameter detected by the CDA; (c) this study's adjusted count areas NR1a-NR4a (blue polygons, 0.86 km^2) for North Ray Crater on NAC image pair M129187331R/L; (d) adjusted CSFD and absolute model age for areas NR1a-NR4a using 48 automatically detected craters between 17 m to 40 m in diameter. The grey 47 Ma isochron plotted on panels b and d corresponds to that reported by Hiesinger et al. (2012). The crater images are presented in a stereographic map projection, with the count area locations (see Table 4.1) as the projection centre point.

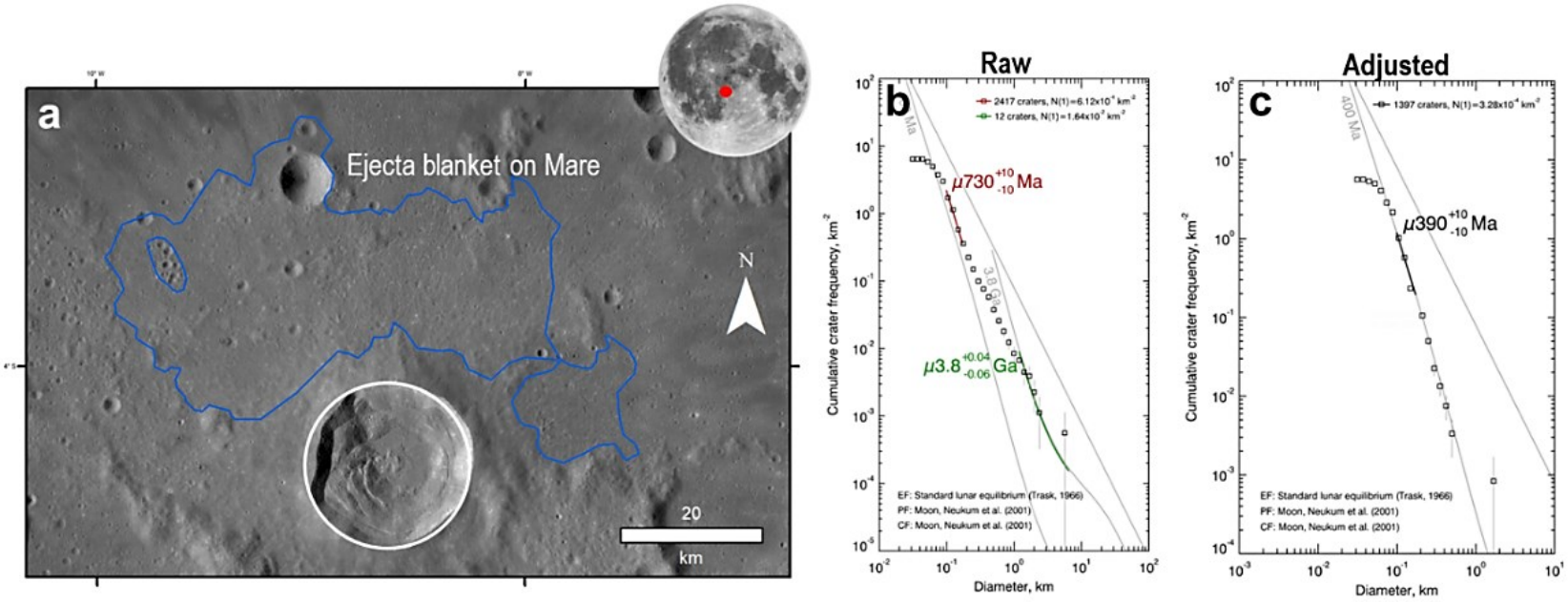

Figure 4.5: (a) Xu et al. (2022)'s Lalande 'ejecta blanket on mare' count area of Lalande crater (blue polygons, 1780 km2) on Kaguya TC tiles; (b) CSFD and model age isochrons for the 'ejecta blanket on mare' count area using 2,417 detections ranging between 100 m and 170 m in diameter (red isochron), and 12 detections between 1.2 km and 7 km in diameter (green isochron); (c) CSFD and model age isochron using the remaining 1,397 craters ranging between 100 m and 170 km in diameter. The grey 400 Ma isochron plotted on panels b and c corresponds to that reported by Xu et al. (2022) for the 'ejecta blanket on mare' count area. The crater images are presented in a stereographic map projection, with the count area locations (see Table 4.1) as the projection centre point.

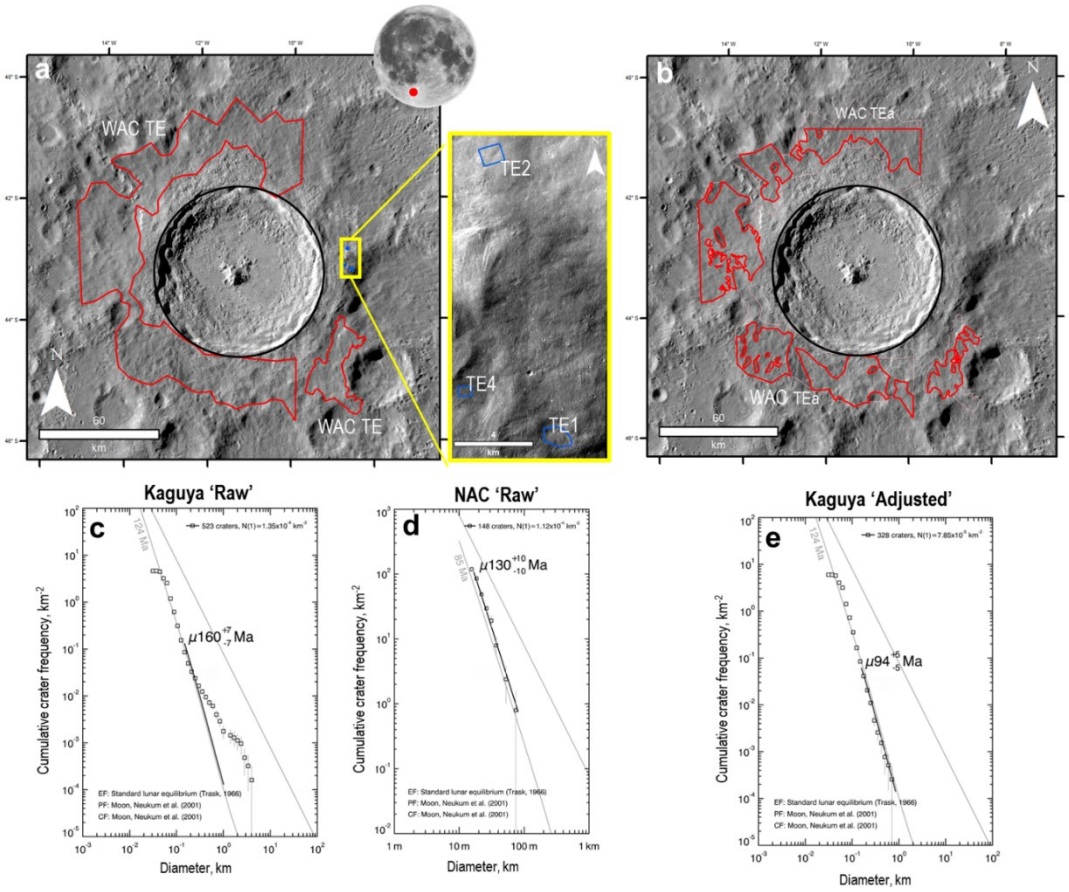

Figure 4.6: (a) Hiesinger et al. (2012)'s WAC TE (red polygons, 6710 km2) and NAC TE1,2,4 count areas (blue polygons, 0.407 km2) for Tycho crater ejecta on Kaguya image tiles and NAC image pair M104570590R/L; (b) adjusted Tycho count areas WAC TEa (red polygons, 3980 km2) and NAC TEa areas (blue polygons, 9.09 km2) on Kaguya image tiles and NAC image pair M104570590R/L; (c) CSFD and model age isochron for the WAC TE areas over the Kaguya image tile detections using 523 craters between 200 m and 1 km in diameter (Note that this CSFD shows an obvious representation of large craters (>500 m) overlaid by the ejecta, implying that Hiesinger et al. (2012) discarded most of these craters in their counting); (d) CSFD and model age isochron for areas TE1, 2 and 4 using 504 NAC detections between 20 m and 100 m in diameter; (e) CSFD and model age isochron for the adjusted WAC TEa areas over the Kaguya image tiles, using 328 craters between 200 m and 1 km in diameter. The grey 124 Ma and 85 Ma isochron plotted on panels c, d and e correspond to the model age Hiesinger et al. (2012) reported for the WAC and NAC count areas. The crater images are presented in a stereographic map projection, with the count area locations (see Table 4.1) as the projection centre point.

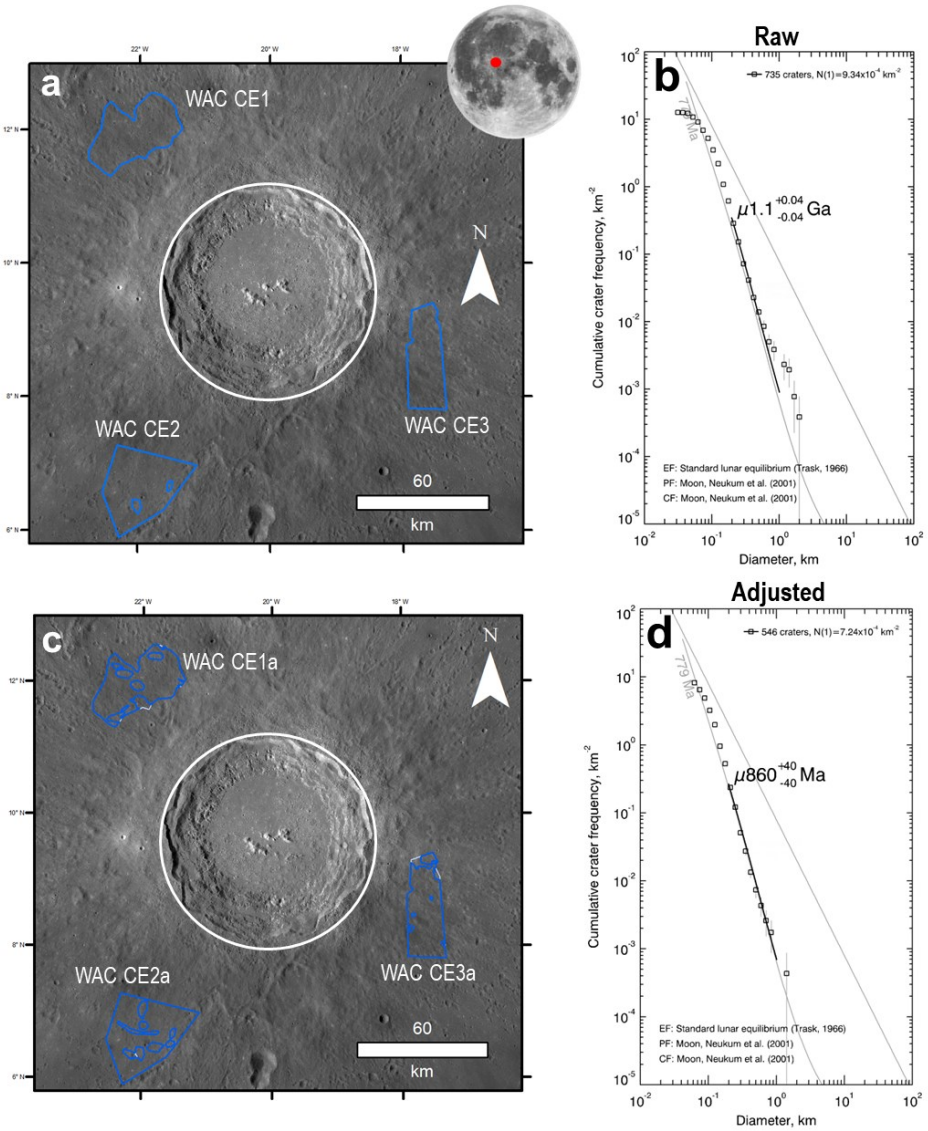

Figure 4.7: (a) Hiesinger et al. (2012)'s Copernicus WAC CE1-3 count areas (blue polygons, 2630 km2); (b) CSFD and model age isochron for areas WAC CE1-3 using 735 craters between 200 m and 1 km in diameter; (c) this study's adjusted WAC CE1a-3a count areas (blue polygon, 2305 km2); (d) adjusted CSFD and model age isochron for areas WAC CE1a-3a using the remaining 546 craters between 200 m and 1 km in diameter. The grey 779 Ma isochron plotted on panels b and d refers to the model age Hiesinger et al. (2012) reported for the WAC CE1-3 count areas. The crater images are presented in a stereographic map projection, with the count area locations (see Table 4.1) as the projection centre point.

4.3.2 Mare

The same age derivation processes were conducted over the four mare sites, where only the Kaguya CDA model was applied to the Kaguya images. The 'raw' crater detections within published count areas (Table 4.2) for Chang'E-5 area #21 and #05 (Figure 4.8.a, 8.c), as well as units P60 (Figure 4.9.a) and I30 (Figure 4.10.a) were plotted as CSFDs. Isochrons were drawn, and the raw model ages and N(1) values were calculated for each site (Figure 4.8-4.10). Three of the four mare sites showed considerably older ages and higher N(1) values when compared to the values reported by Giguere et al. (2022), Hiesinger et al. (2000, 2011), and Hiesinger (2003). This difference ranged from 20% to 45%, with site #05 showing the lowest difference and areas P60 and I30 collectively showing the highest (Figure 4.11.c). Chang'E-5 site #21 (i.e., the CE-5 land site) was particularly interesting, as this showed the lowest difference of all sites analysed within this study, at 10% (Figure 4.11.c). The significance of the Chang'E-5 results will be discussed in a later section.

Secondary crater clusters that can contaminate the crater dataset were also investigated on each mare site. However, we did not conduct a 'pre-existing' crater analysis, as thick continuous impact ejecta does not overlay these sites. Moreover, we did not adjust Giguere et al. (2022)'s count area #21 and #05 for Chang'E-5 (Figure 8.b, 8.d), as the authors investigated and removed secondary craters to a sufficient level. However, for the unit P60 and I30 count areas, we did map significant amounts of secondary crater clusters cutting across the units, likely deposited from the nearby Aristarchus and Copernicus impacts (Figure 4.9.c, 4.10.c). The 'adjusted' area model ages and N(1) for these sites showed minimal differences (< 20%) when compared against the published ages (Figure 4.11.f). All the results for each mare site are summarised and displayed in Table 4.3 and Figure 44.11.

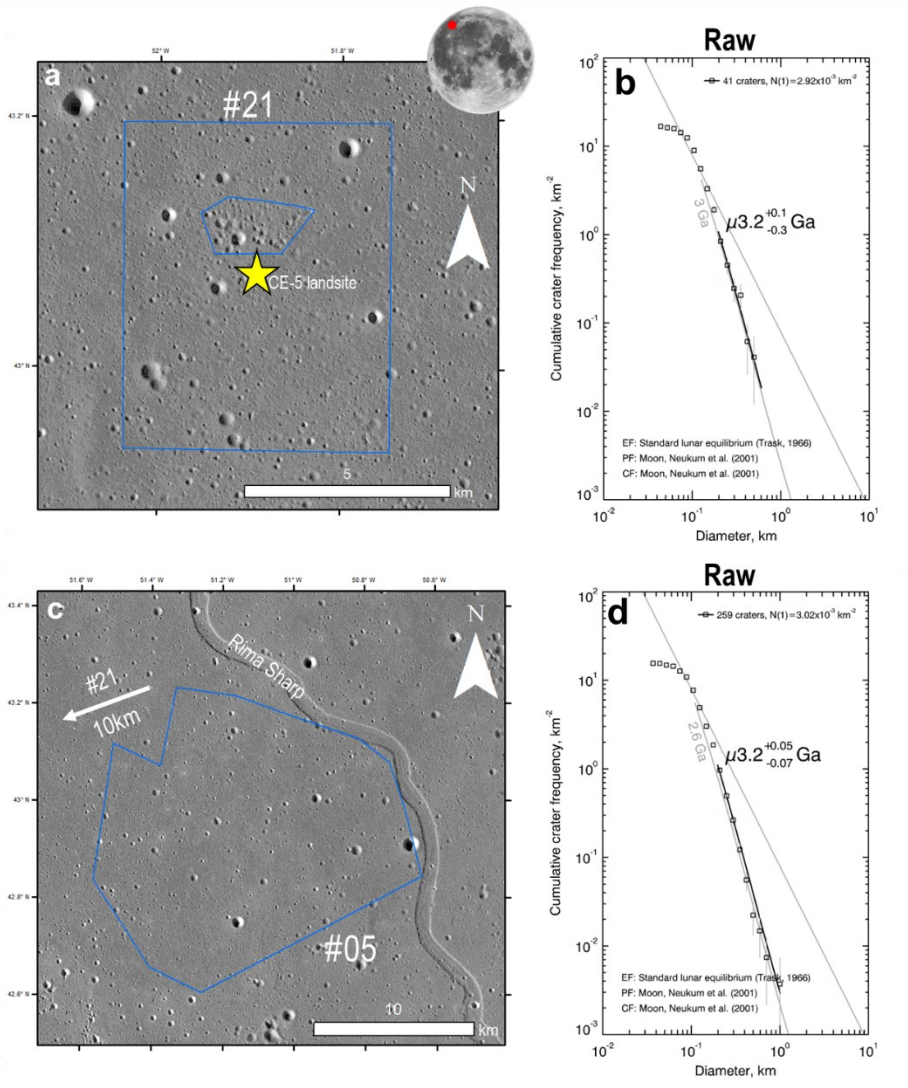

Figure 4.8: (a) Giguere et al. (2022)'s count area #21 of the Chang'E-5 (blue polygon, 48 km2) on a Kaguya tile, the yellow star is the Chang'E-5 lander landing site (43.05°N 51.91°W); (b) CSFD and model age isochron of area #21 using Kaguya 41 detections between 200 m and 600 m in diameter; (c) Giguere et al. (2022)'s count area #05 (blue polygon, 270 km2) on a Kaguya image tile; (d) CSFD and model age isochron of area #05 using 259 craters between 200 m and 1 km in diameter. The grey 3.0 Ga and 2.6 Ga isochrons plotted on panels b and d correspond to the model age Giguere et al. (2022) reported for count areas #21 and #05, respectively. The crater images are presented in a stereographic map projection, with the count area locations (see Table 4.1) as the projection centre point.

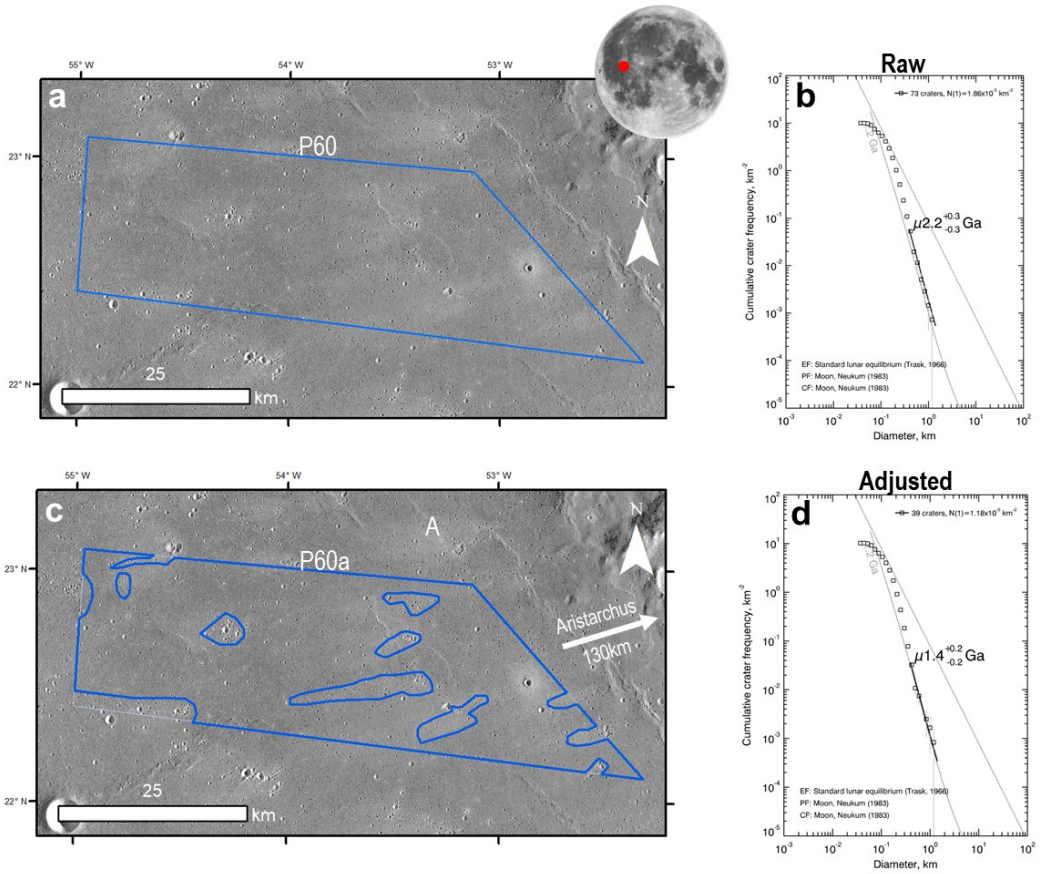

Figure 4.9: (a) Hiesinger (2003) count area for unit P60 (blue polygon, 1930 km2) on Kaguya image tiles; (b) CSFD and model age isochron for P60 using 73 craters between 400 m and 1.7 km in diameter; (c) this study's adjusted count area of unit P60a (blue polygons, 1210 km2) on Kaguya image tiles; (d) adjusted CSFD and model isochron for area P60a, using 39 craters between 400 m and 1.7 km in diameter. The grey 1.2 Ga isochron plotted on panels b and d corresponds to that of Hiesinger (2003)'s reported for the P60 count area. The crater images are presented in a stereographic map projection, with the count area locations (see Table 4.1) as the projection centre point.

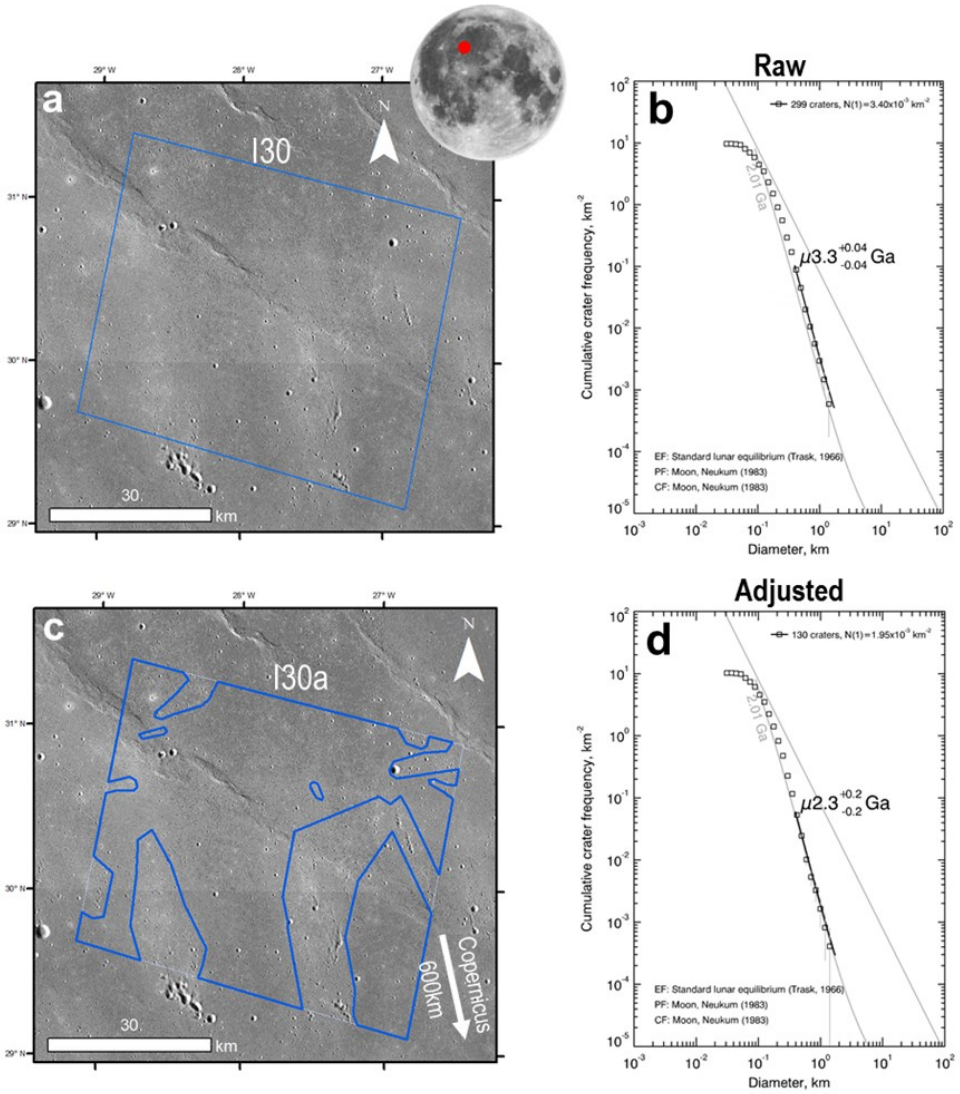

Figure 4.10: (a) Hiesinger et al. (2000) count area for unit I30 (blue polygon, 3108 km2) on Kaguya image tiles; (b) CSFD and model age isochron for I30 using 299 craters between 400m and 1.5 km in diameter; (c) this study's adjusted count area of unit I30a (blue polygons, 2450 km2) on Kaguya image tiles; (d) adjusted CSFD and model isochron for area I30a, using 130 craters between 400 m and 1.5 km in diameter. The grey 2.01 Ga isochron plotted on panels b and d corresponds to Hiesinger et al.'s (2000) age for the I30 count area. The crater images are presented in a stereographic map projection, with the count area locations (see Table 4.1) as the projection centre point.

Table 4.3: Summary of our Raw and Adjusted results for each counting area, including location, area ID, image data, area size, Ncum(1) [per km2], and model ages (with errors).

				Raw					Adjusted				
Location	Image Data	Count Area	Fit Range	Area (km²)	Craters fitted	$N_{cum}(1)$	Model age (Ma)	Error (Ma)	Area (km²)	Craters fitted	$N_{cum}(1)$	Model age (Ma)	Error (Ma)
North Ray	NAC	*NR1-4*	20m-100m	2.12	137	6.03E-05	72	6 -6	0.86	48	4.69E-05	56	8 -8
Lalande	Kaguya TC	*Ejecta blanket on Mare*	100m-170m	1780	2417	6.12E-04	730	10 -10	/	1397	3.27E-04	390	10 -10
			>1.2km		12	1.81E-02	3800	40 -60		/	/	/	/ /
Tycho	NAC	*TE*	20m-100m	0.41	148	1.09E-04	130	10 -10	/	/	/	/	/ /
	Kaguya TC	*WAC TE*	150m-1km	6710	523	1.34E-04	160	7 -7	3980	328	7.88E-05	94	5 -5
Copernicus	Kaguya TC	*WAC CE1-3*	200m-1km	2630	735	9.22E-04	1100	40 -40	2305	546	7.21E-04	860	40 -40
Chang'E-5	Kaguya TC	*#21*	200m-600m	48	41	2.91E-03	3200	100 -300	/	/	/	/	/ /
		#05	250m-1km	272	259	3.23E-03	3300	50 -70	/	/	/	/	/ /
Oceanus Procellarum	Kaguya TC	*P60*	>400m	1930	73	1.84E-03	2200	300 -300	1210	39	1.17E-03	1400	200 -200
Mare Imbrian	Kaguya TC	*I30*	>400m	3108	299	3.23E-03	3300	40 -40	2450	130	1.93E-03	2300	200 -200

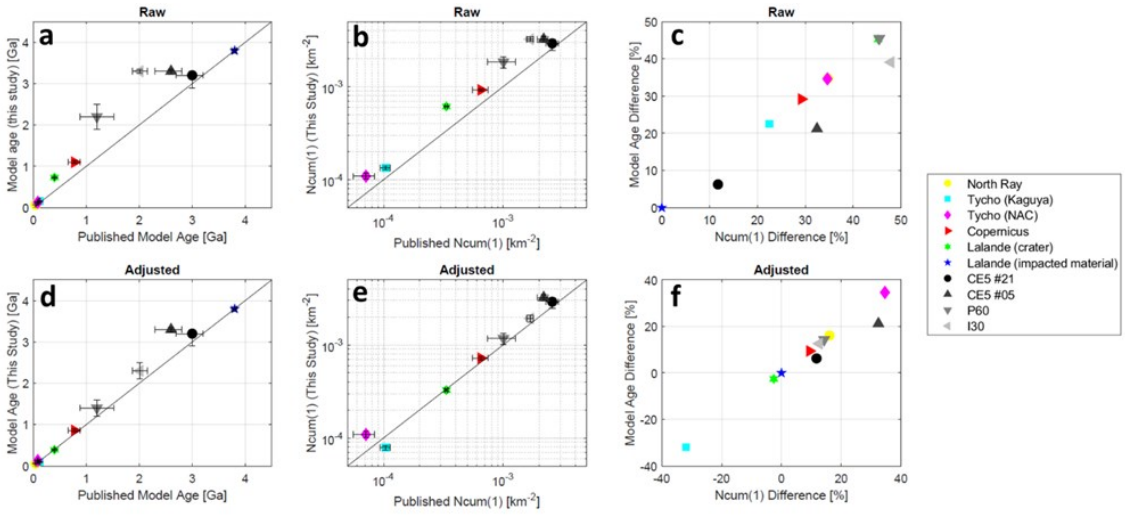

Figure 4.11: The comparison of results for the nine analysed count areas. (a) Raw model ages calculated in this study against the published model ages for each count area; (b) Raw N(1) densities from this study against the published N(1) densities for each count area; (c) The per cent differences between the Raw and published model ages and cratering densities for each count area; (d) Adjusted model ages calculated in this study against the published model ages for each count area; and (e) Adjusted N(1) densities from this study against the published N(1) densities for each count area. (f) The percentage differences between the adjusted and published model ages and N(1) densities for each count area. The diagonal black lines in panels a, b, d, and e show the linear relationship between this study and the published data (i.e., the closer the data plots are to the line, the more similar they are).

4.4 Discussion

4.4.1 The CDAs Performance in Model Age Derivations

The CDA performed adequately, as shown by the validation metrics (Recall, Precision and F1 values) in the presented evaluations (see Appendix 4.4, Table S4.2) and efficiently detected craters across all the studied sites (Figure 4.2). While only looking at the raw detection data across all the studied count areas, there was a regular overestimation in the N(1) values and model ages compared to the published values. This overestimation ranged from 10% to 45% (Figure 4.11.c). As stated above, the evaluation of the detection model trained on Kaguya TC images shows similar performance to human mapping (diameter estimation (see Appendix 4.3, Figure S4.2), Recall, and Precision (see Appendix 4.4, Table S4.1). The increased model age and crater density can be attributed to secondary crater clusters and pre-existing craters included within the raw count dataset for the CSFDs. These raw CSFD results emphasize that it is up to the researcher to decide which counted craters represent the geological surface they wish to date and not blindly rely on automated crater detections. We argue that for automated crater datasets to be appropriately used for crater counting, the researcher must undertake a process of due diligence and geologic reasoning before using the results. We examined and adjusted the count areas and crater dataset in this analysis.

Adjusting the crater datasets for each site (i.e., secondary and pre-existing craters removal and reduction of the count areas) results in younger model ages and CSFDs more comparable with manual counts (Figure 4.11.f). The semi-automatic removal of pre-existing craters is not perfect. Flagged craters can also be made up of young, degraded craters. However, as the studied craters are semi-fresh due to Lalande's young age, the likelihood of such craters being flagged is low. Overall, the N(1) values and the subsequent ages for 6 out of the 9 count areas range from -3% to +18%, with some outliers (Figure 4.11.f). It is reasonable to attribute a systematic difference to an automated technique. However, this could also reflect researcher crater detection variability (Robbins et al., 2014) or the differences between image datasets (Giguere et al., 2022). We argue that the reduction in model ages could be attributed to the reduction of the count areas, which can introduce a non-random pattern in the cratering record.

This could lead to the exclusion of larger primary craters surviving obliteration processes (Warner et al., 2015). Moreover, the reduction could also reflect the successful removal of secondary crater clusters, lowering the relative N(1) values.

However, the small differences (<20%) between the adjusted and published model ages for 6 out of the 9 count areas (Figure 4.11.f) reflect an acceptable reproducibility of the manual crater count findings. The discrepancies regarding the Tycho areas (WAC TE and NAC TE) and the Chang'E-5 #05 will be discussed in the following subsection, where we look at possible reasons for the differences.

4.4.1.a The Tycho Crater Ages

The results obtained on the adjusted Tycho WAC count area on the Kaguya TC image tiles (Figure 4.6.e) were significantly different compared to the values reported by Hiesinger et al. (2012) and the other values reported within this study. The WAC TE count area was the only site that displayed an underestimation in the cratering density and model age values (Figure 4.11.f). An underestimation would reflect that our CDA significantly did not detect as many craters compared to the base study, but we argue this was not an error. For the Tycho crater dataset, no craters within the count area were flagged as 'pre-existing'; therefore, no degraded craters were outright removed. Therefore, the observed underestimation of crater density could be attributed to the inclusion of additional, or interpreted (see Figure S3), craters by Hiesinger et al. (2012) in their dataset or the removal of additional secondary crater clusters that Hiesinger et al. (2012) did not identify. We argue that it may have been portions of both. The base study reported craters down to ~100 m in diameter and derived an age using an isochron fitted between ~150m and 1km. This fit range is substantially below the 10-pixel accuracy/reliability cut-off now recommended for crater counting (Robbins et al., 2014; Wang et al., 2020). Therefore, the crater dataset can include other circular structures, such as large boulders (100m – 200m), which are very difficult to resolve at the WAC resolution scale (100 m/px) (see Appendix 4.3, Figure S4.4). This will lead to overestimating the base crater density and, thus, to the lower crater density we measured.

Conversely, the CSFD we extracted on the adjusted NAC Tycho TE count areas led to overestimating the crater density and model age by the highest amount at +30% (Figure 4.11.f). Based on a check of the CDA performance and a visual inspection of the craters detected in these areas, this discrepancy likely originates from a difference in identifying primary and secondary craters between our study and Hiesinger et al. (2012)'s mapping.

Furthermore, the defined NAC count areas have complex lighting conditions across the count areas (see Appendix 4.3, Figure S4.5), where crater identification can significantly differ between those NAC count areas, leading to fewer (or more) identified craters (Giguere et al., 2022). Additionally, we excluded a count area (NAC TE3) due to its location on the crater rim slope with less non-ideal lighting conditions (incidence angle of ~42°). This will affect the model age, but we could not reconstruct the published NAC TE CSFDs, as there is no supplied list of Hiesinger et al. (2012)'s crater datasets. Therefore, it is impossible to reconstruct all the counts to determine regions where the crater counting was significantly different or if potential mapping variability or errors were made (on both sides).

Following this notion, both values (published and CDA) for the Tycho count areas are realistic when placed in the scope of other crater count analyses (though conducted on different geographical areas with different production functions using different methods). For example, using lunar impact ejecta thermophysical characteristics, Mazrouei et al. (2019) report a significantly different model age of 85 Ma. Whereas using crater counts on the proximal ejecta blanket with the Neukum (1984) functions, Terada et al. (2020) derived a model age of 58 Ma. Placing all values in the scope of other studies, the result of our semi-automatic model age derivation technique falls within a realistic range of reported values for the formation age of Tycho crater.

4.4.1.b The Chang'E-5 Site Ages

The count areas, Chang'E-5 #21 and #05, which were not adjusted in this study, show a model age overestimation that ranges from 10% to ~20% (Figure 11.c), respectively. The crater density N(1) of area #21 is well within what the manual crater identification variability between experts could lead at this mapping scale on mare areas (± ~20%, Robbins et al., 2014).

In contrast, area #05 had the second greatest N(1) difference observed at +32%. We also note that our derived N(1) values for these sites, distant only of ~15 km between each other, were very similar (area #21, 2.91×10^{-3} km^{-2}; area #05, 3.23×10^{-3} km^{-2}), whereas Giguere et al. (2022)'s crater densities differ by ~17%. The crater density we report is almost twice as high as those measured in previous studies aiming to extract the CSFD around the Chang'E-5 landing site (area #21), mainly for the lunar chronology recalibration (Jia et al., 2020; Wu et al., 2018; Qian et al., 2021). Although this is out of the scope of this study, the variability in crater densities measured in this area will be worth investigating in future studies. Mare site #05 was further investigated, and a significant difference in total craters counted was found between Giguere et al. (2022) and our CDA (Figure 12). Most count differences were restricted to craters between 200 m and 400 m, where the CDA detected over twice as many craters (Appendix 4.4, Table S4.3), of which most were moderately degraded. Giguere et al. (2022) discussed the influence of lighting conditions and image quality on the resulting crater measurements and argued that this ingrains inconsistencies between researchers. Where Giguere et al. (2022) used a series of NAC images with different lighting conditions, we used a single Kaguya TC tile with consistent lighting across the area. It is most likely that this effect resulted in the different crater rim measurements and crater identification.

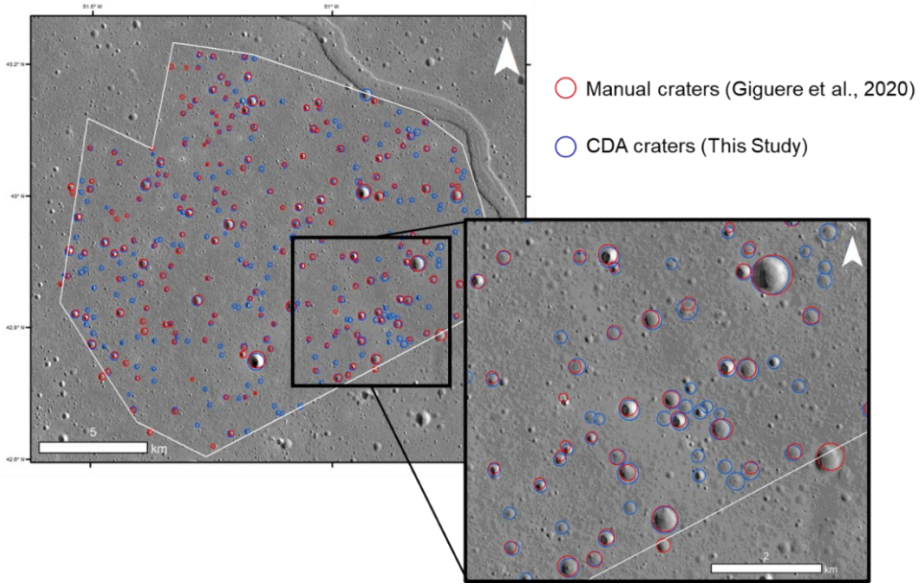

Figure 4.12: Total crater counts ≥200 m in diameter over Giguere et al. (2022)'s Chang'E-5 #05 count area. The white polygon denotes the #05 count area boundary, the red circles represent 178 craters measured by Giguere et al. (2022), and the blue circles represent the 314 craters detected by the CDA (Appendix 4.4., Table S4.3).

4.5 Conclusion

This study compares and assesses the viability of using model ages and crater densities derived from an automatic detection method using a Crater Detection Algorithm (CDA). We compare our values to current published manual counts for nine different lunar crater count areas distributed over the lunar near-side. The results show that using a CDA trained on Lunar Reconnaissance Orbiter - Narrow Angle Camera (LRO-NAC) and Kaguya Terrain Camera (Kaguya TC) images is a viable and timely approach for detecting small craters on young lunar surfaces. The study results show that using a CDA can be an effective tool in deriving model ages and crater densities with an acceptable level of reproducibility concurrent with human mapping with respect to manual crater count variability, estimated to be as high as 30% (Robbins et al., 2014). When unadjusted, the results of the CDA can lead to an overestimation of crater density by up to ~50%. However, with sufficient semi-automated processing to adjust the population and the removal of regions with secondary clusters or pre-existing craters, the derived model ages and crater densities were consistent with their published values. However, the derived model ages and crater densities significantly differed from the published values for two areas, Tycho's ejecta and the Chang'E-5 #05 area. After careful examination, the differences were determined primarily due to the differences in image quality, resolution, and researcher variability, which led to inconsistent crater identification. In this respect, this study demonstrates the potential for a CDA to analyse numerous lunar sites to derive model ages on a global scale. This use, however, must be in addition to carefully checking the detections and semi-automatic approaches to remove potential secondary and underlying crater contamination, along with careful geological mapping and interpretations. The CDA could be used to provide valuable information on the recent events that shaped the surface of the Moon and can lead to a better understanding of its recent geological history.

Data Availability Statement

The supporting material is all available in an online repository (https://doi.org/10.5281/zenodo.8045606). The code required to reproduce our algorithm is on the Yolov5-ultralytics GitHub (https://github.com/ultralytics/yolov5). The CraterStats II Software can be downloaded Freie Universität Berlin software portal (https://www.geo.fu-berlin.de/en/geol/fachrichtungen/planet/software/_content/software/craterstats.html). The CSFDs for each count area are available in Supplemental Dataset S3. The Lunar Reconnaissance Orbiter Narrow-Angle Camera (LRO-NAC) images were downloaded from the LROC website (http://wms.lroc.asu.edu/lroc/search). The Isbell et al. (2014) Kaguya TC tiles (both morning and evening) are available at the Kaguya Data Archive (https://darts.isas.jaxa.jp/planet/pdap/selene/).

Acknowledgements

We thank the three reviewers for their contribution during the review phase of this work. This work was supported by the resources provided by the Pawsey Supercomputing Centre with funding from the Australian Government, The Commonwealth Scientific and Industrial Research Organization, the Australian Space Data Analysis Facility, Curtin University, and the Government of Western Australia. This research is funded by the Australia Research Council (DP210100336, DP170102972, and FT170100024) and Curtin University. We are thankful to the LROC, SELENE/Kaguya and NASA PDS teams for their work in making the image datasets freely available for use and download. This research has used the USGS Integrated Software for Imagers and Spectrometers (ISIS).

4.6 References

Ali-Dib, M., Menou, K., Jackson, A. P., Zhu, C., & Hammond, N. (2020). Automated crater shape retrieval using weakly-supervised deep learning. Icarus, 345, 113749. https://doi.org/10.1016/j.icarus.2020.113749

Baldwin, R. B. (1964). Lunar crater counts. The Astronomical Journal, 69, 377. https://doi.org/10.1086/109289

Benedix, G. K., Lagain, A., Chai, K., Meka, S., Anderson, S., Norman, C., et al. (2020). Deriving surface ages on Mars using automated crater counting. Earth and Space Science, 7(3). https://doi.org/10.1029/2019EA001005

Bogard, D. D., Garrison, D. H., McKay, D. S., & Wentworth, S. J. (1992). The age of Copernicus: New evidence for 800+15 million years. 23, 133.

Cadogan, P. H. (2020). Automated precision counting of very small craters at lunar landing sites. Icarus, 348, 113822. https://doi.org/10.1016/j. icarus.2020.113822

Che, X., Nemchin, A., Liu, D., Long, T., Wang, C., Norman, M. D., et al. (2021). Age and composition of young basalts on the Moon, measured from samples returned by Chang'E-5. Science, 374(6569), 887–890. https://doi.org/10.1126/science.abl7957

Craddock, R. A., & Howard, A. D. (2000). Simulated degradation of lunar impact craters and a new method for age dating farside mare deposits. Journal of Geophysical Research, 105(E8), 20387–20401. https://doi.org/10.1029/1999JE001099

Crater analysis techniques working group. (1979). Standard techniques for presentation and analysis of crater size-frequency data. Icarus, 37(2), 467–474. https://doi.org/10.1016/0019-1035(79)90009-5

DeLatte, D. M., Crites, S. T., Guttenberg, N., & Yairi, T. (2019). Automated crater detection algorithms from a machine learning perspective in the convolutional neural network era. Advances in Space Research, 64(8), 1615–1628. https://doi.org/10.1016/j.asr.2019.07.017

Drozd, R. J., Hohenberg, C. M., Morgan, C. J., Podosek, F. A., & Wroge, M. L. (1977). Cosmic ray exposure history at Taurus-Littrow (Vol. 8, p. 254).

Drozd, R. J., Hohenberg, C. M., Morgan, C. J., & Ralston, C. E. (1974). Cosmic-ray exposure history at the Apollo 16 and other lunar sites: Lunar surface dynamics. Geochimica et Cosmochimica Acta, 38(10), 1625–1642. https://doi.org/10.1016/0016-7037(74)90178-1

Dundas, C. M., & McEwen, A. S. (2007). Rays and secondary craters of Tycho. Icarus, 186(1), 31–40. https://doi.org/10.1016/j.icarus.2006.08.011

Fairweather, J. H., Lagain, A., Servis, K., Benedix, G. K., Kumar, S. S., & Bland, P. A. (2022). Automatic mapping of small lunar impact craters using LRO-NAC images. Earth and Space Science, 9(7). https://doi.org/10.1029/2021EA002177

Fassett, C. I. (2016). Analysis of impact crater populations and the geochronology of planetary surfaces in the inner solar system: Crater Populations and Surface Chronology. Journal of Geophysical Research: Planets, 121(10), 1900–1926. https://doi.org/10.1002/2016JE005094

Fassett, C. I., & Thomson, B. J. (2014). Crater degradation on the lunar Maria: Topographic diffusion and the rate of erosion on the Moon: Crater degradation on the lunar Maria. Journal of Geophysical Research: Planets, 119(10), 2255–2271. https://doi.org/10.1002/2014JE004698

Fortezzo, C. M., Spudis, P. D., & Harrel, S. L. (2020). Release of the digital unified global geologic map of the Moon at 1:5,000,000-scale. 2760.

Giguere, T. A., Boyce, J. M., Gillis-Davis, J. J., Trang, D., & Stopar, J. D. (2022). Lava flow ages in northeastern Oceanus Procellarum: The need for calibrating crater counting procedures. Icarus, 375, 114838. https://doi.org/10.1016/j.icarus.2021.114838

Haruyama, J., Ohtake, M., Matsunaga, T., Morota, T., Yokota, Y., Honda, C., et al. (2008). Planned radiometrically calibrated and geometrically corrected products of lunar high-resolution Terrain Camera on SELENE. Advances in Space Research, 42(2), 310–316. https://doi. org/10.1016/j.asr.2007.04.062

Hiesinger, H. (2003). Ages and stratigraphy of mare basalts in Oceanus Procellarum, mare Nubium, mare Cognitum, and mare Insularum. Journal of Geophysical Research, 108(E7), 5065. https://doi.org/10.1029/2002JE001985

Hiesinger, H., Head, J. W., Wolf, U., Jaumann, R., & Neukum, G. (2011). Ages and stratigraphy of lunar mare basalts: A synthesis. In W. A. Ambrose & D. A. Williams (Eds.), Recent advances and current research issues in lunar stratigraphy. Geological Society of America. https:// doi.org/10.1130/2011.2477(01

Hiesinger, H., Jaumann, R., Neukum, G., & Head, J. W. (2000). Ages of mare basalts on the lunar nearside. Journal of Geophysical Research, 105(E12), 29239–29275. https://doi.org/10.1029/2000JE001244

Hiesinger, H., van der Bogert, C. H., Pasckert, J. H., Funcke, L., Giacomini, L., Ostrach, L. R., & Robinson, M. S. (2012). How old are young lunar craters? Journal of Geophysical Research, 117(E12), E00H10. https://doi.org/10.1029/2011JE003935

Hildebrand, A. R., Pilkington, M., Ortiz-Aleman, C., Chavez, R. E., Urrutia-Fucugauchi, J., Connors, M., et al. (1998). Mapping Chicxulub crater structure with gravity and seismic reflection data. Geological Society, London, Special Publications, 140(1), 155–176. https://doi.org/10.1144/ GSL.SP.1998.140.01.12

Isbell, C., Gaddis, L., Garcia, P., Hare, T., & Bailen, M. (2014). Kaguya terrain camera mosaics. #2268.

Jia, M., Yue, Z., Di, K., Liu, B., Liu, J., & Michael, G. (2020). A catalogue of impact craters larger than 200 m and surface age analysis in the Chang'E-5 landing area. Earth and Planetary Science Letters, 541, 116272. https://doi.org/10.1016/j.epsl.2020.116272

Jocher, G. (2022). Ultralytics YOLOv5. (Python). GitHub. Retrieved from https://github.com/ultralytics/yolov5

Kirchoff, M. R., Marchi, S., Bottke, W. F., Chapman, C. R., & Enke, B. (2021). Suggestion that recent (≤3 Ga) flux of kilometer and larger impactors in the Earth-Moon system has not been constant. Icarus, 355, 114110. https://doi.org/10.1016/j.icarus.2020.114110

Lagain, A., Benedix, G. K., Servis, K., Baratoux, D., Doucet, L. S., Rajšic, A., et al. (2021). The Tharsis mantle source of depleted shergottites revealed by 90 million impact craters. Nature Communications, 12(1), 6352. https://doi.org/10.1038/s41467-021-26648-3

Lagain, A., Bouley, S., Baratoux, D., Costard, F., & Wieczorek, M. (2020). Impact cratering rate consistency test from ages of layered ejecta on Mars. Planetary and Space Science, 180, 104755. https://doi.org/10.1016/j.pss.2019.104755

Lagain, A., Bouley, S., Zanda, B., Miljković, K., Rajšić, A., Baratoux, D., et al. (2022). Early crustal processes revealed by the ejection site of the oldest Martian meteorite. Nature Communications, 13(1), 3782. https://doi.org/10.1038/s41467-022-31444-8

Lagain, A., Kreslavsky, M. A., Baratoux, D., Liu, Y., Devillepoix, H. A. R., Bland, P. A., et al. (2022). Has the impact flux of small and large asteroids varied through time on Mars, the Earth and the Moon? Earth and Planetary Science Letters, 579, 117362. https://doi.org/10.1016/j.epsl.2021.117362

Lagain, A., Servis, K., Benedix, G. K., Norman, C., Anderson, S., & Bland, P. A. (2021). Model age derivation of large Martian impact craters, using automatic crater counting methods. Earth and Space Science, 8(2). https://doi.org/10.1029/2020EA001598

Li, H.-C., Zhang, N., Yue, Z.-Y., & Zhang, Y.-Z. (2021). Lunar cratering asymmetries with high lunar orbital obliquity and inclination of the Moon. Research in Astronomy and Astrophysics, 21(6), 140. https://doi.org/10.1088/1674-4527/21/6/140

Mazrouei, S., Ghent, R. R., Bottke, W. F., Parker, A. H., & Gernon, T. M. (2019). Earth and Moon impact flux increased at the end of the Paleozoic. Science, 363(6424), 253–257. https://doi.org/10.1126/science.aar4058

Melosh, H. J. (1989). Impact cratering: A geologic process. Oxford University Press. Retrieved from https://books.google.com.au/books?id=nZwRAQAAIAAJ

Michael, G. G., & Neukum, G. (2010). Planetary surface dating from crater size–frequency distribution measurements: Partial resurfacing events and statistical age uncertainty. Earth and Planetary Science Letters, 294(3–4), 223–229. https://doi.org/10.1016/j.epsl.2009.12.041

Neukum, G. (1984). Meteoritenbombardement und Datierung planetarer Oberflachen (Meteorite bombardment and dating of planetary surfaces). University of Munich.

Neukum, G., Ivanov, B. A., & Hartmann, W. K. (2001). Cratering records in the inner solar system in relation to the lunar reference system. In R. Kallenbach, J. Geiss, & W. K. Hartmann (Eds.), Chronology and evolution of Mars (Vol. 12, pp. 55–86). Springer Netherlands. https://doi.org/10.1007/978-94-017-1035-0_3

Öpik, E. J. (1960). The lunar surface as an impact counter. Monthly Notices of the Royal Astronomical Society, 120(5), 404–411. https://doi.org/10.1093/mnras/120.5.404

Pawsey (2023). Pawsey supercomputing centre. Retrieved from https://pawsey.org.au/

Pike, R. J. (1974). Ejecta from large craters on the Moon: Comments on the geometric model of McGetchin et al. Earth and Planetary Science Letters, 23(3), 265–271. https://doi.org/10.1016/0012-821X(74)90114-9

Pozzobon, R., Tusberti, F., Pajola, M., & Massironi, M. (2020). Geologic map, landing site selection and Traverse planning in Copernicus crater. https://doi.org/10.5281/ZENODO.5127777

Qian, Y., Xiao, L., Head, J. W., van der Bogert, C. H., Hiesinger, H., & Wilson, L. (2021). Young lunar mare basalts in the Chang'E-5 sample return region, northern Oceanus Procellarum. Earth and Planetary Science Letters, 555, 116702. https://doi.org/10.1016/j.epsl.2020.116702

Redmon, J., Vivvala, S., Girshick, R., & Farhadi, A. (2016). You only look once: Unified, real-time object detection. Proceedings of the IEEE Conference on Computer Vision and Pattern Recognition (CVPR), 779–788.

Robbins, S. J. (2014). New crater calibrations for the lunar crater-age chronology. Earth and Planetary Science Letters, 403, 188–198. https:// doi.org/10.1016/j.epsl.2014.06.038

Robbins, S. J., Antonenko, I., Kirchoff, M. R., Chapman, C. R., Fassett, C. I., Herrick, R. R., et al. (2014). The variability of crater identification among expert and community crater analysts. Icarus, 234, 109–131. https://doi.org/10.1016/j.icarus.2014.02.022

Robinson, M. S., Brylow, S. M., Tschimmel, M., Humm, D., Lawrence, S. J., Thomas, P. C., et al. (2010). Lunar reconnaissance orbiter camera(LROC) instrument overview. Space Science Reviews, 150(1–4), 81–124. https://doi.org/10.1007/s11214-010-9634-2

Salamunićcar, G., Lončarić, S., Grumpe, A., & Wöhler, C. (2014). Hybrid method for crater detection based on topography reconstruction from optical images and the new LU78287GT catalogue of lunar impact craters. Advances in Space Research, 53(12), 1783–1797. https://doi. org/10.1016/j.asr.2013.06.024

Sawabe, Y., Matsunaga, T., & Rokugawa, S. (2006). Automated detection and classification of lunar craters using multiple approaches. Advances in Space Research, 37(1), 21–27. https://doi.org/10.1016/j.asr.2005.08.022

Schmitt, H. H., Petro, N. E., Wells, R. A., Robinson, M. S., Weiss, B. P., & Mercer, C. M. (2017). Revisiting the field geology of Taurus–Littrow. Icarus, 298, 2–33. https://doi.org/10.1016/j.icarus.2016.11.042

Sharpton, V. L. (2014). Outcrops on lunar crater rims: Implications for rim construction mechanisms, ejecta volumes and excavation depths: Outcrops constrain crater rim components. Journal of Geophysical Research: Planets, 119(1), 154–168. https://doi.org/10.1002/2013JE004523

Shoemaker, E. M., & Hackman, R. J. (1962). Stratigraphic basis for a lunar time scale. The Moon, 14, 289–300. https://doi.org/10.1017/ s007418090017826x

Speyerer, E. J., Robinson, M. S., & Denevi, B. W., & LROC Science Team. (2011). Lunar reconnaissance orbiter camera global morphological map of the Moon. #2387.Update the acknowledgements with.

Stopar, J. D., Robinson, M. S., Barnouin, O. S., McEwen, A. S., Speyerer, E. J., Henriksen, M. R., & Sutton, S. S. (2017). Relative depths of simple craters and the nature of the lunar regolith. Icarus, 298, 34–48. https://doi.org/10.1016/j.icarus.2017.05.022

Terada, K., Morota, T., & Kato, M. (2020). Asteroid shower on the Earth-Moon system immediately before the Cryogenian period revealed by KAGUYA. Nature Communications, 11(1), 3453. https://doi.org/10.1038/s41467-020-17115-6

Trask, N. J. (1966). Size and spatial distribution of craters estimated from the Ranger photographs. Retrieved from https://ntrs.nasa.gov/ citations/19660015760

Wang, Y., Xie, M., Xiao, Z., & Cui, J. (2020). The minimum confidence limit for diameters in crater counts. Icarus, 341, 113645. https://doi. org/10.1016/j.icarus.2020.113645

Wang, Y., Zhu, X., & Wu, B. (2019). Automatic detection of individual oil palm trees from UAV images using HOG features and an SVM classifier. International Journal of Remote Sensing, 40(19), 7356–7370. https://doi.org/10.1080/01431161.2018.1513669

Warner, N. H., Gupta, S., Calef, F., Grindrod, P., Boll, N., & Goddard, K. (2015). Minimum effective area for high resolution crater counting of Martian terrains. Icarus, 245, 198–240. https://doi.org/10.1016/j.icarus.2014.09.024

Wilhelms, D. E. (1987). The geologic history of the Moon (USGS numbered series No. 1348; professional paper, p. 337). United States Geological Survey. https://doi.org/10.3133/pp1348

Wu, B., Huang, J., Li, Y., Wang, Y., & Peng, J. (2018). Rock abundance and crater density in the candidate Chang'E-5 landing region on the Moon. Journal of Geophysical Research: Planets, 123(12), 3256–3272. https://doi.org/10.1029/2018JE005820

Xiao, Z., & Strom, R. G. (2012). Problems determining relative and absolute ages using the small crater population. Icarus, 220(1), 254–267. https://doi.org/10.1016/j.icarus.2012.05.012

Xiao, Z., & Werner, S. C. (2015). Size-frequency distribution of crater populations in equilibrium on the Moon. Journal of Geophysical Research: Planets, 120(12), 2277–2292. https://doi.org/10.1002/2015JE004860

Xie, M., & Xiao, Z. (2023). A new chronology from debiased crater densities: Implications for the origin and evolution of lunar impactors. Earth and Planetary Science Letters, 602, 117963. https://doi.org/10.1016/j.epsl.2022.117963

Xie, M., & Zhu, M.-H. (2016). Estimates of primary ejecta and local material for the Orientale basin: Implications for the formation and ballistic sedimentation of multi-ring basins. Earth and Planetary Science Letters, 440, 71–80. https://doi.org/10.1016/j.epsl.2016.02.0122

Xu, L., Qiao, L., Xie, M., & Wu, Y. (2022). Formation age of lunar Lalande crater and its implications for the source region of the KREEP-rich meteorite Sayh al Uhaymir 169. Icarus, 386, 115166. https://doi.org/10.1016/j.icarus.2022.115166

Xu, L., & Xie, M. (2020). Ejecta thickness distribution of the Schrödinger basin on the Moon. Journal of Geophysical Research: Planets, 125(12), e2020JE006506. https://doi.org/10.1029/2020JE006506

Yang, C., Zhao, H., Bruzzone, L., Benediktsson, J. A., Liang, Y., Liu, B., et al. (2020). Lunar impact crater identification and age estimation with Chang'E data by deep and transfer learning. Nature Communications, 11(1), 6358. https://doi.org/10.1038/s41467-020-20215-y

Zanetti, M., Stadermann, A., Jolliff, B., Hiesinger, H., Van Der Bogert, C. H., & Plescia, J. (2017). Evidence for self-secondary cratering of Copernican-age continuous ejecta deposits on the Moon. Icarus, 298, 64–77. https://doi.org/10.1016/j.icarus.2017.01.030

Chapter 5: Recent Change in The Impact Flux on The Moon Revealed by Automatic Model Ages

Abstract

Dating young lunar surfaces, such as impact ejecta blankets and terrains associated with recent volcanic activities, provides critical information on the recent events that shaped the surface of the Moon. Model age derivation of young or small areas using The crater production of the inner Solar System is assumed to be approximately constant over the last ~3 Ga. This assumption is a consequence of the relationship between the radiometric ages of lunar samples and the crater density of the terrains where they have been collected. Nevertheless, previous studies have hypothesised that the impact flux of small (meters to hundreds of meters) and/or large (kilometric) impactors may have experienced surges on the Moon, the Earth and Mars, translating into temporal variations in the production rate of impact craters on terrestrial bodies. Here, we derive model ages of 211 lunar craters >20km formed >3.2 Ga ago using an automatic crater detection technique, thus allowing us to compare the constant rate of small craters used to date the formation of the larger ones. The analysis of the model age distribution of the crater population ranging from 20 to 40 km shows a significant deviation from a constant production rate for this size range. Considering the possible mechanisms that could explain such variations (asteroid breakups, collisional cascades and thermal forces), this result indicates that the impact flux of 2-4 km impactors significantly varied since 3 Ga, while that of 10-100m impactors remained relatively constant. This result has implications for the Earth-Moon system, particularly regional and global changes. The timing of potential source asteroid populations is discussed, and further analysis using independent methods is needed (e.g., impact crater radiometric dating from lunar samples).

5.1 Introduction

Analysis of an impact crater density on a planetary surface is a widely used indicator of the age of geological events and the duration of surface processes. The crater production (or accumulation) rate, which has been calibrated to the radiometric ages of lunar samples, is used to assign an absolute model age to any cratered surface (Neukum, 1984; Neukum et al., 2001; Stöffler and Ryder, 2001; Fassett, 2016 and references therein). This technique has been successfully developed for the Moon and used to understand various geological surfaces, ranging from lava flows to impact ejecta blankets (Fassett, 2016). For example, inferences about the change in crater production and longevity of various geological activities were predicted by crater chronologies and later verified through radiometric measurements, such as the age distribution of the Lunar Maria and the period of heavy bombardment (Bottke and Norman, 2017; Heiken et al., 1991; Hiesinger et al., 2011; Fassett, 2016).

Analyses looking at the relationship between the cratering density and the ages of some lunar samples have assumed that the crater production within the inner solar system has remained relatively constant for the past 3 billion years [within a factor of ~2] (see Bottke et al., 2015; Hartmann, 1977; Marchi et al., 2009; Morbidelli et al., 2018; Neukum et al., 2001; Neukum and Ivanov, 1994; Stöffler et al., 2006). However, this assumption is likely due to the lack of direct sampling of units younger than ~3 Ga (Stöffler and Ryder, 2001), which significantly limits the evolution of crater production over this time range.

Various studies have investigated potential temporal fluctuations in the crater production rate over the last ~3 Ga using the age distributions of significant impact events (e.g., Kirchoff et al., 2021; Lagain et al., 2020; 2022; Mazrouei et al., 2019; Terada et al., 2020; Hartmann et al., 2007; Quantin et al., 2007). Significant fluctuation in the production could be described as a relative increase, decrease, or a longer-term change in the overall crater density – such as a slow overall decline as proposed by Hartmann et al. (2007) and Quantin et al. (2007). Specifically in the more current literature, Terada et al. (2020) and Kirchoff et al. (2021) used crater count data on the ejecta blankets and crater floors of lunar craters > 20 km and > 50 km, respectively. Based on their age distributions of large craters, both studies differ

in their conclusion; the former concluded an increase in the cratering rate 800 Ma ago, while the latter inferred a cratering spike 2 Ga ago followed by a period of lull 1 Ga ago. In contrast, Mazrouei et al. (2019) utilised a rock abundance model on the ejecta blankets (see Bandfield et al., 2011; Ghent et al., 2014) to determine model ages of lunar craters > 10 km and inferred that the impact flux experienced an increase by a factor of ~2.6 over the last 300 Ma. Though, Hergarten et al. (2019) has shown that the rock abundance method for model age derivation (see Ghent et al., 2014) might be poorly calibrated, leading to an artefact in the crater age distribution. In similar analyses, Lagain et al. (2020) and Lagain et al. (2022) focused on the Martian cratering record by analysing the model ages of km-sized craters. The first study suggested a decoupling between the formation rates of small and large impactors based on the analysis of 53 model ages. In comparison, the second study did not show any significant changes in the formation rates over the last ~600 Ma (based on 49 crater model ages). All these results, summarised in Table 5.1, considerably vary to a point where it is difficult to draw clear conclusions regarding the variability within the crater production rates for the inner solar system.

Table 5.1: Summary of studies exploring potential variations of the impact of flux.

Published study	Body	Method	Sample size	Time Range	Resolution	Diameter range	Conclusions
Terada et al. (2020)	Moon	Manual crater count on ejecta layer	59 Craters	<3 Ga	~20 / Ga	>20 km	800 Ma spike for km-sized impactors
Kirchoff et al. (2021)	Moon	Manual crater count on crater floor	43 Craters	<3.2 Ga	~13.5 / Ga	>50 km	2 Ga spike and 1 Ga lull for km-sized impactors
Mazrouei et al., 2019	Moon	Rock abundance measurement in large crater ejecta	111 Craters	<1 Ga	111 / Ga	>10km	Increase by a factor of 2-3 in the last 300 Ma for km-sized impactors
Lagain et al., 2020	Mars	Manual crater count on ejecta layer	53 Craters	<2.2 Ga	~ 24 / Ga	>5 km	Decoupling between sub-km and km-sized impactors in the last ~2.5 Ga
Lagain et al., 2022	Mars	Automatic crater count on ejecta layer	49 craters (521 in total, including incomplete crater population >600 Ma)	<600 Ma	~ 82 / Ga	>20 km	No significant decoupling between sub-km and km-sized impactors in the last ~600 Ma
Quantin et al., 2007	Mars	Manual crater count on landslides	26 landslides (56 in total, including those with poor model age determination)	<3 Ga	~ 9 / Ga	100 m	Long-term decline by a factor of ~3 since 3 Ga for 10s of meters impactors

This study investigates the hypothesis that the lunar crater production rate has been approximately constant for the last ~3 Ga. It primarily differs from previous published studies as we aim to significantly increase the statistical sample of dated craters on the Moon using the crater counting method, thus increasing the temporal resolution and the statistical significance of the results. To do this, we implement a Crater Detection Algorithm (CDA) (see Benedix et al., 2020; Fairweather et al., 2022, 2023; Lagain et al., 2021a,b; 2022) trained and applied on the Kaguya Terrain Camera (TC) image (Isbell et al. 2014) to detect impact craters superposed on the ejecta blankets of 211 impact craters larger than 20 km in diameter. We focus on Copernican (<1.1 Ga) and Eratosthenian (1.1 Ga to ~3.2 Ga) craters using the unified geologic map of the Moon by Fortezzo et al. (2020). Additionally, we compared this study's derived model ages to those inferred by Kirchoff et al. (2021) and Terada et al. (2020) for the same impact craters. We also investigate the crater age distribution using different chronology models. This global-scale analysis aims to provide additional data points to aid in refining the evolution of the crater production of the inner solar system.

5.2 Instrumentation and Methods

5.2.1 Global Datasets

In this study, we used four global datasets to identify, map, and infer the model age of large lunar impact craters. The following points below briefly describe their respective contribution to the present study.

1. The Lunar Reconnaissance Orbiter Wide-Angle Camera (LRO-WAC) mosaic (Speyerer et al., 2011) provides a complete view of the lunar surface at 100 m/px (Robinson et al., 2010). This dataset lets us reliably identify features such as melt ponds, regions dominated by sizeable rocky ejecta, and large secondary crater clusters. These should be discarded from count areas before inferring reliable model ages (Fairweather et al., 2023; Xu et al., 2022).
2. The USGS unified geologic map of the Moon at 1:5,000,000 (Fortezzo et al., 2020) provides a stratigraphic framework of lunar geological units. Wherein impact craters larger than 10 - 20 km, which exhibit morphological evidence of various degrees of freshness, are assigned to

different periods, including the Copernican and the Eratosthenian, spanning ~3.2 Ga (Wilhelms and Mc Cauley, 1971; Lucchitta, 1978; Wilhelms et al., 1979; Wilhelms and El-Baz, 1977; Stuart-Alexander, 1978; Scott et al., 1977; Wilhelms, 1987). These units are what is to be used to select the craters considered in this study.

3. The Clementine UV-VIS Warped Colour Ratio image mosaic at 200 m/px and the Clementine UV-VIS 750nm Global Mosaic at 118 m/px (Lucey et al., 2000; McEwen and Robinson, 1997; Lee et al., 2009) have been used to identify compositional changes between the crater ejecta and the underlying regolith units, thus aiding in mapping accurate ejecta boundaries of large craters.
4. The Kaguya Terrain Camera (TC) morning (east-west sunlight) and evening (west-east sunlight) mosaics, both composed of images captured at an incidence angle of ~60° offer a resolution of ~7.5 m/px with near-global coverage (Isbell et al., 2014; Haruyama et al., 2008). This data is used to detect small craters superposed on the ejecta blankets of large craters selected in this study via a machine learning algorithm detailed in section 5.2.3.

5.2.2 Crater Selection and Mapping

We confined the craters selected in this study to ± 60° latitude, which reduces the significant lighting variabilities observed at the polar latitudes (Mazarico et al., 2011). Such variability can influence the identification of small craters superposed on the ejecta blankets. This selection also reduces the chances of analysing a crater with no Kaguya TC coverage (Haruyama et al., 2008; Isbell et al., 2014). Within this area, all singular Copernican and Eratosthenian craters larger than 20 km were selected using the unified geologic map of the Moon by Fortezzo et al. (2020) and were filtered using the above criteria, which results in 211 impact craters ranging from 20.2 km to 132 km in diameter (Table 5.2 and Figure 5.1). The diameters and names for each crater were extracted using the Lunar Planetary Institute (LPI) lunar crater catalogue (see Losiak et al., 2009).

Table 5.2: The number of Copernican and Eratosthenian craters within each criteria group.

Lunar Geological Period [Wilhelms, 1987]	Number of craters (Fortezzo et al., 2020)	within ±60° latitude	≥ 20 km
Copernican [0-1.1 Ga]	221	204	67
Eratosthenian [1.1-3.2 Ga]	431	381	144
Total	652	585	**211**

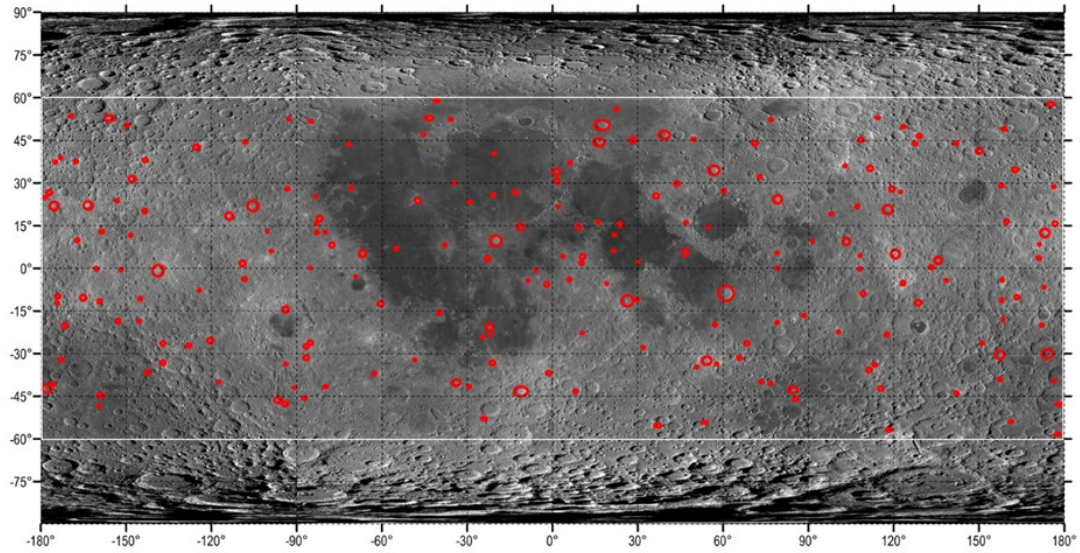

Figure 5.1: Location of impact craters selected in this study (red circles, n=211). The white outline denotes the ±60° latitude count area boundary. The base image shown here is the LRO-WAC Mosaic (Speyerer et al., 2011) in a simple cylindrical projection.

The count areas associated with the 211 craters were initially extracted from the digitised geologic map (i.e. the Copernican and Eratosthenian crater material). The areas were subsequently modified and reduced following the methodology outlined and tested in Fairweather et al. (2023). A brief description of this method is summarised below.

Each of the 211 count area shapefiles are modified using ESRI's ArcMap (version 10.7). This involved discarding unfavourable areas, specifically regions with post-impact melt (melt points), inconsistent lighting, cross-cutting secondary crater rays/clusters, and areas with no Kaguya TC data coverage. All this was achieved using the four global datasets introduced in section 5.2.1. Additionally, we discarded the crater floor and rim from the count areas by defining an inner boundary for each mapped crater unit at 1.3 radii from the crater centroid (see Figure 5.2.a). We then removed all visible/significant clusters of secondary craters contained within the remaining areas. Although tedious and subjective, this step is vital to derive an

accurate crater count model age of the impact event (Robbins & Hynek, 2014; Lagain et al., 2020). Therefore, we do not claim to have removed all secondary craters from the crater count areas. However, we only state that we discarded the most significant secondary crater chains/clusters. Each of the 211 large craters shown in Figure 5.1 is thus associated with one count area that displays appropriate lighting for acceptable and homogeneous performance for crater identification, simple topography, and minimal secondary craters/rays, all with full Kaguya TC image coverage. These are steps essential for accurate automatic crater detection and performance (Fairweather et al., 2023). All the crater area shapefiles are provided in Appendix 5.5.3.

5.2.3 The Crater Detection Algorithm

We used a Crater Detection Algorithm (CDA) to automatically count the small craters needed to measure crater model ages. This CDA is a Convolutional Neural Network-based object detection algorithm designed initially and trained to identify Martian impact craters on high-resolution image datasets at multiple scales (Benedix et al., 2020; Lagain et al., 2021, 2022). In previous works, we adapted the algorithm and retrained the network on LRO-NAC (Fairweather et al., 2022) and Kaguya TC images (Fairweather et al., 2023). The latter is used here, as it has successfully been shown to provide results on the lunar surface similar to published manually mapped crater counts (see Fairweather et al., 2023). Specifically, this model has an average Recall of 0.98, a Precision of 0.94, and an F1 score of 0.96 for craters > 100 m in diameter (with a diameter accuracy of ± 10%) (Fairweather et al., 2023). The algorithm was applied across the morning and the evening Kaguya TC tiles (3° by 3°) covering each crater count area (Figure 5.2.b.c). The tiles (either morning or evening) with the highest number of crater detections were kept and used for model age derivation. This decision is favourable, as some count areas might be in complete shadow in one tile (e.g., evening) but completely illuminated in another (e.g., morning). Therefore, the tile with the highest detections should reflect the tile with the most complete illumination.

5.2.4 Model Age Derivation

To derive a model age for each impact crater, we used a crater count dataset without 'pre-existing' craters (for this term, refer to Fairweather et al., 2023). This dataset was compiled using the methodology detailed in Fairweather et al. (2023) and Xu et al. (2022), which is summarised below. Small impact craters (typically in the 0.1 – 1 km diameter range) overprinted by the ejecta layer of a large crater pre-date the impact event and should be discarded from the crater count population. We model the ejecta thickness to determine if a buried pre-existing crater is identifiable at specific distances from the main impact. If an impact crater meets this requirement, it is discarded. The remaining crater detections are then processed in CraterStats II (Michael and Neukum, 2010), where a Crater-Size-Frequency-Distribution (CSFD) is generated in differential form (Figure 5.2.d) and fitted using a chronology model with the Poisson fitting method (Michael et al., 2016). All 211 CSFDs are provided in Appendix 5.5.4. As crater count model ages are entirely dependent on the chronology model used; therefore, we also calculated model ages using five other chronologies (see Appendices 5.5.1 and 5.5.5) developed by Robbins (2014), Hartmann et al. (2007), Marchi et al. (2009), Le Feuvre and Wieczorek (2011), and Lagain et al. (2024).

The distribution of the 211 crater model ages thus obtained can be analysed to investigate any changes in the impact flux of ~2 to ~30 km impactors (corresponding to the size range of dated large craters; see Collins et al., 2005) and ~10 to ~100m impactors (corresponding to the size range of small craters used to date, Collins et al., 2005).

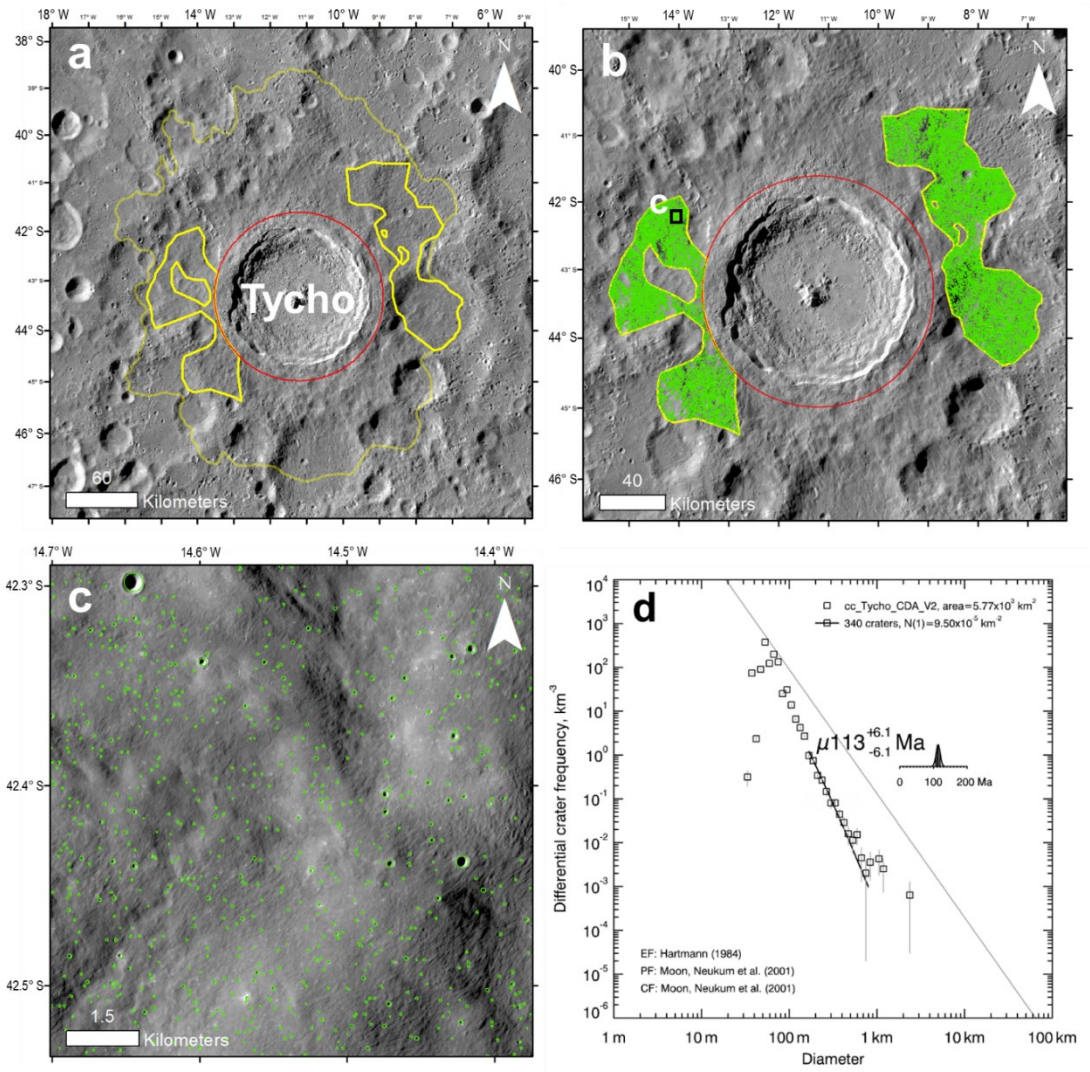

Figure 5.2: (a) The Tycho crater count area. The faded yellow outline is the crater unit taken from Fortezzo et al. (2020) 's geologic map of the Moon, while the solid yellow line defines the modified count area according to the criteria outlined in the main text. The red circle denotes the removed crater floor and rim (at a 1.3 crater radii). (b) Crater detections (n = 44,224) on Tycho's count area. (c) Close-up of the NW section of the Tycho count area depicting the detected craters (n = 602) on Kaguya TC tile TCO_MAPe04_S42E345S45E348SC (Isbell et al., 2014). (d) Crater size-frequency distribution obtained on Tycho's crater, with an isochron fitted using 340 craters with a size ranging between 170m to 750m.

5.3 Results

5.3.1 Crater Population Completeness

We derived model ages for 211 large lunar impact craters ranging between 20.2 km and 132 km in diameter. The oldest crater was Rydberg crater (48 km) with a model age of 3.58 ± 0.02 Ga, while the youngest was Giordano Bruno (22 km) with a model age of 33 ± 5 Ma. All crater age data is available in Appendices 5.5.2, 5.5.3 and 5.5.4. The analysis of the crater age distribution detailed in the following sub-sections presupposes that a complete crater population is captured over a given time range for any selected surface. To estimate the completeness of our crater population, we compare the size-frequency distribution of all craters younger than a given model age to the model age inferred from fitting the same crater-size distribution with a chronology model, an approach used in Lagain et al. (2021, 2022). When subdividing the dated impact crater dataset into model age groups, each should represent a complete crater distribution accumulated over a specific period if the obtained model age matches the age threshold of the analysed set of craters. Here, we present this analysis for seven age groups ranging from ≤ 500 Ma to ≥ 3.5 Ga in increasing 500 Ma intervals.

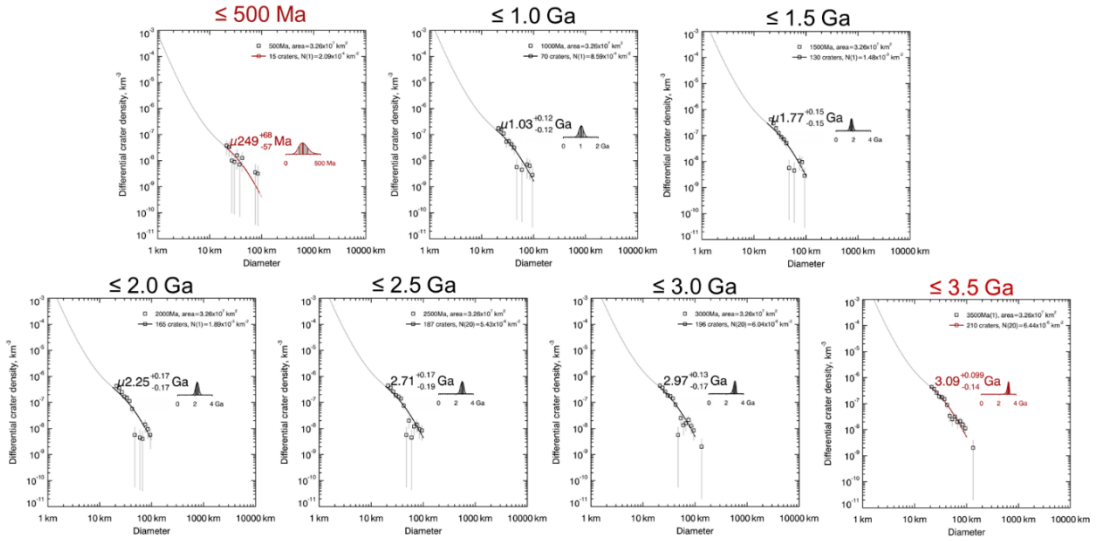

Figure 5.3: CSFDs of specific age groups. All isochrons were fitted using the Poisson fitting method using the Neukum et al. (2001) chronology system. The age groups with craters younger than 500 Ma and 3.5 Ga (denoted by a red CSFD) show a crater density about twice lower than the Neukum et al. (2001) chronology model predicts in the study area.

Figure 5.3 shows that the CSFDs of craters ≤ 500 Ma and ≤ 3.5 Ga produce a model age significantly lower than the model age expected from the Neukum et al. (2001) chronology. A lower model age would suggest a deficit of mapped craters across the last 3.5 Ga and 0.5 Ga in this study. However, the intermediate age groups show a consistent relationship between the observed and expected size-frequency of craters**.**

The deficit of craters older than 3 Ga is most likely due to a lack of identified impact craters, primarily due to their diminished morphological characteristics denoting their freshness. Whereas the lack of young craters cannot be attributed to the same selection bias, as young craters are expected to be the most easily identifiable crater population on the Moon's surface (Wilhelms and Mc Cauley, 1971; Lucchitta, 1978; Wilhelms et al., 1979; Wilhelms and El-Baz, 1977; Stuart-Alexander, 1978; Scott et al., 1977; Wilhelms, 1987). Therefore, the crater population selected here and younger than 3 Ga can be considered complete.

5.3.2 The Crater Production Over the Last ~3 Ga

Probability Density Functions (PDFs) are computed for individual crater model ages in Gaussian form and summed to obtain a relative crater production. The average crater production is also computed every 200 Ma time interval. In this section, results obtained from two chronology models are presented: Neukum et al. (2001) and Lagain et al. (2024), the latter accounting for an additional calibration point provided by the Chang'e-5 mission (Li et al., 2021) as well as the spatial variation of the cratering rate on the lunar surface inferred from orbital characteristics of both the Moon and impactor populations (Robertson et al., 2021, 2023; Granvik et al., 2018; Pokorny et al., 2013). The statistical significance of the crater age distribution's deviation from a constant crater production model is also calculated by implementing a series of Kolmogorov-Smirnov (KS) tests. This approach does not assume any underlying pattern and is well-suited to model a random crater production. Hence, to test whether the craters formed under a steady-state rate regime, we perform a one-sampled KS test to compare one set of crater ages to a random distribution. We further resampled the crater model ages by repeatedly performing the KS tests for 1000 iterations to account for the crater age uncertainties. Crater age distributions with p-values below 0.05 can be considered significantly different from a random/constant distribution.

The crater PDFs and associated KS test results are presented for our dated crater population (Figure 5.4) and for three specific samples of crater sizes: 20 km < D < 30 km, 30 km < D < 40 km, and D > 40 km (Figure 5.5).

Figure 5.4 shows that the summed PDF for 211 craters larger than 20 km has a low relative cratering production between ~2 and ~3.5 Ga, followed by an increased production at ~1 Ga by a factor of ~2. This is then followed by a substantial decrease from ~500 Ma onwards. However, this total distribution was found to be dependent on the crater size ranges. Presented below, we break down and present the relative crater distribution by diameter (Figure 5.5):

a. The first model age distribution of 20 - 30 km craters (n = 107, impactors ~3 - 4 km) distinctly displays a peak at about 1 - 1.5 Ga, which then significantly decreases by a factor of ~3 for the last 500 Ma (Figure 5.5.a,d). The lack of craters > 2 Ga within this size range is likely due to a selection bias in the geological map.
b. The second age distribution of 30 - 40 km craters (n = 52, impactors ~4 - 6 km) is similar to the above distribution, showing a high cratering rate between 1 - 1.5 Ga. Comparatively, this population has more craters older than 2 Ga and displays a varied, but still increased, relative crater production between 2.5 Ga and 0.8 Ga (Figure 5.5.b,e).
c. The third age distribution, consisting of craters larger than 40 km (N = 52, impactors > 6 km), shows a relatively steady production rate (Figure 5.5.c,f). The crater production is relatively higher > 3 Ga, slowly decreasing and staying broadly constant between 2 Ga and 0.1 Ga.

The application of different chronology models to derive crater ages does not significantly change the distribution trend, as shown in Figures 5.4, 5.5, and Appendix 5.5.5.

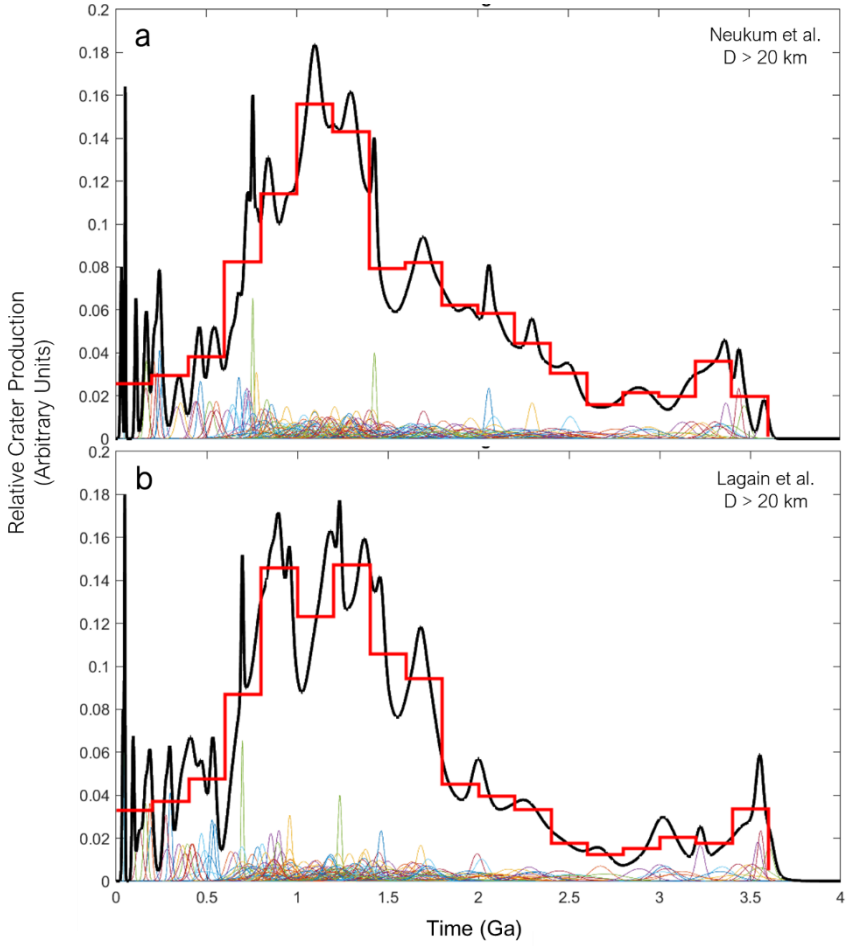

Figure 5.4: Relative crater production obtained from ages derived using the Neukum et al. (2001) chronology (panel a) and the Lagain et al. (2024) chronology (panel b). The multi-coloured curves represent the normalised age distribution for each crater's derived model age. The black line denotes the calculated sum of the age distributions, while the red stepped line represents the average sum distribution in 0.2 Ga intervals.

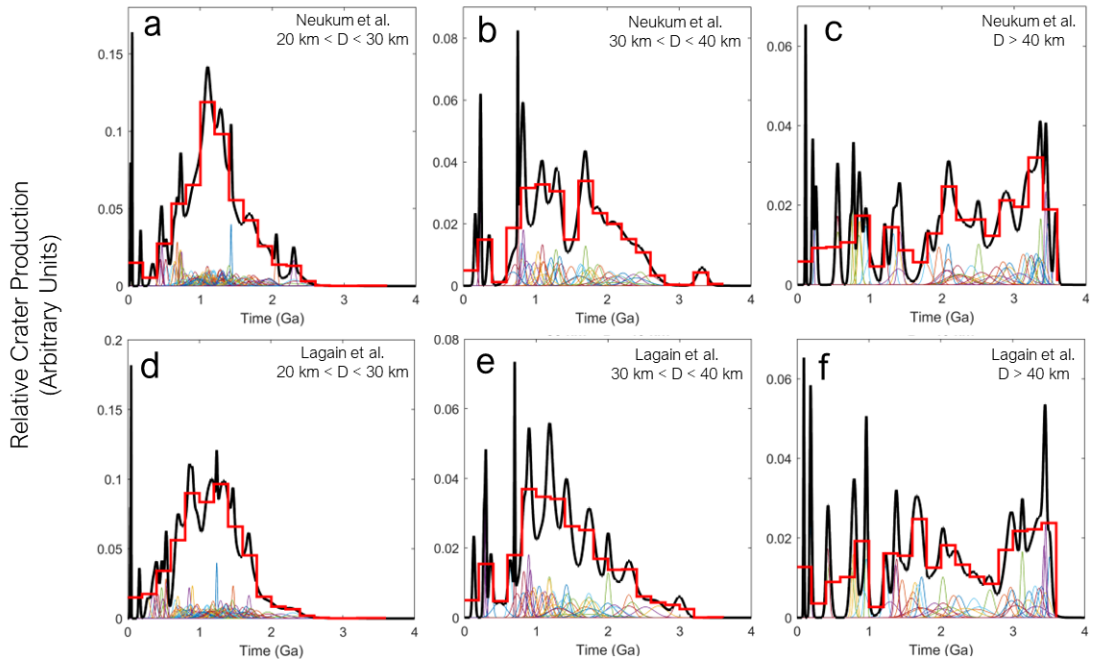

Figure 5.5: Relative crater production subdivided into three crater diameter groups across two chronology models. [Left to right] 20 km < D < 30 km (n=107), 30 km < D < 40 km (n=52), and D > 40km (n=52), using the Neukum et al. (2001) chronology [top row] and the Lagain et al. (2024) chronology [bottom row].

Figure 5.6 presents the results of the KS tests linked to the crater populations described above, wherein craters between 20 km and 30 km have a statistically significant relative crater production distribution (p-values << 0.05, Figure 5.6.a,d). However, for craters ranging between 30 km and 40 km and those larger than 40 km in diameter, the KS tests show a marginal or a non-statistically significant change (p-values ~0.05 and > 0.05, shown in Figures 5.6.b,e and 5.6.c.f), respectively. Accordingly, we will focus our discussion on the 20 - 40 km crater distribution results, as this shows the most significant trends.

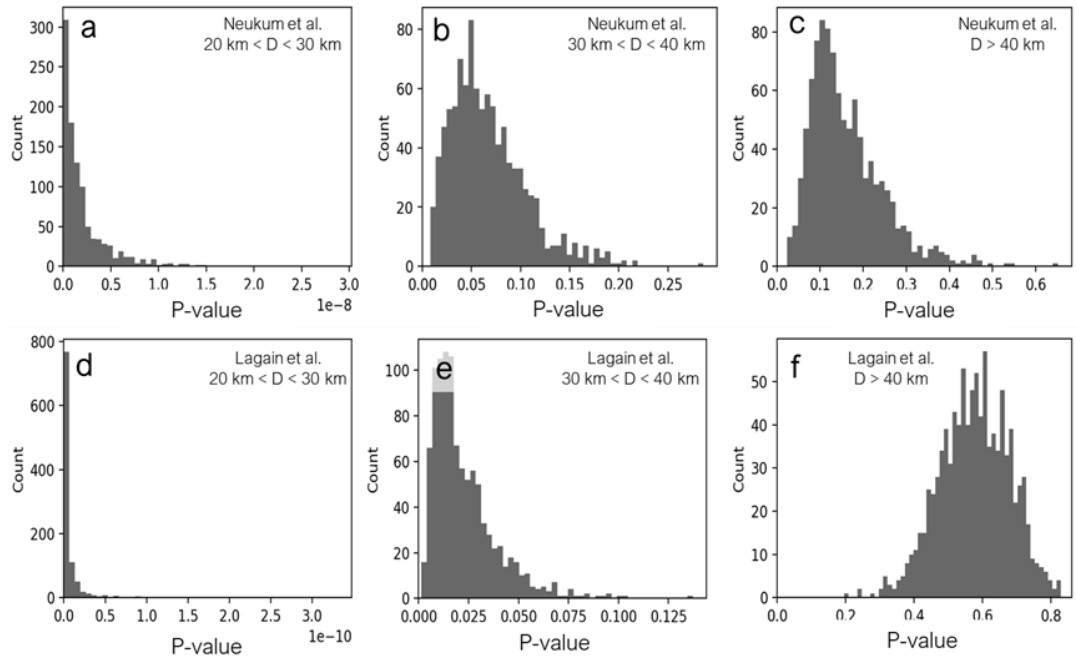

Figure 5.6: P-value histograms of the Kolmogorov-Smirnov test for a crater distribution younger than 3 Ga. The analyses are subdivided into three crater diameter groups across two chronology models: [Left to right] 20 km < D < 30 km, 30 km < D < 40 km, and D > 40km, [top row] Neukum et al. (2001) and [bottom row] Lagain et al. (2024).

5.4 Discussion

5.4.1 Model Age Accuracy

We have shown in prior studies that semi-automatic crater detection methods can produce model ages comparable with manually derived ages (see Fairweather et al., 2023; Lagain et al., 2021, 2022; Benedix et al., 2020). Nonetheless, validating and discussing the crater model ages we obtained against previously published results is necessary. Briefly comparing this study's model ages to used radiometric age benchmarks – for example, Tycho (109 ± 4 Ma), Copernicus (800 ± 15 Ma), and Eratosthenes (3.2 Ga) (see Stöffler and Ryder, 2001) – yields very similar ages. Wherein we derived 113 ± 6 Ma for Tycho crater, 853 ± 32 Ma for Copernicus crater, and $3.13^{+0.052}_{-0.064}$ Ga for Eratosthenes. Examples of other studies show crater count model ages of 58 ± 3 Ma (Terada et al., 2020), 663 ± 22 Ma (Terada et al., 2020), and 2.6 ± 0.4 Ga (Kirchoff et al., 2021) for Tycho, Copernicus, and Eratosthenes, respectively (the crater list is given in Appendix 5.5.2). We acknowledge that these ages are contentious within the scientific community and may not reflect the true age of those impacts (for this discussion, see Robbins, 2014; Schmitt et al., 2017; Xie and Xiao, 2023). Therefore, where applicable, we compared this study's crater count model ages against other studies' crater count model ages, namely Terada et al. (2020) and Kirchoff et al. (2021). For this comparison, the model ages are all reported as N(1) values (i.e., the cumulative density of craters >1 km per km^2), which negates the influence of the chronology models.

It is important to note that Kirchoff et al. (2021) counted craters superimposed upon crater floors, while Terada et al. (2020) counted craters superimposed on ejecta blankets. Both analyses defined different count areas, with the latter using a different image dataset (i.e., LRO-WAC and NAC images). Hence, a perfect comparative analysis is not possible. Although this study used automatic crater detections, we are still comparing it against manual crater counts; therefore, we must also be mindful of model age error and crater count variability between researchers - estimated to be as high as ~30% by Robbins et al. (2014).

Overall, this study's N(1) values are similar to those reported in the two other studies (Figure 5.7). Specifically, 90% of our ages coincide with the inferred model ages by Terada et al. (2020), which was expected as their crater counts were also performed on crater ejecta blankets. On the other hand, the N(1) reported by Kirchoff et al. (2021) exhibits much greater variability, particularly for craters with N(1) values larger than ~3.00 x 10^{-3} (craters older than ~3 Ga), where a majority of Kirchoff et al. (2021)'s dated craters lie (Figure 5.7.a). This cluster of crater ages is also noteworthy as it may reflect our two studies' methodological differences.

Large impact craters typically feature a floor composed of regolith underlain by semi-crystalline basaltic melt rock, as opposed to the layers of unconsolidated regolith typically expected in an ejecta blanket (Melosh, 1989). The differing rheology affects the final crater diameter (assuming the same impactor and impact conditions), which can introduce more variability to the model crater ages. This variability can produce an older age ranging from a few percentages to an order of magnitude (see Holsapple, 1993; Williams et al., 2018; 2022). We conclude that most model ages derived in this study are comparable, considering the complex combination of differing count areas, image datasets, terrain types, counting methodology, and rheology. Therefore, the methodology employed here is acceptable for determining a crater model age and reliable for assessing potential rate changes within lunar crater production.

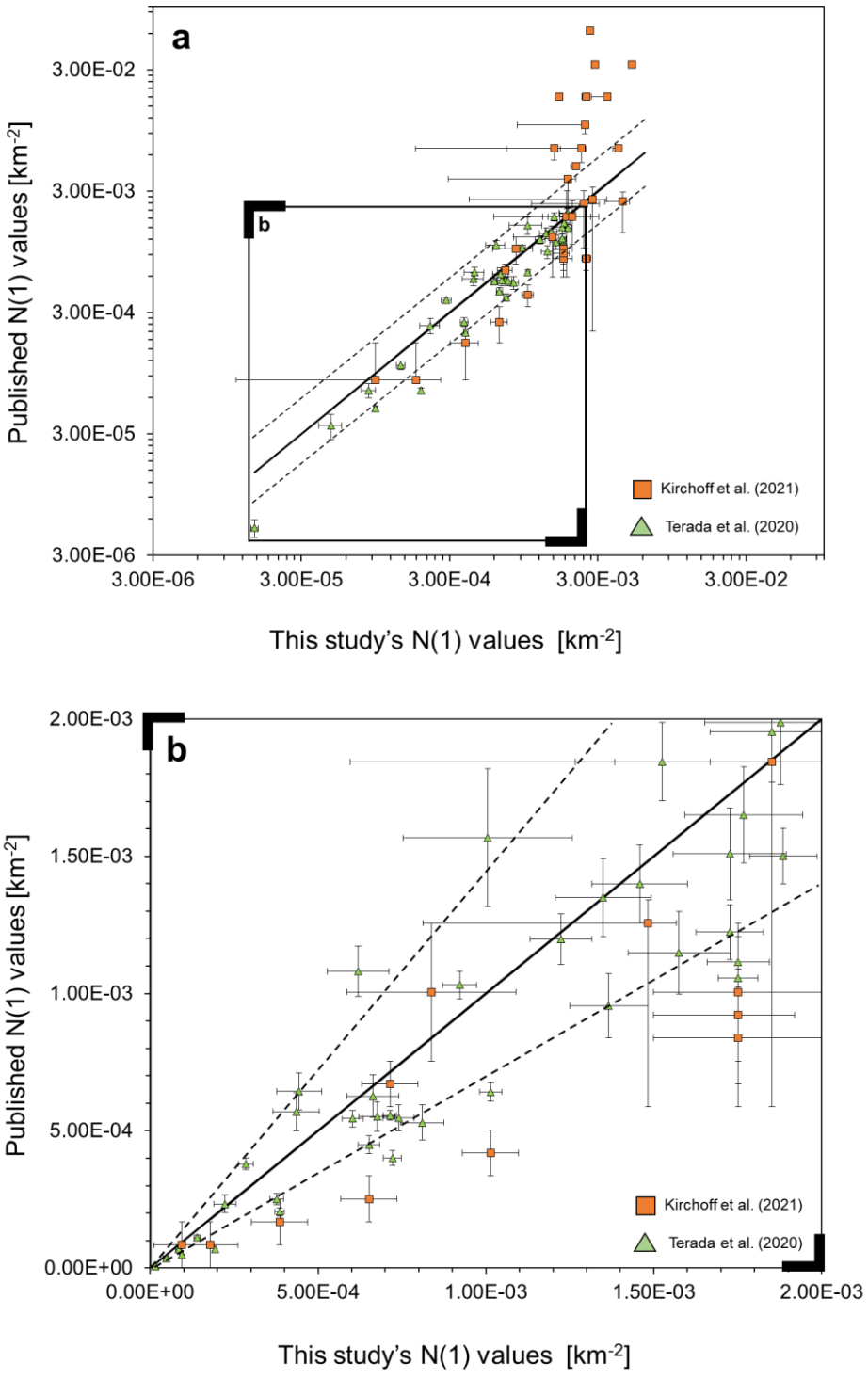

Figure 5.7: Comparison of N(1) values calculated in this study and those from Kirchoff et al. (2021) [n=29] and Terada et al. (2020) [n=38]. Panel (a) is presented on a Log10 scale, and panel (b) is presented on a linear scale. The black line shows the 1:1 correspondence with our values (this line represents a specific model age range of 33 Ma to 3.58 Ga). The dashed line represents a variability of ~30%, equal to the variability seen in N(1) values when assuming a constant production rate.

5.4.2 Determining a Change in the Crater Production

Our results indicate that the production rate of 20 - 40 km craters significantly differs from the expected constant production proposed by any other models (Figures 5.5, 5.6 and Appendix 5.5.5). The drop-off in the relative rate of craters < 0.5 Ga for this size range likely reflects a true change in crater production. Moreover, this age group should be the least affected by erosion, which allows us to reasonably discard the possibility that such results stem from a selection bias due to potential errors in the geological map.

Firstly, It is essential to present the main limitation of the method employed here, which is that our presented crater-age distribution of large craters (20 - 40 km) is calculated from the density of smaller craters (0.1 - 1 km). By doing so, we have made a presumption that the cratering rate of either population is known. Hence, we cannot precisely use a derived crater-age distribution as a precise proxy to infer where and how these cratering rates have changed. This is significant; not only does it confine this presented study but also prior studies that have used such a method to study to claim temporal fluctuations of the impact rate (e.g. Terada et al., 2020; Kirchoff et al., 2021; Lagain et al., 2020, 2022, Table 5.1). The following example will summarise this problem: if a surface 'A' is bombarded by small impactors at a constant rate for 3 Ga, and a surface 'B' is hit with twice as many impactors for the first 1.5 Ga and then not hit at all for the other 1.5 Ga, the two surface's crater accumulation will be identical, despite the extreme changes in the crater production rates.

According to the results of the completeness test detailed in section 5.3.1, the crater density and size selected in this study are in accordance with the expected crater population accumulated on the Moon over the last ~3 Ga (Neukum et al., 2001). This means that any change in the crater production must average out to approximately mimic a constant crater production rate, as Neukum et al. (2001) described (Figure 5.8).

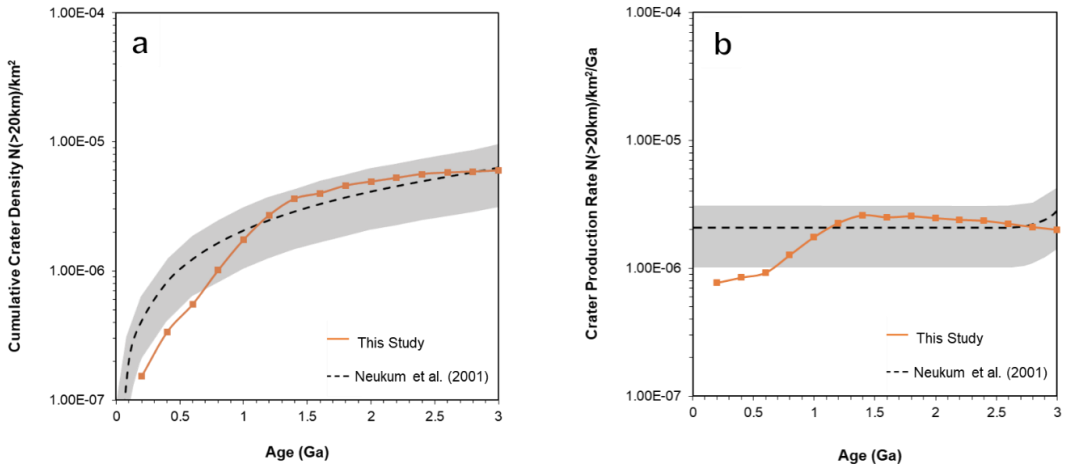

Figure 5.8: The inferred large crater production (orange line) and the Neukum et al. (2001) crater production (black dashed line) for the last 3 Ga. (Left) Crater production rate for craters >20km per km2 per Ga, and (Right) Cumulative Crater Density for craters >20km per km2. The orange points denote this study's N(20km) values per 0.2 Ga interval. The grey areas represent a 2-factor error.

We cannot determine precisely when and how the crater production changed over the last 3 Ga, only that the production rate of small impactors (~10 – 100 m) must be decoupled from the large impactors (~2 km and more) and that we can only use our large crater distribution to infer an interpolated cratering rate. Therefore, we present three possible scenarios that must have occurred to explain our large crater production rate presented in Figure 5.8:

1. Both the small (10-100 m) and large (2-4 km) crater production rates have significantly changed beyond a constant rate.
2. The large (2-4 km) crater production rate has significantly changed, while that of the small (10-100 m) crater production rate has remained approximately constant.
3. The small crater production rate has significantly changed, while the 2-4 km cratering rate has remained approximately constant.

5.4.3 Common Impactor Generating and Delivery Processes

Processes involved in crater production are directly tied to changes in the characteristics of impactor populations (i.e., number, size, orbital distribution) (Mazrouei et al., 2019; Lagain et al., 2020, 2022; Bottke et al., 2015; Kirchoff et al., 2021). Specifically, asteroid breakup events, collisional cascades and orbital resonances are common processes that inject main asteroid belt material into the inner solar system and increase the probability of impacts (e.g., Bottke et al., 2015 and references therein).

Debris produced following an asteroid breakup can form a family of asteroids with similar orbits (Nesvorný et al., 2015). Due to the chaotic nature of orbital evolution, the absolute timing and magnitude of these events are difficult to determine but can be constrained, within error, by dynamic modelling (Nesvorný et al., 2015; Spotto et al., 2015). Mechanisms such as YORP (Yarkovsky–O'Keefe–Radzievskii–Paddack) and Yarkovsky forces (Vokrouhlický et al., 2000) can modify orbits. These forces occur when sunlight hits an asteroid's body unevenly, which will cause slight changes in its rotation rate and trajectory over time due to the resulting thermal radiation. This increases an asteroids' major axis over time, which leads to material drifting into orbital resonances (e.g., resonances 3:1, 5:2, ν6; see Gladman et al., 1997). Such resonances inject them into the inner Solar System and increase their probability of colliding with terrestrial planets and the Moon. The combination of asteroid breakups and thermal forces was proposed in prior crater production studies (Mazrouei et al., 2019; Terada et al., 2020; Kirchoff et al., 2021) to explain the potential variations seen in their impact production rates.

The efficiency of such thermal forces is, however, very size dependent. As in, smaller-body asteroids (1 - 100 m) drift more quickly towards orbital resonances following an asteroid breakup than kilometric ones (e.g., Bottke et al., 2002, 2006; Granvik et al., 2016). Nevertheless, collisional and dynamical modelling has shown that 10s-of-metre-sized asteroids produced from an asteroid breakup are rapidly ground down through collisional cascades within a few million to tens-of-millions of years (see Bottke et al., 2007; Bottke et al., 2015). The collisional lifetime of small bodies is much shorter than the timescale of their escape route from the main belt through orbital resonances.

Thus, collisional cascades within the small impactor populations created by asteroid disruptions are unlikely to dominate a background impact rate for long periods. Considering the combined effect of asteroid breakups, thermal forces, and collisional cascades, the production of small craters is likely to be a steady-state process across a geological timescale of ~3 Ga, even if an asteroid event occurred close to resonance. Therefore, scenario 2 (the large crater production rate has significantly changed, while the small crater production has remained approximately constant) is proposed and is consistent with our understanding of the collisional and orbital evolution of the main asteroid belt.

5.4.4 Asteroid Breakup Events and Crater Populations

Considering scenario 2, so that the steady state of the small crater production can be used to date larger craters, we can assume that the crater production rates are decoupled based on crater size. Therefore, the age distributions and accumulation rates of large craters, shown in Figures 5.5 and 5.8, could reflect a significant temporal fluctuation of the large crater production. Specifically, this trend shows an increase of approximately 1 - 2 Ga, followed by a lull in large impacts < 0.5 Ga.

Although our method does not allow us to precisely determine when temporal variation occurred due to the model-dependent method used and its inherent uncertainties (i.e, the crater chronology function is based on a predefined crater production), it is worth noting that such age variations would be emphasised for surfaces with few calibration points (i.e., events between ~3 Ga and ~1 Ga; Neukum et al., 2001). The constant impact rate is the consequence of the calibration points, so the variation we have measured most likely took place $\lesssim$ 2 Ga or within a short time scale beyond the resolution of the calibration points.

Asteroid breakup events can produce the required temporal surges of large kilometric impactors that deliver material into the inner solar system. Dynamical modelling suggests that the secular v6 and the 3:1 resonance with Jupiter (which define the inner and outer edges of the main belt, respectively) serve as the primary escape routes for bodies with a high potential to impact inner-system bodies (Bottke et al., 2006; Morbidelli and Vokrouhlický, 2003; Ito and Malhotra, 2006). Asteroid breakups occurring in this part of the main belt are, therefore, most likely responsible for a change in the ~2-4 km lunar impactor rates, which are reflected in the model age distributions presented in this study (Figures 5.5 and 5.8).

Among asteroid breakup events widely referenced in the literature, the L-Chondrite Parent Body (LCPB) breakup is understood to be one of the most significant in the last ~3 Ga (Korochantsveva et al., 2007; Liao et al., 2020; Nesvorný et al., 2009, Terfelt and Schmitz, 2021).

This event has been proposed to substantially increase the flux of micrometeorites throughout the ~mid-Ordovician period (472-461 Ma) (Schmitz et al., 2019; Terfelt and Schmitz, 2021) and is thought to be responsible for the majority of current L-chondrite falls on Earth. Nevertheless, no consistent evidence supports the surge of large impactors caused by this event (Lagain et al., 2022).

The formation of other asteroid families via asteroid collisions has been strongly proposed for a change in the impact flux in the inner Solar System. These include the [403]Baptistina (< 0.3 Ga, Bottke et al., 2007); [1272]Gefion (~470 Ma, Nesvorny et al., 2009), [170]Maria (1.5 – 2.3 Ga, Brož, 2013; Spoto et al., 2015; Kirchoff et al., 2021, Aljbaae et al., 2017), [142]New Polana (>2 Ga, Walsh et al., 2013); [8]Flora (1 - 1.5 Ga, Vokrouhlický et al., 2017) and [495]Eulalia (~0.9-1.5 Ga, Bottke et al., 2015; Walsh et al., 2013) asteroid families. While the Baptistina and Gefion family ages are likely too young, and the New Polana ages are likely too old, to explain the variations discussed in the present study, the uncertainties in both crater count chronologies and age estimations of family forming events mean we cannot truly discount these events. However, other events can be considered more plausible for a significant surge in kilometric objects observed in our impact production rate.

Specifically, it has been shown through dynamical modelling that Flora formed at least 1 Ga ago and was a significant contributor of ~800 kilometric impactors to the Earth-Moon system for ~100-500 Ma following the disruption (Vokrouhlický et al., 2017). Such an event would produce a measurable fluctuation in the large crater record. Other events, such as Maria and Eulalia, also discussed in Kirchoff et al. (2021) and Terada et al. (2020), are other likely contributors to the kilometric impactor population over the last ~3 Ga. Modelling by Alibaae et al. (2017) suggested that the potential impact of the Maria family on current Near-Earth orbit population is low and that only >1% of kilometric objects have transitioned into such orbits within the last 500 Ma, which might support our recorded impact rate decrease over such time (Figures 5.5 and 5.8). Moreover, dynamic modelling of the Eulalia family shows that approximately half of the kilometric-sized material entered the 3:1 resonance ~0.5 Ga after formation, resulting in a potential increase of the cratering rates of the inner solar system at ~1 Ga (Bottke et al., 2015). In particular, Terada et al. (2020) argued that this specific event produced a cratering spike between 800 and 830 Ma. However, crater count model ages and asteroid dynamic models are not

accurate enough to distinguish such precise spikes (or lulls) for such narrow time intervals (Kirchoff et al., 2021). A complex combination of the Flora, Maria, and Eulalia family events likely caused the crater density fluctuations in our observed large crater population between ~0.5 and ~2.5 Ga (Figures 5.5 and 5.8). Additionally, the cratering rate decrease seen from ~0.5 Ga onwards might reflect a lull of kilometric impactor forming events (with respect to scenario 2 - the large crater production rate has significantly changed, while that of the small crater production rate has remained approximately constant). A lull over this period would have profound implications concerning the evolution of our planet's complex biosphere (Rampino, 2020; Smith and Harper, 2013).

Another approach to understanding how our potential age distribution of impactors evolved is to examine other planetary crater populations, such as those on Earth and Mars, to identify if similar trends may be linked to significant asteroid breakup events. Earth's crater population is affected by preservation biases (see Grieve and Shoemaker, 1994; Johnson and Bowling, 2014; Lagain et al., 2022; Stuart and Binzel et al., 2004), which will lead to a non-reliable comparison. For Mars, Lagain et al. (2022) conducted a detailed study on the production of Martian craters with diameters greater than 20 km. They inferred a relatively constant production rate for crater ages ≤ 600 Ma. If we filtered our crater record to only craters younger than 600 Ma, we, too, can infer a statistically constant production. An extensive comparison between the Moon and other cratering records across the inner planets must be conducted to confirm such fluctuations. Such comparisons are made complex on the Earth and Mars due to erosive conditions. However, looking at Mercury, Ceres, or other major asteroids can shed some insight into this discussion and aid in narrowing down the evolution of the small and large crater productions.

5.5. Conclusions

In this study, we conducted an exhaustive analysis of the relative crater production over the last ~3 Ga by examining the age distribution of 211 large lunar impact craters. We selected Copernican and Eratosthenian craters from the Moon's geological map and extracted the mapped units for the crater count areas. We applied a trained Crater Detection Algorithm (CDA) to Kaguya Terrain Camera (TC) image tiles to automatically count craters within the adjusted count areas. We derived crater model ages for 211 craters larger than 20 km. Additionally, we have determined that this study has analysed an approximately complete crater production.

Plotting the crater's age distribution, we have identified statistically significant changes in the relative crater production for large (>20 km) craters. Overall, we inferred an increase in the relative production of large craters dated between around ~0.5 Ga and ~2.5 Ga. This is followed by a substantial decrease in the crater production from ~0.5 Ga to now, which could have implications for the development of life on our planet. These shifts likely represent fundamental changes in the large crater production, favouring a scenario where the large (2-4 km) crater production rate has significantly changed, while that of the small (10-100 m) crater production rate has remained approximately constant.

By exploring potential explanations for the fluctuations in the large crater age distributions, we determined that asteroid family events, specifically ones that produce an ample supply of kilometric impactors near favourable orbital resonances, caused the fluctuations seen. The asteroid families Flora, Maria, and Eulalia, which formed between 0.9 - 2.3 Ga, likely contributed enough material to cause a drastic fluctuation over the last 3 Ga. Therefore, we have supplied more evidence to reject the hypothesis that the crater production could be considered constant over the last ~3 Ga. Additionally, within this analysis, we compared our semi-automatically derived crater count densities to the manual counts of two other studies. We determined that our crater densities are acceptable and within variability. The few significant age discrepancies come from choice crater count methodologies and ages outside the specified time ranges of this analysis. This study also stresses the necessity of more in-situ radiometric samples or crater count analyses on other terrestrial bodies.

5.6 References

Aljbaae, S., Carruba, V., Masiero, J. R., Domingos, R. C., & Huaman, M. (2017). The Maria asteroid family. Monthly Notices of the Royal Astronomical Society, 471(4), 4820–4826. https://doi.org/10.1093/mnras/stx1921

Bandfield, J. L., Ghent, R. R., Vasavada, A. R., Paige, D. A., Lawrence, S. J., & Robinson, M. S. (2011). Lunar surface rock abundance and regolith fines temperatures derived from LRO Diviner Radiometer data. Journal of Geophysical Research, 116, E00H02. https://doi.org/10.1029/2011JE003866

Benedix, G. K., Lagain, A., Chai, K., Meka, S., Anderson, S., Norman, C., Bland, P. A., Paxman, J., Towner, M. C., & Tan, T. (2020). Deriving Surface Ages on Mars Using Automated Crater Counting. Earth and Space Science, 7(3). https://doi.org/10.1029/2019EA001005

Bottke, W. F., & Norman, M. D. (2017). The Late Heavy Bombardment. Annual Review of Earth and Planetary Sciences, 45(1), 619–647. https://doi.org/10.1146/annurev-earth-063016-020131

Bottke, W. F., Brož, M., O'Brien, D. P., Campo Bagatin, A., Morbidelli, A., & Marchi, S. (2015). The Collisional Evolution of the Main Asteroid Belt. In P. Michel, F. E. DeMeo, & W. F. Bottke (Eds.), Asteroids IV. University of Arizona Press. https://doi.org/10.2458/azu_uapress_9780816532131-ch036

Bottke, W. F., Jr., Vokrouhlický, D., Rubincam, D. P., & Broz, M. (2002a). The Effect of Yarkovsky Thermal Forces on the Dynamical Evolution of Asteroids and Meteoroids. In Asteroids III (pp. 395–408). https://ui.adsabs.harvard.edu/abs/2002aste.book..395B

Bottke, W. F., Vokrouhlický, D., & Nesvorný, D. (2007). An asteroid breakup 160 Myr ago as the probable source of the K/T impactor. Nature, 449(7158), 48–53. https://doi.org/10.1038/nature06070

Bottke, W., Morbidelli, A., Jedicke, R., Petit, J., Levison, H., Michel, P., & Metcalfe, T. (2002b). Debiased Orbital and Absolute Magnitude Distribution of the Near-Earth Objects. Icarus, 156(2), 399–433. https://doi.org/10.1006/icar.2001.6788

Bray, V. J., Collins, G. S., Morgan, J. V., & Schenk, P. M. (2008). The effect of target properties on crater morphology: Comparison of central peak craters on the Moon and Ganymede. Meteoritics & Planetary Science, 43(12), 1979–1992. https://doi.org/10.1111/j.1945-5100.2008.tb00656.x

Brož, M., Morbidelli, A., Bottke, W. F., Rozehnal, J., Vokrouhlický, D., & Nesvorný, D. (2013). Constraining the cometary flux through the asteroid belt during the late heavy bombardment. Astronomy & Astrophysics, 551, A117. https://doi.org/10.1051/0004-6361/201219296

Collins, G. S., Melosh, H. J., & Marcus, R. A. (2005). Earth Impact Effects Program: A Web-based computer program for calculating the regional environmental consequences of a meteoroid impact on Earth. Meteoritics & Planetary Science, 40(6), 817–840. https://doi.org/10.1111/j.1945-5100.2005.tb00157.x

Crater analysis techniques working group. (1979). Standard techniques for presentation and analysis of crater size-frequency data. Icarus, 37(2), 467–474. https://doi.org/10.1016/0019-1035(79)90009-5

Fairweather, J. H., Lagain, A., Servis, K., & Benedix, G. K. (2023). Lunar Surface Model Age Derivation: Comparisons Between Automatic and Human Crater Counting Using LRO-NAC and Kaguya TC Images. Earth and Space Science, 10(7), e2023EA002865. https://doi.org/10.1029/2023EA002865

Fairweather, J. H., Lagain, A., Servis, K., Benedix, G. K., Kumar, S. S., & Bland, P. A. (2022). Automatic Mapping of Small Lunar Impact Craters Using LRO-NAC Images. Earth and Space Science, 9(7). https://doi.org/10.1029/2021EA002177

Fassett, C. I. (2016). Analysis of impact crater populations and the geochronology of planetary surfaces in the inner solar system: Crater Populations and Surface Chronology. Journal of Geophysical Research: Planets, 121(10), 1900–1926. https://doi.org/10.1002/2016JE005094

Fassett, C. I., & Thomson, B. J. (2014). Crater degradation on the lunar maria: Topographic diffusion and the rate of erosion on the Moon: Crater degradation on the lunar maria. Journal of Geophysical Research: Planets, 119(10), 2255–2271. https://doi.org/10.1002/2014JE004698

Fortezzo, C. M., Spudis, P. D., & Harrel, S. L. (2020). Release of the Digital Unified Global Geologic Map of the Moon at 1:5,000,000-Scale. 2760.

Ghent, R. R., Hayne, P. O., Bandfield, J. L., Campbell, B. A., Allen, C. C., Carter, L. M., & Paige, D. A. (2014). Constraints on the recent rate of lunar ejecta breakdown and implications for crater ages. Geology, 42(12), 1059–1062. https://doi.org/10.1130/G35926.1

Gladman, B. J., Migliorini, F., Morbidelli, A., Zappalà, V., Michel, P., Cellino, A., Froeschlé, C., Levison, H. F., Bailey, M., & Duncan, M. (1997). Dynamical Lifetimes of Objects Injected into Asteroid Belt Resonances. Science, 277(5323), 197–201. https://doi.org/10.1126/science.277.5323.197

Granvik, M., Morbidelli, A., Jedicke, R., Bolin, B., Bottke, W. F., Beshore, E., Vokrouhlický, D., Nesvorný, D., & Michel, P. (2018). Debiased orbit and absolute-magnitude distributions for near-Earth objects. Icarus, 312, 181–207. https://doi.org/10.1016/j.icarus.2018.04.018

Grieve, R. A., & Shoemaker, E. M. (1994). The record of past impacts on Earth. Hazards due to comets and asteroids, 417-462. https://doi.org/10.2307/j.ctv23khmpv

Hartmann, W. K. (1977). Relative crater production rates on planets. Icarus, 31(2), 260–276. https://doi.org/10.1016/0019-1035(77)90037-9

Hartmann, W. K. (2005). Martian cratering 8: Isochron refinement and the chronology of Mars. Icarus, 174(2), 294–320. https://doi.org/10.1016/j.icarus.2004.11.023

Hartmann, W. K. (2007). Martian cratering 9: Toward resolution of the controversy about small craters. Icarus, 189(1), 274–278. https://doi.org/10.1016/j.icarus.2007.02.011

Haruyama, J., Matsunaga, T., Ohtake, M., Morota, T., Honda, C., Yokota, Y., Torii, M., Ogawa, Y., & LISM Working Group. (2008). Global lunar-surface mapping experiment using the Lunar Imager/Spectrometer on SELENE. Earth, Planets and Space, 60(4), 243–255. https://doi.org/10.1186/BF03352788

Heiken, G., Vaniman, D., & French, B. M. (1991). Lunar Sourcebook: A User's Guide to the Moon. CUP Archive.

Hergarten, S., Wulf, G., & Kenkmann, T. (2019). Comment on "Earth and Moon impact flux increased at the end of the Paleozoic". Science, 365(6450), eaaw7471. https://doi.org/10.1126/science.aaw7471

Hiesinger, H., Head, J. W., Wolf, U., Jaumann, R., & Neukum, G. (2011). Ages and stratigraphy of lunar mare basalts: A synthesis. In W. A. Ambrose & D. A. Williams, Recent Advances and Current Research Issues in Lunar Stratigraphy. Geological Society of America. https://doi.org/10.1130/2011.2477(01)

Holsapple, K. A. (1993). The Scaling of Impact Processes in Planetary Sciences. Annual Review of Earth and Planetary Sciences, 21(1), 333–373. https://doi.org/10.1146/annurev.ea.21.050193.002001

Isbell, C., Gaddis, L., Garcia, P., Hare, T., & Bailen, M. (2014). Kaguya Terrain Camera Mosaics. 2268.

Ito, T., & Malhotra, R. (2010). Asymmetric impacts of near-Earth asteroids on the Moon. Astronomy and Astrophysics, 519, A63. https://doi.org/10.1051/0004-6361/200912901

Ivanov, B. A., Neukum, G., & Wagner, R. (2001). Size-Frequency Distributions of Planetary Impact Craters and Asteroids. In M. Ya. Marov & H. Rickman (Eds.), Collisional Processes in the Solar System (Vol. 261, pp. 1–34). Springer Netherlands. https://doi.org/10.1007/978-94-010-0712-2_1

Johnson, B. C., & Bowling, T. J. (2014). Where have all the craters gone? Earth's bombardment history and the expected terrestrial cratering record. Geology, 42(7), 587–590. https://doi.org/10.1130/G35754.1

Kirchoff, M. R., Marchi, S., Bottke, W. F., Chapman, C. R., & Enke, B. (2021). Suggestion that recent (≤ 3 Ga) flux of kilometer and larger impactors in the Earth-Moon system has not been constant. Icarus, 355, 114110. https://doi.org/10.1016/j.icarus.2020.114110

Korochantseva, E. V., Trieloff, M., Lorenz, C. A., Buykin, A. I., Ivanova, M. A., Schwarz, W. H., Hopp, J., & Jessberger, E. K. (2007). L-chondrite asteroid breakup tied to Ordovician meteorite shower by multiple isochron 40 Ar- 39 Ar dating. Meteoritics & Planetary Science, 42(1), 113–130. https://doi.org/10.1111/j.1945-5100.2007.tb00221.x

Lagain, A., Benedix, G. K., Servis, K., Baratoux, D., Doucet, L. S., Rajšic, A., Devillepoix, H. A. R., Bland, P. A., Towner, M. C., Sansom, E. K., & Miljković, K. (2021a). The Tharsis mantle source of depleted shergottites revealed by 90 million impact craters. Nature Communications, 12(1), 6352. https://doi.org/10.1038/s41467-021-26648-3

Lagain, A., Bouley, S., Baratoux, D., Costard, F., & Wieczorek, M. (2020). Impact cratering rate consistency test from ages of layered ejecta on Mars. Planetary and Space Science, 180, 104755. https://doi.org/10.1016/j.pss.2019.104755

Lagain, A., Devillepoix, H. A. R., Vernazza, P., Robertson, D., Granvik, M., Pokorny, P., Ozerov, A., Shober, P. M., Jorda, L., Servis, K., Fairweather, J. H., Quesnel, Y., & Benedix, G. K. (2024). Recalibration of the lunar chronology due to spatial cratering-rate variability. Icarus, 411, 115956. https://doi.org/10.1016/j.icarus.2024.115956

Lagain, A., Kreslavsky, M., Baratoux, D., Liu, Y., Devillepoix, H., Bland, P., Benedix, G. K., Doucet, L. S., & Servis, K. (2022). Has the impact flux of small and large asteroids varied through time on Mars, the Earth and the Moon? Earth and Planetary Science Letters, 579, 117362. https://doi.org/10.1016/j.epsl.2021.117362

Lagain, A., Servis, K., Benedix, G. K., Norman, C., Anderson, S., & Bland, P. A. (2021b). Model Age Derivation of Large Martian Impact Craters, Using Automatic Crater Counting Methods. Earth and Space Science, 8(2). https://doi.org/10.1029/2020EA001598

Le Feuvre, M., & Wieczorek, M. A. (2011). Nonuniform cratering of the Moon and a revised crater chronology of the inner Solar System. Icarus, 214(1), 1–20. https://doi.org/10.1016/j.icarus.2011.03.010

Lee, E. M., Gaddis, L. R., Weller, L., Richie, J. O., Becker, T., Shinaman, J., Rosiek, M. R., & Archinal, B. A. (2009). A New Clementine Basemap of the Moon. 2445.

Li, H.C., Zhang, N., Yue, Z.-Y., & Zhang, Y.-Z. (2021a). Lunar Cratering Asymmetries with High Orbital Obliquity and Inclination of the Moon. Research in Astronomy and Astrophysics, 21(6), 140. https://doi.org/10.1088/1674-4527/21/6/140

Li, Q.L., Zhou, Q., Liu, Y., Xiao, Z., Lin, Y., Li, J.-H., Ma, H.-X., Tang, G.-Q., Guo, S., Tang, X., Yuan, J.-Y., Li, J., Wu, F.-Y., Ouyang, Z., Li, C., & Li, X.-H. (2021b). Two-billion-year-old volcanism on the Moon from Chang'e-5 basalts. Nature, 600(7887), 54–58. https://doi.org/10.1038/s41586-021-04100-2

Liao, S., Huyskens, M. H., Yin, Q.-Z., & Schmitz, B. (2020). Absolute dating of the L-chondrite parent body breakup with high-precision U–Pb zircon geochronology from Ordovician limestone. Earth and Planetary Science Letters, 547, 116442. https://doi.org/10.1016/j.epsl.2020.116442

Losiak, A., Kohout, T., O'Sulllivan, K., Thaisen, K., Weider, S. (2009). Lunar Impact Crater Database. LPI Lunar Exploration Intern Program (2009) Revised by T. Öhman, LPI (2011) and (2015). https://www.lpi.usra.edu/lunar/surface/#craters

Lucchitta, B. K. (1979). Geologic map of the North side of the Moon (Map I-1062). United States Geological Survey. https://doi.org/10.3133/i1062

Lucey, P. G., Blewett, D. T., Taylor, G. J., & Hawke, B. R. (2000). Imaging of lunar surface maturity. Journal of Geophysical Research: Planets, 105(E8), 20377–20386. https://doi.org/10.1029/1999JE001110

Marchi, S., Bottke, W. F., Kring, D. A., & Morbidelli, A. (2012). The onset of the lunar cataclysm as recorded in its ancient crater populations. Earth and Planetary Science Letters, 325–326, 27–38. https://doi.org/10.1016/j.epsl.2012.01.021

Marchi, S., Mottola, S., Cremonese, G., Massironi, M., & Martellato, E. (2009). A New Chronology For The Moon And Mercury. The Astronomical Journal, 137(6), 4936–4948. https://doi.org/10.1088/0004-6256/137/6/4936

Mazarico, E., Neumann, G. A., Smith, D. E., Zuber, M. T., & Torrence, M. H. (2011). Illumination conditions of the lunar polar regions using LOLA topography. Icarus, 211(2), 1066–1081. https://doi.org/10.1016/j.icarus.2010.10.030

Mazrouei, S., Ghent, R. R., Bottke, W. F., Parker, A. H., & Gernon, T. M. (2019). Earth and Moon impact flux increased at the end of the Paleozoic. Science, 363(6424), 253–257. https://doi.org/10.1126/science.aar4058

McEwen, A. S., & Robinson, M. S. (1997). Mapping of the Moon by Clementine. Advances in Space Research, 19(10), 1523–1533. https://doi.org/10.1016/S0273-1177(97)00365-7

Melosh, H. J. (1989). Impact Cratering: A Geologic Process. Oxford University Press. https://books.google.com.au/books?id=nZwRAQAAIAAJ

Melosh, H. J., & Ivanov, B. A. (1999). Impact Crater Collapse. Annual Review of Earth and Planetary Sciences, 27(1), 385–415. https://doi.org/10.1146/annurev.earth.27.1.385

Michael, G. G., & Neukum, G. (2010). Planetary surface dating from crater size–frequency distribution measurements: Partial resurfacing events and statistical age uncertainty. Earth and Planetary Science Letters, 294(3–4), 223–229. https://doi.org/10.1016/j.epsl.2009.12.041

Michael, G. G., Kneissl, T., & Neesemann, A. (2016). Planetary surface dating from crater size-frequency distribution measurements: Poisson timing analysis. Icarus, 277, 279–285. https://doi.org/10.1016/j.icarus.2016.05.019

Morbidelli, A., & Vokrouhlický, D. (2003). The Yarkovsky-driven origin of near-Earth asteroids. Icarus, 163(1), 120–134. https://doi.org/10.1016/S0019-1035(03)00047-2

Morbidelli, A., Nesvorny, D., Laurenz, V., Marchi, S., Rubie, D. C., Elkins-Tanton, L., Wieczorek, M., & Jacobson, S. (2018). The timeline of the lunar bombardment: Revisited. Icarus, 305, 262–276. https://doi.org/10.1016/j.icarus.2017.12.046

Nesvorný, D., Broz, M., & Carruba, V. (2015). Identification and Dynamical Properties of Asteroid Families. https://doi.org/10.48550/ARXIV.1502.01628

Nesvorný, D., Vokrouhlický, D., Morbidelli, A., & Bottke, W. F. (2009). Asteroidal source of L chondrite meteorites. Icarus, 200(2), 698–701. https://doi.org/10.1016/j.icarus.2008.12.016

Neukum, G. (1984). Meteoritenbombardement und Datierung planetarer Oberflachen (Meteorite bombardment and dating of planetary surfaces). University of Munich, Germany.

Neukum, G., & Ivanov, B. A. (1994). Crater Size Distributions and Impact Probabilities on Earth from Lunar, Terrestrial-planet, and Asteroid Cratering Data (p. 359). https://ui.adsabs.harvard.edu/abs/1994hdtc.conf..359N

Neukum, G., Ivanov, B. A., & Hartmann, W. K. (2001). Cratering Records in the Inner Solar System in Relation to the Lunar Reference System. In R. Kallenbach, J. Geiss, & W. K. Hartmann (Eds.), Chronology and Evolution of Mars (Vol. 12, pp. 55–86). Springer Netherlands. https://doi.org/10.1007/978-94-017-1035-0_3

Opik, E. J. (1960). The Lunar Surface as an Impact Counter. Monthly Notices of the Royal Astronomical Society, 120(5), 404–411. https://doi.org/10.1093/mnras/120.5.404

Pike, R. J. (1974). Ejecta from large craters on the Moon: Comments on the geometric model of McGetchin et al. Earth and Planetary Science Letters, 23(3), 265–271. https://doi.org/10.1016/0012-821X(74)90114-9

Pokorný, P., & Vokrouhlický, D. (2013). Öpik-type collision probability for high-inclination orbits: Targets on eccentric orbits. Icarus, 226(1), 682–693. https://doi.org/10.1016/j.icarus.2013.06.015

Quantin, C., Mangold, N., Hartmann, W. K., & Allemand, P. (2007). Possible long-term decline in impact rates. Icarus, 186(1), 1–10. https://doi.org/10.1016/j.icarus.2006.07.008

Rampino, M. R. (2020). Relationship between impact-crater size and severity of related extinction episodes. Earth-Science Reviews, 201, 102990. https://doi.org/10.1016/j.earscirev.2019.102990

Redmon, J., Divvala, S., Girshick, R., & Farhadi, A. (2015). You Only Look Once: Unified, Real-Time Object Detection. https://doi.org/10.48550/ARXIV.1506.02640

Richardson, M., Malagón, A. A. P., Lebofsky, L. A., Grier, J., Gay, P., Robbins, S. J., & Team, T. C. (2022). The CosmoQuest Moon Mappers Community Science Project: The Effect of Incidence Angle on the Lunar Surface Crater Distribution. https://doi.org/10.48550/ARXIV.2110.13404

Robbins, S. J. (2014). New crater calibrations for the lunar crater-age chronology. Earth and Planetary Science Letters, 403, 188–198. https://doi.org/10.1016/j.epsl.2014.06.038

Robbins, S. J., & Hynek, B. M. (2012). A New Global Database of Mars Impact Craters ≥1 km: 1. Database creation, properties, and parameters. Journal of Geophysical Research: Planets, 117(E5), n/a-n/a. https://doi.org/10.1029/2011JE003966

Robertson, D., Ozerov, A., Wheeler, L., Pokorný, P., Granvik, M., & Rumpf, C. (2023). Erratum: "Latitude Variation of Flux and Impact Angle of Asteroid Collisions with Earth and the Moon" (2021, PSJ, 2, 88). The Planetary Science Journal, 4(1), 19. https://doi.org/10.3847/PSJ/aca1a7

Robertson, D., Pokorný, P., Granvik, M., Wheeler, L., & Rumpf, C. (2021). Latitude Variation of Flux and Impact Angle of Asteroid Collisions with Earth and the Moon. The Planetary Science Journal, 2(3), 88. https://doi.org/10.3847/PSJ/abefda

Robinson, M. S., Brylow, S. M., Tschimmel, M., Humm, D., Lawrence, S. J., Thomas, P. C., Denevi, B. W., Bowman-Cisneros, E., Zerr, J., Ravine, M. A., Caplinger, M. A., Ghaemi, F. T., Schaffner, J. A., Malin, M. C., Mahanti, P., Bartels, A., Anderson, J., Tran, T. N., Eliason, E. M., … Hiesinger, H. (2010). Lunar Reconnaissance Orbiter Camera (LROC) Instrument Overview. Space Science Reviews, 150(1–4), 81–124. https://doi.org/10.1007/s11214-010-9634-2

Schmitz, B., Feist, R., Meier, M. M. M., Martin, E., Heck, P. R., Lenaz, D., Topa, D., Busemann, H., Maden, C., Plant, A. A., & Terfelt, F. (2019). The micrometeorite flux to Earth during the Frasnian–Famennian transition reconstructed in the Coumiac GSSP section, France. Earth and Planetary Science Letters, 522, 234–243. https://doi.org/10.1016/j.epsl.2019.06.025

Sharpton, V. L. (2014). Outcrops on lunar crater rims: Implications for rim construction mechanisms, ejecta volumes and excavation depths: Outcrops constrain crater rim components. Journal of Geophysical Research: Planets, 119(1), 154–168. https://doi.org/10.1002/2013JE004523

Smith, M. P., & Harper, D. A. T. (2013). Causes of the Cambrian Explosion. Science, 341(6152), 1355–1356. https://doi.org/10.1126/science.1239450

Speyerer, E. J., Robinson, M. S., Denevi, B. W., & LROC Science Team. (2011). Lunar Reconnaissance Orbiter Camera Global Morphological Map of the Moon. 2387.

Spoto, F., Milani, A., & Knezevic, Z. (2015). Asteroid family ages. https://doi.org/10.48550/ARXIV.1504.05461

Stöffler, D. (2006). Cratering History and Lunar Chronology. Reviews in Mineralogy and Geochemistry, 60(1), 519–596. https://doi.org/10.2138/rmg.2006.60.05

Stöffler, D., & Ryder, G. (2001). Stratigraphy and Isotope Ages of Lunar Geologic Units: Chronological Standard for the Inner Solar System. Space Science Reviews, 96(1/4), 9–54. https://doi.org/10.1023/A:1011937020193

Stuart, J. S., & Binzel, R. P. (2004). Bias-corrected population, size distribution, and impact hazard for the near-Earth objects. Icarus, 170(2), 295–311. https://doi.org/10.1016/j.icarus.2004.03.018

Stuart-Alexander, D. E. (1978). Geologic map of the central far side of the Moon (Map I-1047). United States Geological Survey. https://doi.org/10.3133/i1047

Terada, K., Morota, T., & Kato, M. (2020). Asteroid shower on the Earth-Moon system immediately before the Cryogenian period revealed by KAGUYA.

Nature Communications, 11(1), 3453. https://doi.org/10.1038/s41467-020-17115-6

Terfelt, F., & Schmitz, B. (2021). Asteroid break-ups and meteorite delivery to Earth the past 500 million years. Proceedings of the National Academy of Sciences, 118(24), e2020977118. https://doi.org/10.1073/pnas.2020977118

Vokrouhlický, D., Bottke, W. F., & Nesvorný, D. (2017). Forming the Flora Family: Implications for the Near-Earth Asteroid Population and Large Terrestrial Planet Impactors. The Astronomical Journal, 153(4), 172. https://doi.org/10.3847/1538-3881/aa64dc

Vokrouhlický, D., Milani, A., & Chesley, S. R. (2000). Yarkovsky Effect on Small Near-Earth Asteroids: Mathematical Formulation and Examples. Icarus, 148(1), 118–138. https://doi.org/10.1006/icar.2000.6469

Walsh, K. J., Delbó, M., Bottke, W. F., Vokrouhlický, D., & Lauretta, D. S. (2013). Introducing the Eulalia and new Polana asteroid families: Re-assessing primitive asteroid families in the inner Main Belt. Icarus, 225(1), 283–297. https://doi.org/10.1016/j.icarus.2013.03.005

Wilhelms, D. E. (1987). The geologic history of the Moon (USGS Numbered Series 1348; Professional Paper, p. 337). United States Geological Survey. https://doi.org/10.3133/pp1348

Wilhelms, D. E., & El-Baz, F. (1977). Geologic map of the east side of the Moon (Map I-948). United States Geological Survey. https://doi.org/10.3133/i948

Wilhelms, D. E., & McCauley, J. F. (1971). Geologic map of the near side of the Moon (Map I-703). United States Geological Survey. https://doi.org/10.3133/i703

Wilhelms, D. E., Howard, K. A., & Wilshire, H. G. (1979). Geologic map of the south side of the Moon (Map I-1162). United States Geological Survey. https://doi.org/10.3133/i1162

Williams, J. -P., Pathare, A. V., Costello, E. S., Gallinger, C. L., Hayne, P. O., Ghent, R. R., Paige, D. A., Siegler, M. A., Russell, P. S., & Elder, C. M. (2022). The Effects of Terrain Properties Upon the Small Crater Population Distribution at Giordano Bruno: Implications for Lunar Chronology. Journal of Geophysical Research: Planets, 127(5), e2021JE007131. https://doi.org/10.1029/2021JE007131

Williams, J.-P., van der Bogert, C. H., Pathare, A. V., Michael, G. G., Kirchoff, M. R., & Hiesinger, H. (2018). Dating very young planetary surfaces from crater statistics: A review of issues and challenges. Meteoritics & Planetary Science, 53(4), 554–582. https://doi.org/10.1111/maps.12924

Wisdom, J. (1982). The origin of the Kirkwood gaps—A mapping for asteroidal motion near the 3/1 commensurability. The Astronomical Journal, 87, 577. https://doi.org/10.1086/113132

Xie, M., & Xiao, Z. (2023). A new chronology from debiased crater densities: Implications for the origin and evolution of lunar impactors. Earth and Planetary Science Letters, 602, 117963. https://doi.org/10.1016/j.epsl.2022.117963

Xu, L., Qiao, L., Xie, M., & Wu, Y. (2022). Formation age of lunar Lalande crater and its implications for the source region of the KREEP-rich meteorite Sayh al Uhaymir 169. Icarus, 386, 115166. https://doi.org/10.1016/j.icarus.2022.115166

Chapter 6: Conclusions and Perspectives

The Moon's surface is a dynamic geological system that constantly interacts with the space environment and records those interactions through impact craters. Looking at the density of impact craters over a given surface allows for determining its formation age. As the Moon has no major erosional processes, those impact craters are preserved for billions of years. In this thesis, Chapters 1 and 2 introduce the Moon as a record of our past and how we can access and quantify that record meaningfully while also identifying the current limitations of the methods we use to access this record. Crater counting (mapping impact craters to generate a surface density) and geology (thinking about rocks, not as mundane objects, but as a 4-D sample of the solar system) pair together to allow researchers like us to understand the evolution of cosmic events.

Chapter 3 placed the technical framework for automated crater mapping on surfaces with millions of small lunar impact craters. The current limitations of prior lunar crater catalogues restricted the ability to investigate finer-scale geological processes. We showcased the adaptability and accuracy of machine learning techniques in lunar mapping by adopting an existing CNN algorithm initially designed for detecting Martian craters. Our Crater Detection Algorithm (CDA) demonstrated its accuracy in identifying lunar impact craters using Lunar Reconnaissance Orbiter - Narrow Angle Camera (LRO-NAC) images. Our approach's methodology and technical framework allowed us to process thousands of raw LRO-NAC images and generate accurate detections of impact craters larger than ~20 m. This pipeline, which combines image processing and machine learning, advances the scale at which we can look at the lunar surface.

In Chapter 4, we utilised our CDA to derive model ages for young lunar craters and mare surfaces. This novel approach, combining automatic lunar crater detection and model age derivation, was compared to traditional manual counts. Our findings through this comparison emphasised the viability and efficiency of the CDA in detecting small craters on young lunar surfaces. Our study pointed out that unadjusted CDA results can lead to incorrect overestimations of cratering densities, while post-processing adjustments significantly improved CDA-derived model ages. This was a significant outcome, explaining that automatic crater datasets can be

used, but only in the presence of careful due-diligence and geological reasoning. Though, even after our post-processing, we still had discrepancies in certain study areas (i.e., the Chang'e-5 landsite). These discrepancies were mostly likely due to significant differences in image quality, resolution, and researcher variability – and not to the limitations of automatic crater methods. This study highlights the CDA's potential for global-scale analysis of lunar sites, providing valuable insights into the Moon's recent geological history. However, it also heavily emphasises the importance of a combined computer-human approach; this involves geological mapping and interpretations to ensure accurate and meaningful model age results.

Chapter 5 of this thesis delved into the investigation of crater production over the last ~3 Ga, utilising the distribution of dated lunar impact craters as a proxy. Using the current geologic map of the Moon, we selected Copernican and Eratosthenian craters and utilised our CDA alongside Kaguya TC image tiles. This automated process, combined with pre-existing craters removal process, enabled the derivation of model ages for 211 craters larger than 20 km. Analysis revealed a significant deviation from the expected constant production rate for craters in the 20 to 40 km size range, suggesting fluctuations in the impact flux of 2-4 km impactors since 3 Ga, while that of 10-100 meter impactors remained relatively constant. This finding has implications for understanding regional and global changes in the Earth-Moon system, prompting further investigation into the timing of potential source asteroid populations using independent methods such as impact crater radiometric dating from lunar samples.

This PhD Project has emphasised the critical role of automated crater mapping, highlighting the potential and challenges of utilising a Crater Detection Algorithm for deriving lunar model ages. We accomplished this in three parts: (1) adapting and testing a machine learning algorithm for use on the Moon, (2) showing that the results from this algorithm were comparable with manual methods, and (3) using those crater detections to investigate the evolution of the crater production over the last 3 Ga. Overall, this work demonstrates the relationship between technological innovation, systematic analysis, and geological reasoning, contributing to our collective understanding of the solar system and life in general.

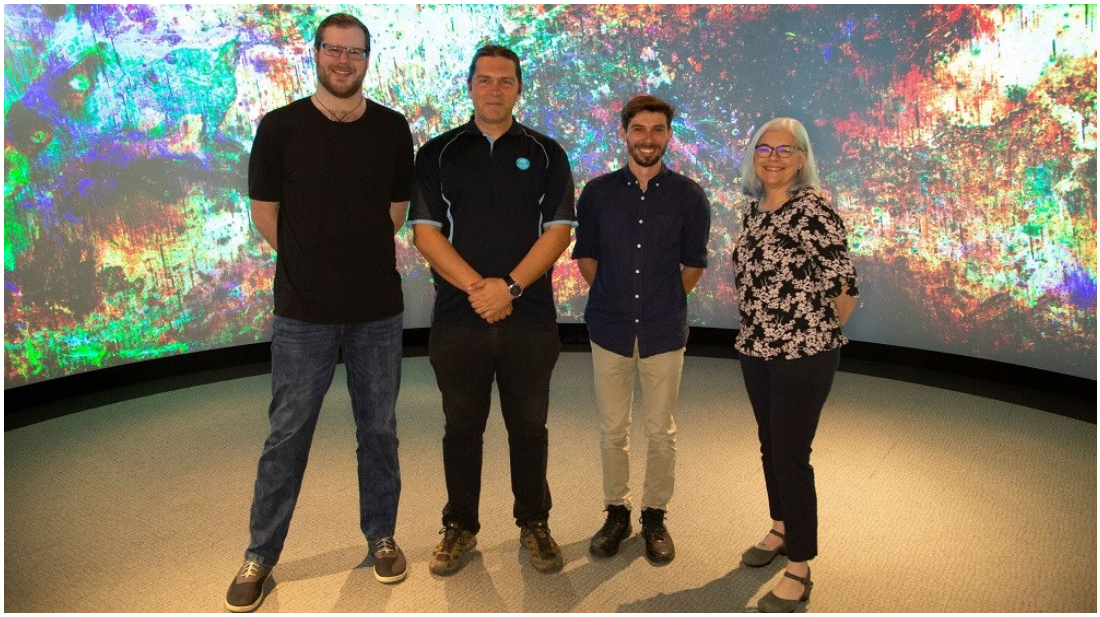

Figure 6.1: The Curtin CDA Team (2021). [Left to right] John Fairweather, Kostantinos Servis, Anthony Lagain, Gretchen Benedix.

Bibliography

Acton, C. H. (1996). Ancillary data services of NASA's Navigation and Ancillary Information Facility. Planetary and Space Science, 44(1), 65–70. https://doi.org/10.1016/0032-0633(95)00107-7

Adams, J. B. (1967). Lunar surface composition and particle size: Implications from laboratory and lunar spectral reflectance data. Journal of Geophysical Research, 72(22), 5717–5720. https://doi.org/10.1029/JZ072i022p05717

Ajit, A., Acharya, K., & Samanta, A. (2020). A Review of Convolutional Neural Networks. 2020 International Conference on Emerging Trends in Information Technology and Engineering (Ic-ETITE), 1–5. https://doi.org/10.1109/ic-ETITE47903.2020.049

Albawi, S., Mohammed, T. A., & Al-Zawi, S. (2017). Understanding of a convolutional neural network. 2017 International Conference on Engineering and Technology (ICET), 1–6. https://doi.org/10.1109/ICEngTechnol.2017.8308186

Alexander, C. M. O., McKeegan, K. D., & Altwegg, K. (2018). Water Reservoirs in Small Planetary Bodies: Meteorites, Asteroids, and Comets. Space Science Reviews, 214(1), 36. https://doi.org/10.1007/s11214-018-0474-9

Ali-Dib, M., Menou, K., Jackson, A. P., Zhu, C., & Hammond, N. (2020). Automated crater shape retrieval using weakly-supervised deep learning. Icarus, 345, 113749. https://doi.org/10.1016/j.icarus.2020.113749

Anantrasirichai, N., Biggs, J., Albino, F., & Bull, D. (2019). A deep learning approach to detecting volcano deformation from satellite imagery using synthetic datasets. Remote Sensing of Environment, 230, 111179. https://doi.org/10.1016/j.rse.2019.04.032

Anderson, S., Towner, M., Bland, P., Haikings, C., Volante, W., Sansom, E., Devillepoix, H., Shober, P., Hartig, B., Cupak, M., Jansen-Sturgeon, T., Howie, R., Benedix, G., & Deacon, G. (2020). Machine learning for semi-automated meteorite recovery. Meteoritics & Planetary Science, 55(11), 2461–2471. https://doi.org/10.1111/maps.13593

Artemieva, N., & Ivanov, B. (2004). Launch of martian meteorites in oblique impacts. Icarus, 171(1), 84–101. https://doi.org/10.1016/j.icarus.2004.05.003

Arvidson, R., Drozd, R., Guinness, E., Hohenberg, C., Morgan, C., Morrison, R., & Oberbeck, V. (1976). Cosmic ray exposure ages of Apollo 17 samples and the age of Tycho. Lunar and Planetary Science Conference Proceedings, 3, 2817–2832.

Bailey, M. E. (1991). Comet craters versus asteroid craters. Advances in Space Research, 11(6), 43–60. https://doi.org/10.1016/0273-1177(91)90231-8

Baldwin, R. B. (1964). Lunar crater counts. The Astronomical Journal, 69, 377. https://doi.org/10.1086/109289

Baldwin, R. B. (1965). Mars: An Estimate of the Age of Its Surface. Science, 149(3691), 1498–1499. https://doi.org/10.1126/science.149.3691.1498

Baldwin, R. B. (1987). On the relative and absolute ages of seven lunar front face basins: I. From Viscosity Arguments. Icarus, 71(1), 1–18. https://doi.org/10.1016/0019-1035(87)90158-8

Bandfield, J. L., Ghent, R. R., Vasavada, A. R., Paige, D. A., Lawrence, S. J., & Robinson, M. S. (2011). Lunar surface rock abundance and regolith fines temperatures derived from LRO Diviner Radiometer data. Journal of Geophysical Research, 116, E00H02. https://doi.org/10.1029/2011JE003866

Barker, M. K., Mazarico, E., Neumann, G. A., Zuber, M. T., Haruyama, J., & Smith, D. E. (2016). A new lunar digital elevation model from the Lunar Orbiter Laser Altimeter and SELENE Terrain Camera. Icarus, 273, 346–355. https://doi.org/10.1016/j.icarus.2015.07.039

Barnes, J. J., Kring, D. A., Tartèse, R., Franchi, I. A., Anand, M., & Russell, S. S. (2016). An asteroidal origin for water in the Moon. Nature Communications, 7(1), 11684. https://doi.org/10.1038/ncomms11684

Bart, G. D., Nickerson, R. D., Lawder, M. T., & Melosh, H. J. (2011). Global survey of lunar regolith depths from LROC images. Icarus, 215(2), 485–490. https://doi.org/10.1016/j.icarus.2011.07.017

Basilevsky, A. T., Head, J. W., & Horz, F. (2013). Survival times of meter-sized boulders on the surface of the Moon. Planetary and Space Science, 89, 118–126. https://doi.org/10.1016/j.pss.2013.07.011

Basilevsky, A. T., Kreslavsky, M. A., Karachevtseva, I. P., & Gusakova, E. N. (2014). Morphometry of small impact craters in the Lunokhod-1 and Lunokhod-2 study areas. Planetary and Space Science, 92, 77–87. https://doi.org/10.1016/j.pss.2013.12.016

Benedix, G. K., Lagain, A., Chai, K., Meka, S., Anderson, S., Norman, C., Bland, P. A., Paxman, J., Towner, M. C., & Tan, T. (2020). Deriving Surface Ages on Mars Using Automated Crater Counting. Earth and Space Science, 7(3). https://doi.org/10.1029/2019EA001005

Benjamin, J., O'Leary, M., McDonald, J., Wiseman, C., McCarthy, J., Beckett, E., Morrison, P., Stankiewicz, F., Leach, J., Hacker, J., Baggaley, P., Jerbić, K., Fowler, M., Fairweather, J., Jeffries, P., Ulm, S., & Bailey, G. (2020). Aboriginal artefacts on the continental shelf reveal ancient drowned cultural landscapes in northwest Australia. PLOS ONE, 15(7), e0233912. https://doi.org/10.1371/journal.pone.0233912

Bhavsar, H., & Ganatra, A. (2012). A Comparative Study of Training Algorithms for Supervised Machine Learning. International Journal of Soft Computing and Engineering (IJSCE), 2(4), 74–81.

Bickel, V. T., Aaron, J., Manconi, A., Loew, S., & Mall, U. (2020). Impacts drive lunar rockfalls over billions of years. Nature Communications, 11(1), 2862. https://doi.org/10.1038/s41467-020-16653-3

Bickel, V. T., Conway, S. J., Tesson, P.-A., Manconi, A., Loew, S., & Mall, U. (2020). Deep Learning-Driven Detection and Mapping of Rockfalls on Mars. IEEE Journal of Selected Topics in Applied Earth Observations and Remote Sensing, 13, 2831–2841. https://doi.org/10.1109/JSTARS.2020.2991588

Bierhaus, E. B., Chapman, C. R., & Merline, W. J. (2005). Secondary craters on Europa and implications for cratered surfaces. Nature, 437(7062), 1125–1127. https://doi.org/10.1038/nature04069

Bierhaus, E. B., McEwen, A. S., Robbins, S. J., Singer, K. N., Dones, L., Kirchoff, M. R., & Williams, J. -P. (2018). Secondary craters and ejecta across the solar system: Populations and effects on impact-crater–based chronologies. Meteoritics & Planetary Science, 53(4), 638–671. https://doi.org/10.1111/maps.13057

Bogard, D. D. (1995). Impact ages of meteorites: A synthesis. Meteoritics, 30(3), 244–268. https://doi.org/10.1111/j.1945-5100.1995.tb01124.x

Bogard, D. D., Garrison, D. H., McKay, D. S., & Wentworth, S. J. (1992). The Age of Copernicus: New Evidence for 800+15 Million Years. 23, 133.

Bottke, W. F., Brož, M., O'Brien, D. P., Campo Bagatin, A., Morbidelli, A., & Marchi, S. (2015). The Collisional Evolution of the Main Asteroid Belt. In P. Michel, F. E. DeMeo, & W. F. Bottke (Eds.), Asteroids IV. University of Arizona Press. https://doi.org/10.2458/azu_uapress_9780816532131-ch036

Bottke, W. F., & Norman, M. D. (2017). The Late Heavy Bombardment. Annual Review of Earth and Planetary Sciences, 45(1), 619–647. https://doi.org/10.1146/annurev-earth-063016-020131

Bottke, W., Morbidelli, A., Jedicke, R., Petit, J., Levison, H., Michel, P., & Metcalfe, T. (2002). Debiased Orbital and Absolute Magnitude Distribution of the Near-Earth Objects. Icarus, 156(2), 399–433. https://doi.org/10.1006/icar.2001.6788

Boyce, J. M., & Johnson, D. A. (1977). Ages of flow units in Mare Crisium based on crater density. Lunar and Planetary Science Conference Proceedings, 3, 3495–3502.

Bray, V. J., Collins, G. S., Morgan, J. V., & Schenk, P. M. (2008). The effect of target properties on crater morphology: Comparison of central peak craters on the Moon and Ganymede. Meteoritics & Planetary Science, 43(12), 1979–1992. https://doi.org/10.1111/j.1945-5100.2008.tb00656.x

Brown, P., Spalding, R. E., ReVelle, D. O., Tagliaferri, E., & Worden, S. P. (2002). The flux of small near-Earth objects colliding with the Earth. Nature, 420(6913), 294–296. https://doi.org/10.1038/nature01238

Bulyshev, A., Vanek, M., Amzajerdian, F., Pierrottet, D., Hines, G., & Reisse, R. (2011). A super-resolution algorithm for enhancement of FLASH LIDAR data (C. A. Bouman, I. Pollak, & P. J. Wolfe, Eds.; p. 78730F). https://doi.org/10.1117/12.876283

Bussey, B., & Spudis, P. (2004). The Clementine Atlas of the Moon (1st ed.). Cambridge University Press. https://doi.org/10.1017/CBO9780511470820

Cadogan, P. H. (2020). Automated precision counting of very small craters at lunar landing sites. Icarus, 348, 113822. https://doi.org/10.1016/j.icarus.2020.113822

Cambioni, S., Delbo, M., Ryan, A. J., Furfaro, R., & Asphaug, E. (2019). Constraining the thermal properties of planetary surfaces using machine learning: Application to airless bodies. Icarus, 325, 16–30. https://doi.org/10.1016/j.icarus.2019.01.017

Canup, R. M., & Asphaug, E. (2001). Origin of the Moon in a giant impact near the end of the Earth's formation. Nature, 412(6848), 708–712. https://doi.org/10.1038/35089010

Carr, M. H. (1974). The role of lava erosion in the formation of lunar rilles and Martian channels. Icarus, 22(1), 1–23. https://doi.org/10.1016/0019-1035(74)90162-6

Chapman, C. R. (2015). A Critique of Methods for Analysis of Crater Size-Frequency Distributions.

Chapman, C. R., & Haefner, R. R. (1967). A critique of methods for analysis of the diameter-frequency relation for craters with special application to the Moon. Journal of Geophysical Research, 72(2), 549–557. https://doi.org/10.1029/JZ072i002p00549

Che, X., Nemchin, A., Liu, D., Long, T., Wang, C., Norman, M. D., Joy, K. H., Tartese, R., Head, J., Jolliff, B., Snape, J. F., Neal, C. R., Whitehouse, M. J., Crow, C., Benedix, G., Jourdan, F., Yang, Z., Yang, C., Liu, J., … Webb, S. G. (2021). Age and composition of young basalts on the Moon, measured

from samples returned by Chang'e-5. Science, 374(6569), 887–890. https://doi.org/10.1126/science.abl7957

Chen, M., Lei, M., Liu, D., Zhou, Y., Zhao, H., & Qian, K. (2017). Morphological Features-Based Descriptive Index System for Lunar Impact Craters. ISPRS International Journal of Geo-Information, 7(1), 5. https://doi.org/10.3390/ijgi7010005

Chen, Y., Huang, Q., Zhao, J., & Hu, X. (2021). Unsupervised Machine Learning on Domes in the Lunar Gardner Region: Implications for Dome Classification and Local Magmatic Activities on the Moon. Remote Sensing, 13(5), 845. https://doi.org/10.3390/rs13050845

Cheng, H.-T., Sun, F.-T., Buthpitiya, S., Zhang, Y., & Nefian, A. V. (2010). Lunar Image Classification for Terrain Detection. In G. Bebis, R. Boyle, B. Parvin, D. Koracin, R. Chung, R. Hammound, M. Hussain, T. Kar-Han, R. Crawfis, D. Thalmann, D. Kao, & L. Avila (Eds.), Advances in Visual Computing (Vol. 6455, pp. 1–8). Springer Berlin Heidelberg. https://doi.org/10.1007/978-3-642-17277-9_1

Chin, G., Brylow, S., Foote, M., Garvin, J., Kasper, J., Keller, J., Litvak, M., Mitrofanov, I., Paige, D., Raney, K., Robinson, M., Sanin, A., Smith, D., Spence, H., Spudis, P., Stern, S. A., & Zuber, M. (2007). Lunar Reconnaissance Orbiter Overview: The Instrument Suite and Mission. Space Science Reviews, 129(4), 391–419. https://doi.org/10.1007/s11214-007-9153-y

Cintala, M. J., & Grieve, R. A. F. (1998). Scaling impact melting and crater dimensions: Implications for the lunar cratering record. Meteoritics & Planetary Science, 33(4), 889–912. https://doi.org/10.1111/j.1945-5100.1998.tb01695.x

Cintala, M. J., Wood, C. A., & Head, J. W. (1977). The effects of target characteristics on fresh crater morphology: Preliminary results for the moon and Mercury. Lunar and Planetary Science Conference Proceedings, 3, 3409–3425.

Cole, G. H. A. (2002). Planetary Science: The Science of Planets Around Stars (1st ed.). Taylor & Francis. https://doi.org/10.1201/9781420056853

Collins, G. S., Melosh, H. J., & Ivanov, B. A. (2004). Modeling damage and deformation in impact simulations. Meteoritics & Planetary Science, 39(2), 217–231. https://doi.org/10.1111/j.1945-5100.2004.tb00337.x

Collins, G. S., Melosh, H. J., & Osinski, G. R. (2012). The Impact-Cratering Process. Elements, 8(1), 25–30. https://doi.org/10.2113/gselements.8.1.25

Craddock, R. A., & Howard, A. D. (2000). Simulated degradation of lunar impact craters and a new method for age dating farside mare deposits. Journal of Geophysical Research: Planets, 105(E8), 20387–20401. https://doi.org/10.1029/1999JE001099

Crater analysis techniques working group. (1979). Standard techniques for presentation and analysis of crater size-frequency data. Icarus, 37(2), 467–474. https://doi.org/10.1016/0019-1035(79)90009-5

Crawford, I. A. (2015). Lunar resources: A review. Progress in Physical Geography: Earth and Environment, 39(2), 137–167. https://doi.org/10.1177/0309133314567585

Curtis, A. (2021). Solar System Treks Mosaic Pipeline (SSTMP) [Python]. NASA Jet Propulsion Laboratory. https://github.com/nasa-jpl/sstmp (Original work published 2020)

Daubar, I. J., Atwood-Stone, C., Byrne, S., McEwen, A. S., & Russell, P. S. (2014). The morphology of small fresh craters on Mars and the Moon: Fresh Crater d/D on Mars and the Moon. Journal of Geophysical Research: Planets, 119(12), 2620–2639. https://doi.org/10.1002/2014JE004671

DeLatte, D. M., Crites, S. T., Guttenberg, N., & Yairi, T. (2019). Automated crater detection algorithms from a machine learning perspective in the convolutional neural network era. Advances in Space Research, 64(8), 1615–1628. https://doi.org/10.1016/j.asr.2019.07.017

Demidova, S. I., Nazarov, M. A., Lorenz, C. A., Kurat, G., Brandstätter, F., & Ntaflos, Th. (2007). Chemical composition of lunar meteorites and the lunar crust. Petrology, 15(4), 386–407. https://doi.org/10.1134/S0869591107040042

Denevi, B. W., Robinson, M. S., Boyd, A. K., Sato, H., Hapke, B. W., & Hawke, B. R. (2014). Characterization of space weathering from Lunar Reconnaissance Orbiter Camera ultraviolet observations of the Moon. Journal of Geophysical Research: Planets, 119(5), 976–997. https://doi.org/10.1002/2013JE004527

Di, K., Li, W., Yue, Z., Sun, Y., & Liu, Y. (2014). A machine learning approach to crater detection from topographic data. Advances in Space Research, 54(11), 2419–2429. https://doi.org/10.1016/j.asr.2014.08.018

Di Tommaso, P., Chatzou, M., Floden, E. W., Barja, P. P., Palumbo, E., & Notredame, C. (2017). Nextflow enables reproducible computational workflows. Nature Biotechnology, 35(4), 316–319. https://doi.org/10.1038/nbt.3820

Drozd, R. J., Hohenberg, C. M., Morgan, C. J., Podosek, F. A., & Wroge, M. L. (1977). Cosmic Ray Exposure History at Taurus-Littrow. 8, 254.

Drozd, R. J., Hohenberg, C. M., Morgan, C. J., & Ralston, C. E. (1974). Cosmic-ray exposure history at the Apollo 16 and other lunar sites: Lunar surface dynamics. Geochimica et Cosmochimica Acta, 38(10), 1625–1642. https://doi.org/10.1016/0016-7037(74)90178-1

Dundas, C. M., & McEwen, A. S. (2007). Rays and secondary craters of Tycho. Icarus, 186(1), 31–40. https://doi.org/10.1016/j.icarus.2006.08.011

Dureja, A., & Pahwa, P. (2019). Analysis of Non-Linear Activation Functions for Classification Tasks Using Convolutional Neural Networks. Recent Patents on Computer Science, 12(3), 156–161. https://doi.org/10.2174/2213275911666181025143029

Fassett, C. I. (2016). Analysis of impact crater populations and the geochronology of planetary surfaces in the inner solar system: Crater Populations and Surface Chronology. Journal of Geophysical Research: Planets, 121(10), 1900–1926. https://doi.org/10.1002/2016JE005094

Fassett, C. I., & Thomson, B. J. (2014). Crater degradation on the lunar maria: Topographic diffusion and the rate of erosion on the Moon: Crater degradation on the lunar maria. Journal of Geophysical Research: Planets, 119(10), 2255–2271. https://doi.org/10.1002/2014JE004698

Federico, A., Karagiannis, T., Karri, K., Kishore, D., Koga, Y., Campbell, J. D., & Monti, S. (2019). Pipeliner: A Nextflow-Based Framework for the Definition of Sequencing Data Processing Pipelines. Frontiers in Genetics, 10, 614. https://doi.org/10.3389/fgene.2019.00614

Fielder, G. (1965). Distribution of Craters on the Lunar Surface. Monthly Notices of the Royal Astronomical Society, 129(5), 351–361. https://doi.org/10.1093/mnras/129.5.351

Fortezzo, C. M., Spudis, P. D., & Harrel, S. L. (2020). Release of the Digital Unified Global Geologic Map of the Moon at 1:5,000,000-Scale. 2760.

French, B. M. (1998). Traces of Catastrophe: A Handbook of Shock-Metamorphic Effects in Terrestrial Meteorite Impact Structures. In Traces of Catastrophe: A Handbook of Shock-Metamorphic Effects in Terrestrial Meteorite Impact Structures. LPI Contribution No. 954. https://ui.adsabs.harvard.edu/abs/1998trca.book.....F

Gaffey, M. J., Telles, E., Dupke, R., & Lazzaro, D. (2011). Mineralogy of Asteroids. 129–169. https://doi.org/10.1063/1.3636041

Galilei, G. (1610). Sidereus Nuncius. Thomas Baglioni, Venice, Italy, 1–29.

Gault, D. E. (1970). Saturation and Equilibrium Conditions for Impact Cratering on the Lunar Surface: Criteria and Implications. Radio Science, 5(2), 273–291. https://doi.org/10.1029/RS005i002p00273

Ghent, R. R., Hayne, P. O., Bandfield, J. L., Campbell, B. A., Allen, C. C., Carter, L. M., & Paige, D. A. (2014). Constraints on the recent rate of lunar ejecta breakdown and implications for crater ages. Geology, 42(12), 1059–1062. https://doi.org/10.1130/G35926.1

Giguere, T. A., Boyce, J. M., Gillis-Davis, J. J., Trang, D., & Stopar, J. D. (2022). Lava flow ages in northeastern Oceanus Procellarum: The need for calibrating crater counting procedures. Icarus, 375, 114838. https://doi.org/10.1016/j.icarus.2021.114838

Gladman, B. J., Migliorini, F., Morbidelli, A., Zappalà, V., Michel, P., Cellino, A., Froeschlé, C., Levison, H. F., Bailey, M., & Duncan, M. (1997). Dynamical Lifetimes of Objects Injected into Asteroid Belt Resonances. Science, 277(5323), 197–201. https://doi.org/10.1126/science.277.5323.197

Golovko, V., Kroshchanka, A., & Treadwell, D. (2016). The nature of unsupervised learning in deep neural networks: A new understanding and novel approach. Optical Memory and Neural Networks, 25(3), 127–141. https://doi.org/10.3103/S1060992X16030073

Goulas, A., & Friel, R. J. (2016). 3D printing with moondust. Rapid Prototyping Journal, 22(6), 864–870. https://doi.org/10.1108/RPJ-02-2015-0022

Grady, M. M., Hutchison, R., McCall, G. J. H., & Rothery, D. A. (1998). Meteorites: Their flux with time and impact effects. Geological Society, London, Special Publications, 140(1), 1–5. https://doi.org/10.1144/GSL.SP.1998.140.01.01

Gråe Jørgensen, U., Appel, P. W. U., Hatsukawa, Y., Frei, R., Oshima, M., Toh, Y., & Kimura, A. (2009). The Earth–Moon system during the late heavy bombardment period – Geochemical support for impacts dominated by comets. Icarus, 204(2), 368–380. https://doi.org/10.1016/j.icarus.2009.07.015

Grier, J. A., McEwen, A. S., Lucey, P. G., Milazzo, M., & Strom, R. G. (2001). Optical maturity of ejecta from large rayed lunar craters. Journal of Geophysical Research: Planets, 106(E12), 32847–32862. https://doi.org/10.1029/1999JE001160

Gu, J., Wang, Z., Kuen, J., Ma, L., Shahroudy, A., Shuai, B., Liu, T., Wang, X., Wang, G., Cai, J., & Chen, T. (2018). Recent advances in convolutional neural networks. Pattern Recognition, 77, 354–377. https://doi.org/10.1016/j.patcog.2017.10.013

Hartmann, W. (2001). Martian Cratering 7: The Role of Impact Gardening. Icarus, 149(1), 37–53. https://doi.org/10.1006/icar.2000.6532

Hartmann, W. K. (1965). Terrestrial and lunar flux of large meteorites in the last two billion years. Icarus, 4(2), 157–165. https://doi.org/10.1016/0019-1035(65)90057-6
Hartmann, W. K. (1966). Martian Cratering. Icarus, 5(1–6), 565–576. https://doi.org/10.1016/0019-1035(66)90071-6
Hartmann, W. K. (1971a). Martian cratering II: Asteroid impact history. Icarus, 15(3), 396–409. https://doi.org/10.1016/0019-1035(71)90118-7
Hartmann, W. K. (1971b). Martian cratering III: Theory of crater obliteration. Icarus, 15(3), 410–428. https://doi.org/10.1016/0019-1035(71)90119-9
Hartmann, W. K. (1972). Paleocratering of the Moon: Review of post-Apollo data. Astrophysics and Space Science, 17(1), 48–64. https://doi.org/10.1007/BF00642541
Hartmann, W. K. (1973). Ancient lunar mega-regolith and subsurface structure. Icarus, 18(4), 634–636. https://doi.org/10.1016/0019-1035(73)90066-3
Hartmann, W. K. (1977). Relative crater production rates on planets. Icarus, 31(2), 260–276. https://doi.org/10.1016/0019-1035(77)90037-9
Hartmann, W. K. (1984). Does crater “saturation equilibrium” occur in the solar system? Icarus, 60(1), 56–74. https://doi.org/10.1016/0019-1035(84)90138-6
Hartmann, W. K. (1995). Planetary cratering 1. The question of multiple impactor populations: Lunar evidence. Meteoritics, 30(4), 451–467. https://doi.org/10.1111/j.1945-5100.1995.tb01152.x
Hartmann, W. K. (1999). Martian cratering VI: Crater count isochrons and evidence for recent volcanism from Mars Global Surveyor. Meteoritics & Planetary Science, 34(2), 167–177. https://doi.org/10.1111/j.1945-5100.1999.tb01743.x
Hartmann, W. K. (2005). Martian cratering 8: Isochron refinement and the chronology of Mars. Icarus, 174(2), 294–320. https://doi.org/10.1016/j.icarus.2004.11.023
Hartmann, W. K. (2007). Martian cratering 9: Toward resolution of the controversy about small craters. Icarus, 189(1), 274–278. https://doi.org/10.1016/j.icarus.2007.02.011
Hartmann, W. K., & Daubar, I. J. (2017). Martian cratering 11. Utilizing decameter scale crater populations to study Martian history. Meteoritics & Planetary Science, 52(3), 493–510. https://doi.org/10.1111/maps.12807
Hartmann, W. K., & Davis, D. R. (1975). Satellite-sized planetesimals and lunar origin. Icarus, 24(4), 504–515. https://doi.org/10.1016/0019-1035(75)90070-6
Hartmann, W. K., & Neukum, G. (2001). Cratering Chronology and the Evolution of Mars. In R. Kallenbach, J. Geiss, & W. K. Hartmann (Eds.), Chronology and Evolution of Mars (Vol. 12, pp. 165–194). Springer Netherlands. https://doi.org/10.1007/978-94-017-1035-0_6
Haruyama, J., Ohtake, M., Matsunaga, T., Morota, T., Yokota, Y., Honda, C., Hirata, N., Demura, H., Iwasaki, A., Nakamura, R., & Kodama, S. (2008). Planned radiometrically calibrated and geometrically corrected products of lunar high-resolution Terrain Camera on SELENE. Advances in Space Research, 42(2), 310–316. https://doi.org/10.1016/j.asr.2007.04.062
Hashimoto, S., & Mori, K. (2019). Lunar Crater Detection based on Grid Partition using Deep Learning. 2019 IEEE 13th International Symposium on Applied Computational Intelligence and Informatics (SACI), 75–80. https://doi.org/10.1109/SACI46893.2019.9111474
He, F. (2020). Remote sensing of planetary space environment. Chinese Science Bulletin, 65(14), 1305–1319. https://doi.org/10.1360/TB-2019-0804

Head, J. W. (2010). Transition from complex craters to multi-ringed basins on terrestrial planetary bodies: Scale-dependent role of the expanding melt cavity and progressive interaction with the displaced zone: COMPLEX CRATERS TO MULTI-RINGED BASINS. Geophysical Research Letters, 37(2), n/a-n/a. https://doi.org/10.1029/2009GL041790

Head, J. W., Fassett, C. I., Kadish, S. J., Smith, D. E., Zuber, M. T., Neumann, G. A., & Mazarico, E. (2010). Global Distribution of Large Lunar Craters: Implications for Resurfacing and Impactor Populations. Science, 329(5998), 1504–1507. https://doi.org/10.1126/science.1195050

Head, J. W., & Wilson, L. (2020). Rethinking Lunar Mare Basalt Regolith Formation: New Concepts of Lava Flow Protolith and Evolution of Regolith Thickness and Internal Structure. Geophysical Research Letters, 47(20). https://doi.org/10.1029/2020GL088334

Heiken, G., Vaniman, D., & French, B. M. (1991). Lunar Sourcebook: A User's Guide to the Moon. CUP Archive.

Herrick, R. R., Bateman, E. M., Crumpacker, W. G., & Bates, D. (2018). Observations From a Global Database of Impact Craters on Mercury With Diameters Greater than 5 km. Journal of Geophysical Research: Planets, 123(8), 2089–2109. https://doi.org/10.1029/2017JE005516

Hiesinger, H. (2003). Ages and stratigraphy of mare basalts in Oceanus Procellarum, Mare Nubium, Mare Cognitum, and Mare Insularum. Journal of Geophysical Research, 108(E7), 5065. https://doi.org/10.1029/2002JE001985

Hiesinger, H. (2006a). NEW AGES FOR BASALTS IN MARE FECUNDITATIS BASED ON CRATER SIZE-FREQUENCY MEASUREMENTS. 2.

Hiesinger, H. (2006b). New Views of Lunar Geoscience: An Introduction and Overview. Reviews in Mineralogy and Geochemistry, 60(1), 1–81. https://doi.org/10.2138/rmg.2006.60.1

Hiesinger, H., Head, J. W., Wolf, U., Jaumann, R., & Neukum, G. (2005). New ages for basalts in Mare Fecunditatis based on crater size-frewuency measurements. 1303, abstract-1151. https://www.lpi.usra.edu/meetings/lpsc2006/pdf/1151.pdf

Hiesinger, H., Head, J. W., Wolf, U., Jaumann, R., & Neukum, G. (2011). Ages and stratigraphy of lunar mare basalts: A synthesis. In W. A. Ambrose & D. A. Williams, Recent Advances and Current Research Issues in Lunar Stratigraphy. Geological Society of America. https://doi.org/10.1130/2011.2477(01)

Hiesinger, H., Jaumann, R., Neukum, G., & Head, J. W. (2000). Ages of mare basalts on the lunar nearside. Journal of Geophysical Research: Planets, 105(E12), 29239–29275. https://doi.org/10.1029/2000JE001244

Hiesinger, H., Marchi, S., Schmedemann, N., Schenk, P., Pasckert, J. H., Neesemann, A., O'Brien, D. P., Kneissl, T., Ermakov, A. I., Fu, R. R., Bland, M. T., Nathues, A., Platz, T., Williams, D. A., Jaumann, R., Castillo-Rogez, J. C., Ruesch, O., Schmidt, B., Park, R. S., … Raymond, C. A. (2016). Cratering on Ceres: Implications for its crust and evolution. Science, 353(6303), aaf4759. https://doi.org/10.1126/science.aaf4759

Hiesinger, H., van der Bogert, C. H., Pasckert, J. H., Funcke, L., Giacomini, L., Ostrach, L. R., & Robinson, M. S. (2012). How old are young lunar craters?: HOW OLD ARE YOUNG LUNAR CRATERS? Journal of Geophysical Research: Planets, 117(E12), n/a-n/a. https://doi.org/10.1029/2011JE003935

Hildebrand, A. R., Pilkington, M., Ortiz-Aleman, C., Chavez, R. E., Urrutia-Fucugauchi, J., Connors, M., Graniel-Castro, E., Camara-Zi, A., Halpenny, J.

F., & Niehaus, D. (1998). Mapping Chicxulub crater structure with gravity and seismic reflection data. Geological Society, London, Special Publications, 140(1), 155–176. https://doi.org/10.1144/GSL.SP.1998.140.01.12

Hirabayashi, M., Minton, D. A., & Fassett, C. I. (2017). An analytical model of crater count equilibrium. Icarus, 289, 134–143. https://doi.org/10.1016/j.icarus.2016.12.032

Holsapple, K. A., & Schmidt, R. M. (1982). On the scaling of crater dimensions: 2. Impact processes. Journal of Geophysical Research, 87(B3), 1849. https://doi.org/10.1029/JB087iB03p01849

Hörz, F., Grieve, R., Heiken, G., Spudis, P., & Binder, A. (1991). Chapter 4: Lunar Surface Processes. In Lunar Sourcebook: A User's Guide to the Moon (pp. 61–120). https://ui.adsabs.harvard.edu/abs/1991lsug.book...61H

Hughes, D. W. (2003). The approximate ratios between the diameters of terrestrial impact craters and the causative incident asteroids. Monthly Notices of the Royal Astronomical Society, 338(4), 999–1003. https://doi.org/10.1046/j.1365-8711.2003.06157.x

Iqbal, W., Hiesinger, H., & van der Bogert, C. H. (2020). Geological mapping and chronology of lunar landing sites: Apollo 12. Icarus, 352, 113991. https://doi.org/10.1016/j.icarus.2020.113991

Isbell, C., Gaddis, L., Garcia, P., Hare, T., & Bailen, M. (2014). Kaguya Terrain Camera Mosaics. 2268.

Ito, T., & Malhotra, R. (2010). Asymmetric impacts of near-Earth asteroids on the Moon. Astronomy and Astrophysics, 519, A63. https://doi.org/10.1051/0004-6361/200912901

Ivanov, B. A. (2001). Mars/Moon Cratering Rate Ratio Estimates. Space Science Reviews, 96(1/4), 87–104. https://doi.org/10.1023/A:1011941121102

Ivanov, B. A. (2006). Earth/Moon impact rate comparison: Searching constraints for lunar secondary/primary cratering proportion. Icarus, 183(2), 504–507. https://doi.org/10.1016/j.icarus.2006.04.004

Ivanov, B. A., Neukum, G., Bottke, W. F., & Hartmann, W. K. (2002). The Comparison of Size-Frequency Distributions of Impact Craters and Asteroids and the Planetary Cratering Rate. Asteroids III, 1. https://www.researchgate.net/publication/253429785

Ivanov, B. A., Neukum, G., & Wagner, R. (2001). Size-Frequency Distributions of Planetary Impact Craters and Asteroids. In M. Ya. Marov & H. Rickman (Eds.), Collisional Processes in the Solar System (Vol. 261, pp. 1–34). Springer Netherlands. https://doi.org/10.1007/978-94-010-0712-2_1

Ivanov, B., Bazilevskiy, A., & Sazonova, L. G. (1986). Formation of the central uplift in meteoric craters. Meteoritika, 40.

Ji, J., Guo, D., Liu, J., Chen, S., Ling, Z., Ding, X., Han, K., Chen, J., Cheng, W., Zhu, K., Liu, J., Wang, J., Chen, J., & Ouyang, Z. (2022). The 1:2,500,000-scale geologic map of the global Moon. Science Bulletin, 67(15), 1544–1548. https://doi.org/10.1016/j.scib.2022.05.021

Jia, M., Yue, Z., Di, K., Liu, B., Liu, J., & Michael, G. (2020). A catalogue of impact craters larger than 200 m and surface age analysis in the Chang'e-5 landing area. Earth and Planetary Science Letters, 541, 116272. https://doi.org/10.1016/j.epsl.2020.116272

Jia, Y., Liu, L., Wan, G., & Zhang, C. (2020). Research Progress of Lunar Impact Crater Detection. 2020 International Conference on Computer Science and

Management Technology (ICCSMT), 91–95. https://doi.org/10.1109/ICCSMT51754.2020.00025
Jocher, G. (2021). Ultralytics YOLOv3 [Python]. Ultralytics. https://github.com/ultralytics/yolov3
Jocher, G. (2022). Ultralytics YOLOv5 [Python]. Ultralytics. https://github.com/ultralytics/yolov5 (Original work published 2020)
Johnson, B. C., & Bowling, T. J. (2014). Where have all the craters gone? Earth's bombardment history and the expected terrestrial cratering record. Geology, 42(7), 587–590. https://doi.org/10.1130/G35754.1
Kallio, E., Dyadechkin, S., Wurz, P., & Khodachenko, M. (2019). Space weathering on the Moon: Farside-nearside solar wind precipitation asymmetry. Planetary and Space Science, 166, 9–22. https://doi.org/10.1016/j.pss.2018.07.013
Khan-Mayberry, N. (2008). The lunar environment: Determining the health effects of exposure to moon dusts. Acta Astronautica, 63(7–10), 1006–1014. https://doi.org/10.1016/j.actaastro.2008.03.015
Kieffer, S. W., & Simonds, C. H. (1980). The role of volatiles and lithology in the impact cratering process. Reviews of Geophysics, 18(1), 143. https://doi.org/10.1029/RG018i001p00143
Kirchoff, M. R., Marchi, S., Bottke, W. F., Chapman, C. R., & Enke, B. (2021). Suggestion that recent (≤ 3 Ga) flux of kilometer and larger impactors in the Earth-Moon system has not been constant. Icarus, 355, 114110. https://doi.org/10.1016/j.icarus.2020.114110
Kirchoff, M. R., & Schenk, P. (2015). Dione's resurfacing history as determined from a global impact crater database. Icarus, 256, 78–89. https://doi.org/10.1016/j.icarus.2015.04.010
Kirkland, C. L., Sutton, P. J., Erickson, T., Johnson, T. E., Hartnady, M. I. H., Smithies, H., & Prause, M. (2022). Did transit through the galactic spiral arms seed crust production on the early Earth? Geology, 50(11), 1312–1317. https://doi.org/10.1130/G50513.1
Kneissl, T., van Gasselt, S., & Neukum, G. (2011). Map-projection-independent crater size-frequency determination in GIS environments—New software tool for ArcGIS. Planetary and Space Science, 59(11–12), 1243–1254. https://doi.org/10.1016/j.pss.2010.03.015
Kodikara, G. R. L., & McHenry, L. J. (2020). Machine learning approaches for classifying lunar soils. Icarus, 345, 113719. https://doi.org/10.1016/j.icarus.2020.113719
Kopal, Z. (2013). Physics and Astronomy of the Moon. Academic Press.
Korochantseva, E. V., Trieloff, M., Lorenz, C. A., Buykin, A. I., Ivanova, M. A., Schwarz, W. H., Hopp, J., & Jessberger, E. K. (2007). L-chondrite asteroid breakup tied to Ordovician meteorite shower by multiple isochron 40 Ar- 39 Ar dating. Meteoritics & Planetary Science, 42(1), 113–130. https://doi.org/10.1111/j.1945-5100.2007.tb00221.x
Koushik, J. (2016). Understanding Convolutional Neural Networks. https://doi.org/10.48550/ARXIV.1605.09081
Krüger, T., Hergarten, S., & Kenkmann, T. (2018). Deriving Morphometric Parameters and the Simple-to-Complex Transition Diameter From a High-Resolution, Global Database of Fresh Lunar Impact Craters (D ≥ ~ 3 km). Journal of Geophysical Research: Planets, 123(10), 2667–2690. https://doi.org/10.1029/2018JE005545

La Grassa, R., Cremonese, G., Gallo, I., Re, C., & Martellato, E. (2023). YOLOLens: A Deep Learning Model Based on Super-Resolution to Enhance the Crater Detection of the Planetary Surfaces. Remote Sensing, 15(5), 1171. https://doi.org/10.3390/rs15051171

Lagain, A., Benedix, G. K., Servis, K., Baratoux, D., Doucet, L. S., Rajšic, A., Devillepoix, H. A. R., Bland, P. A., Towner, M. C., Sansom, E. K., & Miljković, K. (2021). The Tharsis mantle source of depleted shergottites revealed by 90 million impact craters. Nature Communications, 12(1), 6352. https://doi.org/10.1038/s41467-021-26648-3

Lagain, A., Bouley, S., Baratoux, D., Costard, F., & Wieczorek, M. (2020). Impact cratering rate consistency test from ages of layered ejecta on Mars. Planetary and Space Science, 180, 104755. https://doi.org/10.1016/j.pss.2019.104755

Lagain, A., Bouley, S., Baratoux, D., Marmo, C., Costard, F., Delaa, O., Pio Rossi, A., Minin, M., Benedix, G. K., Ciocco, M., Bedos, B., Guimpier, A., Dehouck, E., Loizeau, D., Bouquety, A., Zhao, J., Vialatte, A., Cormau, M., Le Conte des Floris, E., … Gamblin, O. (2021a). Mars Crater Database: A participative project for the classification of the morphological characteristics of large Martian craters. In W. U. Reimold & C. Koeberl (Eds.), Large Meteorite Impacts and Planetary Evolution VI. Geological Society of America. https://doi.org/10.1130/2021.2550(29)

Lagain, A., Bouley, S., Zanda, B., Miljković, K., Rajšić, A., Baratoux, D., Payré, V., Doucet, L. S., Timms, N. E., Hewins, R., Benedix, G. K., Malarewic, V., Servis, K., & Bland, P. A. (2022). Early crustal processes revealed by the ejection site of the oldest martian meteorite. Nature Communications, 13(1), 3782. https://doi.org/10.1038/s41467-022-31444-8

Lagain, A., Devillepoix, H., & Shober, P. (2021b). Latitudinal dependency of the impact rate: Any room for a recalibration of crater chronologies ? [dataset]. In Earth and Planetary Science Letters (1.2). https://doi.org/10.5281/ZENODO.5140495

Lagain, A., Kreslavsky, M., Baratoux, D., Liu, Y., Devillepoix, H., Bland, P., Benedix, G. K., Doucet, L. S., & Servis, K. (2022). Has the impact flux of small and large asteroids varied through time on Mars, the Earth and the Moon? Earth and Planetary Science Letters, 579, 117362. https://doi.org/10.1016/j.epsl.2021.117362

Lagain, A., Servis, K., Benedix, G. K., Norman, C., Anderson, S., & Bland, P. A. (2021c). Model Age Derivation of Large Martian Impact Craters, Using Automatic Crater Counting Methods. Earth and Space Science, 8(2). https://doi.org/10.1029/2020EA001598

Lai, J., Xu, Y., Zhang, X., Xiao, L., Yan, Q., Meng, X., Zhou, B., Dong, Z., & Zhao, D. (2019). Comparison of Dielectric Properties and Structure of Lunar Regolith at Chang'e-3 and Chang'e-4 Landing Sites Revealed by Ground-Penetrating Radar. Geophysical Research Letters, 46(22), 12783–12793. https://doi.org/10.1029/2019GL084458

Laul, J. C., & Papike, J. J. (1980). The lunar regolith: Comparative chemistry of the Apollo sites. Lunar and Planetary Science Conference Proceedings, 2, 1307–1340.

Le Feuvre, M., & Wieczorek, M. A. (2011). Nonuniform cratering of the Moon and a revised crater chronology of the inner Solar System. Icarus, 214(1), 1–20. https://doi.org/10.1016/j.icarus.2011.03.010

Lee, C. (2019). Automated crater detection on Mars using deep learning. Planetary and Space Science, 170, 16–28. https://doi.org/10.1016/j.pss.2019.03.008

Lee, C., & Hogan, J. (2021). Automated crater detection with human level performance. Computers & Geosciences, 147, 104645. https://doi.org/10.1016/j.cageo.2020.104645

Lee, C. M., Cable, M. L., Hook, S. J., Green, R. O., Ustin, S. L., Mandl, D. J., & Middleton, E. M. (2015). An introduction to the NASA Hyperspectral InfraRed Imager (HyspIRI) mission and preparatory activities. Remote Sensing of Environment, 167, 6–19. https://doi.org/10.1016/j.rse.2015.06.012

Legett, C., IV, Glotch, T. D., & Lucey, P. G. (2015). Quantifying the VNIR Effects of Nanophase Iron Generated through the Space Weathering of Silicates: Reconciling Modeled Data with Laboratory Observations. 2015, P44A-03.

Li, C., Su, Y., Pettinelli, E., Xing, S., Ding, C., Liu, J., Ren, X., Lauro, S. E., Soldovieri, F., Zeng, X., Gao, X., Chen, W., Dai, S., Liu, D., Zhang, G., Zuo, W., Wen, W., Zhang, Z., Zhang, X., & Zhang, H. (2020). The Moon's farside shallow subsurface structure unveiled by Chang'E-4 Lunar Penetrating Radar. Science Advances, 6(9), eaay6898. https://doi.org/10.1126/sciadv.aay6898

Li, H.-C., Zhang, N., Yue, Z.-Y., & Zhang, Y.-Z. (2021). Lunar cratering asymmetries with high lunar orbital obliquity and inclination of the Moon. Research in Astronomy and Astrophysics, 21(6), 140. https://doi.org/10.1088/1674-4527/21/6/140

Li, Y., Basilevsky, A. T., Xie, M., & Ip, W.-H. (2018). Correlations between ejecta boulder spatial density of small lunar craters and the crater age. Planetary and Space Science, 162, 52–61. https://doi.org/10.1016/j.pss.2017.08.007

Liao, S., Huyskens, M. H., Yin, Q.-Z., & Schmitz, B. (2020). Absolute dating of the L-chondrite parent body breakup with high-precision U–Pb zircon geochronology from Ordovician limestone. Earth and Planetary Science Letters, 547, 116442. https://doi.org/10.1016/j.epsl.2020.116442

Magdalena-Benedito, R., Martínez-Sober, M., Martínez-Martínez, J. M., Vila-Francés, J., & Escandell-Montero, P. (Eds.). (2012). Intelligent Data Analysis for Real-Life Applications: Theory and Practice. IGI Global. https://doi.org/10.4018/978-1-4666-1806-0

Mahanti, P., Robinson, M. S., Thompson, T. J., & Henriksen, M. R. (2018). Small lunar craters at the Apollo 16 and 17 landing sites—Morphology and degradation. Icarus, 299, 475–501. https://doi.org/10.1016/j.icarus.2017.08.018

Marchi, S., Bottke, W. F., Kring, D. A., & Morbidelli, A. (2012). The onset of the lunar cataclysm as recorded in its ancient crater populations. Earth and Planetary Science Letters, 325–326, 27–38. https://doi.org/10.1016/j.epsl.2012.01.021

Mazarico, E., Neumann, G. A., Smith, D. E., Zuber, M. T., & Torrence, M. H. (2011). Illumination conditions of the lunar polar regions using LOLA topography. Icarus, 211(2), 1066–1081. https://doi.org/10.1016/j.icarus.2010.10.030

Mazrouei, S., Ghent, R. R., Bottke, W. F., Parker, A. H., & Gernon, T. M. (2019). Earth and Moon impact flux increased at the end of the Paleozoic. Science, 363(6424), 253–257. https://doi.org/10.1126/science.aar4058

McDonald, J., Mulvaney, K., Beckett, E., Fairweather, J., Morrison, P., de Koning, S., Dortch, J., & Jeffries, P. (2021). Seeing and managing rock art at Nganjarli: A tourist destination in Murujuga National Park, Western Australia.

Australian Archaeology, 87(3), 268–293. https://doi.org/10.1080/03122417.2021.1978915
McEwen, A. S., & Bierhaus, E. B. (2006). The Importance of Secondary Cratering to Age Constraints on Planetary Surfaces. Annual Review of Earth and Planetary Sciences, 34(1), 535–567. https://doi.org/10.1146/annurev.earth.34.031405.125018
McEwen, A. S., Gaddis, L. R., Neukum, G., Hoffman, H., Pieters, C. M., & Head, J. W. (1993). Galileo observations of post-imbrium lunar craters during the first Eearth-Moon flyby. Journal of Geophysical Research, 98(E9), 17207. https://doi.org/10.1029/93JE01137
McGetchin, T. R., Settle, M., & Head, J. W. (1973). Radial thickness variation in impact crater ejecta: Implications for lunar basin deposits. Earth and Planetary Science Letters, 20(2), 226–236. https://doi.org/10.1016/0012-821X(73)90162-3
Mckay, D. S., Fruland, R. M., & Heiken, G. H. (1974). Grain size and the evolution of lunar soils. 1, 887–906.
Mckay, D. S., Heiken, G., Basu, A., Blanford, G., Simon, S., Reedy, R., French, B. M., & Papike, J. (1991). Chapter 7: The Lunar Regolith. In Lunar Sourcebook: A User's Guide to the Moon (pp. 285–356). Cambridge University Press. https://citeseerx.ist.psu.edu/viewdoc/download?doi=10.1.1.251.2682&rep=rep1&type=pdf
Mckay, D. S., & Ming, D. W. (1990). Properties of Lunar Regolith. In Developments in Soil Science (Vol. 19, pp. 449–462). Elsevier. https://doi.org/10.1016/S0166-2481(08)70360-X
McMahon, S. K. (1996). Overview of the Planetary Data System. Planetary and Space Science, 44(1), 3–12. https://doi.org/10.1016/0032-0633(95)00101-8
Melosh, H. J. (1989). Impact Cratering: A Geologic Process. Oxford University Press. https://books.google.com.au/books?id=nZwRAQAAIAAJ
Melosh, H. J., & Ivanov, B. A. (1999). Impact Crater Collapse. Annual Review of Earth and Planetary Sciences, 27(1), 385–415. https://doi.org/10.1146/annurev.earth.27.1.385
Michael, G. G. (2013). Planetary surface dating from crater size–frequency distribution measurements: Multiple resurfacing episodes and differential isochron fitting. Icarus, 226(1), 885–890. https://doi.org/10.1016/j.icarus.2013.07.004
Michael, G. G., Kneissl, T., & Neesemann, A. (2016). Planetary surface dating from crater size-frequency distribution measurements: Poisson timing analysis. Icarus, 277, 279–285. https://doi.org/10.1016/j.icarus.2016.05.019
Michael, G. G., & Neukum, G. (2010). Planetary surface dating from crater size–frequency distribution measurements: Partial resurfacing events and statistical age uncertainty. Earth and Planetary Science Letters, 294(3–4), 223–229. https://doi.org/10.1016/j.epsl.2009.12.041
Michael, G. G., Platz, T., Kneissl, T., & Schmedemann, N. (2012). Planetary surface dating from crater size–frequency distribution measurements: Spatial randomness and clustering. Icarus, 218(1), 169–177. https://doi.org/10.1016/j.icarus.2011.11.033
Michael, G. G., Yue, Z., Gou, S., & Di, K. (2021). Dating individual several-km lunar impact craters from the rim annulus in region of planned Chang'E-5 landing: Poisson age-likelihood calculation for a buffered crater counting area.

Earth and Planetary Science Letters, 568, 117031. https://doi.org/10.1016/j.epsl.2021.117031
Mighani, S., Wang, H., Shuster, D. L., Borlina, C. S., Nichols, C. I. O., & Weiss, B. P. (2020). The end of the lunar dynamo. Science Advances, 6(1), eaax0883. https://doi.org/10.1126/sciadv.aax0883
Ming, D. W., & Henninger, D. L. (1994). Use of lunar regolith as a substrate for plant growth. Advances in Space Research, 14(11), 435–443. https://doi.org/10.1016/0273-1177(94)90333-6
Minton, D. A., Fassett, C. I., Hirabayashi, M., Howl, B. A., & Richardson, J. E. (2019). The equilibrium size-frequency distribution of small craters reveals the effects of distal ejecta on lunar landscape morphology. Icarus, 326, 63–87. https://doi.org/10.1016/j.icarus.2019.02.021
Moore, H. J., Boyce, J. M., & Hahn, D. A. (1980). Small impact craters in the lunar regolith—Their morphologies, relative ages, and rates of formation. The Moon and the Planets, 23(2), 231–524.
Morgan, E. (2001). The Moon and Life on Earth. In C. Barbieri & F. Rampazzi (Eds.), Earth-Moon Relationships (pp. 279–290). Springer Netherlands. https://doi.org/10.1007/978-94-010-0800-6_25
Morgan, J. V., Gulick, S. P. S., Bralower, T., Chenot, E., Christeson, G., Claeys, P., Cockell, C., Collins, G. S., Coolen, M. J. L., Ferrière, L., Gebhardt, C., Goto, K., Jones, H., Kring, D. A., Le Ber, E., Lofi, J., Long, X., Lowery, C., Mellett, C., … Zylberman, W. (2016). The formation of peak rings in large impact craters. Science, 354(6314), 878–882. https://doi.org/10.1126/science.aah6561
Murphy Jr, T. W., Adelberger, E. G., Battat, J. B. R., Hoyle, C. D., Johnson, N. H., McMillan, R. J., Michelsen, E. L., Stubbs, C. W., & Swanson, H. E. (2011a). Laser Ranging to the Lost Lunokhod~1 Reflector. Icarus, 211(2), 1103–1108. https://doi.org/10.1016/j.icarus.2010.11.010
Murphy Jr, T. W., Adelberger, E. G., Battat, J. B. R., Hoyle, C. D., Johnson, N. H., McMillan, R. J., Michelsen, E. L., Stubbs, C. W., & Swanson, H. E. (2011b). Laser Ranging to the Lost Lunokhod~1 Reflector. Icarus, 211(2), 1103–1108. https://doi.org/10.1016/j.icarus.2010.11.010
Namiki, N., & Honda, C. (2003). Testing hypotheses for the origin of steep slope of lunar size-frequency distribution for small craters. Earth, Planets and Space, 55(1), 39–51. https://doi.org/10.1186/BF03352461
National Research Council and National Academy of Sciences. (1989). Supercomputers: Directions in Technology and Applications (p. 1405). National Academies Press. https://doi.org/10.17226/1405
Nemtchinov, I. V., Svetsov, V. V., Kosarev, I. B., Golub', A. P., Popova, O. P., Shuvalov, V. V., Spalding, R. E., Jacobs, C., & Tagliaferri, E. (1997). Assessment of Kinetic Energy of Meteoroids Detected by Satellite-Based Light Sensors. Icarus, 130(2), 259–274. https://doi.org/10.1006/icar.1997.5821
Nesvorny, D., Broz, M., & Carruba, V. (2015). Identification and Dynamical Properties of Asteroid Families. https://doi.org/10.48550/ARXIV.1502.01628
Nesvorný, D., Vokrouhlický, D., Morbidelli, A., & Bottke, W. F. (2009). Asteroidal source of L chondrite meteorites. Icarus, 200(2), 698–701. https://doi.org/10.1016/j.icarus.2008.12.016
Neukum, G. (1984). Meteoritenbombardement und Datierung planetarer Oberflachen (Meteorite bombardment and dating of planetary surfaces). University of Munich, Germany.

Neukum, G., Ivanov, B. A., & Hartmann, W. K. (2001). Cratering Records in the Inner Solar System in Relation to the Lunar Reference System. In R. Kallenbach, J. Geiss, & W. K. Hartmann (Eds.), Chronology and Evolution of Mars (Vol. 12, pp. 55–86). Springer Netherlands. https://doi.org/10.1007/978-94-017-1035-0_3

Neukum, G., Koenig, B., Fechtig, H., & Storzer, D. (1975). Cratering in the earth-moon system: Consequences for age determination by crater counting. Lunar and Planetary Science Conference Proceedings, 3, 2597–2620.

Nordyke, M. D. (1961). Nuclear craters and preliminary theory of the mechanics of explosive crater formation. Journal of Geophysical Research, 66(10), 3439–3459. https://doi.org/10.1029/JZ066i010p03439

Norman, M. D. (2009). The Lunar Cataclysm: Reality or 'Mythconception'? Elements, 5(1), 23–28. https://doi.org/10.2113/gselements.5.1.23

Oberbeck, V. R., & Quaide, W. L. (1968). Genetic implications of Lunar regolith thickness variations. Icarus, 9(1–3), 446–465. https://doi.org/10.1016/0019-1035(68)90039-0

Öhman, T. (2015). A beginner's guide to stereo-derived DEM production and analysis using ISIS, ASP, and ArcMap. https://doi.org/10.13140/RG.2.1.1743.7609

Ono, T., Kumamoto, A., Nakagawa, H., Yamaguchi, Y., Oshigami, S., Yamaji, A., Kobayashi, T., Kasahara, Y., & Oya, H. (2009). Lunar Radar Sounder Observations of Subsurface Layers Under the Nearside Maria of the Moon. Science, 323(5916), 909–912. https://doi.org/10.1126/science.1165988

Opik, E. J. (1936). Researches on the Physical Theory of Meteor Phenomena. I. Theory of the Formation of Meteor Craters. Publications of the Tartu Astrofizica Observatory, 28, 1–12.

Opik, E. J. (1958). Meteor Impact on Solid Surface. Irish Astronomical Journal, 5, 14.

Opik, E. J. (1960). The Lunar Surface as an Impact Counter. Monthly Notices of the Royal Astronomical Society, 120(5), 404–411. https://doi.org/10.1093/mnras/120.5.404

O'Shea, K., & Nash, R. (2015). An Introduction to Convolutional Neural Networks. https://doi.org/10.48550/ARXIV.1511.08458

Papike, J. J., Ryder, G., & Shearer, C. K. (1998). Chapter 5. LUNAR SAMPLES. In J. J. Papike (Ed.), Planetary Materials (pp. 719–952). De Gruyter. https://doi.org/10.1515/9781501508806-020

Papike, J. J., Simon, S. B., & Laul, J. C. (1982). The lunar regolith: Chemistry, mineralogy, and petrology. Reviews of Geophysics, 20(4), 761. https://doi.org/10.1029/RG020i004p00761

Petro, N. E., & Pieters, C. M. (2004). Surviving the heavy bombardment: Ancient material at the surface of South Pole-Aitken Basin. Journal of Geophysical Research, 109(E6), E06004. https://doi.org/10.1029/2003JE002182

Petro, N. E., & Pieters, C. M. (2008). The lunar-wide effects of basin ejecta distribution on the early megaregolith. Meteoritics & Planetary Science, 43(9), 1517–1529. https://doi.org/10.1111/j.1945-5100.2008.tb01025.x

Pike, R. J. (1974). Ejecta from large craters on the Moon: Comments on the geometric model of McGetchin et al. Earth and Planetary Science Letters, 23(3), 265–271. https://doi.org/10.1016/0012-821X(74)90114-9

Pike, R. J. (1977). Apparent depth/apparent diameter relation for lunar craters. Lunar and Planetary Science Conference Proceedings, 3, 3427–3436.

Pike, R. J., & Wilhelms, D. E. (1978). Secondary-Impact Craters on the Moon: Topographic Form and Geologic Process. 907–909.

Povilaitis, R. Z., Robinson, M. S., van der Bogert, C. H., Hiesinger, H., Meyer, H. M., & Ostrach, L. R. (2018). Crater density differences: Exploring regional resurfacing, secondary crater populations, and crater saturation equilibrium on the moon. Planetary and Space Science, 162, 41–51. https://doi.org/10.1016/j.pss.2017.05.006

Powell, T. M., Rubanenko, L., Williams, J.-P., & Paige, D. A. (2021). The role of secondary craters on Martian crater chronology. In Mars Geological Enigmas (pp. 123–145). Elsevier. https://doi.org/10.1016/B978-0-12-820245-6.00006-9

Pozzobon, R., Tusberti, F., Pajola, M., & Massironi, M. (2020). Geologic Map, Landing Site Selection and Traverse Planning In Copernicus Crater. https://doi.org/10.5281/ZENODO.5127777

Price, D. G. (1995). Weathering and weathering processes. Quarterly Journal of Engineering Geology and Hydrogeology, 28(3), 243–252. https://doi.org/10.1144/GSL.QJEGH.1995.028.P3.03

Qian, Y., Xiao, L., Head, J. W., van der Bogert, C. H., Hiesinger, H., & Wilson, L. (2021). Young lunar mare basalts in the Chang'e-5 sample return region, northern Oceanus Procellarum. Earth and Planetary Science Letters, 555, 116702. https://doi.org/10.1016/j.epsl.2020.116702

Qian, Y., Xiao, L., Head, J. W., Wöhler, C., Bugiolacchi, R., Wilhelm, T., Althoff, S., Ye, B., He, Q., Yuan, Y., & Zhao, S. (2021). Copernican-Aged (<200 Ma) Impact Ejecta at the Chang'e-5 Landing Site: Statistical Evidence From Crater Morphology, Morphometry, and Degradation Models. Geophysical Research Letters, 48(20). https://doi.org/10.1029/2021GL095341

Qian, Y., Xiao, L., Wang, Q., Head, J. W., Yang, R., Kang, Y., van der Bogert, C. H., Hiesinger, H., Lai, X., Wang, G., Pang, Y., Zhang, N., Yuan, Y., He, Q., Huang, J., Zhao, J., Wang, J., & Zhao, S. (2021). China's Chang'e-5 landing site: Geology, stratigraphy, and provenance of materials. Earth and Planetary Science Letters, 561, 116855. https://doi.org/10.1016/j.epsl.2021.116855

Qiao, L., Head, J. W., Xiao, L., Wilson, L., & Dufek, J. D. (2018). The role of substrate characteristics in producing anomalously young crater retention ages in volcanic deposits on the Moon: Morphology, topography, subresolution roughness, and mode of emplacement of the Sosigenes lunar irregular mare patch. Meteoritics & Planetary Science, 53(4), 778–812. https://doi.org/10.1111/maps.13003

Rajšić, A., Miljković, K., Collins, G. S., Wünnemann, K., Daubar, I. J., Wójcicka, N., & Wieczorek, M. A. (2021). Seismic Efficiency for Simple Crater Formation in the Martian Top Crust Analog. Journal of Geophysical Research: Planets, 126(2). https://doi.org/10.1029/2020JE006662

Rajšić, A., Miljković, K., Wójcicka, N., Collins, G. S., Onodera, K., Kawamura, T., Lognonné, P., Wieczorek, M. A., & Daubar, I. J. (2021). Numerical Simulations of the Apollo S-IVB Artificial Impacts on the Moon. Earth and Space Science, 8(12). https://doi.org/10.1029/2021EA001887

Redmon, J., Divvala, S., Girshick, R., & Farhadi, A. (2015). You Only Look Once: Unified, Real-Time Object Detection. https://doi.org/10.48550/ARXIV.1506.02640

Redmon, J., & Farhadi, A. (2018). YOLOv3: An Incremental Improvement. ArXiv Preprint ArXiv. https://arxiv.org/abs/1804.02767

Redmon, J., Vivvala, S., Girshick, R., & Farhadi, A. (2016). You Only Look Once: Unified, Real-Time Object Detection. Proceedings of the IEEE Conference on Computer Vision and Pattern Recognition (CVPR), 779–788.

Richardson, J. E. (2009). Cratering saturation and equilibrium: A new model looks at an old problem. Icarus, 204(2), 697–715. https://doi.org/10.1016/j.icarus.2009.07.029

Richardson, M., Malagón, A. A. P., Lebofsky, L. A., Grier, J., Gay, P., Robbins, S. J., & Team, T. C. (2022). The CosmoQuest Moon Mappers Community Science Project: The Effect of Incidence Angle on the Lunar Surface Crater Distribution. https://doi.org/10.48550/ARXIV.2110.13404

Robbins, S. J. (2014). New crater calibrations for the lunar crater-age chronology. Earth and Planetary Science Letters, 403, 188–198. https://doi.org/10.1016/j.epsl.2014.06.038

Robbins, S. J. (2019). A New Global Database of Lunar Impact Craters >1–2 km: 1. Crater Locations and Sizes, Comparisons with Published Databases, and Global Analysis. Journal of Geophysical Research: Planets, 124(4), 871–892. https://doi.org/10.1029/2018JE005592

Robbins, S. J., Antonenko, I., Kirchoff, M. R., Chapman, C. R., Fassett, C. I., Herrick, R. R., Singer, K., Zanetti, M., Lehan, C., Huang, D., & Gay, P. L. (2014). The variability of crater identification among expert and community crater analysts. Icarus, 234, 109–131. https://doi.org/10.1016/j.icarus.2014.02.022

Robbins, S. J., & Hynek, B. M. (2012). A New Global Database of Mars Impact Craters ≥1 km: 1. Database creation, properties, and parameters. Journal of Geophysical Research: Planets, 117(E5), n/a-n/a. https://doi.org/10.1029/2011JE003966

Robbins, S. J., Riggs, J. D., Weaver, B. P., Bierhaus, E. B., Chapman, C. R., Kirchoff, M. R., Singer, K. N., & Gaddis, L. R. (2018). Revised recommended methods for analyzing crater size-frequency distributions. Meteoritics & Planetary Science, 53(4), 891–931. https://doi.org/10.1111/maps.12990

Robbins, S. J., Watters, W. A., Chappelow, J. E., Bray, V. J., Daubar, I. J., Craddock, R. A., Beyer, R. A., Landis, M., Ostrach, L. R., Tornabene, L., Riggs, J. D., & Weaver, B. P. (2018). Measuring impact crater depth throughout the solar system. Meteoritics & Planetary Science, 53(4), 583–637. https://doi.org/10.1111/maps.12956

Robens, E., Bischoff, A., Schreiber, A., Dąbrowski, A., & Unger, K. K. (2007). Investigation of surface properties of lunar regolith: Part I. Applied Surface Science, 253(13), 5709–5714. https://doi.org/10.1016/j.apsusc.2006.12.098

Robinson, M. S., Brylow, S. M., Tschimmel, M., Humm, D., Lawrence, S. J., Thomas, P. C., Denevi, B. W., Bowman-Cisneros, E., Zerr, J., Ravine, M. A., Caplinger, M. A., Ghaemi, F. T., Schaffner, J. A., Malin, M. C., Mahanti, P., Bartels, A., Anderson, J., Tran, T. N., Eliason, E. M., … Hiesinger, H. (2010). Lunar Reconnaissance Orbiter Camera (LROC) Instrument Overview. Space Science Reviews, 150(1–4), 81–124. https://doi.org/10.1007/s11214-010-9634-2

Roncoli, R., & Fujii, K. (2010, August 2). Mission Design Overview for the Gravity Recovery and Interior Laboratory (GRAIL) Mission. AIAA/AAS Astrodynamics Specialist Conference. AIAA/AAS Astrodynamics Specialist Conference, Toronto, Ontario, Canada. https://doi.org/10.2514/6.2010-8383

Rubincam, D. P. (2000). Radiative Spin-up and Spin-down of Small Asteroids. Icarus, 148(1), 2–11. https://doi.org/10.1006/icar.2000.6485

Salamunićcar, G., Lončarić, S., Grumpe, A., & Wöhler, C. (2014). Hybrid method for crater detection based on topography reconstruction from optical images and the new LU78287GT catalogue of Lunar impact craters. Advances in Space Research, 53(12), 1783–1797. https://doi.org/10.1016/j.asr.2013.06.024

Salamunićcar, G., Lončarić, S., & Mazarico, E. (2012). LU60645GT and MA132843GT catalogues of Lunar and Martian impact craters developed using a Crater Shape-based interpolation crater detection algorithm for topography data. Planetary and Space Science, 60(1), 236–247. https://doi.org/10.1016/j.pss.2011.09.003

Salamunićcar, G., Lončarić, S., Pina, P., Bandeira, L., & Saraiva, J. (2011). MA130301GT catalogue of Martian impact craters and advanced evaluation of crater detection algorithms using diverse topography and image datasets. Planetary and Space Science, 59(1), 111–131. https://doi.org/10.1016/j.pss.2010.11.003

Sato, H., Denevi, B., Robinson, M., Hapke, B., & McEwen, A. (2011). Photometric normalization of LROC WAC global color mosaic.

Sawabe, Y., Matsunaga, T., & Rokugawa, S. (2006). Automated detection and classification of lunar craters using multiple approaches. Advances in Space Research, 37(1), 21–27. https://doi.org/10.1016/j.asr.2005.08.022

Schmedemann, N., Kneissl, T., Ivanov, B. A., Michael, G. G., Wagner, R. J., Neukum, G., Ruesch, O., Hiesinger, H., Krohn, K., Roatsch, T., Preusker, F., Sierks, H., Jaumann, R., Reddy, V., Nathues, A., Walter, S. H. G., Neesemann, A., Raymond, C. A., & Russell, C. T. (2014). The cratering record, chronology and surface ages of (4) Vesta in comparison to smaller asteroids and the ages of HED meteorites. Planetary and Space Science, 103, 104–130. https://doi.org/10.1016/j.pss.2014.04.004

Schmitt, H. H., Petro, N. E., Wells, R. A., Robinson, M. S., Weiss, B. P., & Mercer, C. M. (2017). Revisiting the field geology of Taurus–Littrow. Icarus, 298, 2–33. https://doi.org/10.1016/j.icarus.2016.11.042

Scholten, F., Oberst, J., Matz, K.-D., Roatsch, T., Wählisch, M., Speyerer, E. J., & Robinson, M. S. (2012). GLD100: The near-global lunar 100 m raster DTM from LROC WAC stereo image data: THE 100 M RASTER DTM GLD100. Journal of Geophysical Research: Planets, 117(E12), n/a-n/a. https://doi.org/10.1029/2011JE003926

Sears, D. W. (1978). The nature and origin of meteorites. In Monographs on Astronomical Subjects. https://ui.adsabs.harvard.edu/abs/1978nom..book.....S

See, J. E., Howe, S. R., Warm, J. S., & Dember, W. N. (1995). Meta-analysis of the sensitivity decrement in vigilance. Psychological Bulletin, 117(2), 230–249. https://doi.org/10.1037/0033-2909.117.2.230

Sharpton, V. L. (2014). Outcrops on lunar crater rims: Implications for rim construction mechanisms, ejecta volumes and excavation depths: Outcrops constrain crater rim components. Journal of Geophysical Research: Planets, 119(1), 154–168. https://doi.org/10.1002/2013JE004523

Shkuratov, Y. (2001). Regolith Layer Thickness Mapping of the Moon by Radar and Optical Data. Icarus, 149(2), 329–338. https://doi.org/10.1006/icar.2000.6545

Shoemaker, E. M. (1964). THE GEOLOGY OF THE MOON. Scientific American, 211, 38–47.

Shoemaker, E. M. (1965). Preliminary Analysis of the Fine Structure of the Lunar Surface in Mare Cognitum. In The Nature of the Lunar Surface (p. 23). https://ui.adsabs.harvard.edu/abs/1965nls..conf...23S

Shoemaker, E. M., & Hackman, R. J. (1962). Stratigraphic Basis for a Lunar Time Scale. In The Moon (Vol. 14, pp. 289–300). https://ui.adsabs.harvard.edu/abs/1962IAUS...14..289S

Shoemaker, E. M., Hackman, R. J., & Eggleton, R. E. (1963). Interplanetary Correlation of Geologic Time. Advances in Astronautical Sciences, 8.

Shoemaker, E. M., Hait, M. H., Swann, G. A., Schleicher, D. L., Dahlem, D. H., Schaber, G. G., & Sutton, R. L. (1970). Lunar Regolith at Tranquillity Base. Science, 167(3918), 452–455. https://doi.org/10.1126/science.167.3918.452

Silber, E. A., Osinski, G. R., Johnson, B. C., & Grieve, R. A. F. (2017). Effect of impact velocity and acoustic fluidization on the simple-to-complex transition of lunar craters: EFFECT OF IMPACT VELOCITY ON CRATERS. Journal of Geophysical Research: Planets, 122(5), 800–821. https://doi.org/10.1002/2016JE005236

Silburt, A., Ali-Dib, M., Zhu, C., Jackson, A., Valencia, D., Kissin, Y., Tamayo, D., & Menou, K. (2019). Lunar crater identification via deep learning. Icarus, 317, 27–38. https://doi.org/10.1016/j.icarus.2018.06.022

Smith, D. E., Zuber, M. T., Neumann, G. A., Lemoine, F. G., Mazarico, E., Torrence, M. H., McGarry, J. F., Rowlands, D. D., Head, J. W., Duxbury, T. H., Aharonson, O., Lucey, P. G., Robinson, M. S., Barnouin, O. S., Cavanaugh, J. F., Sun, X., Liiva, P., Mao, D., Smith, J. C., & Bartels, A. E. (2010). Initial observations from the Lunar Orbiter Laser Altimeter (LOLA): LOLA INITIAL OBSERVATIONS. Geophysical Research Letters, 37(18), n/a-n/a. https://doi.org/10.1029/2010GL043751

Soderblom, L. A. (1970). A model for small-impact erosion applied to the lunar surface. Journal of Geophysical Research, 75(14), 2655–2661. https://doi.org/10.1029/JB075i014p02655

Speyerer, E. J., Povilaitis, R. Z., Robinson, M. S., Thomas, P. C., & Wagner, R. V. (2016). Quantifying crater production and regolith overturn on the Moon with temporal imaging. Nature, 538(7624), 215–218. https://doi.org/10.1038/nature19829

Speyerer, E. J., Robinson, M. S., Denevi, B. W., & LROC Science Team. (2011). Lunar Reconnaissance Orbiter Camera Global Morphological Map of the Moon. 2387.

Spoto, F., Milani, A., & Knezevic, Z. (2015). Asteroid family ages. https://doi.org/10.48550/ARXIV.1504.05461

Stadermann, A. C., Zanetti, M. R., Jolliff, B. L., Hiesinger, H., van der Bogert, C. H., & Hamilton, C. W. (2018). The age of lunar mare basalts south of the Aristarchus Plateau and effects of secondary craters formed by the Aristarchus event. Icarus, 309, 45–60. https://doi.org/10.1016/j.icarus.2018.02.030

Starukhina, L. V. (2003). Computer Simulation of Sputtering of Lunar Regolith by Solar Wind Protons: Contribution to Change of Surface Composition and to Hydrogen Flux at the Lunar Poles. Solar System Research, 37(1), 36–50. https://doi.org/10.1023/A:1022347821862

Still, M. (2006). The definitive guide to ImageMagick. Apress. https://link.springer.com/content/pdf/10.1007/978-1-4302-0112-0.pdf

Stoffler, D. (2006). Cratering History and Lunar Chronology. Reviews in Mineralogy and Geochemistry, 60(1), 519–596. https://doi.org/10.2138/rmg.2006.60.05

Stöffler, D., & Ryder, G. (2001). Stratigraphy and Isotope Ages of Lunar Geologic Units: Chronological Standard for the Inner Solar System. Space Science Reviews, 96(1/4), 9–54. https://doi.org/10.1023/A:1011937020193

Stopar, J. D., Robinson, M. S., Barnouin, O. S., McEwen, A. S., Speyerer, E. J., Henriksen, M. R., & Sutton, S. S. (2017). Relative depths of simple craters and the nature of the lunar regolith. Icarus, 298, 34–48. https://doi.org/10.1016/j.icarus.2017.05.022

Stopar, J. D., Robinson, M. S., Speyerer, E. J., Burns, K., Gengl, H., & Lroc Team. (2012). Regolith Characterization Using LROC NAC Digital Elevation Models of Small Lunar Craters. 2729.

Stuart, J. S., & Binzel, R. P. (2004). Bias-corrected population, size distribution, and impact hazard for the near-Earth objects. Icarus, 170(2), 295–311. https://doi.org/10.1016/j.icarus.2004.03.018

Sturm, S., Kenkmann, T., & Hergarten, S. (2016). Ejecta thickness and structural rim uplift measurements of Martian impact craters: Implications for the rim formation of complex impact craters: RIM FORMATION OF MARTIAN IMPACT CRATERS. Journal of Geophysical Research: Planets, 121(6), 1026–1053. https://doi.org/10.1002/2015JE004959

Szalay, J. R., Pokorný, P., Sternovsky, Z., Kupihar, Z., Poppe, A. R., & Horányi, M. (2019). Impact Ejecta and Gardening in the Lunar Polar Regions. Journal of Geophysical Research: Planets, 124(1), 143–154. https://doi.org/10.1029/2018JE005756

Tang, H., Wang, S., & Li, X. (2012). Simulation of nanophase iron production in lunar space weathering. Planetary and Space Science, 60(1), 322–327. https://doi.org/10.1016/j.pss.2011.10.006

Taylor, L. A. (1992). Resources for a lunar base: Rocks, minerals, and soil of the Moon (Vol. 2, pp. 361–377). https://ui.adsabs.harvard.edu/abs/1992lbsa.conf..361T

Taylor, L., Schmitt, H., Carrier, W., & Nakagawa, M. (2005, January 30). Lunar Dust Problem: From Liability to Asset. 1st Space Exploration Conference: Continuing the Voyage of Discovery. 1st Space Exploration Conference: Continuing the Voyage of Discovery, Orlando, Florida. https://doi.org/10.2514/6.2005-2510

Terada, K., Morota, T., & Kato, M. (2020). Asteroid shower on the Earth-Moon system immediately before the Cryogenian period revealed by KAGUYA. Nature Communications, 11(1), 3453. https://doi.org/10.1038/s41467-020-17115-6

Terfelt, F., & Schmitz, B. (2021). Asteroid break-ups and meteorite delivery to Earth the past 500 million years. Proceedings of the National Academy of Sciences, 118(24), e2020977118. https://doi.org/10.1073/pnas.2020977118

The Click Reader. (2020, November 24). Building A Convolutional Neural Network—The Click Reader. https://www.theclickreader.com/building-a-convolutional-neural-network/

Thesniya, P. M., Rajesh, V. J., & Flahaut, J. (2020). Ages and chemistry of mare basaltic units in the Grimaldi basin on the nearside of the Moon: Implications for the volcanic history of the basin. Meteoritics & Planetary Science, 55(11), 2375–2403. https://doi.org/10.1111/maps.13579

Trang, D., Gillis-Davis, J. J., & Boyce, J. M. (2015). Absolute model ages from lunar crater morphology: Age determination from crater morphology. Journal of Geophysical Research: Planets, 120(4), 725–738. https://doi.org/10.1002/2014JE004639

Trask, N. J. (1966). Size and spatial distribution of craters estimated from the Ranger photographs. https://ntrs.nasa.gov/citations/19660015760

Tyrie, A. (1988). Age dating of mare in the lunar crater Tsiolkovsky by crater-counting method. Earth, Moon and Planets, 42(3), 245–264. https://doi.org/10.1007/BF00058489

Urbach, E. R., & Stepinski, T. F. (2009). Automatic detection of sub-km craters in high resolution planetary images. Planetary and Space Science, 57(7), 880–887. https://doi.org/10.1016/j.pss.2009.03.009

van der Bogert, C. H., Hiesinger, H., Dundas, C. M., Krüger, T., McEwen, A. S., Zanetti, M., & Robinson, M. S. (2017). Origin of discrepancies between crater size-frequency distributions of coeval lunar geologic units via target property contrasts. Icarus, 298, 49–63. https://doi.org/10.1016/j.icarus.2016.11.040

Vickery, A. M., & Melosh, H. J. (1987). The Large Crater Origin of SNC Meteorites. Science, 237(4816), 738–743. https://doi.org/10.1126/science.237.4816.738

Vokrouhlický, D., Milani, A., & Chesley, S. R. (2000). Yarkovsky Effect on Small Near-Earth Asteroids: Mathematical Formulation and Examples. Icarus, 148(1), 118–138. https://doi.org/10.1006/icar.2000.6469

Wallace, W. T., Phillips, C. J., Jeevarajan, A. S., Chen, B., & Taylor, L. A. (2010). Nanophase iron-enhanced chemical reactivity of ground lunar soil. Earth and Planetary Science Letters, 295(3–4), 571–577. https://doi.org/10.1016/j.epsl.2010.04.042

Wang, J., Cheng, W., & Zhou, C. (2015). A Chang'E-1 global catalog of lunar impact craters. Planetary and Space Science, 112, 42–45. https://doi.org/10.1016/j.pss.2015.04.012

Wang, Y., Wu, B., Xue, H., Li, X., & Ma, J. (2021). An Improved Global Catalog of Lunar Impact Craters (≥1 km) With 3D Morphometric Information and Updates on Global Crater Analysis. Journal of Geophysical Research: Planets, 126(9). https://doi.org/10.1029/2020JE006728

Wang, Y., Xie, M., Xiao, Z., & Cui, J. (2020). The minimum confidence limit for diameters in crater counts. Icarus, 341, 113645. https://doi.org/10.1016/j.icarus.2020.113645

Wang, Y., Zhu, X., & Wu, B. (2019). Automatic detection of individual oil palm trees from UAV images using HOG features and an SVM classifier. International Journal of Remote Sensing, 40(19), 7356–7370. https://doi.org/10.1080/01431161.2018.1513669

Ward, I., McDonald, J., Monks, C., & Fairweather, J. (2022). Use of micro-analysis to augment the macro-archaeological investigation of an elevated Holocene shell midden, Dampier Archipelago, NW Australia. Frontiers in Earth Science, 10, 837338. https://doi.org/10.3389/feart.2022.837338

Warner, N. H., Gupta, S., Calef, F., Grindrod, P., Boll, N., & Goddard, K. (2015). Minimum effective area for high resolution crater counting of martian terrains. Icarus, 245, 198–240. https://doi.org/10.1016/j.icarus.2014.09.024

Wehner, G. K. (1961). Sputtering Effects on the Moon's Surface. ARS Journal, 31(3), 438–439. https://doi.org/10.2514/8.5498

Weissman, P., A'Hearn, M., Rickman, H., & Mcfadden, L. (1989). Evolution of comets into asteroids. Asteroids II.

Wetherill, G. W. (1975). Late heavy bombardment of the moon and terrestrial planets. Lunar and Planetary Science Conference Proceedings, 2, 1539–1561.

Wetzler, P. G., Honda, R., Enke, B., Merline, W. J., Chapman, C. R., & Burl, M. C. (2005). Learning to Detect Small Impact Craters. 2005 Seventh IEEE Workshops on Applications of Computer Vision (WACV/MOTION'05) - Volume 1, 178–184. https://doi.org/10.1109/ACVMOT.2005.68

Whitten, S. J., Head, J., Staid, M., Pieters, C., Mustard, J., Taylor, L., Mccord, T., Isaacson, P., Klima, R., Nettles, J., & Team. (2010). Characteristics, affinities and ages of volcanic deposits associated with the Orientale basin from Chandrayaan-1 Moon Mineralogy Mapper (M3) data: Mare stratigraphy. Lunar Planet. 41st Lunar and Planetary Science Conference.

Wiggins, S. E., Johnson, B. C., Bowling, T. J., Melosh, H. J., & Silber, E. A. (2019). Impact Fragmentation and the Development of the Deep Lunar Megaregolith. Journal of Geophysical Research: Planets, 124(4), 941–957. https://doi.org/10.1029/2018JE005757

Wilcox, B. B., Robinson, M. S., Thomas, P. C., & Hawke, B. R. (2005). Constraints on the depth and variability of the lunar regolith. Meteoritics & Planetary Science, 40(5), 695–710. https://doi.org/10.1111/j.1945-5100.2005.tb00974.x

Wilhelms, D. E. (1987). The geologic history of the Moon (USGS Numbered Series 1348; Professional Paper, p. 337). United States Geological Survey. https://doi.org/10.3133/pp1348

Williams, J.-P., van der Bogert, C. H., Pathare, A. V., Michael, G. G., Kirchoff, M. R., & Hiesinger, H. (2018). Dating very young planetary surfaces from crater statistics: A review of issues and challenges. Meteoritics & Planetary Science, 53(4), 554–582. https://doi.org/10.1111/maps.12924

Wu, B., Huang, J., Li, Y., Wang, Y., & Peng, J. (2018). Rock Abundance and Crater Density in the Candidate Chang'E-5 Landing Region on the Moon. Journal of Geophysical Research: Planets, 123(12), 3256–3272. https://doi.org/10.1029/2018JE005820

Wu, B., & Liu, W. C. (2017). Calibration of boresight offset of LROC NAC imagery for precision lunar topographic mapping. ISPRS Journal of Photogrammetry and Remote Sensing, 128, 372–387. https://doi.org/10.1016/j.isprsjprs.2017.04.012

Wu, B., Ross W. K., P., Ludivig, P., Chung, A. S., & Seabrook, T. (2019). Absolute Localization Through Orbital Maps and Surface Perspective Imagery: A Synthetic Lunar Dataset and Neural Network Approach. 2019 IEEE/RSJ International Conference on Intelligent Robots and Systems (IROS), 3262–3267. https://doi.org/10.1109/IROS40897.2019.8968124

Wu, X. (1999). Performance evaluation, prediction and visualization of parallel systems. Boston : Kluwer Academic Publishers. http://archive.org/details/performanceevalu0000wuxi

Wünnemann, K., & Ivanov, B. A. (2003). Numerical modelling of the impact crater depth–diameter dependence in an acoustically fluidized target. Planetary and Space Science, 51(13), 831–845. https://doi.org/10.1016/j.pss.2003.08.001

Xiao, Z. (2016). Size-frequency distribution of different secondary crater populations: 1. Equilibrium caused by secondary impacts: EQUILIBRIUM CAUSED BY SECONDARIES. Journal of Geophysical Research: Planets, 121(12), 2404–2425. https://doi.org/10.1002/2016JE005139

Xiao, Z., & Strom, R. G. (2012). Problems determining relative and absolute ages using the small crater population. Icarus, 220(1), 254–267. https://doi.org/10.1016/j.icarus.2012.05.012

Xiao, Z., & Werner, S. C. (2015). Size-frequency distribution of crater populations in equilibrium on the Moon. Journal of Geophysical Research: Planets, 120(12), 2277–2292. https://doi.org/10.1002/2015JE004860

Xie, M., & Xiao, Z. (2023). A new chronology from debiased crater densities: Implications for the origin and evolution of lunar impactors. Earth and Planetary Science Letters, 602, 117963. https://doi.org/10.1016/j.epsl.2022.117963

Xie, M., Xiao, Z., Zhang, X., & Xu, A. (2020). The Provenance of Regolith at the Chang'e-5 Candidate Landing Region. Journal of Geophysical Research: Planets, 125(5). https://doi.org/10.1029/2019JE006112

Xie, M., & Zhu, M.-H. (2016). Estimates of primary ejecta and local material for the Orientale basin: Implications for the formation and ballistic sedimentation of multi-ring basins. Earth and Planetary Science Letters, 440, 71–80. https://doi.org/10.1016/j.epsl.2016.02.012

Xu, L., Qiao, L., Xie, M., & Wu, Y. (2022). Formation age of lunar Lalande crater and its implications for the source region of the KREEP-rich meteorite Sayh al Uhaymir 169. Icarus, 386, 115166. https://doi.org/10.1016/j.icarus.2022.115166

Xu, L., & Xie, M. (2020). Ejecta Thickness Distribution of the Schrödinger Basin on the Moon. Journal of Geophysical Research: Planets, 125(12). https://doi.org/10.1029/2020JE006506

Yamamoto, S., Matsunaga, T., Nakamura, R., Sekine, Y., Hirata, N., & Yamaguchi, Y. (2017). An Automated Method for Crater Counting Using Rotational Pixel Swapping Method. IEEE Transactions on Geoscience and Remote Sensing, 55(8), 4384–4397. https://doi.org/10.1109/TGRS.2017.2691758

Yang, C., Zhao, H., Bruzzone, L., Benediktsson, J. A., Liang, Y., Liu, B., Zeng, X., Guan, R., Li, C., & Ouyang, Z. (2020). Lunar impact crater identification and age estimation with Chang'E data by deep and transfer learning. Nature Communications, 11(1), 6358. https://doi.org/10.1038/s41467-020-20215-y

Young, J. (1940). A statistical investigation of diameter and distribution of lunar craters. J. Brit. Astron. Assoc, 50(9), 309–326.

Young, R. A., Brennan, W. J., & Nichols, D. J. (1974). Problem in the interpretation of lunar mare stratigraphy and relative ages indicated by ejecta from small impact craters. Lunar and Planetary Science Conference Proceedings, 1, 159–170.

Zanetti, M., Stadermann, A., Jolliff, B., Hiesinger, H., Van Der Bogert, C. H., & Plescia, J. (2017). Evidence for self-secondary cratering of Copernican-age continuous ejecta deposits on the Moon. Icarus, 298, 64–77. https://doi.org/10.1016/j.icarus.2017.01.030

Zhang, Y. (2010). New Advances in Machine Learning. BoD – Books on Demand.

Zhao, J., Xiao, L., Qiao, L., Glotch, T. D., & Huang, Q. (2017). The Mons Rümker volcanic complex of the Moon: A candidate landing site for the Chang'E-5 mission: Geology of Lunar Mons Rümker Region. Journal of Geophysical Research: Planets, 122(7), 1419–1442. https://doi.org/10.1002/2016JE005247

Zou, Y.-L., Liu, J.-Z., Liu, J.-J., & Xu, T. (2004). Reflectance Spectral Characteristics of Lunar Surface Materials. Chinese Journal of Astronomy and Astrophysics, 4(1), 97–104. https://doi.org/10.1088/1009-9271/4/1/97

Zuber, M. T., Smith, D. E., Watkins, M. M., Asmar, S. W., Konopliv, A. S., Lemoine, F. G., Melosh, H. J., Neumann, G. A., Phillips, R. J., Solomon, S. C., Wieczorek, M. A., Williams, J. G., Goossens, S. J., Kruizinga, G., Mazarico, E., Park, R. S., & Yuan, D.-N. (2013). Gravity Field of the Moon from the Gravity Recovery and Interior Laboratory (GRAIL) Mission. Science, 339(6120), 668–671. https://doi.org/10.1126/science.1231507

Appendices

Appendix 1: Chapter 1

1.1: Other examples of the geological time scales for the Moon.

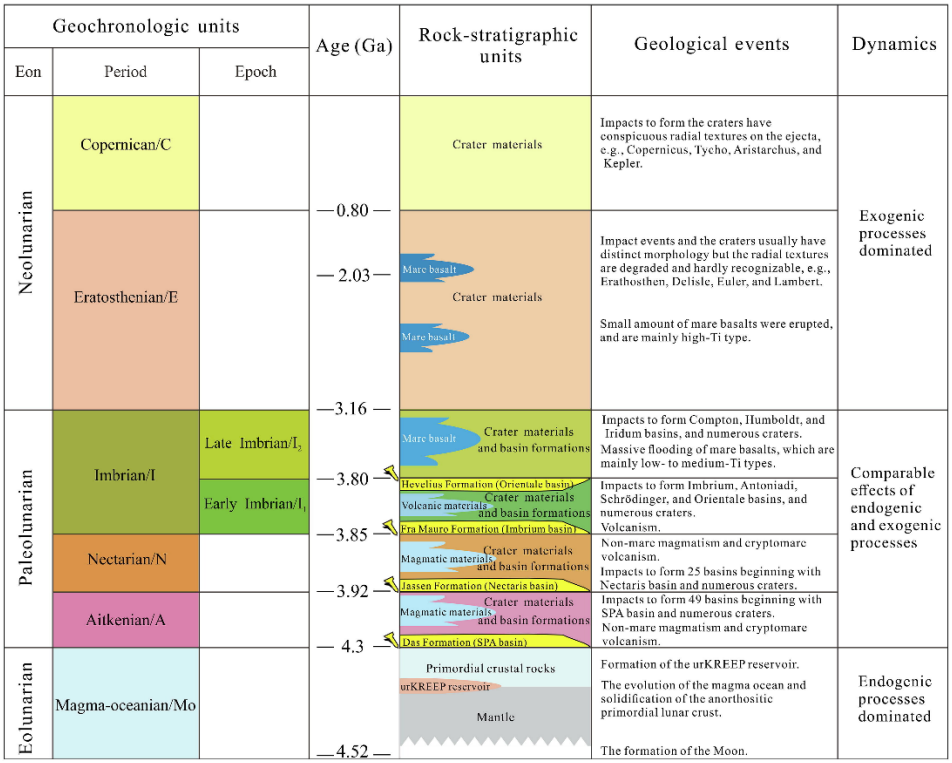

Figure S1.1: Ji et al. (2022)'s Geologic timescale for the Moon.

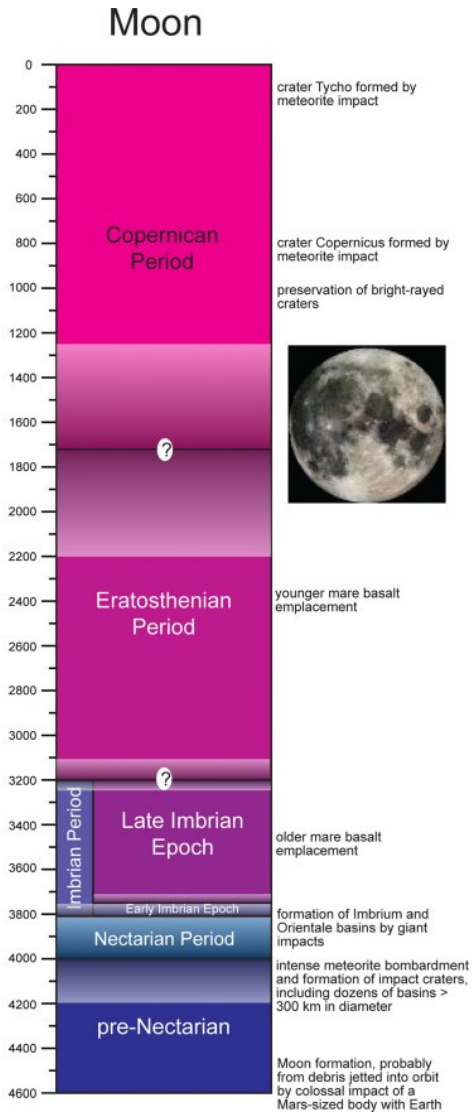

Figure S1.2: Hiesinger and Tanaka (2020)'s Geologic timescale for the Moon.

References for Appendix 1: Chapter 1

Hiesinger, H., & Tanaka, K. (2020). The Planetary Time Scale. In Geologic Time Scale 2020 (pp. 443–480). Elsevier. https://doi.org/10.1016/B978-0-12-824360-2.00015-2

Ji, J., Guo, D., Liu, J., Chen, S., Ling, Z., Ding, X., Han, K., Chen, J., Cheng, W., Zhu, K., Liu, J., Wang, J., Chen, J., & Ouyang, Z. (2022). The 1:2,500,000-scale geologic map of the global Moon. Science Bulletin, 67(15), 1544–1548. https://doi.org/10.1016/j.scib.2022.05.021

Appendix 2: Chapter 2

2.1: YOLOv3 Hyper-parameters using for building the NAC detection model.

```
hyp = {'giou':         3.54,   # giou loss gain
       'cls':          37.4,   # cls loss gain
       'cls_pw':       1.0,    # cls BCELoss positive_weight
       'obj':          64.3,   # obj loss gain (*=img_size/416 if img_size != 416)
       'obj_pw':       1.0,    # obj BCELoss positive_weight
       'iou_t':        0.225,  # iou training threshold
       'lr0':          0.00579,  # initial learning rate (SGD=1E-3, Adam=9E-5)
       'lrf':          -4.,    # final LambdaLR learning rate = lr0 * (10 ** lrf)
       'momentum':     0.937,  # SGD momentum
       'weight_decay': 0.000484,  # optimizer weight decay
       'fl_gamma':     0.5,    # focal loss gamma
       'hsv_h':        0.0138, # image HSV-Hue augmentation (fraction)
       'hsv_s':        0.678,  # image HSV-Saturation augmentation (fraction)
       'hsv_v':        0.36,   # image HSV-Value augmentation (fraction)
       'degrees':      180,    # image rotation (+/- deg)
       'translate':    0.01,   # image translation (+/- fraction)
       'scale':        0.05,   # image scale (+/- gain)
       'shear':        0.05}   # image shear (+/- deg)
```

2.2: ISIS commands for batch processing LRO-NAC images. This script assumes the user has installed ISIS3 correctly and all the downloaded images (.IMG) are in the same folder. This script is to be run within the ISIS environment.

```
#echo LRO NAC batch processing of raw EDR images in ISIS
#ls *.IMG | sed s/.IMG// > cube.lis
lronac2isis from=\$1.IMG to=\$1.cub -batchlist=cube.lis
spiceinit from=\$1.cub spksmithed=true web=true -batchlist=cube.lis
lronaccal from=\$1.cub to=\$1.cal.cub -batchlist=cube.lis
lronacecho from=\$1.cal.cub to=\$1.echo.cub -batchlist=cube.lis
trim from=\$1.echo.cub to=\$1.tr.cub left=40 righ=40 -batchlist=cube.lis
stretch from=\$1.tr.cub to=\$1.str.cub usepercentages=yes pairs="0:1 0.5:1 99.5:254
100:254" -batchlist=cube.lis
cam2map from=\$1.str.cub to=\$1.map.cub map=Moon.map pixres=mpp resolution=2
warpalgorithm=forwardpatch patchsize=200 -batchlist=cube.lis
/bin/rm *cal.cub *echo.cub *tr.cub *E.cub
#echo Done
```

2.2.1: Contents of the ‘Moon.map’ file (from 2.2). This file is needed for Moon map projection. This file currently set for an Equirectangular projection.

```
Group = Mapping
  ProjectionName     = Equirectangular
  CenterLongitude    = 0.0
  CenterLatitude     = 0.0
  TargetName         = Moon
  EquatorialRadius   = 1737400.0 <meters>
  PolarRadius        = 1737400.0 <meters>
  LatitudeType       = Planetocentric
  LongitudeDirection = PositiveEast
  LongitudeDomain    = 360
End_Group
End
```

2.2.2: GDAL script to be run in the folder after the (2.1) ISIS script. This converts all ‘map.cub’ files into Tiff files. This process is to be run in the command line outside the ISIS environment.

```
##Use GDAL in command line
for f in *map.cub; do
     gdal_translate "$f" "${f%.*}.tif"
done
```

References for Appendix 2: Chapter 2

ISIS Documentation. (2021). ISIS: Integrated Software for Imagers and Spectrometers. https://isis.astrogeology.usgs.gov/UserDocs/index.html

GDAL documentation. (2021). GDAL. https://gdal.org/

Ultralytics YOLOv3. (2022). [Python]. Ultralytics. https://github.com/ultralytics/yolov3 (Original work published 2018)

Appendix 3: Chapter 3

This Supporting information is published as supplemental material in (fund here: https://doi.org/10.5281/zenodo.6386231): Fairweather, J. H., Lagain, A., Servis, K., Benedix, G. K., Kumar, S. S., & Bland, P. A. (2022). Automatic Mapping of Small Lunar Impact Craters Using LRO-NAC Images. Earth and Space Science, 9(7). https://doi.org/10.1029/2021EA002177.

3.1: The NAC dataset and description of the geo-processing needed for crater detection.

The LRO-NAC image dataset has 0.5-2m/px spatial resolution, with some images down to 0.25-0.3m/px (Robinson et al., 2010). This level of detail comes from the instrument having two Narrow-Angle Cameras, left (NAC-L) and right (NAC-R), with each able to capture ~5km by ~25km area of the Moon's surface (Robinson et al., 2010). The NAC dataset is publicly available and downloadable, courtesy of NASA's Planetary Data System (PDS) (McMahon, 1996). The NAC image dataset is the highest resolution orbital image dataset currently available for the Moon; however, it is not distributed in a georeferenced format (.gtif). For the algorithm to determine the lunar positions of the detection craters within the image, the image must be map projected (i.e., georeferenced). The entire NAC-L-R image dataset is available for download in two forms: (1) Engineer Data Records (EDR); or (2) Calibrated Data Records (CDR). CDR's are NAC images that have undergone photometric calibration but have not been map projected. The pipeline we use only accepts EDR images. The raw NAC images (EDR's) are in .IMG format, with attribute information kept in the file header (McMahon, 1996), allowing the researcher to query the images based on their characteristics (orbit number, camera angle, incidence and emission angle, resolution, and image ID). They need to be converted into a Georeferenced Tag Image File Format (.geotiff or .gtif) so the CDA is able to read and extract the geographical information of the image to compute the impact crater's geographic location and detected diameter. We used the Integrated Software for Imagers and Spectrometers (ISIS) developed by the United States Geological Survey (USGS) for image georeferencing (ISIS3, 2021). In ISIS, each EDR-NAC IMG file is converted into an ISIS cube file. The cube files are calibrated using the Navigation and Ancillary Information Facility (NAIF) SPICE system - a series of files containing spacecraft navigation, flight, and orientation information, which altogether are referred to as 'SPICE kernels (Acton, 1996). Processing with SPICE information is critical to ensure all the NAC images are correctly orthorectified with a lunar DEM (SLDEM_2015 with 60m/px at the equator and ~100m/px at the poles) (Barker et al., 2016; Scholten et al., 2012; Smith et al., 2010). Moreover, throughout the georeferencing pipeline, each NAC image is photometrically calibrated, trimmed (20 pixels around the NAC image to remove the black photo extents), stretched to 8-bit pixel depth, and map projected into a lunar coordinate system Moon_2000 (which uses decimal degrees) (ISIS Documentation, 2021). NAC images situated near the equator (±30° Lat) are projected with a simple-cylindrical projection, images outside that range (near the poles) are projected separately with an orthographic projection defined by the NAC centre point data in the image meta-data. The output of the pipeline is a geometrically and geographically accurate NAC cube file. NAC cube files are then converted into a GeoTiff format using GDAL (GDAL Documentation, 2021).

3.2: Supplemental Figures.

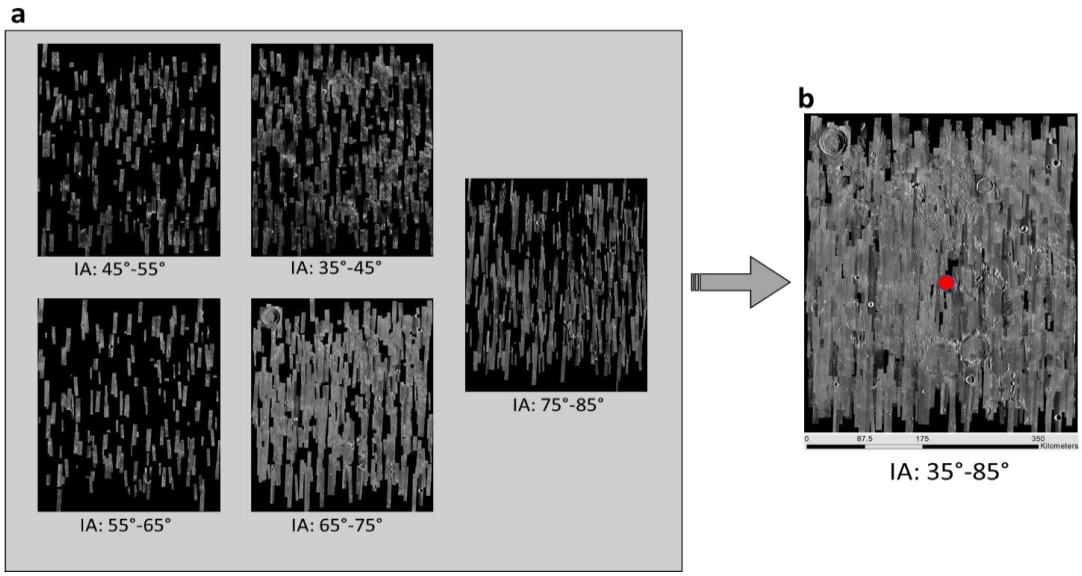

Figure S3.1 Example of the NAC dataset coverage (a) at different Incidence Angle (IA) lighting conditions, and (b) the combined dataset [n=1000]. All images are situated in a 200km radius from the Apollo 14 landing site (red dot). NAC images were downloaded on 12/Jul/2021.

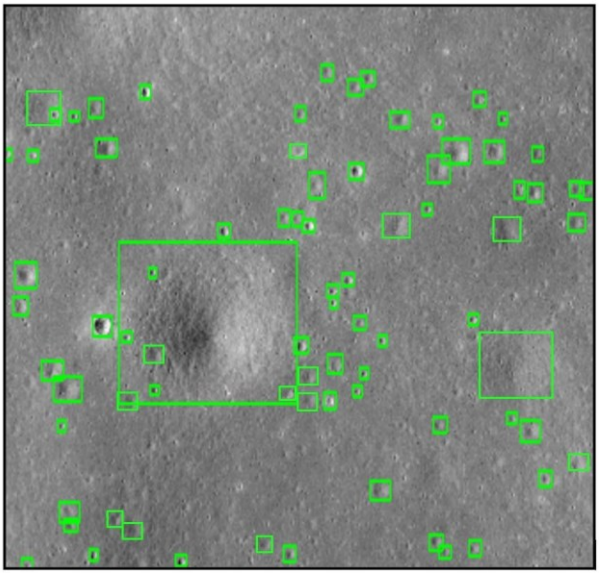

Figure S3.2. Example of a 416-pixel NAC image tile (M1320200353LE) with manual scoring (green boxes). This is the appearance of the image tile and boxes within the Yolo_label marking tool (available at https://github.com/developer0hye/Yolo_Label). The largest degraded crater depicted here is 147m in diameter.

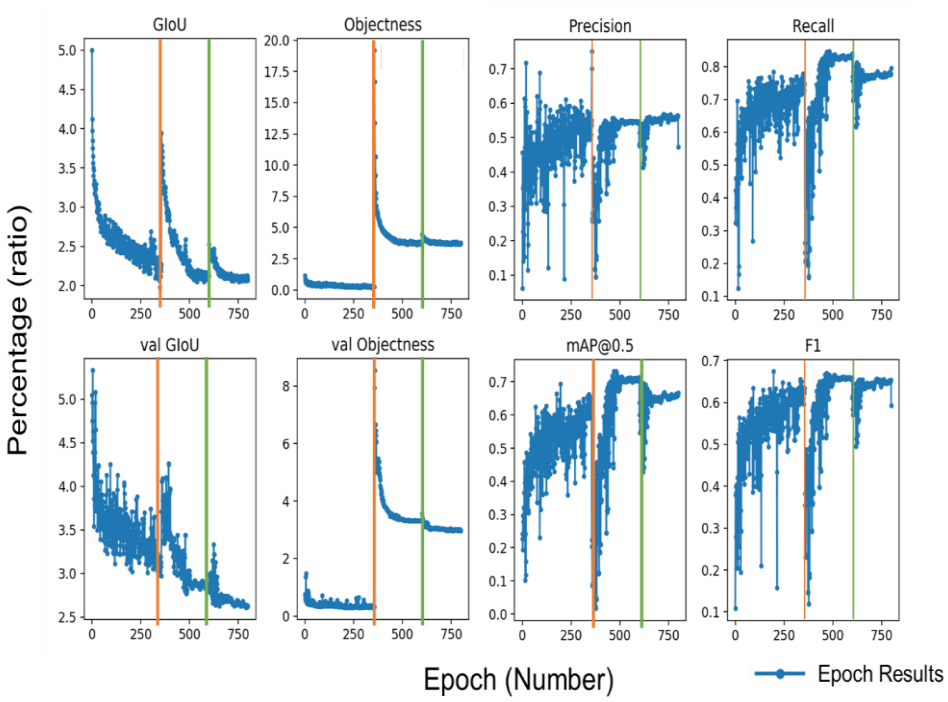

Figure S3.3. Full Training metrics for the lunar crater detection model in YOLOv3. The orange line marks the start of the 1st training session (300-600), Green line marks the start of the 2nd training session (600-800). GIoU (Generalised Intersection over Union) is the overlap area (in ratio format) of the ground truth and predicted bounding box. Val GIoU refers to the metrics for the validation state specifically. Objectness describes the probability that an object exists in an image - It is a measure of how the algorithm is trained to distinguish objects from the background, but as there is only one object (crater) the specific values are meaningless, but the trend of the graph can be used as a proxy for loss (a number indicating how bad the model's prediction was on a single example) and learn rate (variability over time). Val Objectness refers to the metrics for the validation state specifically. mAP@0.5 (mean Average Precision with a 0.5 IoU cut-off) indicates how well the CDA model is at drawing correct bounding box detections on average relative to the mode's ability to detect True positives with a 0.5 IoU cut off – i.e., the weighted mean Precision, Recall, and GIoU. For Precision, Recall, and F1 score refer to the main text. Note, the vertical axis has not been scaled.

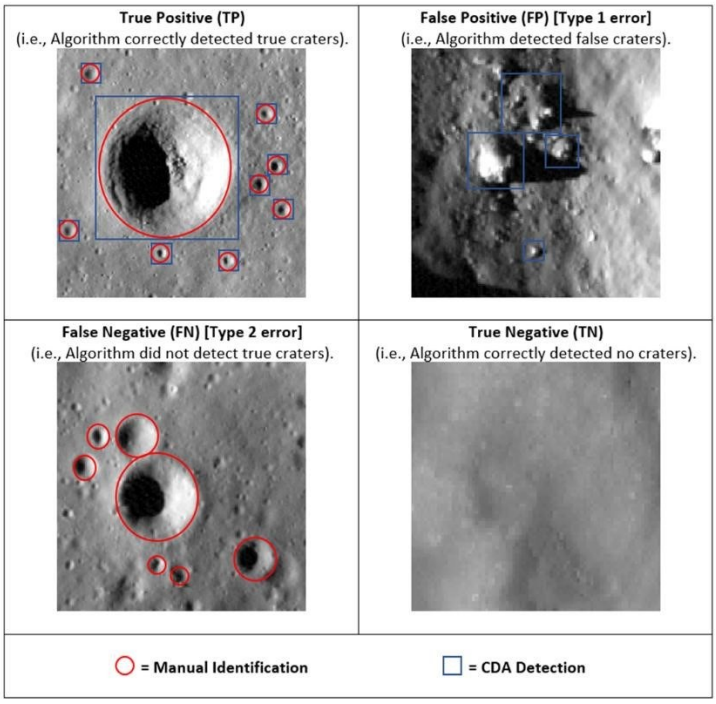

Figure S3.4. Confusion Matrix with image examples and descriptions.

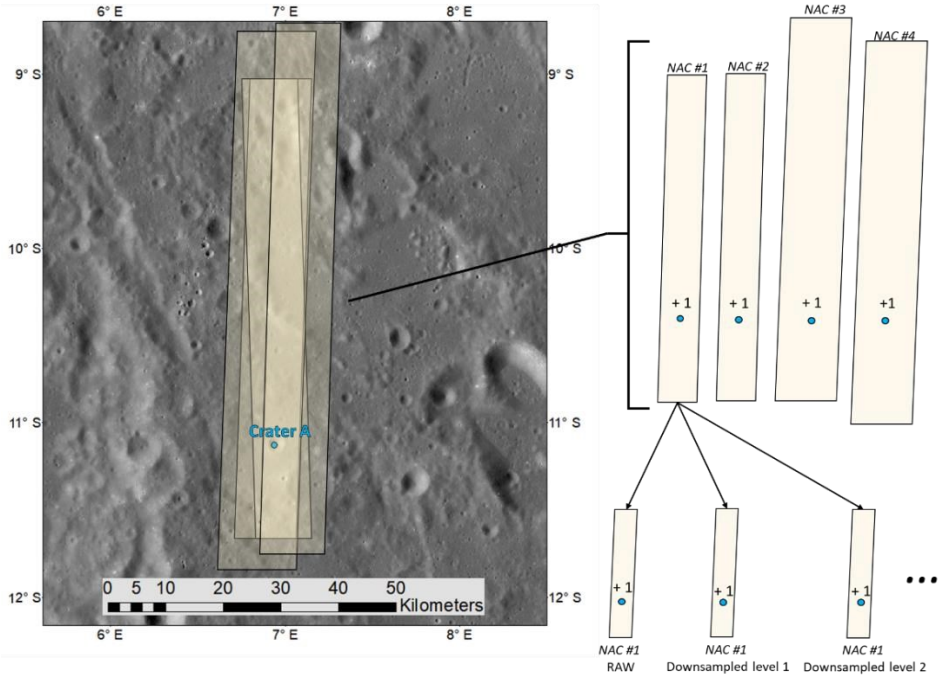

Figure S3.5. Four overlapping LRO-NAC images (locations characterised by the image footprints) can all be used to detect 'Crater A' (blue dot) multiple times (represented by the '+1'). Note, the resulting crater dataset will be inflated with additional craters. Each image is then downsampled, tripling the crater detections for a single NAC image. This is fixed using the non-maximum suppression technique to, which removes overlapping duplicates, or alternately you mediate the issue by mosaicking the images together.

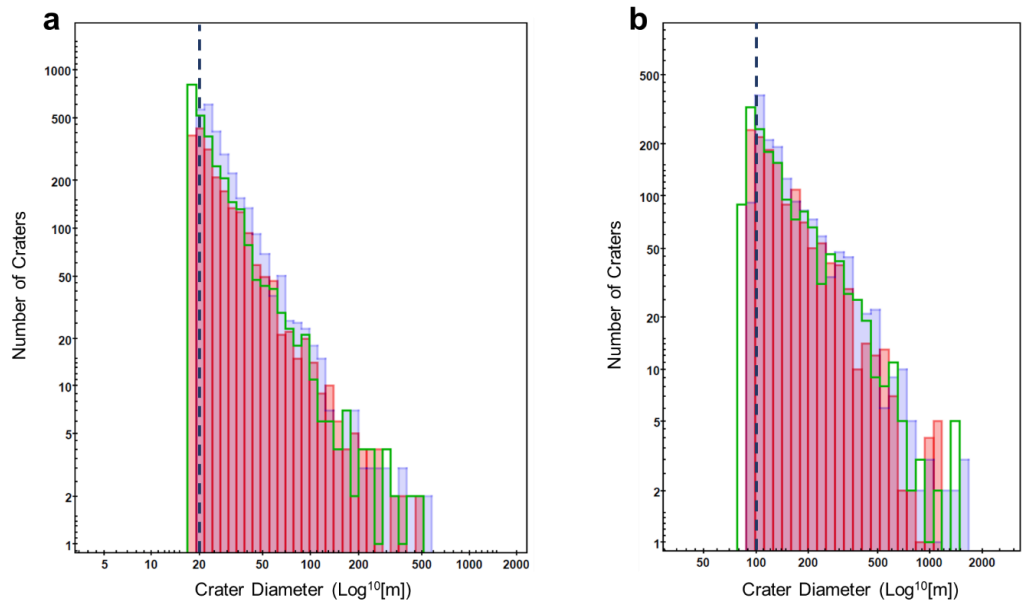

Figure S3.6. Crater size-frequency distribution for the (a) Small Crater Dataset (20 m < D < 500 m), and (b) Large Crater Dataset (100m < D < 1 km), bin size is 1.25 (m_log10). Blue histogram corresponds to the CDA detections and the red one to the manually identified craters; the green line represents the -15% diameter correction factor applied to the detections (in blue). The dashed vertical line denotes the 10-pixel cut-off. Note that the ground truth craters (in red) was mapped with a diameter ±15% error buffer (see main text for details).

3.3: Supplemental Tables.

Table S3.1. Confusion matrix summary table for the 'Small Crater Dataset' and 'Large Crater Dataset' crater values. 'GT' refers to the Ground Truth craters, and 'P' refers to the CDA detections per the NAC area indicated by the table headers. 'TP' means True Positives, 'FP' False Positives, and 'FN' False Negatives.

			IA-1		IA-2		IA-3		
			66.7	33.9	51.7	56.4	41.8	48.9	
Type		Size	Near side Mare	Near side Highland	Near side Mare	Far side Highland	Near side Mare	Far side Highland	SUM
Small Crater Dataset	GT	≥20m	735	822	116	180	79	227	2159
		≥40m	125	150	18	24	25	25	367
		≥60m	69	49	8	7	11	7	151
		≥80m	54	28	4	4	6	4	100
		≥100m	35	18	2	2	5	3	65
	P	≥20m	949	1169	121	180	97	265	2781
		≥40m	164	208	25	28	30	45	500
		≥60m	75	83	16	11	19	14	218
		≥80m	57	38	6	5	12	8	126
		≥100m	38	21	5	3	8	5	80
	TP	≥20m	719	798	102	162	68	209	2058
		≥40m	112	142	17	23	19	23	336
		≥60m	58	45	8	7	10	7	135
		≥80m	43	25	4	4	6	4	86
		≥100m	29	16	2	2	5	3	57
	FP	≥20m	230	371	19	18	29	56	723
		≥40m	52	66	8	5	11	22	164
		≥60m	17	38	8	4	9	7	83
		≥80m	14	13	2	1	6	4	40
		≥100m	9	5	3	1	3	2	23
	FN	≥20m	16	24	14	18	11	18	101
		≥40m	13	8	1	1	6	2	31
		≥60m	11	4	0	0	1	0	16
		≥80m	11	3	0	0	0	0	14
		≥100m	6	2	0	0	0	0	8
Large Crater Dataset	GT	≥100m	331	432	59	121	212	188	1343
		≥300m	35	41	2	12	8	19	117
		≥500m	5	13	0	9	3	6	36
	P	≥100m	403	424	76	143	275	219	1540
		≥300m	60	54	5	11	19	41	190
		≥500m	14	12	0	8	3	10	47
	TP	≥100m	300	369	57	115	192	170	1203
		≥300m	28	34	2	8	8	17	97
		≥500m	4	11	0	7	3	6	31
	FP	≥100m	103	55	19	28	83	49	337
		≥300m	32	20	3	3	11	24	93
		≥500m	10	1	0	1	0	4	16
	FN	≥100m	31	63	2	6	20	18	140
		≥300m	7	7	0	4	0	2	20
		≥500m	1	2	0	2	0	0	5

Table S3.2. Summary table for the 'Large Crater Dataset' degradation class (A/B/C) evaluation. The crater values are grouped based on their lighting condition, terrain, and degradation class.

		Class	Crater Diameter	True Positives	Manual Count
IA-1	Highland	A	≥100m	24	24
			≥300m	5	5
			≥500m	3	3
		B	≥100m	95	97
			≥300m	9	9
			≥500m	1	1
		C	≥100m	250	311
			≥300m	20	27
			≥500m	7	9
	Mare	A	≥100m	10	11
			≥300m	0	0
			≥500m	0	0
		B	≥100m	66	66
			≥300m	8	8
			≥500m	1	1
		C	≥100m	224	254
			≥300m	20	27
			≥500m	3	4
IA-2	Highland	A	≥100m	1	1
			≥300m	1	1
			≥500m	0	0
		B	≥100m	39	39
			≥300m	0	0
			≥500m	0	0
		C	≥100m	75	81
			≥300m	7	10
			≥500m	7	8
	Mare	A	≥100m	5	5
			≥300m	0	0
			≥500m	0	0
		B	≥100m	9	9
			≥300m	2	2
			≥500m	0	0
		C	≥100m	43	45
			≥300m	0	0
			≥500m	0	0
IA-3	Highland	A	≥100m	5	5
			≥300m	0	0
			≥500m	0	0
		B	≥100m	45	46
			≥300m	2	2
			≥500m	0	0
		C	≥100m	120	137
			≥300m	15	17
			≥500m	6	6
	Mare	A	≥100m	15	15
			≥300m	0	0
			≥500m	0	0
		B	≥100m	41	44
			≥300m	3	3
			≥500m	3	3
		C	≥100m	136	153
			≥300m	5	5
			≥500m	0	0

3.4: Supplemental Datasets (Found here: https://doi.org/10.5281/zenodo.6386231).

Dataset S3.1: *total_evaluation_crater_dataset.csv*. This table contained all the CDA and groundtruth (GT) crater data used in this analysis. This table includes the dataset (small crater or large crater dataset) the Incidence angle, terrain type, the crater confidence, centre point latitude and longitude, calculated diameters, and finally the crater degradation level.

Dataset S3.2: *true_positive_crater_dataset.csv*. This table combines the CDA and ground-truth (prefix 'CDA' or 'GT') True Positive crater data. The data included within is the Incidence angle, terrain type, crater Latitude and longitude, calculated diameter and the calculated diameter difference as a percent (%).

Dataset S3.3: *eval_area_images*. folder containing Images of each crater counting area used in the evaluation of the CDA, blue circles and red circles denote CDA and manual results respectively. For the small crater dataset images only craters >20m to ~500m were marked, and for the large crater dataset only craters between >100 m and 1 km were marked. Descriptors for each file are as follows: *H-IA-1_Craters_20m-500m.pdf* - Small crater dataset, near side highland, 9 km^2, NAC image M1338833866L, incidence angle 67°; *M-IA1_Craters_20m-500m.pdf* - Small crater dataset, near side mare, 9 km^2, NAC image M1320016983L, incidence angle 67°; *H-IA-2_Craters_20m-500m.pdf* - Small crater dataset, far side highland, 1 km^2, NAC image M1325197569L, incidence angle 56°; *M-IA-2_Craters_20m500m.pdf* - Small crater dataset, far side mare, 1 km^2, NAC image M112963850L, incidence angle 51°; *H-IA-3_Craters_20m-500m.pdf* - Small crater dataset, far side highland, 1 km^2, NAC image M1288076949L, incidence angle 49°; *M-IA-3_Craters_20m-500m.pdf* - Small crater dataset, near side mare, 1 km^2, NAC image M1361391010L, incidence angle 42°; *H-IA1_Craters_100m-1000m.pdf* - Large crater dataset, near side highland, 148 km^2, NAC image M1338833866L, incidence angle 67°; *M-IA-1_Craters_100m-1000m.pdf* - Large crater dataset, near side mare, 111 km^2, NAC image M1320016983L, incidence angle 66°; *H-IA2_Craters_100m-1000m.pdf* - Large crater dataset, far side highland, 50 km^2, NAC image M1325197569L, incidence angle 56°; *M-IA-2_Craters_100m-1000m.pdf* - Large crater dataset, far side mare, 22 km^2, NAC image M112963850L, incidence angle 51°; *H-IA-3_Craters_100m1000m.pdf* - Large crater dataset, far side highland, 50 km^2, NAC image M1288076949L, incidence angle 48°; and *M-IA-3_Craters_100m-1000m.pdf* - Large crater dataset, near side mare, 50 km^2, NAC image M1361391010L, incidence angle 41°.

Dataset S3.4: *training_tiles*. Folder contains the 248 (416x416-pixel) image tiles (.png), and their accompanying text files (.txt) containing the crater bounding box markings in pixel percent (refer to main text section 2.3 for a description).

References for Appendix 3: Chapter 3.

Acton, C. H. (1996). Ancillary data services of NASA's Navigation and Ancillary Information Facility. Planetary and Space Science, 44(1), 65–70. https://doi.org/10.1016/00320633(95)00107-7

Barker, M. K., Mazarico, E., Neumann, G. A., Zuber, M. T., Haruyama, J., & Smith, D. E. (2016). A new lunar digital elevation model from the Lunar Orbiter Laser Altimeter and SELENE Terrain Camera. Icarus, 273, 346–355. https://doi.org/10.1016/j.icarus.2015.07.039

GDAL documentation. (2021). GDAL. https://gdal.org/

ISIS Documentation. (2021). ISIS: Integrated Software for Imagers and Spectrometers. https://isis.astrogeology.usgs.gov/UserDocs/index.html

ISIS3. (2021). [C++]. USGS Astrogeology. https://github.com/USGS-Astrogeology/ISIS3

McMahon, S. K. (1996). Overview of the Planetary Data System. Planetary and Space Science, 44(1), 3–12. https://doi.org/10.1016/0032-0633(95)00101-8

Robinson, M. S., Brylow, S. M., Tschimmel, M., Humm, D., Lawrence, S. J., Thomas, P. C., Denevi, B. W., Bowman-Cisneros, E., Zerr, J., Ravine, M. A., Caplinger, M. A., Ghaemi, F. T.,

Schaffner, J. A., Malin, M. C., Mahanti, P., Bartels, A., Anderson, J., Tran, T. N., Eliason, E. M., … Hiesinger, H. (2010). Lunar Reconnaissance Orbiter Camera (LROC) Instrument Overview. Space Science Reviews, 150(1–4), 81–124. https://doi.org/10.1007/s11214010-9634-2

Scholten, F., Oberst, J., Matz, K.-D., Roatsch, T., Wählisch, M., Speyerer, E. J., & Robinson, M. S. (2012). GLD100: The near-global lunar 100 m raster DTM from LROC WAC stereo image data: THE 100 M RASTER DTM GLD100. Journal of Geophysical Research: Planets, 117(E12), n/a-n/a. https://doi.org/10.1029/2011JE003926

Smith, D. E., Zuber, M. T., Neumann, G. A., Lemoine, F. G., Mazarico, E., Torrence, M. H., McGarry,

J. F., Rowlands, D. D., Head, J. W., Duxbury, T. H., Aharonson, O., Lucey, P. G., Robinson, M. S., Barnouin, O. S., Cavanaugh, J. F., Sun, X., Liiva, P., Mao, D., Smith, J. C., & Bartels, A. E. (2010). Initial observations from the Lunar Orbiter Laser Altimeter (LOLA): LOLA INITIAL OBSERVATIONS. Geophysical Research Letters, 37(18). https://doi.org/10.1029/2010GL043751

Appendix 4: Chapter 4

This Supporting information is published as supplemental material in (fund here: https://doi.org/10.5281/zenodo.8045606): Fairweather, J. H., Lagain, A., Servis, K., & Benedix, G. K. (2023). Lunar Surface Model Age Derivation: Comparisons Between Automatic and Human Crater Counting Using LRO-NAC and Kaguya TC Images. Earth and Space Science, 10(7), e2023EA002865. https://doi.org/10.1029/2023EA002865.

4.1: Kaguya Model Training

The presented Kaguya crater detection model is a Convolutional Neural Network running through the Ultralytics implementation of 'You Only Look Once' (YOLO) (Redmon et al., 2016). YOLO is a machine learning object detection algorithm optimised to quickly detect 1000s of objects over an image (Redmon et al., 2016; Redmon and Farhadi, 2018). Our team's prior crater detection algorithms utilised YOLO version 3 (Redmon and Farhadi, 2018; Jocher, 2021) as the primary architecture (see Fairweather et al. (2022) for the Moon using NAC images; and Benedix et al. (2020) and Lagain et al. (2021) for Mars over THEMIS Day IR and CTX imagery, respectively).

Our presented model utilises the YOLO version 5 (Jocher, 2022), significantly improving detection performance. Due to this architecture change (V3 to V5), we could not ‘transfer learn’ from our prior model weight files (see Fairweather et al., 2022). Therefore, we must train a new model from the YOLO default starting weights (given by Jocher, 2022). The new Kaguya detection model was trained for 200 Epochs (i.e., learn/validate cycles) using a training dataset of 55,348 craters marked across 485 image tiles. The training dataset is a combination of the Fairweather et al. (2022) NAC training dataset (43,402 craters over 248 tiles), and a new manual dataset over Kaguya morning and evening images (11,946 craters over 237 tiles) with a Learn: Validate split of 3:1 (i.e., 364 images for training and 121 images for validation).

The performance throughout the training session was recorded using Recall, Precision, and F1 scores for each epoch. These were determined using the values from a standard confusion matrix; Ground Truth (GT), True Positive (TP), False Positive (FP), and False Negative (FN). The Recall is calculated with [TP/GT], Precision with [TP/(TP + FP)], and F1 score [TP/(TP + 1/2(FP + FN))]. The higher the values, the more ‘accurate’ the model. Training can be variable, so the final training epoch does not always reflect the best metric performance. Therefore, an epoch with the highest value across the three metrics is selected for the detection model.

Overall, the metric values in the first ~50 epochs are inconsistent but have a slight upward trend, indicating the model is ‘learning’ (Figure S4.1). After ~100 epochs, all three metrics plateau around 0.8, which indicates the model is sufficiently trained (Figure S1). Epoch 167 performed best, with a Recall of 0.78, Precision of 0.82, and F1 score of 0.80 (Figure S4.1). This was used for our Kaguya Crater Detection Algorithm (CDA).

4.2. Kaguya Model Evaluation

To further evaluate the detection model, we compared detections against a manually counted crater dataset over a region of the Moon it was not trained on. We chose Kaguya images from Mare and Highland terrains (Table S4.2) and used the same evaluation area polygons as Fairweather et al. (2022) study. These areas are a suitable size for gathering enough crater counts to generate meaningful metrics. In total, 1845 manually counted craters were compared against 1924 CDA craters ≥ 100 m in diameter across both morning and evening Kaguya image tiles (crater detections are all in Dataset S2). The results were computed in terms of Recall, Precision and F1 score for each count area variation (see Table S4.2). The counts and metrics are all reported in Table S4.2.

The evaluation showed an overall average Recall of 0.98, a Precision of 0.94, and an F1 score of 0.96 (Table S4.2). We also show the metrics subdivided by crater diameter and image types. We observed no significant change in metrics between evening or morning Kaguya TC tiles, nor between mare and highland terrains. There was also no significant evidence to support overtraining or undertraining (See Fairweather et al. 2022). The accuracy of the crater diameter estimation by the Kaguya CDA was also investigated. The diameters of the True Positive detections, which are determined by a successful CDA detection of the ground truth crater, are compared against each other. The Kaguya CDA showed mostly consistent diameter estimations, with 95% crater detections within ±12% of the ground truth values for craters between 100m and 1 km (Figure S4.2). The diameters and detection rates of the detections are more than adequate, especially when compared to the 10% to 35% accuracy variations reported for expert manual counters (Robbins et al., 2014).

4.3: Supplemental Figures

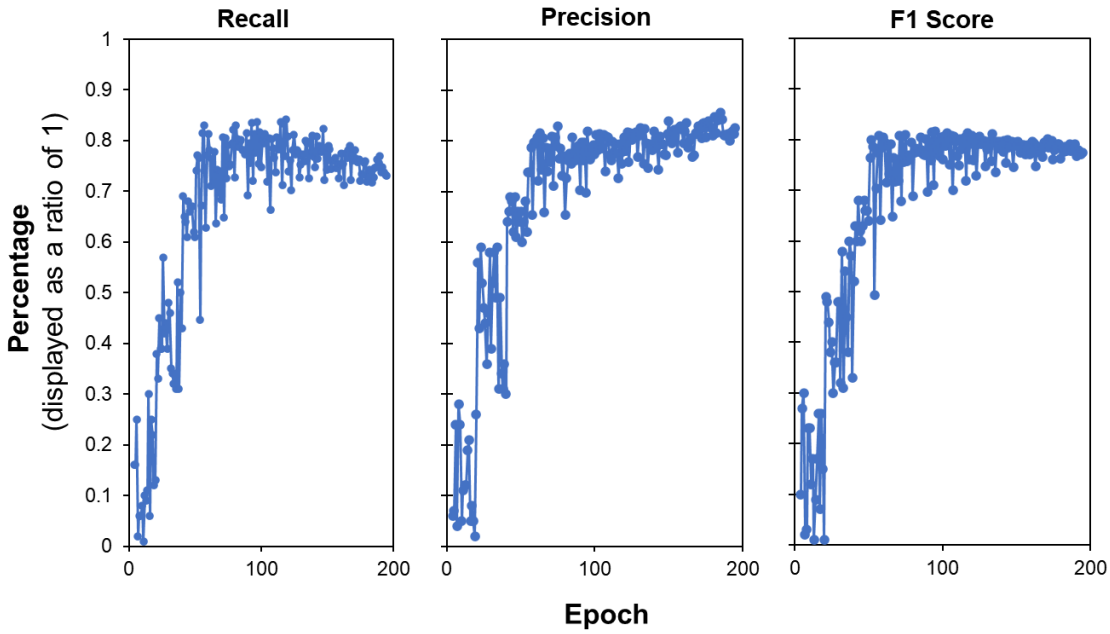

Figure S4.1: The Kaguya training session results (blue dots), displayed as a ratio of 1, for each consecutive Epoch (n=200).

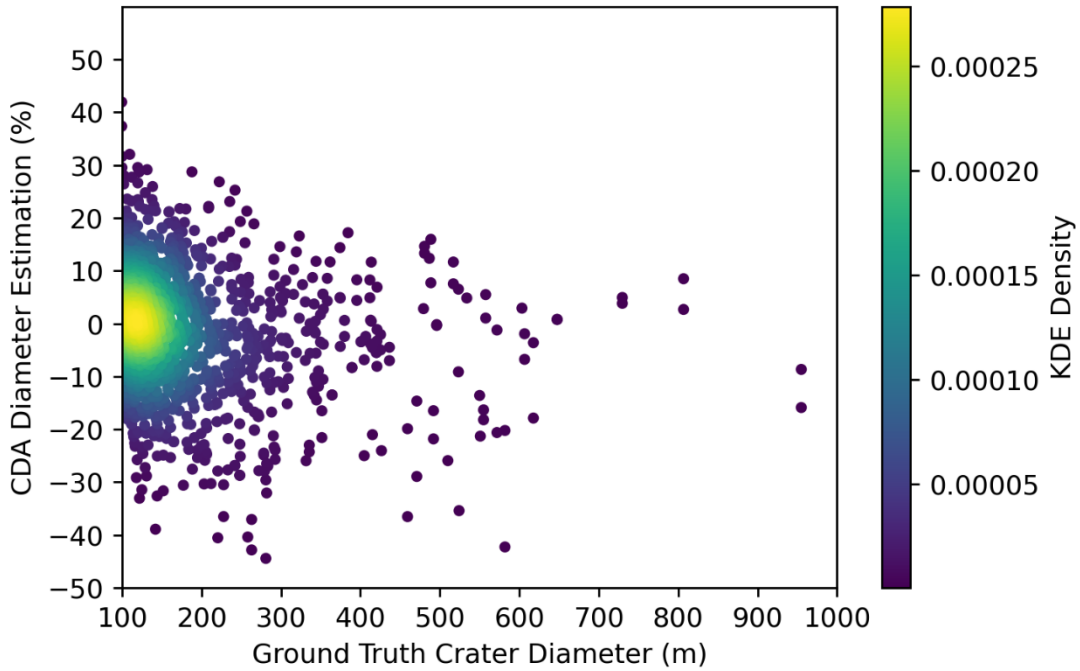

Figure S4.2: Ground Truth crater diameter estimation by the Kaguya CDA (n = 1808). The Point colour coding is calculated using a Kernel Density Estimation (KDE), which colours the spatial density of the points relative to each other; yellow indicates more and blue indicates fewer craters.

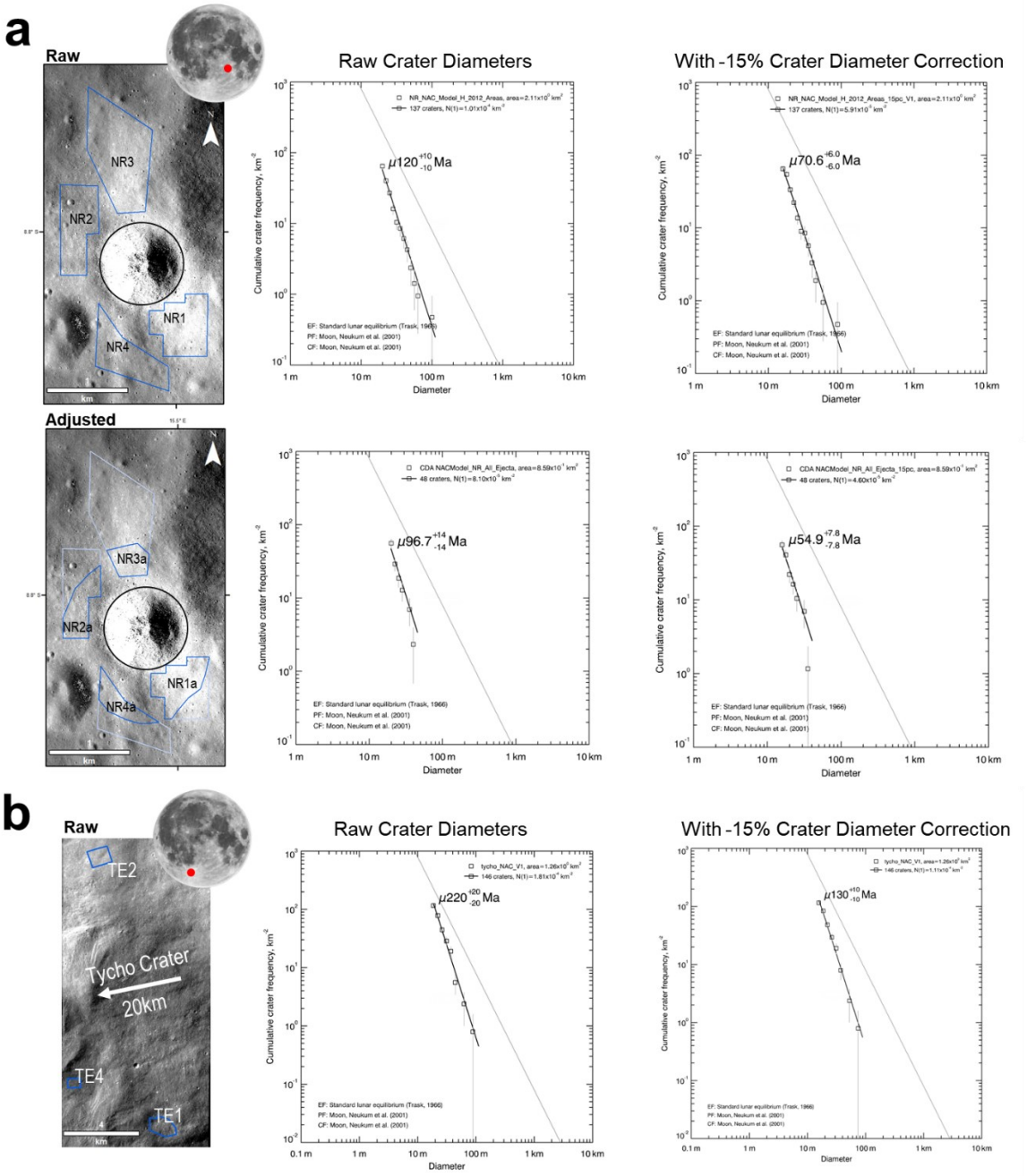

Figure S4.3: CSFD Plots (with count area context images) representing the effects of the 15% diameter correction. (a) North Ray count areas; (b) Tycho NAC count areas. The 'Raw' diameters (left CSFD plots) reflect the craters that have not been corrected. The ages presented in the main manuscript are the corrected ages (right CSFD plots).

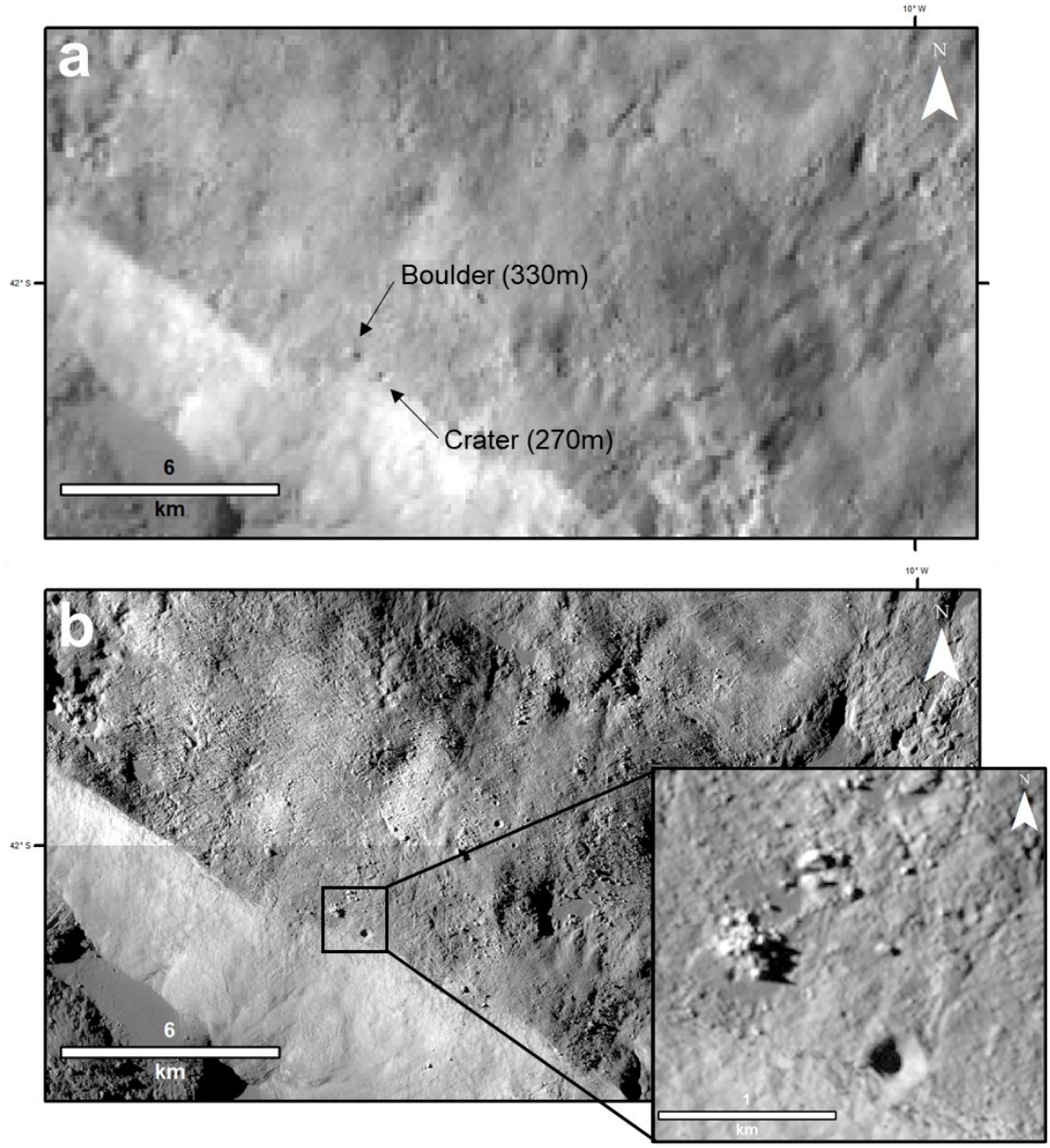

Figure S4.4: (a) Excerpt from the Tycho crater count area displaying the region at 100 m/px (LRO-WAC mosaic, Speyerer et al., 2011); (b) The same area but displayed with the Kaguya TC Tiles morning tiles at ~7 m/px (Isbell et al., 2014), all tile IDs for Tycho are in Table S4.1. Notice the minor differences between a crater and a boulder (of similar size) is difficult to differentiate at lower resolutions.

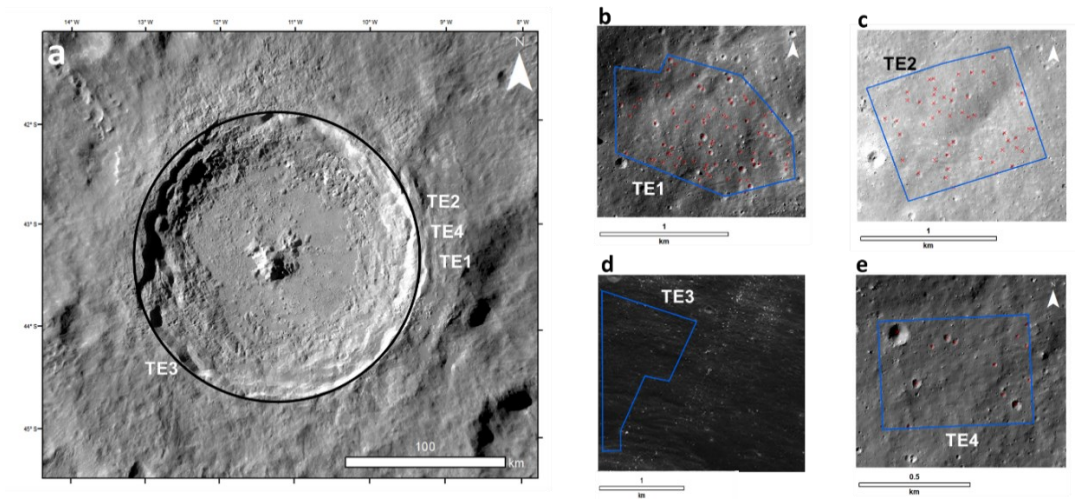

Figure S4.5: Tycho NAC TE crater count areas by Hiesinger et al. (2012) [blue polygons]; (a)Context image showing the locations of each NAC count area around Tycho Crater; (d)Hiesinger et al. (2012) 's count area TE1 (0.58 km^2 on M104570590R/L [Incidence of 62°]);(c) Hiesinger et al. (2012)'s count area TE2 (0.50 km^2 on M104570590R/L [Incidence of 62°]); (d) Hiesinger et al. (2012)'s count area TE3 (1.24 km^2 on M109312132R [Incidence of 43°]);(e) Hiesinger et al. (2012)'s count area TE4 (0.17 km^2 on M104570590R/L [Incidence of 62°]). The red crossed are the CDA crater detections, when present.

4.4: Supplemental Tables

Table S4.1: Kaguya TC 3° x 3° image tiles for each region of interest analysed in this study. In the image tile ID 'MAPe04' refers to evening tiles and 'MAPm04' refers to morning tiles. The coordinates for each image tile are in the tile ID and are in degree east format (the full evening and morning datasets are available at the Kaguya Data Archive, https://darts.isas.jaxa.jp/planet/pdap/selene/).

Tycho	**Chang'e-5**
TCO_MAPm04_S39E345S42E348SC	TCO_MAPe04_N45E306N42E309SC
TCO_MAPm04_S39E348S42E351SC	TCO_MAPe04_N45E309N42E312SC
TCO_MAPm04_S42E345S45E348SC	
TCO_MAPm04_S42E348S45E351SC	**Area P60**
TCO_MAPm04_S42E351S45E354SC	TCO_MAPm04_N24E303N21E306SC
TCO_MAPm04_S45E345S48E348SC	TCO_MAPm04_N24E306N21E309SC
TCO_MAPm04_S45E348S48E351SC	
TCO_MAPm04_S45E351S48E354SC	**Area I30**
	TCO_MAPe04_N30E330N27E333SC
Copernicus	TCO_MAPe04_N30E333N27E336SC
TCO_MAPe04_N09E336N06E339SC	TCO_MAPe04_N33E330N30E333SC
TCO_MAPe04_N09E339N06E342SC	TCO_MAPe04_N33E333N30E336SC
TCO_MAPe04_N09E342N06E345SC	
TCO_MAPe04_N12E336N09E339SC	**Evaluation Mare**
TCO_MAPe04_N12E339N09E342SC	TCO_MAPe04_N30E006N27E009SC
TCO_MAPe04_N12E342N09E345SC	TCO_MAPm04_N30E006N27E009SC
TCO_MAPe04_N15E336N12E339SC	
	Evaluation Highland
Lalande	TCO_MAPe04_S09E006S12E009SC
TCO_MAPe04_S03E348S06E351SC	TCO_MAPm04_S09E006S12E009SC
TCO_MAPe04_S03E351S06E354SC	

Table S4.2: Summary of the Kaguya CDA metrics for the model evaluation, with crater count numbers and metric values subdivided by crater diameter size. 'CDA' refers to the total craters counts made by the CDA.

	Diameter (m)	Morning		Evening		Sum
		Mare	Highland	Mare	Highland	
GT	≥100	377	528	391	549	1845
	≥200	96	101	88	101	386
	≥400	14	23	14	25	76
	≥800	1	4	1	6	12
CDA	≥100	408	531	414	571	1924
	≥200	101	102	139	112	454
	≥400	16	23	17	28	84
	≥800	1	5	1	6	13
TP	≥100	373	513	386	536	1808
	≥200	94	94	84	97	369
	≥400	14	23	13	25	75
	≥800	1	4	1	6	12
FP	≥100	35	18	28	35	116
	≥200	7	8	55	15	85
	≥400	2	0	4	3	9
	≥800	0	1	0	0	1
FN	≥100	4	15	5	13	37
	≥200	2	7	4	4	17
	≥400	0	0	1	0	1
	≥800	0	0	0	0	0
Metric						**Average**
Recall	≥100	0.99	0.97	0.99	0.98	0.98
	≥200	0.98	0.93	0.95	0.96	0.96
	≥400	1.00	1.00	0.93	1.00	0.98
	≥800	1.00	1.00	1.00	1.00	1.00
Precision	≥100	0.91	0.97	0.93	0.94	0.94
	≥200	0.93	0.92	0.60	0.87	0.83
	≥400	0.88	1.00	0.76	0.89	0.88
	≥800	1.00	0.80	1.00	1.00	0.95
F1 Score	≥100	0.95	0.97	0.96	0.96	0.96
	≥200	0.95	0.93	0.74	0.91	0.88
	≥400	0.93	1.00	0.84	0.94	0.93
	≥800	1.00	0.89	1.00	1.00	0.97
Average		0.96	0.95	0.89	0.95	0.94

Table S4.3: Comparison between the number of craters mapped by Giguere et al. (2022) and the craters automatically detected on Kaguya TC images over the area #05.

Crater diameter (m)	Manual Counts (Giguere et al., 2022)	CDA Detections (This study)
Total	212	4187
>100	212	2349
>200	178	314
>400	16	17
>800	1	2
>1000	1	1

4.5: Supplemental Datasets (Found here: https://doi.org/10.5281/zenodo.8045606).

Dataset S4.1: Kaguya evaluation dataset and shapefiles. This file contains a CSV list of the manual Ground Truth crater counts and the Kaguya CDA detections.

Dataset S4.2: Kaguya detections over ROIs and shapefiles. This folder contains a CSV list that contains all the detections for each ROI (North ray, Tycho, Copernicus, Lalande, Chang'E-5#21 and #05, P60 and I30) used in this analysis. This Dataset also contains the shapefiles for each of the count areas.

Dataset S4.3: CraterStats II files. This folder contains the CraterStatsII files (.scc) for each of the ROIs (North Ray, Tycho, Copernicus, Lalande, Chang'E-5#21 and #05, P60 and I30).

References for Appendix 4: Chapter 4.

Benedix, G. K., Lagain, A., Chai, K., Meka, S., Anderson, S., Norman, C., Bland, P. A., Paxman, J., Towner, M. C., & Tan, T. (2020). Deriving Surface Ages on Mars Using Automated Crater Counting. Earth and Space Science, 7(3). https://doi.org/10.1029/2019EA001005

Fairweather, J. H., Lagain, A., Servis, K., Benedix, G. K., Kumar, S. S., & Bland, P. A. (2022). Automatic Mapping of Small Lunar Impact Craters Using LRO-NAC Images. Earth and Space Science, 9(7). https://doi.org/10.1029/2021EA002177

Jocher, G. (2021). Ultralytics YOLOv3. [Python]. Ultralytics. https://github.com/ultralytics/yolov3

Jocher, G. (2022). Ultralytics YOLOv5. [Python]. Ultralytics. https://github.com/ultralytics/yolov5

Lagain, A., Servis, K., Benedix, G. K., Norman, C., Anderson, S., & Bland, P. A. (2021). Model Age Derivation of Large Martian Impact Craters, Using Automatic Crater Counting Methods. Earth and Space Science, 8(2). https://doi.org/10.1029/2020EA001598

Redmon, J., & Farhadi, A. (2018). YOLOv3: An Incremental Improvement. ArXiv Preprint ArXiv. https://arxiv.org/abs/1804.02767

Redmon, J., Vivvala, S., Girshick, R., & Farhadi, A. (2016). You Only Look Once: Unified, Real-Time Object Detection. Proceedings of the IEEE Conference on Computer Vision and Pattern Recognition (CVPR), 779–788.

Speyerer, E. J., Robinson, M. S., Denevi, B. W., & LROC Science Team. (2011). Lunar Reconnaissance Orbiter Camera Global Morphological Map of the Moon. 2387.

Appendix 5: Chapter 5

The files for this Appendix can be found at:https://doi.org/10.5281/zenodo.10886270

5.1: Images of the datasets used in Chapter 5's analysis

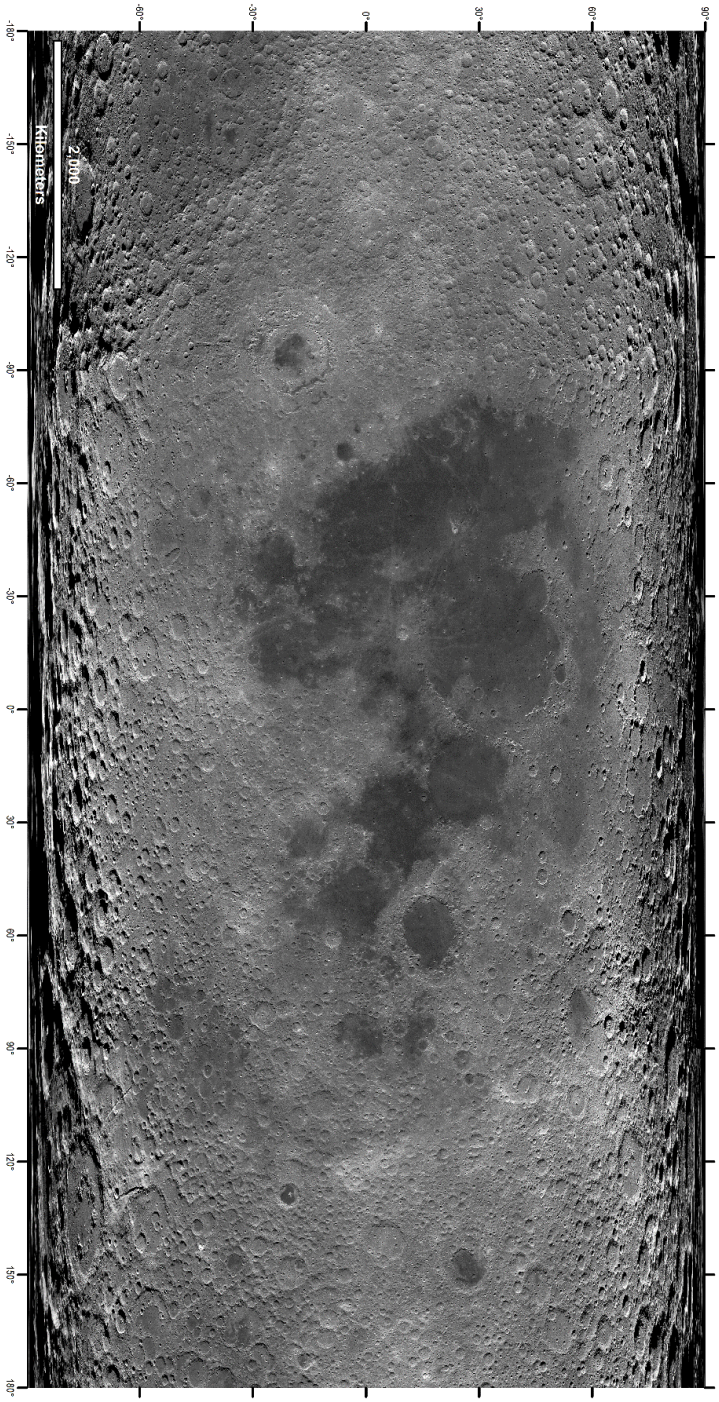

(a) LRO-WAC mosaic (Speyerer et al., 2011) (b [left]) Clementine UVVIS Warped Colour Ratio Mosaic (Lucey et al., 2000)

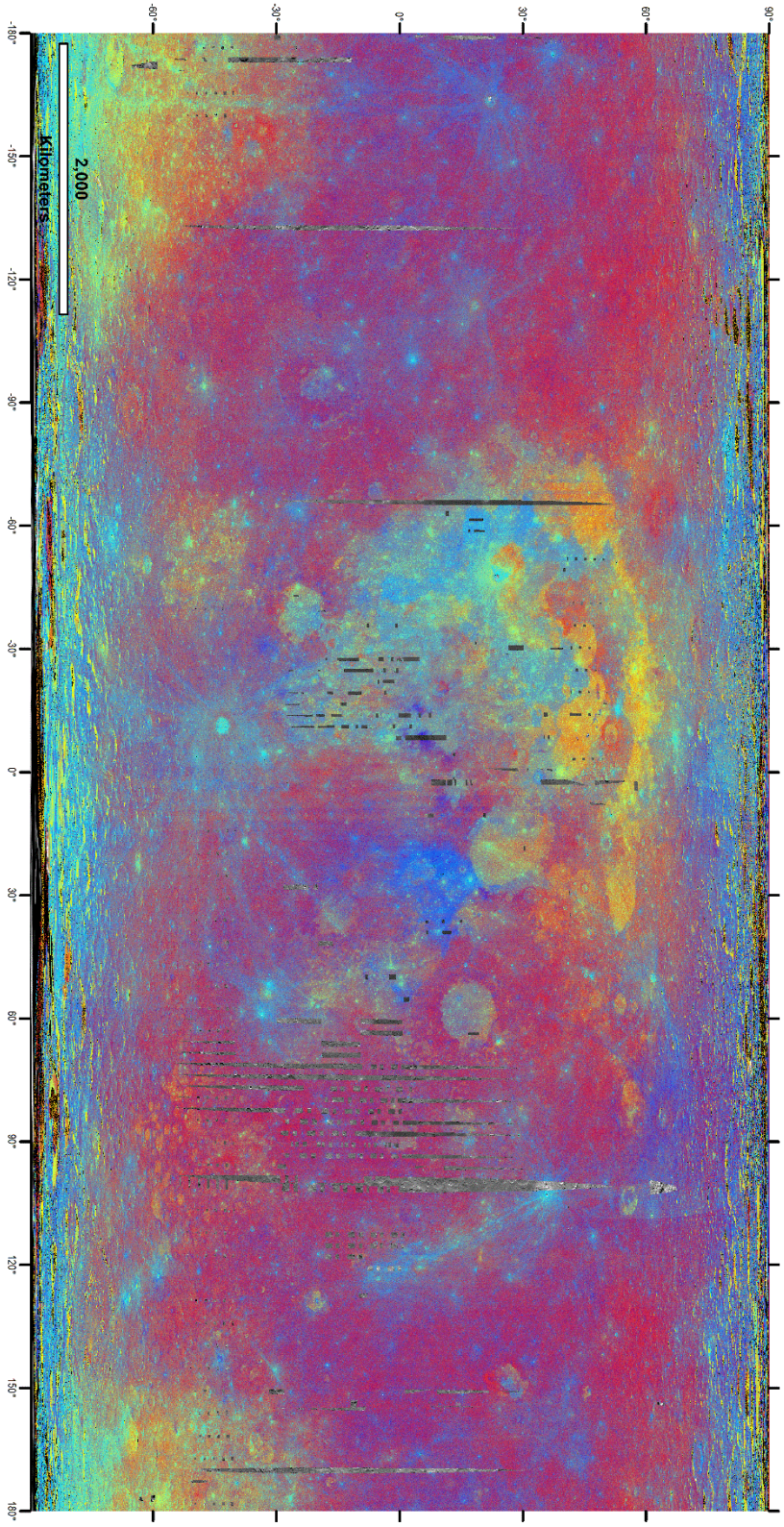

(b [right]) Clementine UVVIS Global Mosaic (Lee et al., 2009).

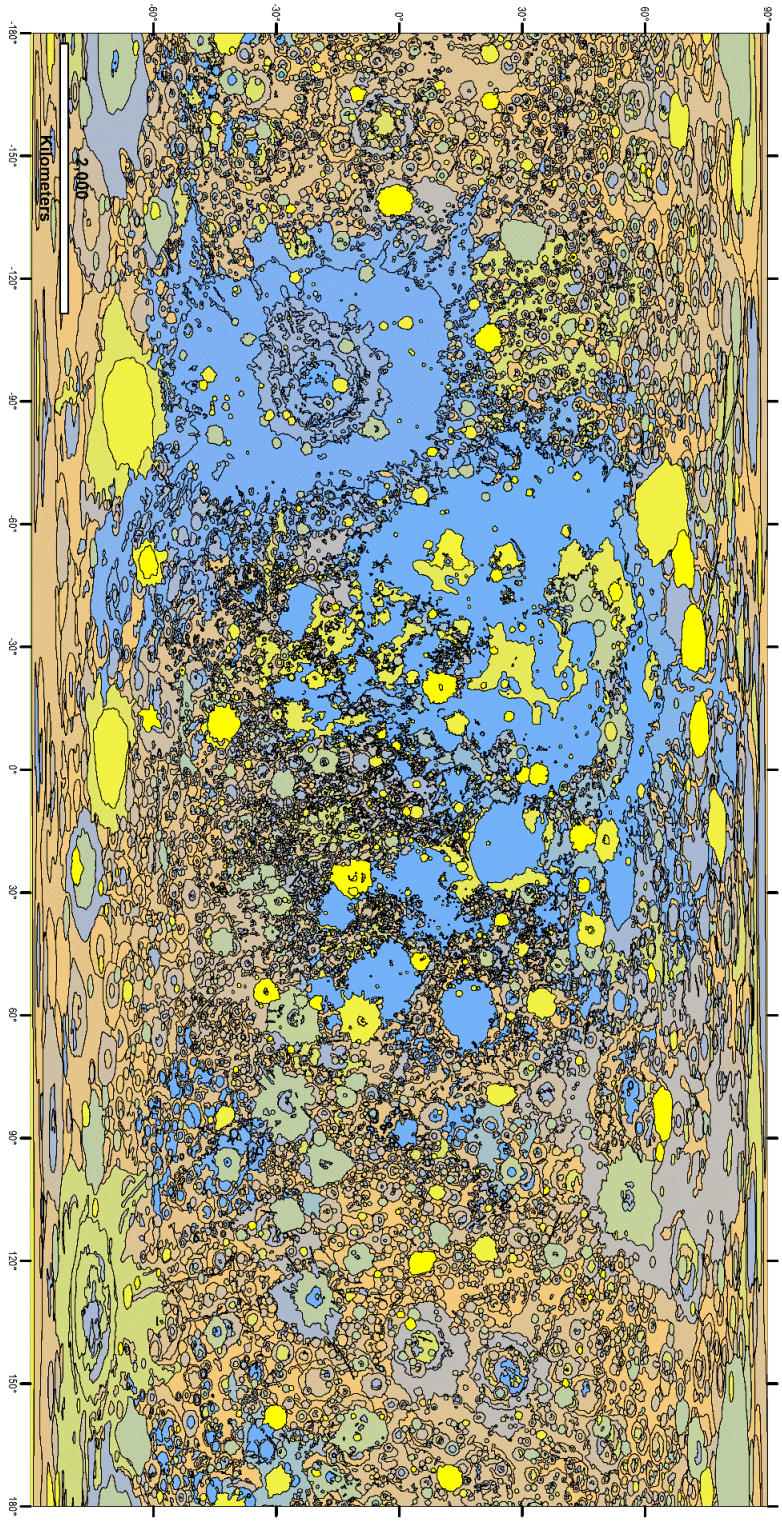

(c) USGS unified geologic map of the Moon (Fortezzo et al., 2020). Note, the yellow and pale-green polygons are Copernican and Eratosthenian craters, respectively.

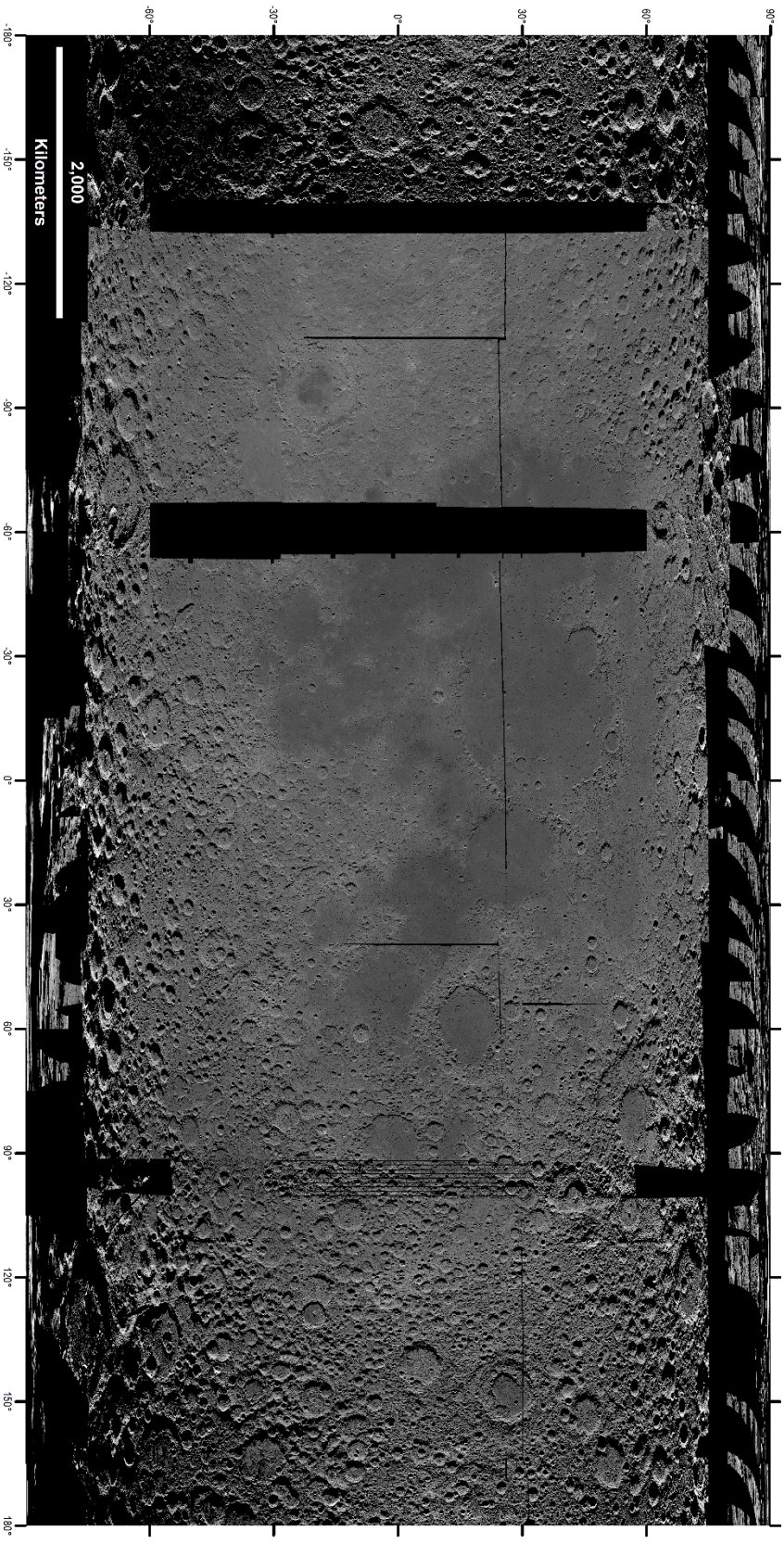

(d) Evening Kaguya TC mosaics (Isbell et al., 2014).

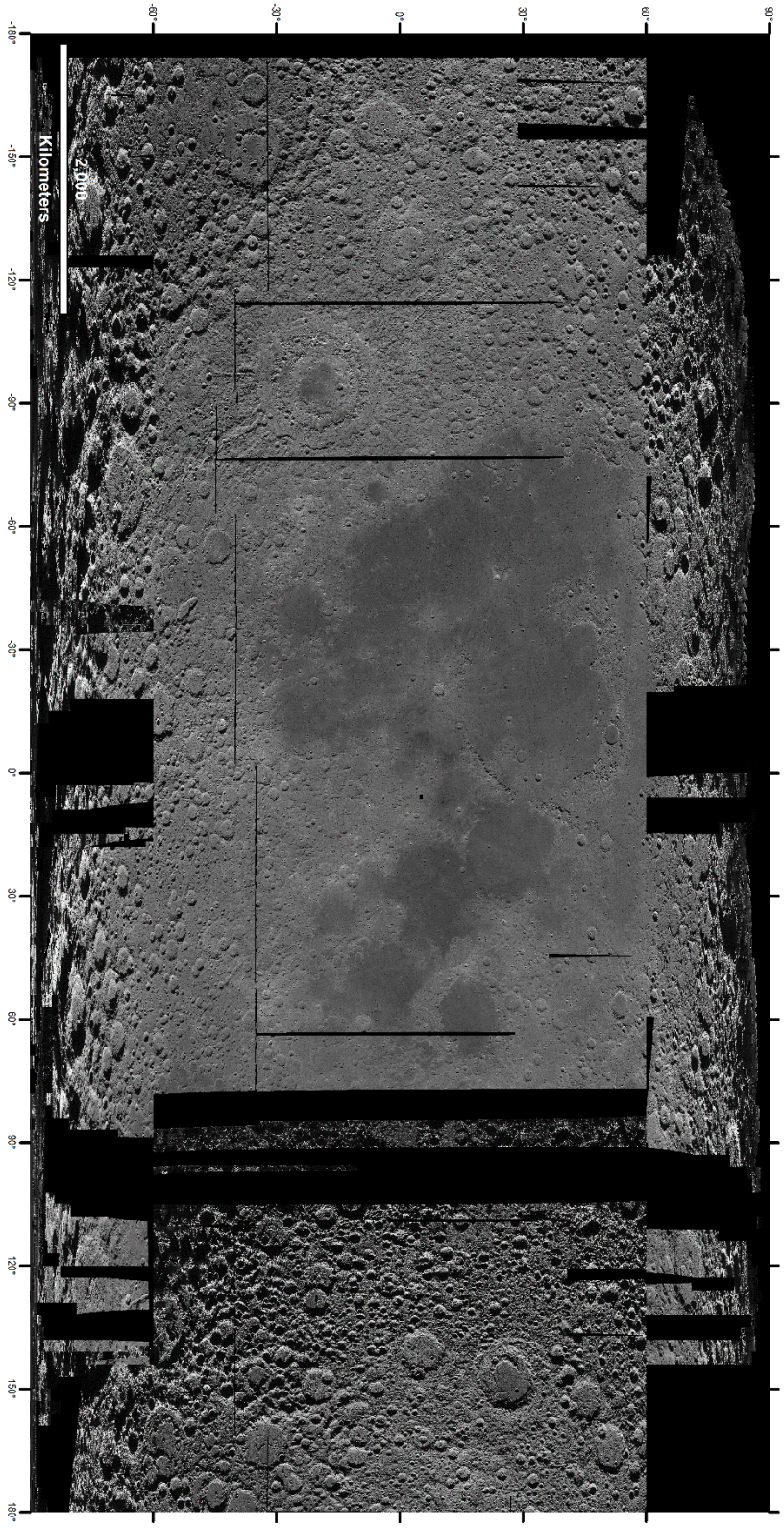

(e) morning Kaguya TC mosaics (Isbell et al., 2014).

5.2: Dated Crater list

DatedCraters.csv

This CSV file contain a list of the 211 crater we analysed in our crater production analysis. In this list we give the locations (longitude and latitude [decimal degrees]), crater diameter (in km), Mapped geological period (as per the Geologic map [Fortezzo et al., 2020], and the derived crater model ages with there +/- error.

The craters files used to derive the model ages are given in Appendix 5.4. Additionally, we have also compiled other analyses model ages for the same craters or nearby surfaces [where applicable] (Heisinger et al., 2011; Kirchoff et al., 2021; Mazrouei et al., 2019; Terada et al., 2020).

The model ages in columns age_L, age_M, age_R, age_H, age_Lef, refer to the chronology models Lagain et al. (2024), Marchi et al. (2009), Robbins (2014), Hartmann et al. (2007), and Le Feuvre and Wieczorek (2011), respectively.

5.3: Crater count area shapefiles

CraterShapefile.zip

This folder contains all the shapefiles used for crater counting. The shapefiles were originally taken from the digitised geologic map of the Moon and then adjusted for our analysis. For the unadjusted shapefiles refer to the geologic map (i.e., Fortezzo, et al. 2020). Note: that this shapefile has craters Reinhold and Von Karman L which are not included in the analysis.

5.4: Dated crater CSFDs, CraterStatsII files (Michael and Neukum, 2010), and CDA craters.

DatedCraterCSFDfiles.zip

This master folder contains 211 sub-folders, one for each analysed crater. Within each subfolder there are the CraterStatIIs input files (V1.scc and V2.scc), the CSFD plot file (.plt and .txt), the crater detections used to generate the CSFD (.csv). Note, V1 files refer to the raw crater detections (those without the pre-existing crater reduction), and V2 refers to the 'adjusted' crater detections (pre-existing craters have been discarded). Some folders have .png images of the craters the CSFDs. Note: this folder has craters Reinhold and Von Karman L which are not includeinIn the analysis.

5.5: Other Chronology Model data

OtherChronModels.zip

This folder contains subfolders with the KS and PDF plots for each of the chronology models used in this analysis. These models are: Neukum et al. (2001), Lagain et al. (2024), Marchi et al. (2009), Robbins (2014), Hartmann et al. (2007), and Le Feuvre and Wieczorek (2011).

References for Appendix 5: Chapter 5.

Fortezzo, C. M., Spudis, P. D., & Harrel, S. L. (2020). Release of the Digital Unified Global Geologic Map of the Moon at 1:5,000,000-Scale. 2760.

Isbell, C., Gaddis, L., Garcia, P., Hare, T., & Bailen, M. (2014). Kaguya Terrain Camera Mosaics. 2268.

Lee, E. M., Gaddis, L. R., Weller, L., Richie, J. O., Becker, T., Shinaman, J., Rosiek, M. R., & Archinal, B. A. (2009). A New Clementine Basemap of the Moon. 2445.

Michael, G. G., & Neukum, G. (2010). Planetary surface dating from crater size–frequency distribution measurements: Partial resurfacing events and statistical age uncertainty. Earth and Planetary Science Letters, 294(3–4), 223–229. https://doi.org/10.1016/j.epsl.2009.12.041

Speyerer, E. J., Robinson, M. S., Denevi, B. W., & LROC Science Team. (2011). Lunar Reconnaissance Orbiter Camera Global Morphological Map of the Moon. 2387.

Hiesinger, H., Head, J. W., Wolf, U., Jaumann, R., & Neukum, G. (2011). Ages and stratigraphy of lunar mare basalts: A synthesis. In W. A. Ambrose & D. A. Williams, Recent Advances and Current Research Issues in Lunar Stratigraphy. Geological Society of America. https://doi.org/10.1130/2011.2477(01)

Kirchoff, M. R., Marchi, S., Bottke, W. F., Chapman, C. R., & Enke, B. (2021). Suggestion that recent (≤ 3 Ga) flux of kilometer and larger impactors in the Earth-Moon system has not been constant. Icarus, 355, 114110. https://doi.org/10.1016/j.icarus.2020.114110

Mazrouei, S., Ghent, R. R., Bottke, W. F., Parker, A. H., & Gernon, T. M. (2019). Earth and Moon impact flux increased at the end of the Paleozoic. Science, 363(6424), 253–257. https://doi.org/10.1126/science.aar4058

Terada, K., Morota, T., & Kato, M. (2020). Asteroid shower on the Earth-Moon system immediately before the Cryogenian period revealed by KAGUYA. Nature Communications, 11(1), 3453. https://doi.org/10.1038/s41467-020-17115-6

Hartmann, W. K., Quantin, C., & Mangold, N. (2007). Possible long-term decline in impact rates. Icarus, 186(1), 11–23. https://doi.org/10.1016/j.icarus.2006.09.009

Lagain, A., Devillepoix, H. A. R., Vernazza, P., Robertson, D., Granvik, M., Pokorny, P., Ozerov, A., Shober, P. M., Jorda, L., Servis, K., Fairweather, J. H., Quesnel, Y., & Benedix, G. K. (2024). Recalibration of the lunar chronology due to spatial cratering-rate variability. Icarus, 411, 115956. https://doi.org/10.1016/j.icarus.2024.115956

Marchi, S., Mottola, S., Cremonese, G., Massironi, M., & Martellato, E. (2009). A New Chronology For The Moon And Mercury. The Astronomical Journal, 137(6), 4936–4948. https://doi.org/10.1088/0004-6256/137/6/4936

Robbins, S. J. (2014). New crater calibrations for the lunar crater-age chronology. Earth and Planetary Science Letters, 403, 188–198. https://doi.org/10.1016/j.epsl.2014.06.038

Le Feuvre, M., & Wieczorek, M. A. (2011). Nonuniform cratering of the Moon and a revised crater chronology of the inner Solar System. Icarus, 214(1), 1–20. https://doi.org/10.1016/j.icarus.2011.03.010

Neukum, G., Ivanov, B. A., & Hartmann, W. K. (2001). Cratering Records in the Inner Solar System in Relation to the Lunar Reference System. In R. Kallenbach, J. Geiss, & W. K. Hartmann (Eds.), Chronology and Evolution of Mars (Vol. 12, pp. 55–86). Springer Netherlands. https://doi.org/10.1007/978-94-017-1035-0_3

THE END

Congratulations on reaching the end of this thesis! You've officially joined an elite club of people with unneeded and unwanted crater-counting knowledge (all assuming you read most of the content … which is unlikely). Remember, the real test begins now: explaining this to your friends and family at gatherings without putting everyone to sleep. Good luck and enjoy the cake!